

Target profiling of PARP inhibitors and necroptosis inhibitors using photoaffinity labelling

Author

RYAN THOMAS HOWARD

Supervisors

PROF. EDWARD TATE

DR. JAMIE SCOTT (AstraZeneca)

Department of Chemistry

IMPERIAL COLLEGE LONDON

Thesis submitted in partial fulfilment of the requirements for the degree of DOCTOR OF
PHILOSOPHY and the DIPLOMA OF IMPERIAL COLLEGE LONDON

11 January 2021

I Declarations

I.i Copyright declaration

The copyright of this Thesis rests with the author. Unless otherwise indicated, its contents are licensed under a [Creative Commons Attribution-NonCommercial 4.0 International Licence](#) (CC BY-NC). Under this licence, you may copy and redistribute the material in any medium or format. You may also create and distribute modified versions of the work. This is on the condition that: you credit the author and do not use it, or any derivative works, for a commercial purpose.

When reusing or sharing this work, ensure you make the licence terms clear to others by naming the licence and linking to the licence text. Where a work has been adapted, you should indicate that the work has been changed and describe those changes. Please seek permission from the copyright holder for uses of this work that are not included in this licence or permitted under UK Copyright Law.

I.ii ACS AuthorChoice licence

For any figure herein that states it is adapted from Howard *et al.* 2020, the following statement applies:

“The adaptation of this figure from “Howard, R. T. *et al.* [Structure-guided design and in-cell target profiling of a cell-active target engagement probe for PARP inhibitors](#). *ACS Chem. Biol.* **15**, 325–333 (2020)” is covered by an ACS AuthorChoice licence which permits the adaptation of any content therein for non-commercial purposes. This is an unofficial adaptation of an article that appeared in an ACS publication. ACS has not endorsed the content of this adaptation or the context of its use.”

I.iii Declaration of originality

I, RYAN THOMAS HOWARD, declare that all of the work published herein is my own, and was produced during my candidature for a DOCTOR OF PHILOSOPHY at IMPERIAL COLLEGE LONDON. Where I have derived information from the work of others, including any direct quotations, this has been appropriately referenced. Any work or materials that are derived from others, or are the result of collaboration with others, have been attributed appropriately. Work that was produced during my preceding MASTERS OF RESEARCH degree at IMPERIAL COLLEGE LONDON has been clearly indicated.

X

RYAN THOMAS HOWARD

Author

“That leaves one, as biology answers do, to ask another question ...”

Derek Lowe, In the Pipeline, 7th October 2019

II Abstract

Target profiling of a small molecule therapeutic is essential to fully understand how that compound works in the clinic. Photoaffinity labelling (PAL) has become a widely utilised strategy for in-cell target identification campaigns for reversible, small molecule drugs. After an overview of target profiling and PAL, this Thesis discusses the application of PAL to two classes of molecules with incomplete target profiles.

The Thesis focusses initially on the generation of the first photo-activatable probe for inhibitors of the PARP family of enzymes, **PARPYnD**, based on a novel anti-cancer PARP1/2/6 inhibitor **AZ0108** with unexplained off-target toxicity. The design, synthesis and validation of the probe is discussed, along with the application of **PARPYnD** to PAL studies. Herein, simultaneous live-cell target engagement of PARP1/2 is shown for the first time by a photo-activatable probe, and this labelling is used to quantify live-cell engagement of these PARPs by known PARP inhibitors in competitive PAL experiments. For **AZ0108** and clinical PARP inhibitor olaparib, novel off-targets are identified, demonstrating the power of PAL to capture weaker, secondary binders. Finally, **PARPYnD** fails to label PARP6 in live cells, but is able to label recombinant PARP6, highlighting a biomolecular disparity that raises questions about the proposed mechanism of action of **AZ0108**.

PAL is then applied to a novel series of inhibitors of necroptosis, an inflammatory form of cell death, with an unknown mechanism of action. Design and synthesis of cell-active photo-activatable probe **7PQYnD1** is presented, along with the development of a bespoke live-cell necroptosis assay to evaluate necroptosis inhibitors in-house. **7PQYnD1** is then applied to the PAL workflow and five *bona fide* target proteins are identified through proteomics. Preliminary functional analysis of these hits is then undertaken to begin to identify the target interaction(s) responsible for the anti-necroptosis phenotype of these compounds.

III Acknowledgements

First and foremost, I would like to thank my supervisor Professor Ed Tate for his outstanding guidance and mentorship. I am grateful to have a supervisor who has really fought my corner, and you have shaped my understanding of what it means to be a great scientist. My research would not have been possible without the consistent support of my AstraZeneca supervisor Dr Jamie Scott, and my other collaborators at AZ: Jeffrey Johannes, Dave Smith, Paul Hemsley and Philip Petteruti. Also, thank you to my collaborators at the University of Lisbon, Professor Rui Moreira and Professor Cecília Rodrigues, for allowing me to join their necroptosis family.

Thank you to AZ/EPSRC for funding this project and to the Institute of Chemical Biology for fostering a great community, especially my extended ICB family Malte, Giulia, Chiara, and Chris. I must also thank the support staff in the Department of Chemistry who facilitated various aspects of this project, particularly Andrew Coulson for managing the Tissue Culture facility, Lisa Haigh and Trevor Ferris for their support with proteomics and mass spectrometry, and Pete Haycock for his NMR expertise.

No document this unwieldy goes unedited, so I am greatly appreciative of the time Tom, Jonathan, Dan L, Wouter, Elena, and Dan C spent proofreading various sections of this Thesis – I owe you all a drink.

As a member of the Tate group, I have been privileged to be a part of a friendly, diverse and impressive group of scientists. Special mention must go to Cassandra, my sister in photochemical arms, who made coming to work every day a joy. I was lucky enough to supervise two very talented students: thank you Javi and Chotima for your efforts. Finally, to Jasmine, Kwang, Wouter, Jennie, Andrea, Theo, Kate, Charlie, and all group members past and present for the bevs and the good times!

On a personal note, I am lucky to call many people my friends, and each have provided me with a much-needed escape after long hours of pipetting. To my Amaretto Crew: Megan, Oliver, and Ariadne – you have made my time in London so special, and your fierce support and high spirits have kept me sane throughout my Ph.D.; the Kahlua shots are on me. To my Manchester gang, Phil and Lee, for always indulging my choice of nightclub and giving me a home away from home, you are the greatest.

To Mum and Dad, nothing achieved thus far in my life could have been done without your love and support. Though you have had to endure time and time again as I have announced my desire to pursue yet another degree, I hope I have made you proud. Also thank you to my sister, Abigail, for whom university life is just beginning; I hope you enjoy the ride as much as I have.

Finally, to my boyfriend Jonathan, I could not have done this without your unending support. You have lifted me up when I am down and celebrated every one of my little wins. You inspire me every day to be a better scientist and a better person. I hope you know how much you mean to me, for the best thing about this entire Ph.D. was that I got to meet you. I love you.

IV Contributions from collaborators

1. The following materials and associated work required to deliver these materials were contributed by AstraZeneca:
 - **AZ9482** – Synthesis and purification,
 - **AZ0108** – Synthesis and purification,
 - **AZ'902** – Synthesis and purification,
 - FLAG-tagged PARP6 gene in a pcDNA3.1 mammalian expression vector – Expression and purification,
 - GST-tagged PARP6 recombinant protein – Expression and purification.
2. Fluorescence anisotropy competition assays for PARP-binding characterisation and the cellular multipolar spindle assay were carried out at AstraZeneca by Philip Petteruti and Paul Hemsley respectively.
3. The LED boxes used for UV-irradiation experiments were constructed in-house by Charlie Saunders.
4. The MDA-MB-468 cells used herein were kindly donated by the Francis Crick Cell Service institute.

V Publications and presentations

V.i Publications

Howard, R. T. *et al.* Structure-guided design and in-cell target profiling of a cell-active target engagement probe for PARP inhibitors. *ACS Chem. Biol.* **15**, 325–333 (2020).

Panyain, N., Kennedy, C. R., Howard, R. T. & Tate, E. W. Activity-Based Protein Profiling. in *Target Discovery and Validation: Methods and Strategies for Drug Discovery* (eds. Plowright, A. T., Mannhold, R., Buschmann, H. & Holenz, J.) 51–83 (WILEY-VCH Verlag, 2019).

Wang, Z. *et al.* Pharmacological Inhibition of PARP6 Triggers Multipolar Spindle Formation and Elicits Therapeutic Effects in Breast Cancer. *Cancer Res.* **78**, 6691–6702 (2018).

V.ii Oral presentations

R. Howard *et al.* ‘Target discovery for novel inhibitors of necroptosis’ *Faculty of Natural Sciences Research Showcase, Imperial College London, London, U.K., September 2020.*

*R. Howard *et al.* ‘Target discovery for novel inhibitors of necroptosis’ *Department of Chemistry Postgraduate Symposium, Imperial College London, London, U.K., July 2020.*

R. Howard *et al.* ‘Target discovery for novel inhibitors of necroptosis’ *Chemical Biology and Drug Discovery Seminar Series, Imperial College London, London, U.K., July 2020.*

V.iii Poster presentations

R. Howard *et al.* ‘A chemical probe for live-cell PARP profiling’ *RSC Twitter Conference, Worldwide, March 2020.*

*R. Howard *et al.* ‘A chemical probe for live-cell PARP profiling’ *RSC Organic Division London & South East Regional Meeting, Kingston University, London, U.K., February 2020.*

R. Howard *et al.* ‘A chemical probe for live-cell PARP profiling’ *Expanding the druggable proteome with Chemical Biology, EMBL, Heidelberg, Germany, February 2020.*

R. Howard *et al.* ‘Photoaffinity labelling: a versatile approach to target identification in two clinically relevant systems’ *London Chemical Biology Symposium, Imperial College London, London, U.K., July 2019.*

R. Howard *et al.* ‘Photoaffinity labelling: a versatile approach to target identification in two clinically relevant systems’ *Department of Chemistry Postgraduate Symposium, Imperial College London, London, U.K., July 2019.*

R. Howard *et al.* ‘Using affinity-based protein profiling to probe the cellular targets of a promising anti-cancer therapeutic’ *RSC Chemical Biology Symposium, Burlington House, London, U.K., May 2019.*

R. Howard *et al.* ‘Using affinity-based protein profiling to probe the cellular targets of a promising anti-cancer therapeutic’ *RSC Postgraduate Symposium in Chemical Biology, University of Southampton, Southampton, U.K., April 2019.*

R. Howard *et al.* ‘Using affinity-based protein profiling to probe the cellular targets of a promising anti-cancer therapeutic’ *Activity-based protein profiling (ABPP), Leuven, Belgium, April 2019.*

(* denotes prize awarded for delivery and content)

VI Table of contents

I	Declarations	3
I.i	Copyright declaration.....	3
I.ii	ACS AuthorChoice licence.....	3
I.iii	Declaration of originality	3
II	Abstract.....	5
III	Acknowledgements.....	6
IV	Contributions from collaborators	7
V	Publications and presentations	8
V.i	Publications.....	8
V.ii	Oral presentations	8
V.iii	Poster presentations	8
VI	Table of contents.....	10
VII	List of figures.....	15
VIII	List of tables.....	18
IX	List of schemes	19
X	List of abbreviations	20
Chapter 1	Introduction.....	28
1.1	The utility of target profiling in drug discovery.....	29
1.1.1	Identifying the target of interest.....	29
1.1.2	Off-target identification	30
1.1.3	Assessing target engagement	31
1.2	Target profiling methodologies.....	31
1.2.1	Label-assisted target profiling.....	33
1.3	Photoaffinity labelling (PAL)	36
1.3.1	AfBP Design	36
1.3.2	Photoreactive warhead	37
1.3.2.1	Diazo compounds.....	37
1.3.2.2	Aryl azides	38
1.3.2.3	Benzophenones	39
1.3.2.4	2-Aryl-5-carboxytetrazoles	40
1.3.2.5	Thienyl-substituted α -ketoamides	41
1.3.2.6	Diazirines	41
1.3.2.7	Comparison of photoreactive warheads	43
1.3.3	Ligation handles.....	44
1.3.4	Minimalist diazine photocrosslinkers.....	47
1.4	Affinity-based protein profiling workflow.....	53

1.4.1 Reporter molecules	53
1.4.2 Analysis techniques.....	55
1.4.2.1 In-gel fluorescence.....	55
1.4.2.2 Western blot.....	56
1.4.2.3 Chemical proteomics.....	57
1.5 Thesis aims.....	60
Chapter 2 Target profiling of novel and existing poly(ADP-ribose) polymerase inhibitors	61
2.1 Poly(ADP-ribose) polymerases (PARPs)	61
2.1.1 PARPs and ADP-ribosylation.....	61
2.1.2 ADP-ribosylation in biology and disease.....	63
2.1.2.1 PARylation.....	63
2.1.2.2 MARylation	65
2.1.3 PARP inhibition	66
2.1.3.1 PARP and BRCA: Synthetic lethality.....	66
2.1.3.1.1 Olaparib and other PARP1 inhibitors	67
2.1.3.1.2 PARPi beyond PARP1 and cancer.....	69
2.1.4 Previous PARP profiling campaigns.....	69
2.1.4.1 Label-free PARP profiling	69
2.1.4.2 Label-assisted PARP profiling.....	70
2.2 Research objectives.....	72
2.3 Results and Discussion	73
2.3.1 Background: AstraZeneca and PARPi.....	73
2.3.1.1 Discovery of AZ0108	73
2.3.1.2 Mechanism of action.....	74
2.3.2 Probe design and synthesis	75
2.3.3 Probe validation	77
2.3.3.1 Biophysical characterisation	77
2.3.3.2 Phenotypic characterization	78
2.3.3.3 Assessment of photocrosslinking efficiency	79
2.3.4 Affinity-based protein profiling.....	81
2.3.4.1 Gel-based analysis.....	81
2.3.4.2 Chemical proteomics.....	83
2.3.4.2.1 Protein labelling profile of PARPYnD	84
2.3.4.2.2 Competition experiments	86
2.3.4.2.3 Non-competed proteins	88
2.3.4.3 Overexpression of FLAG-PARP6	90
2.3.4.4 Recombinant PARP6	91
2.3.4.4.1 Solution-based photocrosslinking	93

2.3.4.4.2 Lysate-based photocrosslinking.....	93
2.3.4.4.3 GST-tag influence on photocrosslinking	95
2.4 Conclusions and future work	97
Chapter 3 Target profiling of novel necroptosis inhibitors.....	99
3.1 Necroptosis and inflammatory cell death.....	99
3.1.1 Cell death in mammalian cells.....	99
3.1.2 Necroptosis	101
3.1.2.1 Cellular mechanism.....	101
3.1.2.2 Association with disease	104
3.1.3 Pharmacological inhibition of necroptosis.....	105
3.1.3.1 RIPK1 inhibitors	105
3.1.3.2 RIPK3 inhibitors	107
3.1.3.3 MLKL inhibitors.....	108
3.1.4 Discovery of novel necroptosis inhibitors.....	109
3.2 Research objectives.....	111
3.3 Results and discussion	112
3.3.1 Probe design and synthesis	112
3.3.1.1 Synthesis of 7PQYnD1	115
3.3.1.2 Synthesis of 7PQYnD2	116
3.3.2 Probe validation	118
3.3.2.1 Necroptosis assay development	118
3.3.2.1.1 Optimisation of Sytox Green	118
3.3.2.1.2 Optimisation of TNF α	122
3.3.2.1.3 Probe and inhibitor testing	124
3.3.2.2 Optimisation of photocrosslinking.....	126
3.3.3 Target profiling	127
3.3.3.1 In-gel fluorescence.....	127
3.3.3.2 Chemical proteomics.....	129
3.3.3.2.1 Label-free quantification.....	129
3.3.3.2.2 Tandem mass tag quantification.....	133
3.3.4 Target validation	137
3.3.5 Functional evaluation of targets.....	139
3.3.5.1 Adenosine deaminase (ADA)	140
3.3.5.2 RNA interference	145
3.3.5.2.1 Validation of knockdown.....	145
3.3.5.2.2 RNAi and necroptosis.....	146
3.4 Conclusions and future work	149
Chapter 4 Conclusions and outlook.....	151

4.1 The merits of target profiling in drug discovery	151
4.2 Future directions	152
Chapter 5 Materials and Methods.....	155
5.1 Materials	155
5.2 Chemical synthesis.....	155
5.2.1 General chemical methods	155
5.2.2 2-(3-methyl-3 <i>H</i> -diazirin-3-yl)ethan-1-ol (13).....	156
5.2.3 2-(3-methyl-3 <i>H</i> -diazirin-3-yl)ethyl 4-methylbenzenesulfonate (14)	157
5.2.4 2-nitro- <i>N</i> -(prop-2-yn-1-yl)benzenesulfonamide (17).....	158
5.2.5 <i>N</i> -(2-(3-methyl-3 <i>H</i> -diazirin-3-yl)ethyl)-2-nitro- <i>N</i> -(prop-2-yn-1-yl)benzenesulfonamide (18)	158
5.2.6 <i>N</i> -(2-(3-methyl-3 <i>H</i> -diazirin-3-yl)ethyl)prop-2-yn-1-amine (19)	159
5.2.7 4-(quinolin-7-yl)aniline (22)	160
5.2.8 4-(quinolin-7-yl)benzenesulfonyl chloride (23).....	160
5.2.9 <i>N</i> -(2-(3-methyl-3 <i>H</i> -diazirin-3-yl)ethyl)- <i>N</i> -(prop-2-yn-1-yl)-4-(quinolin-7-yl)benzenesulfonamide (10 , 7PQYnD1)	161
5.2.10 4-(quinolin-7-yl)benzoic acid (25).....	162
5.3 Cell biology.....	163
5.3.1 Tissue Culture	163
5.3.2 Multipolar Spindle Assay.....	163
5.3.3 Cell Viability Assay (MTS)	164
5.3.4 Necroptosis and cytotoxicity assay	164
5.3.4.1 Plate treatment and image acquisition.....	164
5.3.4.2 Image analysis.....	165
5.3.4.3 Data analysis	166
5.3.5 Probe labelling (photocrosslinking) assays	167
5.3.5.1 MDA-MB-468 cells	167
5.3.5.2 I2.1 cells.....	167
5.3.6 Transient overexpression	168
5.3.7 RNA interference	168
5.3.7.1 siRNA duplexes	168
5.3.7.2 Protocol.....	168
5.4 Biochemistry	169
5.4.1 Click reaction	169
5.4.2 Gel electrophoresis.....	170
5.4.3 Pull down	171
5.4.4 Western Blot	171
5.4.5 In vitro photocrosslinking assays.....	172

5.4.5.1 In solution	172
5.4.5.2 In lysates	172
5.4.5.2.1 Variation with Prescission™ Protease	172
5.5 Chemical proteomics	173
5.5.1 General methods	173
5.5.2 Peptide preparation	173
5.5.2.1 Label-free quantification.....	173
5.5.2.2 Tandem mass tag (TMT) quantification	173
5.5.3 Peptide desalting	174
5.5.3.1 Stage tipping	174
5.5.3.2 3-layer fractionation.....	174
5.5.3.3 6-layer fractionation.....	174
5.5.4 LC-MS/MS methodology	175
5.5.5 Data analysis	175
5.5.5.1 MaxQuant and Perseus.....	175
5.5.5.2 PEAKS.....	176
5.6 Biochemical assays	176
5.6.1 PARP6 auto-ADP ribosylation assay.....	176
5.6.2 In vitro PARP fluorescence anisotropy binding assays	177
5.6.2.1 Dilution of various PARP proteins and fluorescence anisotropy probe.....	177
5.6.2.2 Experimental protocol.....	177
5.7 Molecular Biology	177
5.7.1 General methods	177
5.7.2 Plasmid production	178
Chapter 6 References.....	179
XI Appendices.....	205
XI.i Appendix I – Plasmid map for FLAG-PARP6 in pcDNA3.1	205
XI.ii Appendix II – Amino acid sequence of GST-PARP6.....	206
XI.iii Appendix III – TMT labelling	207
XI.iii.i PARP target profiling.....	207
XI.iii.ii Necroptosis target profiling	208
XI.iv Appendix IV – Supplementary synthetic methods – failed reactions	209
6.1.1 <i>N</i> -(2-(3-methyl-3 <i>H</i> -diazirin-3-yl)ethyl)- <i>N</i> -(prop-2-yn-1-yl)-4-(quinolin-7-yl)benzamide (11 , 7PQYnD2)	209
6.1.2 4-(quinolin-7-yl)benzenesulfonyl chloride (23).....	209

VII List of figures

Figure 1.1 Target profiling and its uses within the drug discovery pipeline.....	30
Figure 1.2 Comparison of methodologies in target profiling.....	33
Figure 1.3 Label-assisted approaches to target profiling.	34
Figure 1.4 General structure of an AfBP.	37
Figure 1.5 Timeline of development of various diazirine-containing “minimalist” diazirine-containing photocrosslinking groups.	49
Figure 1.6 Workflow of affinity-based protein profiling (AfBPP).	54
Figure 1.7 Reporter molecules designed and synthesised in the Tate group.	55
Figure 1.8 The principle of competition experiments.	56
Figure 1.9 Trypsin processing of a probe-modified peptide.	57
Figure 1.10 Peptide labelling with TMT10plex™ reagents.....	59
Figure 2.1 PARPs and ADP-ribosylation.	62
Figure 2.2 Schematic of the DNA-damage repair (DDR) mechanism mediated by PARP1.	64
Figure 2.3 Synthetic lethality between BRCA and PARP1.	67
Figure 2.4 PARPi developed to combat cancers with deficiencies in <i>BRCA</i> and homologous recombination.	68
Figure 2.5 Target profiling probes for PARP enzymes and PARPi.....	71
Figure 2.6 PARP inhibition as a mechanism to induce a cytotoxic multipolar spindle (MPS) phenotype in cancer.	74
Figure 2.7 Design of probe PARPYnD	76
Figure 2.8 Fluorescence anisotropy competition dose-response curves for PARPYnD	78
Figure 2.9 Phenotypic validation of PARPYnD	79
Figure 2.10 Optimisation of PARPYnD photocrosslinking in MDA-MB-231 cells.	80
Figure 2.11 Gel and Western blot analysis of the binding profile of PARPYnD and its parent molecules. MDA-MB-468 cells were treated as indicated, irradiated and lysed.	82
Figure 2.12 Gel and Western blot analysis of the binding profile of PARPYnD at higher concentrations.	83
Figure 2.13 Labelling profile of PARPYnD in MDA-MB-468 cells.....	84
Figure 2.14 Labelling profile of PARPYnD in MDA-MB-468 cells without UV irradiation.	86
Figure 2.15 Volcano plots for PARPYnD competition experiments.	87
Figure 2.16 STRING molecular interaction analysis of proteins enriched by PARPYnD and competed by the parent molecules.	88
Figure 2.17 STRING molecular interaction analysis of all proteins enriched by PARPYnD excluding known background diazirine binders.	89

Figure 2.18 Optimisation of FLAG-PARP6 transfection conditions in MDA-MB-468 cells.	90
Figure 2.19 Attempted enrichment of overexpressed FLAG-PARP6 by PARPYnD	91
Figure 2.20 PARP6 protein constructs used in this work.	92
Figure 2.21 GST-PARP6 auto-modification assay.	92
Figure 2.22 GST-PARP6 labelling by PARPYnD <i>in vitro</i>	93
Figure 2.23 PARPYnD crosslinking to GST-PARP6 in lysates.	94
Figure 2.24 Location of the HRV3C cleavage site in GST-PARP6.	95
Figure 2.25 PARPYnD crosslinking to protease-cleaved GST-PARP6 in MDA-MB-468 lysates.	96
Figure 2.26 Olaparib-based photoreactive AfBPs developed by the van der Stelt group.	98
Figure 3.1 Types of regulated cell death (RCD).	100
Figure 3.2 TNF α induction of apoptosis, necroptosis and the inflammatory response.	102
Figure 3.3 Biomolecular pathway of RIPK1-induced necroptosis.	104
Figure 3.4 Previously reported RIPK1 inhibitors as potential necroptosis modulators.	107
Figure 3.5 Previously reported RIPK3 inhibitors as potential necroptosis modulators.	108
Figure 3.6 Previously reported MLKL inhibitors as potential necroptosis modulators.	109
Figure 3.7 High throughput screening pipeline for new necroptosis inhibitors performed by Brito <i>et al.</i>	110
Figure 3.8 Novel pharmacophores uncovered from HTS with unknown mechanisms of action.	111
Figure 3.9 Structure-activity relationship data of the 7PQ analogues from the HTS.	113
Figure 3.10 Probe designs for 7PQ pharmacophore.	114
Figure 3.11 Apparent instability of 7PQYnD2	117
Figure 3.12 Optimisation of Sytox Green treatment in the necroptosis assay.	120
Figure 3.13 TNF α dose-response in necroptosis assay.	121
Figure 3.14 Optimisation of TNF α in necroptosis assay.	123
Figure 3.15 Nec-1 inhibition of necroptosis.	124
Figure 3.16 Testing of AZ'902 and 7PQYnD1 in necroptosis assay.	125
Figure 3.17 Optimisation of 7PQYnD1 photocrosslinking in I2.1 cells.	127
Figure 3.18 Competition profile of 7PQYnD1 by in-gel fluorescence.	128
Figure 3.19 Label-free quantification target profiling of 7PQYnD1 and AZ'902	130
Figure 3.20 Label-free quantification target profiling of 7PQYnD1 and AZ'902 with missing values imputed.	132
Figure 3.21 Heat map of key proteins identified through LFQ proteomic profiling of 7PQYnD1	133
Figure 3.22 Tandem mass tag target profiling of 7PQYnD1	134
Figure 3.23 Heat map of key proteins identified through TMT proteomic profiling of 7PQYnD1	136
Figure 3.24 Western blot analysis of the 7PQYnD1 enriched proteome.	138
Figure 3.25 STRING molecular interaction analysis of proteins involved in necroptosis (from Figure 3.2, Figure 3.3) and including those identified in 7PQYnD1 competitive AfBPP experiments.	139

Figure 3.26 Adenosine deaminase function and inhibition.....	141
Figure 3.27 7PQYnD1 binding site analysis of adenosine deaminase.	142
Figure 3.28 7PQYnD1 competition at ADA binding site with pentostatin.....	143
Figure 3.29 Necroptosis and cytotoxicity assays with (a) pentostatin and (b) inosine.	144
Figure 3.30 Optimisation of siRNA knockdown of indicated genes in I2.1 cells.....	146
Figure 3.31 Necroptosis assays after siRNA knockdown of indicated genes in I2.1 cells.	147
Figure 5.1 Standard plate map for necroptosis and cytotoxicity assay.	165

VIII List of tables

Table 1.1 Summary of some available strategies to perform drug target profiling.	32
Table 1.2 Comparison of various photoreactive warheads.	44
Table 1.3 Summary of available click reactions for probe/reporter conjugation, adapted from Panyain <i>et al.</i> 2019. ⁷⁵	45
Table 1.4 Representative examples of diazirine affinity-based probes for target ID/profiling studies.	50
Table 2.1 Activity and catalytic motifs of the PARP family of enzymes.	63
Table 2.2 Biochemical/biophysical parameters associated with olaparib, AZ9482 , AZ0108 and PARPYnD	78
Table 2.3 Proteins identified through AfBPP experiments with PARPYnD	85
Table 3.1 Peptide spectral counts and sequence coverage for top 7PQYnD1 protein profiling hits from TMT-proteomics data.	140
Table 5.1 siRNA molecules used in RNAi assays.	169
Table 5.2 SDS-PAGE gel casting recipe (makes two gels).	170
Table 5.3 Buffers used for three-layer fractionation.	174
Table 5.4 Buffers used for six-layer fractionation.	175

IX List of schemes

Scheme 1.1 Synthesis and photoreactivity of diazo compounds.	38
Scheme 1.2 Synthesis and photoreactivity of aryl azides.	38
Scheme 1.3 Synthesis and photoreactivity of benzophenones.	39
Scheme 1.4 Synthesis and photoreactivity of 2-aryl-5-carboxytetrazoles.	40
Scheme 1.5 Synthesis (top) and photoreactivity (bottom) of thienyl-substituted α -ketoamides.	41
Scheme 1.6 (a) Synthesis and (b) photoreactivity of aliphatic and trifluoromethylphenyl diazirines. .	42
Scheme 1.7 Copper catalysed azide-alkyne cycloaddition (CuAAC).....	47
Scheme 2.1 The synthetic route to PARPYnD	77
Scheme 3.1 Synthesis of minimalist “photoclickable” group.	114
Scheme 3.2 Synthesis of 7PQYnD1	115
Scheme 3.3 Attempted synthesis of 7PQYnD2	116

X List of abbreviations

[O]	Oxidant
× g	Times gravity
4HB	4-helix bundle
7PQ	7-phenylquinoline
ABP	Activity-based probe
ABPP	Activity-based protein profiling
Ac	Acyl
ACD	Accidental cell death
ACI	Accelerated chromatographic isolation
ACS	American Chemical Society
ACT	2-Aryl-5-carboxytetrazole
ADA	Adenosine deaminase
ADK	Adenosine kinase
ADME	Absorption, distribution, metabolism and/or excretion
ADP	Adenosine diphosphate
ADPr	ADP-ribose
AfBP	Affinity-based probe
AfBPP	Affinity-based protein profiling
AHR	Aryl-hydrocarbon receptor
AIF	Apoptosis-inducing factor
ALDH1A1	Aldehyde dehydrogenase 1 family member A1
ALS	Amyotrophic lateral sclerosis
AMBIC	Ammonium bicarbonate
ANOVA	Analysis of variance
API	Atmospheric pressure ionisation
APMAP	Adipocyte plasma membrane-associated protein
APTAX	Aprataxin
Ar	Aryl
ARFIP2	Arfaptin-2
ARH3	ADP-ribosyl-acceptor hydrolase 3
ART	ADP-ribosyltransferase
ARTC	ADP-ribosyltransferase cholera toxin like
ARTD	ADP-ribosyltransferase diphtheria toxin like
ATP	Adenosine triphosphate
ATR	Attenuated total reflectance
AUC	Area under curve
AZ	AstraZeneca
AzRB	Azide-arginine-biotin
AzTB	Azide-TAMRA-biotin
boc	<i>tert</i> -butyloxycarbonyl
BODIPY	Boron-dipyrrromethene
BRCA(1/2)	Breast cancer type (1/2) susceptibility protein
<i>BRCAm</i>	<i>BRCA(1/2)</i> mutated

BRET	Bioluminescence resonance energy transfer
BSA	Bovine serum albumin
Cas	CRISPR-associated endonuclease
CAT	Catalase
CB₂	Cannabinoid receptor type 2
CBB	Coomassie Brilliant Blue
CC BY-NC	Creative Commons Attribution-NonCommercial 4.0 International Licence
CD3γ (CD3G)	T-cell surface glycoprotein CD3 gamma chain
CD3ϵ (CD3E)	T-cell surface glycoprotein CD3 epsilon chain
CDC37	HSP90 co-chaperone CDC37
cDNA	Complementary DNA
CES1	Carboxylesterase 1
CETSA	Cellular thermal shift assay
CHK1	Checkpoint kinase 1
CHX	Cycloheximide
CI	Confidence interval
cIAPs	Cellular inhibitors of apoptosis
CK1	Casein kinase 1
CPT2	Carnitine <i>O</i> -palmitoyltransferase 2, mitochondrial
CRISPR	Clustered regularly interspaced short palindromic repeats
CTSD	Cathepsin D
CuAAC	Copper(I)-catalysed azide-alkyne cycloaddition
Cy(n)	Cyanine
CYP27A1	Mitochondrial sterol 26-hydroxylase
d	Doublet
DAI	DNA-dependent activator of IFN-regulatory factors
DAMP	Damage-associated molecular pattern
DAPI	4',6-diamidino-2-phenylindole
DARTS	Drug affinity responsive target stability
DCK	Deoxycytidine kinase
DDR	DNA damage repair
DHCR24	Δ^24 -sterol reductase
DIPEA	<i>N,N</i> -diisopropylethylamine
DMAP	<i>N,N</i> -dimethylaminopyridine
DMEM	Dubecco's Modified Eagle Medium
DMF	<i>N,N</i> -dimethylformamide
DMPK	Drug metabolism and pharmacokinetic(s)
DMSO	Dimethylsulphoxide
DNA	Deoxyribonucleic acid
DR	Death receptor
DSB	Double-stranded break
DTT	Dithiothreitol
EC₅₀	Half-maximal effective concentration
ECH1	Enoyl-CoA hydratase 1
EDCI	1-Ethyl-3-(3-dimethylaminopropyl)carbodiimide

EDTA	Ethylenediaminetetraacetic acid
EPHX1	Epoxide hydrolase 1
EPSRC	Engineering and Physical Sciences Research Council
ES(I)	Electrospray (ionisation)
Et	Ethyl
EWG	Electron-withdrawing group
FA	Fluorescence anisotropy
FAAH	Fatty acid amide hydrolase
FADD	Fas-associated death domain protein
FASL	Fas-ligand
FASR	Fas-receptor
FASTA	FAST-All
FBS	Fetal Bovine Serum
FDFT1	Squalene synthase
FDR	False discovery rate
FLAG	DYKDDDDK peptide tag
FOXA1	Forkhead box protein A1
FP	Fluorophosphonate
FT	Fourier transform
GAPDH	Glyceraldehyde-3-phosphate dehydrogenase
GCU	Green calibrated unit
GI₅₀	Concentration for half-maximal inhibition of cellular proliferation
G_p	Green integrated fluorescence intensity per image / total phase area per image
GSDM	Gasdermin
GSK	GlaxoSmithKline
GSK3β	Glycogen synthase kinase 3 beta
GST	Glutathione <i>S</i> -transferase
H6PD	Hexose-6-phosphate dehydrogenase
Hal	Halogen
HCC	Hepatocellular carcinoma
HCD	Higher-energy collisional dissociation
HeLa	Henrietta Lacks
Hep	Hepatoblastoma
HEPES	4-(2-hydroxyethyl)-1-piperazineethanesulfonic acid
HHQ	4-Hydroxy-2-heptylquinoline
HIF-1	Hypoxia-inducible factor 1
HIV	Human immunodeficiency virus
HM13	Minor histocompatibility antigen H13
HOBt	Hydroxybenzotriazole
HOSA	Hydroxylamine- <i>O</i> -sulphonic acid
HPF1	Histone PARylation factor 1
HPLC	High performance liquid chromatography
HR	Homologous recombination
HRMS	High-resolution mass spectrometry
HRP	Horseradish peroxidase

HRV3C	Human rhinovirus 3C
HSP(70/90)	Heat shock protein (70 kDa/90 kDa)
HTS	High-throughput screen
I	Input
I2.1	<i>FADD</i> ^{-/-} Jurkat T cells
IA	Iodoacetamide
IC₅₀	Half-maximal inhibitory concentration
ICB	Institute of Chemical Biology
ID	Identification
IDH2	Citric acid cycle enzyme isocitrate dehydrogenase [NADP], mitochondrial
IDO1	Indoleamine 2,3-dioxygenase 1
IED-DA	Inverse electron demand-Diels Alder
IFN	Interferon
IMPDH2	Inosine-5'-monophosphate dehydrogenase 2
IR	Infrared
IRI	Ischaemia reperfusion injury
ISC	Intersystem crossing
iTRAQ	Isobaric tags for relative and absolute quantitation
J	Coupling constant
KEGG	Kyoto Encyclopaedia of Genes and Genomes
L	Ligand
L	Levorotary
LB	Lysogeny broth
LBR	Δ^{14} -sterol reductase
LC	Liquid chromatography
LC/MSD	Liquid Chromatograph/Mass Selective Detector
LDS	Lithium dodecyl sulphate
LED	Light-emitting diode
LFQ	Label-free quantification
Lig3α	DNA ligase III α
LSS	Lanosterol synthase
LUBAC	Linear ubiquitin chain assembly complex
m	Multiplet
m/z	Mass to charge ratio
MAR	Mono-ADP-ribose
MAT2B	Methionine adenosyltransferase 2 subunit beta
MB	Metastatic breast
MDA	MD Anderson Cancer Center
MDH2	Malate dehydrogenase 2
Me	Methyl
Med	Medium
MIF	Migration inhibitory factor
MLKL	Mixed-lineage kinase domain-like protein
MPS	Multipolar spindle
MRes	Masters of Research

mRNA	Messenger RNA
MS	Mass spectrometry
MS/MS	Tandem mass spectrometry
MS¹	First mass spectrometer
MS²	Second mass spectrometer
MTS	3-(4,5-dimethylthiazol-2-yl)-5-(3-carboxymethoxyphenyl)-2-(4-sulfophenyl)-2 <i>H</i> -tetrazolium
M_w	Molecular weight
N	Number of biological replicates
N.D.	Not determined
NAD⁺	Nicotinamide adenine dinucleotide
NADH	Reduced nicotinamide adenine dinucleotide
NADP⁺	Nicotinamide adenine dinucleotide phosphate
NADPH	Reduced nicotinamide adenine dinucleotide phosphate
NAMPT	Nicotinamide phosphoribosyl-transferase
NBS	<i>N</i> -bromosuccinimide
NCBI	National Center for Biotechnology Information
Nec	Necrostatin
NER	Nucleotide excision repair
NFDM	Non-fat dried skimmed milk
NF-κB	Nuclear factor kappa-light-chain-enhancer of activated B-cells
NHEJ	Non-homologous end joining
NHS	<i>N</i> -hydroxysuccinimide
nLC	Nano-liquid chromatography
NMR	Nuclear Magnetic Resonance
NPEPPS	Puromycin-sensitive aminopeptidase
NRD1	Nardilysin
NSA	Necrosulfonamide
NSAID	Non-steroidal anti-inflammatory drug
Nu	Nucleophile
NUDT1	7,8-dihydro-8-oxoguanine triphosphatase
P	Pull down
<i>p</i>	Para
PAGE	Polyacrylamide gel electrophoresis
PAL	Photoaffinity labelling
PAR	Poly-ADP-ribose
PARG	Poly-ADP-ribose glycohydrolase
PARP	Poly(ADP-ribose) polymerase
PARPi	PARP inhibitor(s)
PBS	Phosphate-buffered saline
PCD	Programmed cell death
PCYOX1	Prenylcysteine oxidase 1
PDAC	Pancreatic ductal adenocarcinoma
PDB	Protein data bank
PDD	Phenotypic drug discovery

PDIA6	Protein disulphide-isomerase A6
PET	Positron emission tomography
PFDN5	Prefoldin subunit 5
PGRMC2	Membrane-associated progesterone receptor component 2
Ph	Phenyl
PIM-3	Serine/threonine-protein kinase pim-3
PK	Pharmacokinetic
PKA	Protein kinase A
PKM2	Pyruvate kinase M2
PKN2	Serine/threonine-protein kinase N2
PMS	Phenazine methosulfate
PNKP	Bifunctional polynucleotide phosphatase/kinase
Polβ	DNA polymerase beta
PON2	Paraoxonase 2
POR	NADPH-cytochrome P450 reductase
PPACA	Propylphosphonic acid cyclic anhydride
PPAR-γ	Peroxisome proliferator-activated receptor gamma
ppm	Parts per million
PPME1	Protein phosphatase methylesterase 1
PQS	<i>Pseudomonas</i> quinolone signal; 2-heptyl-3-hydroxy-4-quinolone
PTGR2	Prostaglandin reductase 2
PTM	Post-translational modification
qPCR	Quantitative polymerase chain reaction
RCD	Regulated cell death
RefSeq	Reference sequence
R_f	Retention factor
RHS	Right-hand side
RIPK	Receptor-interacting serine/threonine-protein kinase
RISC	RNA-induced silencing complex
RNA	Ribonucleic acid
RNAi	RNA interference
RNase	Ribonuclease
RPL39P5	Putative 60S ribosomal protein L39-like 5
RPMI-1640	Roswell Park Memorial Institute 1640 medium
RPS6KA1	Ribosomal protein S6 kinase alpha-1
rt	Room temperature
R_t	Retention time
RTN1	Reticulon-1
s	Singlet
S. O. C.	Super optimal broth with catabolite repression
S₀	Fudge factor
SAR	Structure-activity relationship
sat.	Saturated
SCCPDH	Saccharopine dehydrogenase-like oxidoreductase
SCID	Severe combined immunodeficiency

SCX	Polystyrene-divinylbenzene copolymer modified with sulfonic acid
SD	Standard deviation
SDB-RPS	Polystyrene-divinylbenzene copolymer partially modified with sulfonic acid
SDB-XC	Polystyrene-divinylbenzene copolymer
SdhC	Succinate dehydrogenase C-subunit
SDS	Sodium dodecyl sulfate
SEM	Standard error of the mean
SG	Sytox™ Green
SILAC	Stable isotope labelling by/with amino acids in cell culture
siRNA	Small interfering RNA
SLC16A2	Solute carrier family 16 member 2; Monocarboxylate transporter 8
SLC25A20	Solute carrier family 25 member 20
SPAAC	Strain-promoted azide-alkyne cycloaddition
SPROX	Stability of proteins from rates of oxidation
SSB	Single-stranded break
STRING	Search Tool for the Retrieval of Interacting Genes/Proteins
t	Triplet
TAMRA	5(6)-carboxytetramethylrhodamine
TBS	Tris-buffered saline
TBS-T	1× Tris-buffered saline, 0.1% (v/v) Tween-20
TBTA	Tris[(1-benzyl-1 <i>H</i> -1,2,3-triazol-4-yl)methyl]amine
TCEP	Tris(2-carboxyethyl)phosphine
TCO	<i>trans</i> -cyclooctene
TDD	Target-based drug discovery
THC	$\Delta^{8/9}$ -Tetrahydrocannabinol
THPTA	Tris(3-hydroxypropyltriazolylmethyl)amine
TLC	Thin-layer chromatography
TLR	Toll-like receptor
TMEM97	Sigma intracellular receptor 2
TMT	Tandem mass tag
TNBC	Triple negative breast cancer
TNFR1	Tumour necrosis factor receptor 1
TNFα	Tumour necrosis factor alpha
TNKS	Tankyrase
TOM	Translocase of the outer membrane of mitochondria
TOMM22	Mitochondrial import receptor subunit TOM22 homolog
TOP2A	DNA topoisomerase 2A
TPD	Trifluoromethylphenyldiazirine
TRADD	TNFR1-associated death domain protein
TRAIL	TNF α -related apoptosis-inducing ligand
TRAILR	TRAIL-receptor
TRAM1	Translocating chain-associated membrane protein 1
Tris	Tris(hydroxymethyl)aminomethane
TRPC3	Transient receptor potential channel 3
Ts	Tosyl

U	Unit
UPLC	Ultra-high performance liquid chromatography
UV	Ultraviolet
v/v	Volume concentration
VDAC	Voltage dependent anion-gated channel
VIM	Vimentin
w/v	Weight concentration
XRCC	X-ray repair cross-complementing protein
YWHAQ	14-3-3 protein theta
ZMPSTE24	CAAX prenyl protease 1 homolog
δ_C	Carbon-13 NMR chemical shift
δ_H	Proton NMR chemical shift
λ_{em}	Emission wavelength
λ_{ex}	Excitation wavelength
λ_{max}	Maximum absorption wavelength
ν_{max}	Maximum absorption wavenumber

Chapter 1 Introduction

Chemical inhibitors of specific biochemical targets are essential clinical tools to combat disease. Discovery of such inhibitors is often achieved by screening compounds for their ability to bind to a purified molecular target that is thought to be essential for disease progression (target-based drug discovery – TDD).¹ Advances in molecular biology, genomics and *in vitro* screening platforms in the late part of the 20th century made TDD popular, with its high efficiency and high-throughput making it attractive for many drug discovery companies.^{2,3} However, TDD can face challenges when developing drug candidates for a single target such as unanticipated off-target binding, the development of resistance to the modulation of that specific target, or even discovery that the target is not essential for the disease after all.⁴

In contrast, compounds can be screened for their ability to inhibit the overall disease phenotype, or an essential pathway in that disease, in a cell-, tissue-, or organism-based assay (phenotypic drug discovery – PDD).⁵ Phenotypic assays are often more difficult to make high-throughput, and selection of a disease model that closely represents the disease state is crucial in the discovery of clinically relevant hit molecules.² When successful however, PDD delivers hit molecules that directly modulate the disease phenotype, and screening in an *in cellulo* or *in vivo* setting ensures from the outset that molecules are likely to be cell penetrant and metabolically inert. Such assays can even demonstrate the toxicity of the molecules if a way to measure this toxicity is built into the screening platform.^{6,7} Hit compounds may also interact with an unknown biomolecular target in that disease pathway, revealing a novel therapeutic strategy for disease treatment.^{8,9}

While the advantages of PDD have made it an attractive drug discovery technology, the molecules discovered through these pipelines do not have a defined molecular target. Subsequent development of that molecule and successful translation to the clinic most often requires knowledge of that target.¹⁰ Furthermore, even in cases where the compound's target is known, actual engagement of the target *in vivo* can be hampered by poor absorption, distribution, metabolism and/or excretion (ADME) or insufficient selectivity, and any such off-target engagement may result in unanticipated toxicity.¹¹ These problems can result in clinical failure: the probability of a drug being approved after entering Phase I clinical trials is around 10%,¹²⁻¹⁵ and insufficient efficacy or unanticipated toxicity accounts for around 80% of these failures.^{12,16} A further 85% of candidates fail to be nominated at the preclinical stage, with the most common reason being toxicological concerns identified through *in vivo/in vitro* studies.¹⁷ Therefore, technologies that can perform on- and off-target identification and accurate assessment of physiological target engagement are essential in the realisation of a drug molecule from concept to therapy. While classically such investigations relied on painstaking biochemical and genetic experiments, the advent of modern chemical biology techniques has allowed for target profiling

strategies to be employed in the earliest stages of the drug discovery pipeline, mitigating these costly failures.¹⁸

1.1 The utility of target profiling in drug discovery

Target profiling is herein used to describe together the concepts of target identification and confirmation, off-target identification and target engagement (**Figure 1.1**):^{18–22}

- Target identification – Discovery of the key interaction(s) between a drug molecule and its biomolecular target(s) that drives the mechanism of action of the therapeutic.
- Target confirmation – Where a drug's target is known or assumed, experimental confirmation of this can be sought in an appropriate biological model to confirm that interaction. Target *invalidation* would be the result of a negative outcome in this experiment, often leading to the *reassignment* of the key biomolecular target.
- Off-target identification – Discovery of interactions between the drug and other biomolecular targets that do not directly contribute to the mechanism of action. These may be bystander interactions, or they may contribute to any significant adverse effects seen upon treatment.
- Target engagement – A semi- or fully quantitative measurement of the degree of interaction a drug molecule has with its biochemical target(s) in the relevant biological system.

1.1.1 Identifying the target of interest

Knowing the biomolecular target that is responsible for a compound's mechanism of action is vital in understanding how the bioactive molecule works. Knowledge of the target or even the mechanism of action of a drug is not necessary for regulatory approval, however this accounts for a limited proportion (<10%) of currently approved drugs.^{23,24} For drugs identified through TDD, the target is known from the outset.¹ By contrast, compounds discovered through PDD will have an unknown molecular mechanism of action, and this lack of target knowledge can represent a barrier to the development of these hit molecules into viable drug candidates.²

Target discovery approaches are therefore vital in uncovering the biomolecular interactions of these compounds. Once the target(s) has been identified, pathway analysis can be used to determine the biological context of this target in the disease, and any key structure-activity relationship (SAR) data discovered can help hone the potency and selectivity of the molecule in lead optimisation studies. Target discovery has identified molecular mechanisms of action in phenotypic campaigns including a pro-adipogenic carbamate series,²⁵ the promising preclinical anti-inflammatory candidate MCC950²⁶ and the clinically stalled utrophin modulator ezutromid,²⁷ with target identification helping to focus and shape these, and many more, drug discovery campaigns.^{10,22}

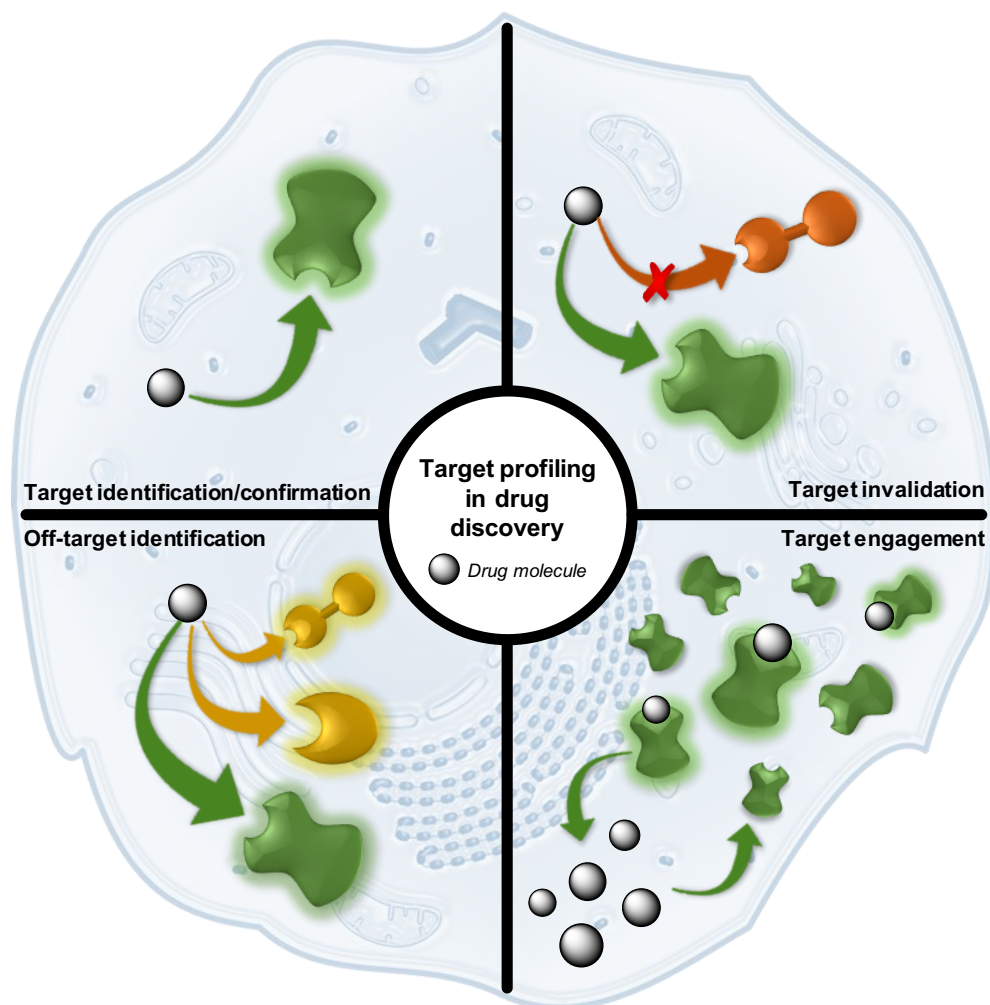


Figure 1.1 Target profiling and its uses within the drug discovery pipeline.

Target identification approaches have even uncovered the targets of already approved drugs such as Orlistat²⁸ and quinine,²⁹ providing new insights into their mechanism of action. Even when the target is thought to be known, confirmation of this can give the medicinal chemist confidence in the direction of the project or, crucially, correct a misassignment of the drug's target, as has been reported for early-stage deubiquitinase inhibitors.³⁰ More recently, an entire suite of cancer inhibitors already undergoing clinical trials were found to be assigned incorrect targets.³¹

1.1.2 Off-target identification

While binding to the primary target(s) is fundamental for biological activity, engagement of off-targets may be the critical factor that prevents a promising new therapeutic reaching the market. Many inhibitors can display poor selectivity and polypharmacology, where they bind to multiple targets in the system. This is not necessarily a disadvantage, with several approved drugs having multiple targets that together elicit a desired therapeutic effect.³² On the other hand, such polypharmacology can result in unwanted off-target engagement, which at best would deplete occupancy of the intended target and at

worst could result in unwanted toxicity and project failure, the financial cost of which is often offset by increasing the price of other, successful drugs.^{11,33}

Target identification campaigns can uncover the complete target profile of a bio-active compound, and this information can help identify any off-target biomolecules. Target profiling of commonly used non-steroidal anti-inflammatory drugs (NSAIDs) revealed previously unknown targets of naproxen and indomethacin that may contribute to their clinical effect.³⁴ Discovery of pernicious drug target interactions has revealed the molecular basis of the photosensitivity experienced by patients administered kinase inhibitors such as Alectinib and Vemurafenib.³⁵ Another target profiling campaign uncovered off-target interactions that drive the ocular toxicity of β -secretase inhibitors, promising treatments for Alzheimer's Disease that have stalled in pre-clinical development due to these associated safety concerns.³⁶ In the extreme, insufficient information regarding off-targets can be disastrous, as demonstrated by the recent tragic death of one participant and permanent neural debilitation of four others in a Phase I trial of a fatty acid amide hydrolase (FAAH) inhibitor.³⁷ This case in particular highlights the need for robust target profiling early in the preclinical stages of the drug discovery pipeline.

1.1.3 Assessing target engagement

Finally, knowing what the targets of a compound are may not be sufficient to assess the molecule's suitability as a therapeutic. Clinical failure can instead be the result of low target occupancy by the candidate molecule in the living system: a combination of potency, selectivity and ADME issues can result in molecules not eliciting a significant biological effect to pass the required efficacy threshold.¹¹ To interrogate this issue, one must quantify the degree of engagement of the target by the molecule, ideally in an appropriate living system, to determine if a threshold for efficacy is being reached. Such target engagement studies have been used to support the clinical nomination of Bruton's tyrosine kinase inhibitors for B-cell lymphoma³⁸ and assisted in the *in vivo* evaluation of clinical Tourette's syndrome candidate ABX-1431.³⁹

1.2 Target profiling methodologies

There is a large suite of strategies available to the chemical biologist to profile the biochemical targets of a small molecule; some of these are summarised in **Table 1.1**.

Pathway analysis, while generally accessible to many laboratories, delivers results that are often suggestive, and provides only indirect evidence of target engagement that must be further validated experimentally. The molecular biology techniques described in **Table 1.1** generally applied by laboratories that have access to large complementary DNA (cDNA) libraries and facilities with which to manipulate and express these constructs to generate effective biological tools. While they have successfully uncovered the targets of compounds with unknown mechanisms of action, these technologies are often

Table 1.1 Summary of some available strategies to perform drug target profiling.

Classification	Methodology	Brief description	Key literature examples
Pathway analysis	Pharmacological profiling	Experimental investigation of the phenotypes and biomarkers affected by the drug through methods such as transcriptomics, proteomics and metabolomics, and comparison to current knowledge to deconvolute the likely target(s).	40,41
	<i>In silico</i>	Computational and bioinformatics analysis of data derived from therapies that elicit similar therapeutic effects and other network analyses to determine potential target(s) which are often then verified experimentally.	42–44
Molecular biology or genetic technologies	Phage display	The drug molecule is immobilised on a solid support and co-incubated with phage virions presenting potential target proteins expressed from a cDNA library. ⁴⁵ Iterative rounds of enrichment and clonal expansion are used to isolate the target(s).	46,47
	mRNA/ribosome display	Similar to phage display, the tethered drug molecule is co-incubated with proteins covalently linked to their corresponding mRNA templates, ⁴⁸ or to whole the ribosome/mRNA complex. Iterative rounds of enrichment and replication are used to identify the target(s).	49,50
	Three-hybrid systems	A biological system such as yeast is genetically modified so that when the drug binds to its genetically encoded target, it is brought together with an effector protein, completing a three-hybrid cassette and generating a positive phenotypic readout. ⁵¹	52–54
	CRISPR-Cas mutagenesis screening	A pooled library of a particular cell line is generated with genetic knock-outs of potential target genes performed by CRISPR-Cas mutagenesis. The pool is then challenged with the drug of interest and knock-out populations are compared to the untreated pool of cell lines using next-generation sequencing.	41,55,56
Label-free	Cellular thermal shift assay (CETSA)	Detection of the stabilisation of target protein(s) when cells or lysates are heat treated in the presence of the drug.	29,35,57–61
	Drug affinity responsive target stability (DARTS)	Detection of the stabilisation of target protein(s) when samples are proteolytically degraded in the presence of the drug.	26,62–65
	Stability of proteins from rates of oxidation (SPROX)	Detection of the changes in chemical denaturant-dependent oxidation rates of the target protein(s) by peroxide in the presence of the drug.	66–69
Label-assisted	Affinity chromatography	The drug is immobilised on a solid support via chemical linkage and incubated with a relevant biological sample. Washing and elution is performed to yield the target proteins.	70–73
	Activity-based protein profiling (ABPP)	Drug targets are profiled using a probe that captures target biomolecules through their intrinsic reactivity to achieve selective labelling.	(Detailed in Section 1.2.1)
	Affinity-based protein profiling (AfBPP)	Drug targets are profiled using a probe that captures biomolecules via the specific <i>non-covalent</i> interaction between probe and target; further covalent labelling using e.g. a photoreactive group can be used to trap this interaction.	(Detailed in Section 1.2.1)

challenging and time consuming. Also, genetic technologies such as the yeast three-hybrid screening described in **Table 1.1** or CRISPR-Cas mutagenesis screening⁴¹ do not provide direct evidence of drug-target engagement. Instead, studies directly demonstrating that the drug binds specifically to one or more targets in a relevant disease model are the gold standard in target profiling. Technologies that achieve this goal can utilise either the unmodified version of the molecule (label-free) or a chemically modified tool compound (label-assisted), often structurally related to the drug, with structural or functional features that facilitate target identification (**Figure 1.2**).⁷⁴ Label-assisted methodologies allow the target(s) to be partitioned from a complex background, thus amplifying the signal-to-noise ratio and facilitating detection of labelled proteins.²⁰ Label-free approaches by contrast most often involve measuring small perturbations within the whole biological system upon compound treatment, and detection of such changes can be technically challenging (**Figure 1.2**).⁴ Furthermore, enhancement or disruption of downstream interactions caused by compound treatment may lead to stabilisation or destabilisation respectively of those proteins, making the assignment of *bona fide* compound-target interactions more difficult. While advances in the sensitivity of mass spectrometry techniques and bioinformatics have yielded several successful label-free target profiling campaigns, label-assisted target profiling is the more well-validated target profiling strategy.⁷⁴

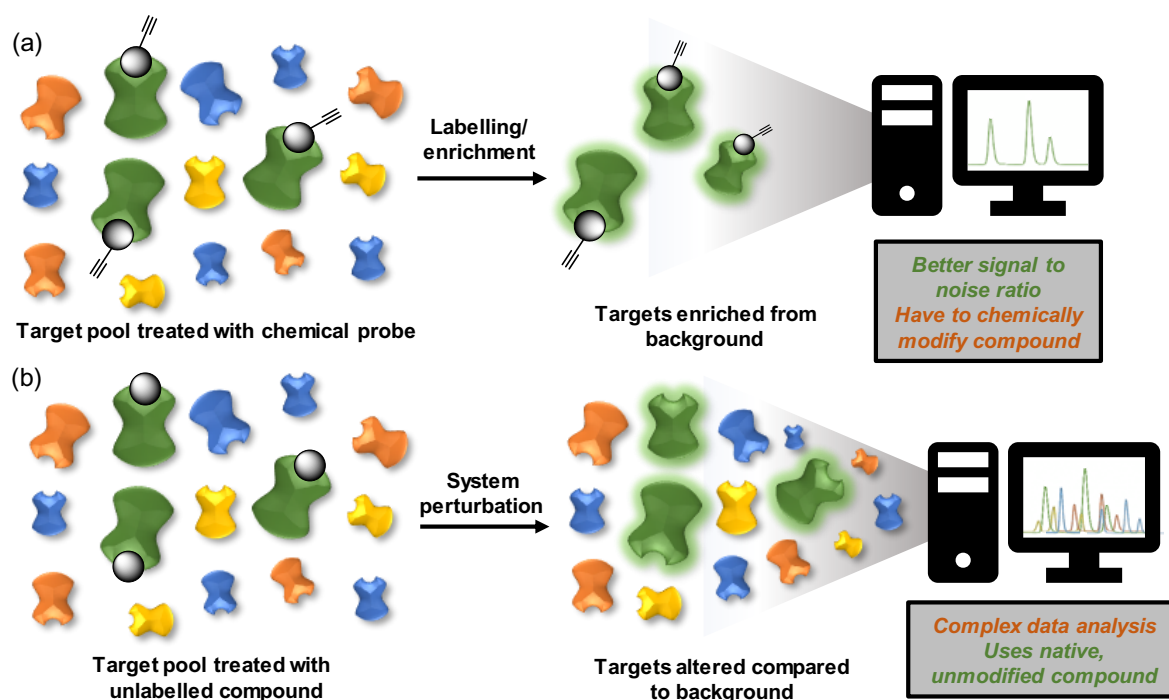


Figure 1.2 Comparison of methodologies in target profiling. (a) Label-assisted, (b) label-free.

1.2.1 Label-assisted target profiling

Label-assisted approaches to drug target identification and validation can be divided into affinity chromatography, activity-based protein profiling and affinity-based protein profiling (**Figure 1.3**).

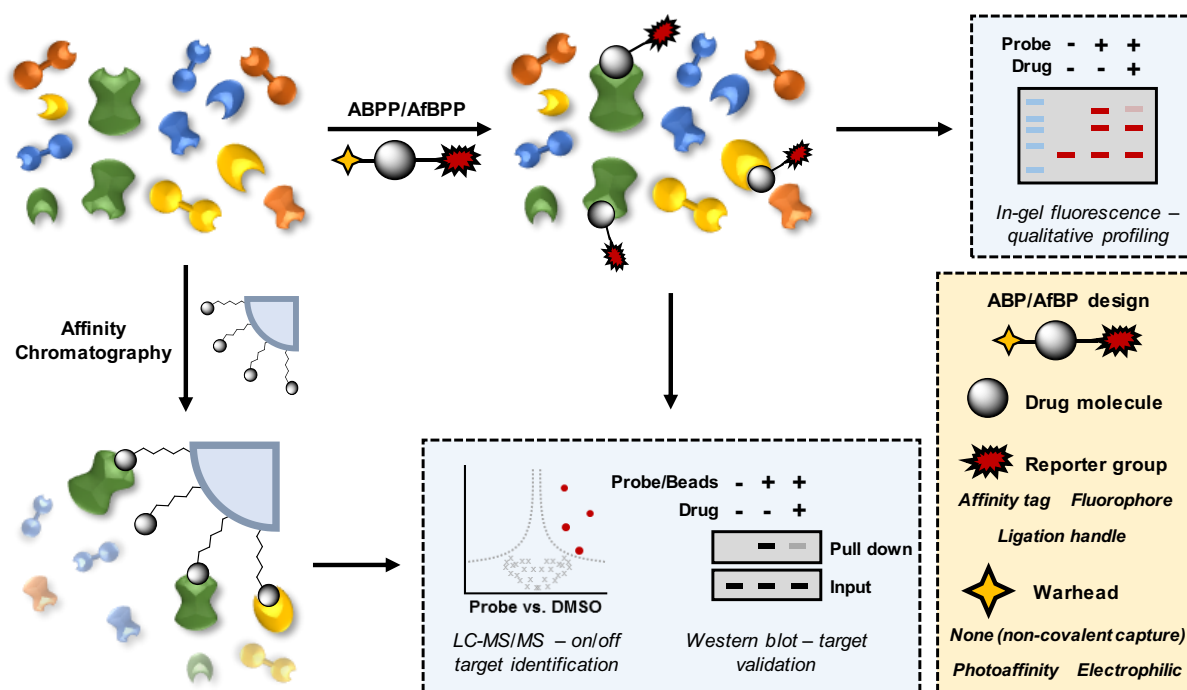


Figure 1.3 Label-assisted approaches to target profiling. Affinity chromatography – direct covalent attachment of the drug to a solid support and immediate enrichment of the targets from a biological sample. Activity/affinity-based protein profiling (ABPP/AfBPP) – uses an activity/affinity-based probe (ABP/AfBP) that can bind to the drug’s targets in lysates or live cells. Further biochemical processing allows the probe-engaged targets to be profiled. Inset, bottom right – design of activity/affinity-based probe.

Affinity chromatography involves the modification of the drug molecule to covalently attach it to a solid support such as agarose beads. The biological sample is incubated with these beads, then subsequent washing and elution allows the target-enriched fraction to be interrogated by Western blot and/or chemical proteomics.^{4,75} This methodology is facile and has been used extensively for primary target identification, perhaps most famously in the identification of the molecular target of the teratogen thalidomide.⁷⁶ However, cells cannot be profiled live and intact, meaning the lysates used for incubation may not reflect the native environment and this may influence the binding profile of the drug. Furthermore, for reversibly binding drugs, this affinity capture method can be transient and miss weak secondary binders.

Alternatively, activity/affinity-based protein profiling (ABPP/AfBPP) uses a small molecule probe (**Figure 1.3**, inset) that is designed from a compound which, through structural similarity, binds to the same targets as that compound in a biological sample.⁷⁷ Importantly however, the probe is modified from the chemical structure of the parent compound to include key chemical functional groups that facilitate the capture and identification of the interacting biomolecules.

Firstly, a reporter group is necessary to distinguish the protein or other biomolecule that is engaged by the probe from the unbound background.⁷⁸ This can consist of a fluorophore to identify bound proteins

by fluorescence imaging methods such as in-gel fluorescence or fluorescence microscopy, or an affinity handle that allows partitioning of the probe-bound biomolecules from the background mixture and subsequent profiling using gel- or proteomics-based methods. Alternatively, a smaller chemical ligation handle can be added to the probe so that these groups can be appended later in a modular fashion (**Section 1.3.3**).⁷⁹ This variability in reporter molecule is a significant advantage over affinity chromatography, as it extends target profiling beyond simple affinity enrichment from biological lysates.

In some cases, the parent scaffold modified with a reporter molecule can constitute an effective ABP/AfBP on its own, however some probes will also include a chemical warhead: a functionality that facilitates the formation of a covalent bond between probe and biomolecule. A bio-active molecule that works through a covalent mechanism of action will already have an electrophilic warhead built into the structure.^{80,81} Probes to profile the biological interactions of these molecules will retain this warhead in the probe design, and by virtue of this reactivity are termed *activity*-based probes (ABPs).²² It should also be noted that ABPs may not be based on the structure of the parent molecule, but can be broad-spectrum probes that label a certain enzyme class or amino acid residue through this electrophilic reactivity. This includes for example fluorophosphonate-biotin (FP-biotin) for the labelling of serine hydrolases⁸² or iodoacetamide (IA)-type probes for reactive cysteine profiling.⁸³ The specific inhibitor-target interaction(s) of a particular molecule of interest can then be investigated by co-incubation of the broad profiling ABP with the molecule and quantification of any loss in probe labelling due to competitive blockade of the binding site by the drug (**Section 1.4.2.1**).^{37,84}

Affinity-based probes (AfBPs) in contrast to ABPs have a core scaffold based on drugs with a non-covalent mechanism of action. Therefore, they have no reactive warhead, instead relying on transient reversible interactions to capture and retain their target.⁸⁵⁻⁸⁷ As highlighted for affinity chromatography, this may be insufficiently sensitive for lower affinity probe-target interactions, for example bound targets with fast off-rates or those that are unstable to repeated washing steps may be lost using this method. In these cases, a photo-reactive warhead can be employed to transform these transient binding events into a permanent covalent linkage between probe and protein upon photo-irradiation.^{88,89} This technique is known as photoaffinity labelling (PAL) and allows for extremely sensitive in-cell target profiling of non-covalent drugs, permitting the unbiased capture of both strong primary and weaker secondary binders and preventing their elution during the washing steps that follow affinity enrichment.⁹⁰ The temporal and spatial nature of this covalent capture methodology can also facilitate the identification of probe binding sites, which can be useful in understanding the mode of binding of a compound to the target.⁸⁹ The remainder of this chapter will discuss PAL, the design of a photoreactive AfBP and the methods employed to utilise them in target profiling.

1.3 Photoaffinity labelling (PAL)

PAL has been used as a tool in chemical biology as early as the 1960s,⁹¹ and was initially used to profile the binding sites of small ligands on recombinant proteins via radio-chromatography or mass spectrometry of individual peptides.⁹² It was not until the early 21st century however that liquid chromatography, mass spectrometry and bioinformatics technologies became sufficiently advanced and widespread that *proteome-wide* profiling became feasible. Activity-based protein profiling was first to integrate these proteomics technologies with chemical tool molecules with the Cravatt group pioneering chemical proteomics as a methodology to interrogate the interactions of a covalent chemical compound with the whole proteome.^{93,94}

In the early 2010s, PAL was being combined with bio-orthogonal ligation chemistry, generating cell-permeable photoreactive AfBPs that could be functionalised after cell lysis with a reporter group for analysis of the labelled proteome through gel-based methods.⁹⁵ However, the Yao group were the first to combine PAL with chemical proteomics for drug-target profiling, identifying the cellular targets of dasatinib *in situ* from the complex proteomes of both hepatoblastoma (Hep-G2) and chronic myelogenous leukaemia (K-562) cell lines.⁹⁶ Since this work, there have been numerous examples of PAL being used to profile the targets of various small molecules and natural ligands including anti-inflammatory agent MCC950,²⁶ the promising Duchenne's muscular dystrophy candidate ezutromid,²⁷ a panel of non-steroidal anti-inflammatory drugs (NSAIDs),³⁴ hypoxia inducible factor 1 (HIF-1) modulator LW6,⁹⁷ CB₂ receptor agonist LEI101,⁹⁸ tetrahydrocannabinol,⁹⁹ sialic acid,¹⁰⁰ the carbohydrate family,¹⁰¹ bacterial quorum sensing molecule 2-heptyl-3-hydroxy-4-quinolone (PQS),¹⁰² and many more.^{88,103}

1.3.1 AfBP Design

To successfully profile the targets of a small molecule using PAL, a photoreactive AfBP must be designed and synthesised with the appropriate functionality to covalently label the target proteins. A bio-orthogonal ligation handle must also be incorporated for downstream biochemical processing. These modifications must not only be synthetically tractable but must be incorporated in such a way that does not significantly perturb the biological activity or cell permeability of the parent molecule. This means that the molecular interactions of the parent molecule with its cellular targets are retained in the probe, making the AfBP an effective tool molecule; it is usually necessary to optimise the structure of the AfBP to retain cellular activity for each new PAL campaign. The general structure of an affinity-based probe is shown in **Figure 1.4**.

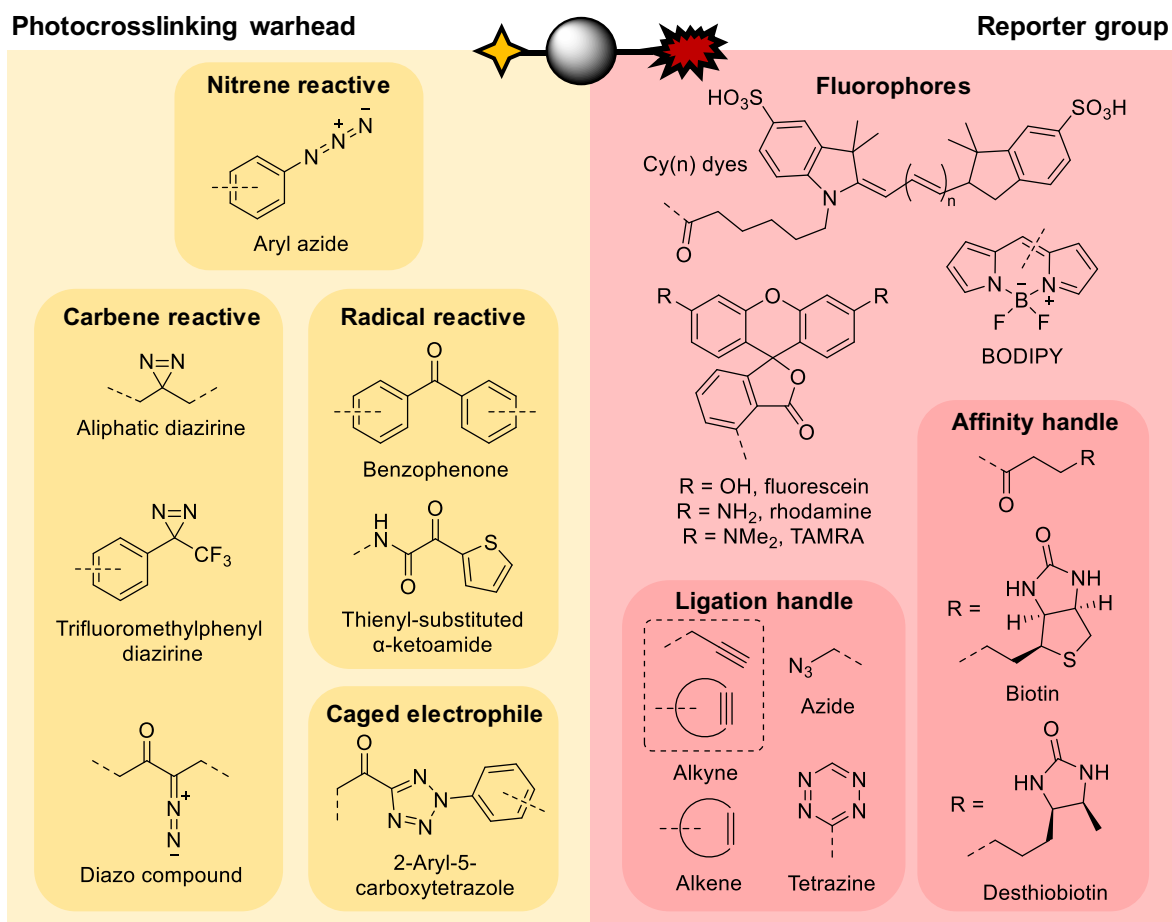


Figure 1.4 General structure of an AfBP. The grey ball represents the core scaffold based on the parent compound. The photocrosslinking warhead converts transient non-covalent interactions to a covalent one by the mechanisms described. The reporter group allows for downstream analysis/functionalisation to profile the labelled proteins, or a ligation handle (see **Section 1.3.3** for complete list) allows for the downstream functionalisation of labelled proteins with fluorophore- and/or enrichment handle-containing reporter tags that possess the corresponding bio-orthogonal chemistry partner.

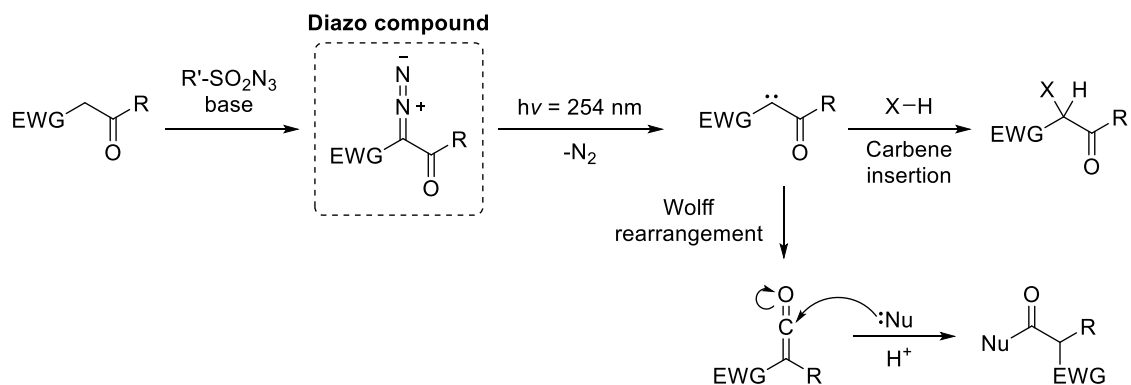
1.3.2 Photoreactive warhead

The choice of photoreactive warhead will depend on a combination of factors including synthetic tractability, chemical and thermal stability, irradiation wavelength, mechanism of photoreactivity and any potential side reactions. This section will outline the most widely used photocrosslinkable groups and provide a summary of their most important properties.

1.3.2.1 Diazo compounds

Diazo compounds are among the earliest examples of photolytic reagents in chemical biology.⁹¹ They can be prepared through a variety of methodologies, but are most readily synthesised α to a carbonyl group via a base-mediated diazo-transfer reaction (**Scheme 1.1**).¹⁰⁴ Irradiation with short wavelengths of UV light (~ 250 nm) liberates nitrogen gas to reveal a singlet carbene species that is able to perform

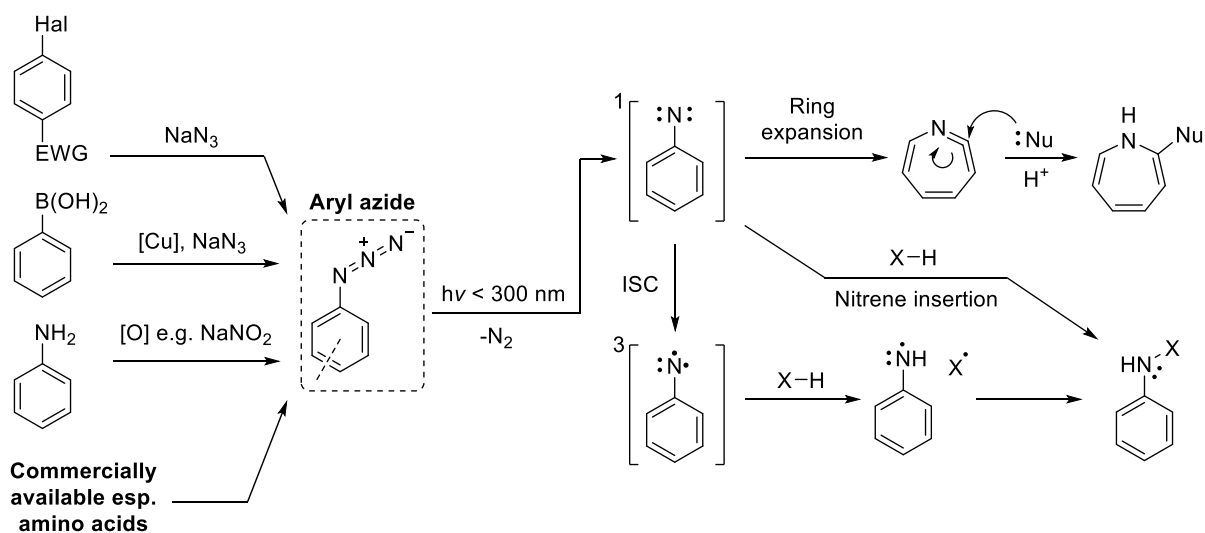
an insertion into a local X–H σ -bond (X = C, N, O, S) e.g. that of a residue of a bound protein partner;¹⁰⁵ the chemistry of carbenes is discussed in greater detail in **Section 1.3.2.6**.



Scheme 1.1 Synthesis and photoreactivity of diazo compounds. EWG = electron-withdrawing group, Nu = nucleophile, X = protein (C, N, O, S).

The diazo group has fallen out of use for photoaffinity labelling, largely due to the chemical and thermal instability of the diazo moiety.¹⁰³ The short irradiation wavelengths required for photoactivation damages biomolecules such as proteins and nucleic acids, making diazo compounds poor choices for the labelling of biological samples, especially in living systems.¹⁰⁶ The unmasked α -carbene is also able to perform an intramolecular Wolff rearrangement, generating an electrophilic ketene species that is relatively long-lived, allowing the photolabelling reagent to diffuse and spuriously react with any available nucleophilic species in the biological sample.¹⁰⁵

1.3.2.2 Aryl azides



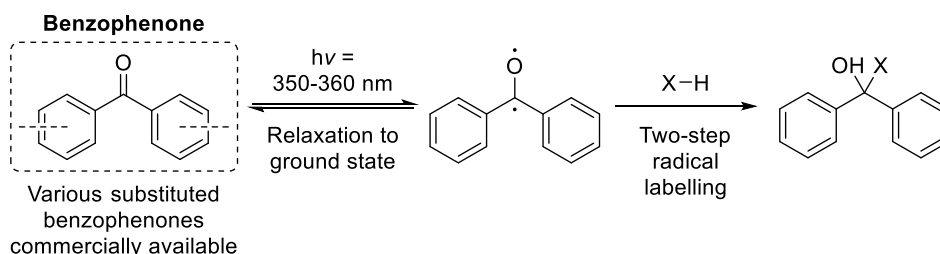
Scheme 1.2 Synthesis and photoreactivity of aryl azides. Hal = halogen, EWG = electron-withdrawing group, [O] = oxidant, ISC = intersystem crossing, Nu = nucleophile, X = protein (C, N, O, S).

Aryl azides (**Scheme 1.2**) also have a long history of use as a photochemical warhead;¹⁰⁷ as with diazo compounds, they require a short irradiation wavelength, however substitution on the aryl ring can shift the maximum absorption wavelength (λ_{max}) to longer wavelengths of UV light, often achieving wavelengths up to 366 nm that are less damaging to the surrounding biological environment.^{105,108} Irradiation of the aryl azide reveals a highly reactive singlet nitrene species (**Scheme 1.2**) which is able to insert via a one-step mechanism into a local X–H bond. Alternatively, the singlet can undergo intersystem crossing (ISC) to the triplet nitrene species which can then perform a two-step radical-type insertion, however this has been reported to be highly inefficient and result in low crosslinking yields.¹⁰⁵ This is further complicated as aryl nitrenes are also prone to rearrangement, with ring expansion to an electrophilic dehydroazepine species leading to spurious nucleophilic trapping.^{103,109}

Nonetheless, aryl azides are extremely synthetically tractable with several synthetic routes available to functionalise an aryl ring with an azide group (**Scheme 1.2**),^{110,111} and this narrow 3-atom “rod” of electron density often makes this group a convenient and structurally discreet modification for AfBPs that already contain an aryl group in their structure. Many commercially available aryl azides are also available to incorporate this group, in particular azide-modified aromatic amino acids that allow the incorporation of such a group into a peptide/protein AfBP.¹¹² Late stage functionalisation of an AfBP to include this warhead however should consider the steric demands that a new aryl ring might place on the probe.

Aryl azides have been used to profile ubiquitin-binding proteins,¹¹³ histone deacetylase inhibitors,¹⁰⁸ and a promising series of tumour selective apoptosis-inducing molecules,¹¹⁴ and have identified the key targets of both an Ebola antiviral compound¹¹⁵ and an isoxazole-based enhancer of cellular glucose uptake.¹¹⁶ In the latter case, identification of the molecule as a peroxisome proliferator-activated receptor gamma (PPAR- γ) agonist allowed for structure-guided optimisation of this compound into an improved clinical candidate.

1.3.2.3 Benzophenones



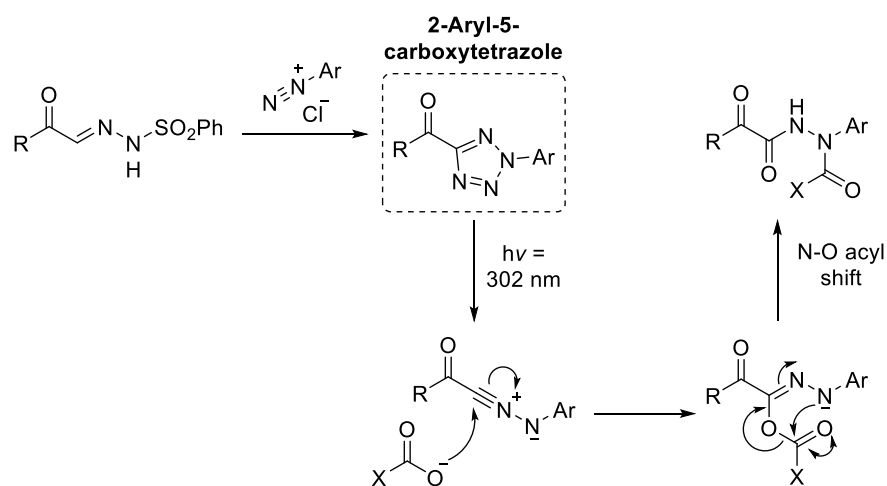
Scheme 1.3 Synthesis and photoreactivity of benzophenones. X = protein (C, N, O, S).

Benzophenones are photochemical warheads that represent a large (~180 Da) structural modification compared to the parent molecule that is often drug-like and therefore less than 500 Da (**Scheme 1.3**); increasing the molecular weight of a chemical inhibitor by more than one third may not be tolerated

when attempting to retain biological activity in the AfBP. They are often most useful when the parent molecule already contains some kind of diphenyl group or a single, readily modifiable phenyl ring. Despite their large size, benzophenones have been extensively used in photoaffinity labelling as there are numerous commercially available benzophenones, and their longer λ_{max} (350–360 nm) makes them extremely biocompatible.^{103,105}

Irradiation of the ketone reveals a ketyl radical species that is able to perform a two-step insertion into a local X–H bond. Long irradiation times are usually required as the radical species can relax back to the ground state which then needs to be re-excited to be reactive again.¹⁰³ Furthermore, their hydrophobic nature leads to a high degree of background crosslinking due to non-specific association with other proteins.¹¹⁷ Nonetheless, benzophenone based probes have been employed in the off-target profiling of β -secretase inhibitors,³⁶ target identification of anti-inflammatory molecule MCC950,²⁶ quantitative profiling of protein kinase active sites,¹¹⁸ and study of trehalose dimycolate binding proteins.¹¹⁹

1.3.2.4 2-Aryl-5-carboxytetrazoles

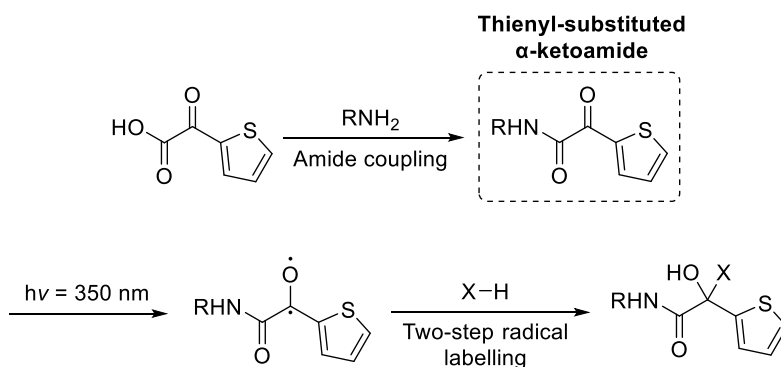


Scheme 1.4 Synthesis and photoreactivity of 2-aryl-5-carboxytetrazoles. Ar = aryl, X = protein (Asp/Glu residue).

2-aryl-5-carboxytetrazoles (ACTs) are a recent addition to the library of available crosslinking reagents (**Scheme 1.4**).¹²⁰ Their structure is quite specific, but they are readily incorporated at the terminal ends of parent molecules, especially α to any carbonyl groups that might be present, and the aryl group provides a modification site to include further reporter tags or ligation handles. They have a unique mode of reactivity upon irradiation that reveals an electrophilic carboxy-nitrile that, when trapped by an aspartate or glutamate residue or protein C-terminus, can undergo an intramolecular rearrangement to generate a permanent covalent adduct. This mechanism reduces the background labelling often seen with the highly reactive intermediates generated with traditional photoreactive warheads, however labelling depends on the availability of a local Asp/Glu residue or an adjacent protein C-terminus, and therefore crosslinking yields are likely to be highly target dependent.

1.3.2.5 Thienyl-substituted α -ketoamides

The thienyl-substituted α -ketoamides were introduced even more recently than ACTs, and were developed to address the need for a more hydrophilic photoaffinity group (**Scheme 1.5**).¹²¹ They work through a similar mechanism to benzophenones, and reversibly generate the ketyl radical at a similar wavelength. In contrast to benzophenones however, thienyl-substituted α -ketoamides were found to be less bulky and more polar, reducing the non-specific hydrophobic labelling experienced when using benzophenones. They can be readily incorporated through an amide coupling of a commercially available starting material, though they require long irradiation times similar to the benzophenones. It is also unclear whether the thiophene ring can be further modified to incorporate reporter tags or ligation handles, potentially limiting the ability to multiplex photoreactivity and reporter readout into one modification.



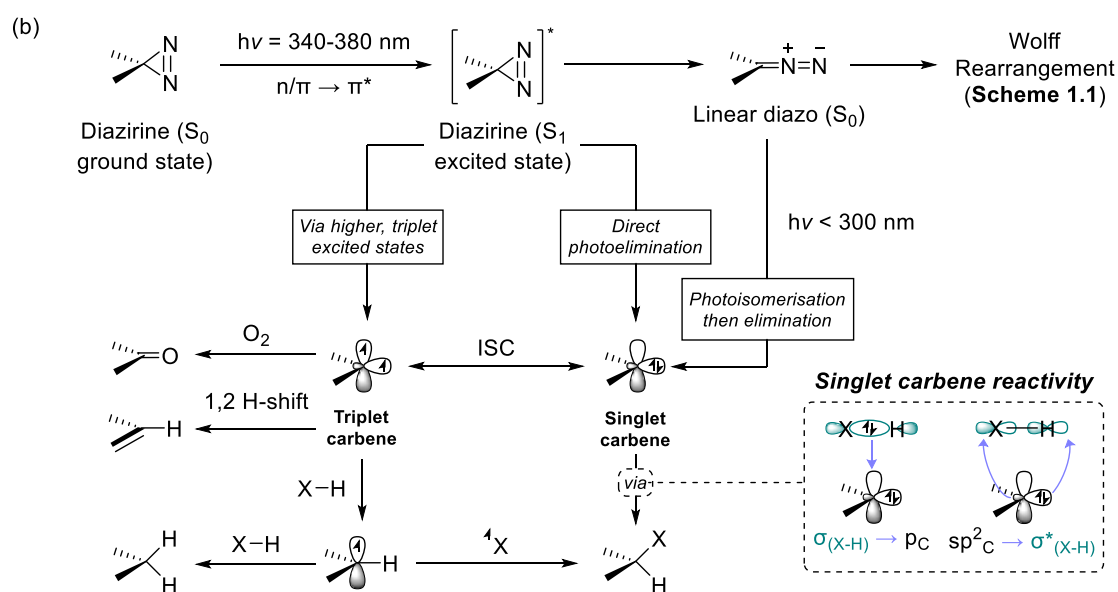
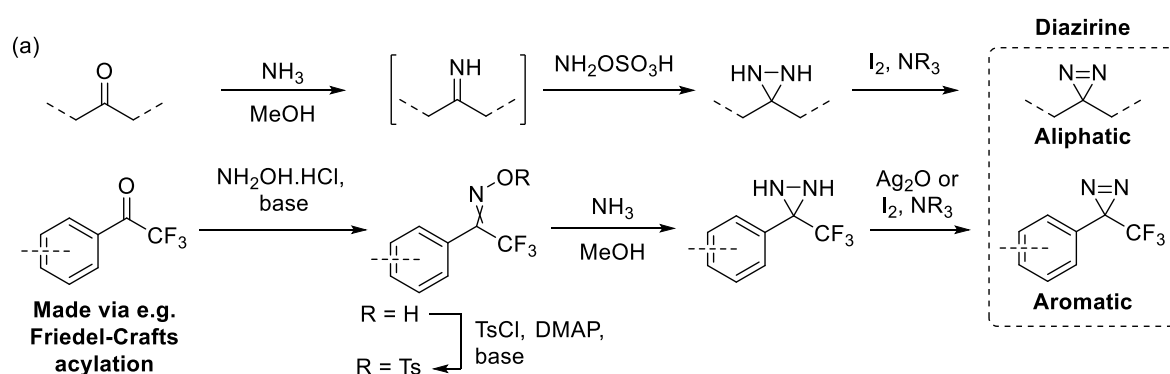
Scheme 1.5 Synthesis (top) and photoreactivity (bottom) of thienyl-substituted α -ketoamides. X = protein (C, N, O, S).

1.3.2.6 Diazirines

Compared to the size of the compound to be modified, diazirines are small, structurally discrete functional groups that have become increasingly popular as a photoreactive warhead for AfBPP.¹²² They are readily synthesised from ketones in either a multi-step methodology for trifluorophenylmethyl diazirines (TPDs)¹²³ or in one overall reaction step for aliphatic diazirines (**Scheme 1.6a**),¹²⁴ and this has recently been optimised further to a convenient “one-pot” procedure.¹²⁵ While these efforts have made diazirines synthetically tractable, a ketone functional group must be present or introduced into the probe. Diazirines are thermally stable⁹⁰ and orthogonal to a large range of chemical transformations including strong acid or base, mild/ionic reductions, oxidations and various coupling reactions.⁸⁸

Irradiation of the diazirine with biocompatible long wavelength UV light (340–380 nm, typically 365 nm)^{90,126,127} generates a singlet excited state by promoting an electron to the N=N π^* from either the diazirine non-bonding orbital ($n \rightarrow \pi^*$ transition)^{128,129} or, in the case of TPDs, the adjacent π orbital ($\pi \rightarrow \pi^*$ transition).¹³⁰ This excited state can then collapse down to a singlet carbene through the elimination of N₂ gas (**Scheme 1.6b**).⁹⁰ There is still debate regarding the exact mechanism of this

collapse; it is known that irradiation of the diazirine also results in photoisomerisation to the linear diazo species, and it has been reported that this is a necessary intermediate in the formation of the carbene.¹³⁰ Other studies have shown that while up to 30% of this diazo species will be formed as a by-product, direct photoelimination of N₂ is the predominant pathway.^{129,131} Likely the mechanism(s) will change according to the substituent groups attached to the diazirine, however such a detailed cross-substrate analysis of diazirine photochemistry remains a gap in the field. In either case, presence of this diazo species can lead to unwanted side-reactions, especially if they are α to a carbonyl group (see Wolff rearrangement, **Scheme 1.1**). Photolysis of the unwanted diazo group can be achieved with a shorter wavelength of light to generate the desired carbene.⁸⁸



Scheme 1.6 (a) Synthesis and (b) photoreactivity of aliphatic and trifluoromethylphenyl diazirines. NR₃ = *N,N*-diisopropylethylamine or triethylamine, ISC = intersystem crossing, X = C, N, O, S. Inset, orbital diagrams of singlet carbene reactivity with a local X–H bond; arrows represent orbital overlap. DMAP = *N,N*-dimethylaminopyridine, Ts = tosyl.

The initial singlet carbene that is formed upon photoirradiation is highly reactive (lifetime <20 ns)¹³² and substrate agnostic. It will readily insert into any local X–H bond (**Scheme 1.6b**, inset) or C–C bond,

and can even add onto C=C π bonds, including those of aromatic rings, making diazirines ideal for labelling a variety of protein binding partners.¹⁰³ This quick reactivity means any unbound probe will be immediately quenched by the surrounding solvent, often leading to a low on-target crosslinking yield. However, this immediate quenching reduces the propensity of the reactive intermediate to diffuse around the biological system and label proteins in a non-specific fashion, resulting in a lower level of background labelling and increasing the signal-to-noise ratio.¹³³

It is also possible for the triplet carbene to form. This can be the result of photoelimination of nitrogen from higher, triplet excited states of the diazirine,¹²⁹ or through ISC from a longer lived singlet carbene.¹³⁴ The ratio of singlet to triplet carbene is determined by the functionality adjacent to the carbon atom. Electron donating substituents are able to stabilise the singlet carbene's empty p-orbital through either π -donation or σ -hyperconjugation, whereas electron withdrawing groups (EWGs) favour the triplet carbene species.¹³⁵ Labelling through the triplet carbene is also possible through a two-step radical-type mechanism, however several side reactions can occur including oxidation, reduction via consecutive H-abstraction, or, if available, a 1,2 H-shift and collapse to the alkene (**Scheme 1.6b**).^{90,132} This is favoured when the resulting alkene is conjugated to an EWG such as a carbonyl, and can be particularly problematic as a potent electrophile is generated that could favour off-target nucleophilic trapping.

From these considerations, TPDs have become popular warheads for AfBPP as π -donation from the adjacent phenyl ring favours the singlet carbene species, and the CF₃ group disfavors rearrangements that promote unwanted side-reactions.¹²³ However, unless a phenyl ring in the parent molecule is readily modifiable with a trifluoromethyl diazirine moiety, the whole TPD must be incorporated into the probe as a complete group, eliminating the advantage of a structurally discrete modification. Aliphatic diazirines can provide a convenient alternative to TPDs where incorporation of a full phenyl group would be disruptive to the biological activity of the parent molecule. While TPDs possess superior photochemical properties, aliphatic diazirines are smaller and can still form semi-stable singlet carbenes via σ -conjugation from adjacent C–C/C–H bonds.¹³⁵ Key examples of the use of both TPDs and aliphatic diazirines in photoaffinity labelling can be found in **Table 1.4 (Section 1.3.4)**, and while beyond the scope of this Thesis, the advantages of diazirines have led them to be used as photoreactive warheads in a range of applications including carbene footprinting,^{136,137} protein-protein interactions,^{138,139} other protein-biomolecule interactions,^{90,101,127} polymer photocrosslinking,^{140,141} photoaffinity chromatography,¹⁴² and DNA-encoded chemical library selection.¹⁴³

1.3.2.7 Comparison of photoreactive warheads

Diazirines, despite their rather limited synthetic accessibility, are small in size, react rapidly and exhibit low background labelling, have long irradiation wavelengths and short irradiation times, and are chemically and thermal stable. They therefore represent the optimal choice for development of an AfBP

(Table 1.2). In particular, aliphatic diazirines can be subtly incorporated into probes, minimally perturbing the SAR of the parent molecule, and their popularity has led to the development of so-called “minimalist” diazirine linkers that have been used to perform late-stage functionalisation of probes with a small photoreactive group (Section 1.3.4).

Table 1.2 Comparison of various photoreactive warheads.

Group	Irradiation wavelength (nm)	Background labelling	Synthetic accessibility	Size (compared to parent molecule)	Labelling specificity
Diazo	254	Moderate	High	Small	Broad
Aryl azide	250–370	Low	High	Moderate	Broad
Benzophenone	350–360	High	High	Large	Preference for C–H adjacent to N/S
ACT	302	Low	Low	Large	Asp/Glu only
α -ketoamides	350	Low	Low	Moderate	Unknown
Diazirines	330–370	Low	Moderate	Small (aliphatic) to moderate (aromatic)	Broad

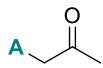
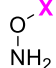
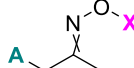
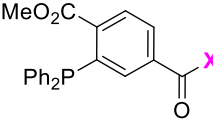
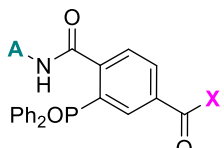
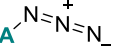
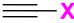
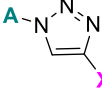

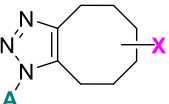
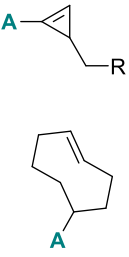
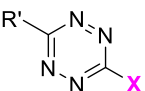
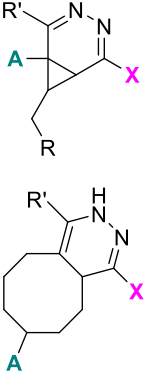
1.3.3 Ligation handles

Once the proteins have been labelled via the photoreactive warhead, profiling of these proteins requires incorporation of a secondary label into the probe that can distinguish the tagged proteins from the background proteome. This is usually a fluorophore which can visualise these targets by microscopy or gel electrophoresis, and/or an enrichment handle to partition the labelled proteins from the bulk proteome (Figure 1.4). These groups however are often large (>300 Da) compared to the probe (typically <500 Da) and can adversely affect the biological activity of the probe compared to the parent molecule. These modifications can also limit the cell permeability of the compound, preventing the probe from being able to efficiently profile living systems.⁷⁷

As a result, incorporating a small bio-orthogonal handle into the probe structure allows it to retain cell permeability and bioactivity. As long as the handle is unaffected by the UV irradiation used to activate the warhead, its bio-orthogonal reactivity can be used to conjugate the probe-tagged protein to a suitably functionalised reporter molecule after cell lysis. The bio-orthogonal reactions used in AfBPP are largely those defined as “click reactions”, described by Prof. Sharpless in a major review paper as reactions that are “*modular, wide in scope, give very high yields, generate only inoffensive byproducts that can be removed by nonchromatographic methods, and be stereospecific (but not necessarily enantioselective). The required process characteristics include simple reaction conditions (ideally, the process should be insensitive to oxygen and water), readily available starting materials and reagents, the use of no solvent or a solvent that is benign (such as water) or easily removed, and simple product isolation.*”¹⁴⁴ This original review also describes how the reactants in click chemistry should be highly reactive but only towards each other, and should be orthogonal to a wide range of interferents.

These conditions have led to the widespread use of click chemistry in chemical biology as they define a set of chemical reactions that are reproducible, efficient at low reagent concentrations, occur in aqueous media amongst a complex biological background, and generate by-products that are tolerated by the biological system.^{145,146} Click chemistry has been used to ligate together a whole host of chemical and biochemical partners including small molecules, polymers and peptides together with each other or with proteins, nucleic acids or lipids.^{147–149} **Table 1.3** summarises the key biorthogonal reactions that have been applied in the field of activity- and affinity-based protein profiling with key references for each.

Table 1.3 Summary of available click reactions for probe/reporter conjugation, adapted from Panyain *et al.* 2019.⁷⁷

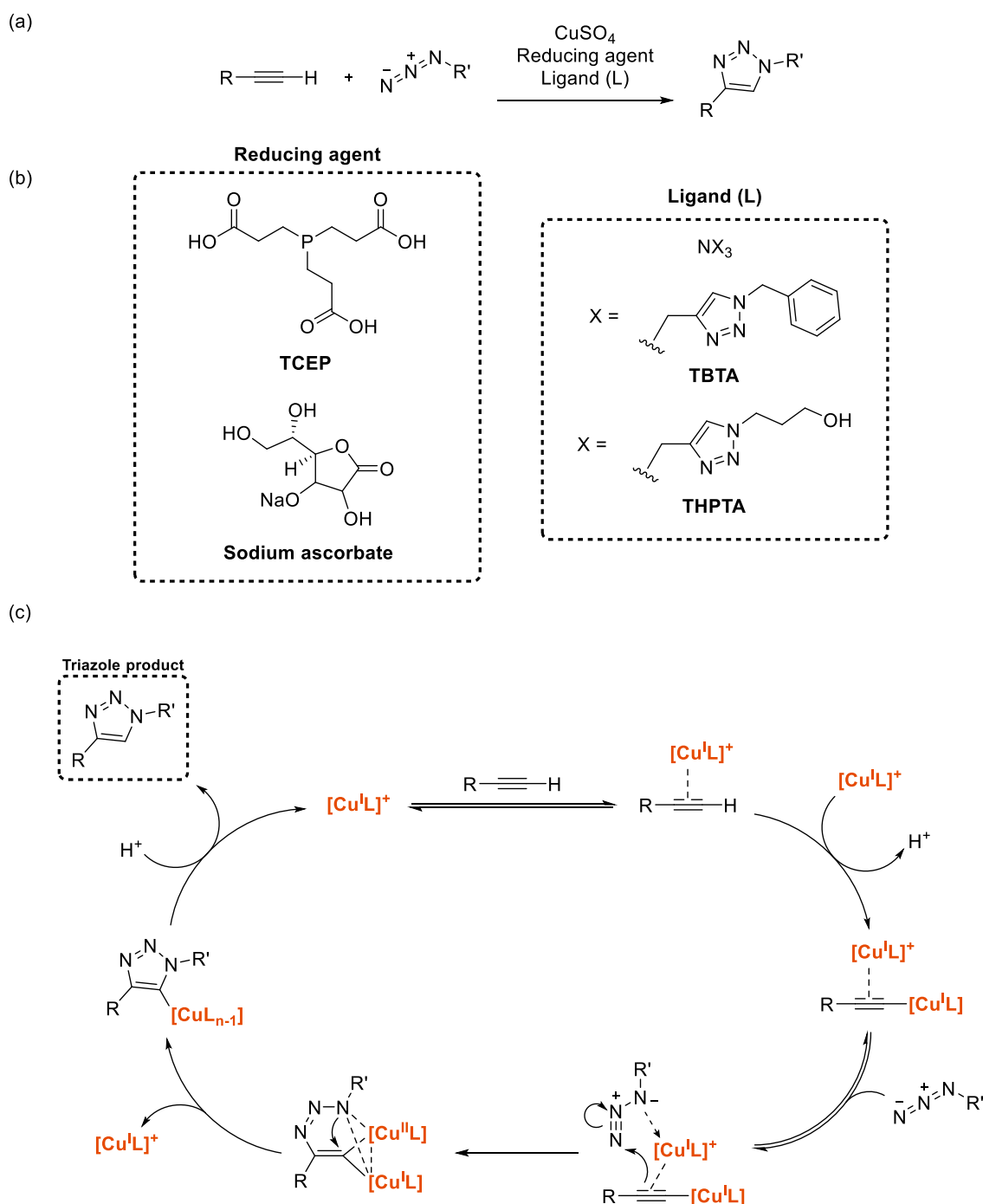
Reaction	Partner A	Partner X	Product	References
Oxime ligation				150–152
Staudinger-Bertozzi ligation				153–155
Copper-catalysed azide-alkyne cycloaddition (CuAAC)				156–159
Strain-promoted azide-alkyne cycloaddition (SPAAC)				160–162
Inverse-electron demand Diels-Alder cycloaddition (IED-DAC)				145,163,164 21,165

Oxime ligations have been widely used to functionalise antibodies and other biological macromolecules.^{166,167} Competing reactivity of endogenous biological amines with the ketone group and the pH dependence of this reaction has however limited the widespread application of oxime ligations in AfBPP.¹⁶⁸ The Staudinger-Bertozzi ligation has been extensively used in chemical biology, especially in native chemical ligation of two polypeptide chains,¹⁶⁹ however this method suffers from a

slow rate of reaction, and phosphines are chemically unstable in biological environments through oxidation of the phosphorous atom.¹⁷⁰ Inverse-electron demand Diels-Alder cycloaddition (IED-DAC) reactions have emerged over the past decade as an efficient, stable reaction that is highly specific between the electron-poor diene e.g. tetrazine and electron-rich dienophile.¹⁴⁵ These large, hydrophobic alkenes have however demonstrated off-target labelling and, along with the tetrazine group, can be challenging to synthesise.¹⁴⁶

Perhaps the most widely used ligation reaction in ABPP/AfBPP is the copper(I)-catalysed azide-alkyne cycloaddition (CuAAC).^{79,146} The small size and linear structure of both the alkyne and azide groups allows them to be placed discretely onto a probe structure, usually with minimal disruption to the biological activity of the compound, and the reaction proceeds specifically and rapidly under physiological conditions. The copper catalyst was found to be necessary to speed up the low and unobservable reaction rate between azides and alkynes at room temperature.¹⁷¹ Additionally, the development of chelating bio-compatible ligands increased this rate of reaction further while also reducing the amount of toxic copper metal needed to progress the reaction.¹⁴⁶ Incorporation of the copper species as a readily available Cu(II) salt such as CuSO₄ has also been made possible by introducing a mild reducing agent such as sodium ascorbate or tris(2-carboxyethyl)phosphine (TCEP) to the reaction that reduces the copper to Cu(I) *in situ*.^{171,172} Further optimisations of these conditions have demonstrated that this reaction gives highly efficient and reproducible labelling.^{173–175} The mechanism by which the triazole species is formed is now thought to be via a dinuclear copper intermediate and is outlined in **Scheme 1.7**, however further work is needed to fully validate this mechanism.¹⁷⁶

The toxicity of the copper catalyst means that CuAAC is not compatible with live-cell labelling, so for these cases the “copper-free” or strain-promoted azide-alkyne cycloaddition (SPAAC) has been used, where a strained alkyne is incorporated into the probe, increasing its reaction rate with the azide partner.¹⁷⁷ This however adds considerable steric bulk, and while this reaction has been used in protein profiling studies,¹⁷⁸ the toxicity of the CuAAC is not problematic for AfBPP considering that the click reaction is performed *in vitro* once the cells are already lysed. Another consideration is that Cu-activation of the alkyne can increase its electrophilicity and lead to off-target labelling by protein nucleophiles, however this can be overcome by keeping the alkyne concentration low, therefore the most common orientation of this labelling pair is an alkyne-labelled probe and an azide reporter.¹⁴⁶



Scheme 1.7 Copper catalysed azide-alkyne cycloaddition (CuAAC). (a) Overall reaction scheme. (b) Structure of common reducing agents and ligands used in CuAAC for AfBPP; TCEP = tris(2-carboxyethyl)phosphine, TBTA = tris[(1-benzyl-1H-1,2,3-triazol-4-yl)methyl]amine, THPTA = tris(3-hydroxypropyltriazolylmethyl)amine. (c) CuAAC mechanism following initial reduction of Cu^{2+} by the reducing agent.

1.3.4 Minimalist diazirine photocrosslinkers

The superior properties of both the alkyne and the diazirine groups have led to the combination of both being a popular choice for the protein profiling scientist. In order to make the incorporation of these group into AfBPs modular and translatable, the past decade has seen the evolution of so-called

“minimalist” linkers that incorporate both the diazirine and terminal alkyne into one molecule. These and some examples with other biorthogonal ligation handles are shown in **Figure 1.5**.

The Yao group pioneered this type of linker with their first generation examples that could be coupled onto an available amine/alcohol (**L1**) or carboxylic acid (**L2**) present or engineered into the parent compound, or through S_N2 displacement with an available nucleophile (**L3**).¹²⁴ This work was extended to generate similar tags for both IED-DAC reactions (**L4**, **L7**, **BD-5**, and **BD-7**) and SPAAC (**BD-6**).^{164,179} The Seiber group reported a smaller version of the original carboxylic acid linker **L1** and used it with success,^{117,180} however as discussed (**Scheme 1.6**), β -diazirines can, via triplet carbenes, collapse to the unsaturated carbonyl that could be labelled by surrounding nucleophiles. An isocyanide-modified version of the first generation linkers that could be incorporated into probes using various multicomponent reactions has also been reported by the Lipinsky group.¹⁸¹

In a desire to simplify what is often a long, linear and low-yielding synthesis, the Cravatt group has developed minimalist groups that can be synthesised in a convergent manner, with the diazirine and alkyne synthesised separately and joined together with the coupling group in the middle (**DA5a**, **DA18**).¹⁸² Further individual cases of efforts to simplify the synthesis of these linkers have been reported, for example a bis-alkyne linker from the Cravatt group coupled onto an azide-containing parent molecule to generate an AfBP,¹⁸³ or a bis-carboxylic acid diazirine molecule coupled on one side to an alkyne, then on the other side through an amine to the parent molecule (Wolan group).¹⁰⁰

These minimalist linkers are moderately sized (~150 Da) compared to a parent drug molecule and are hydrophobic in nature. However, the need to only modify the probe in one place with a bifunctional linker and the potential of late-stage functionalisation has made this a popular strategy to profile the protein binding partners of many small molecule drugs. **Table 1.4** summarises some key examples of the use of minimalist terminal alkyne-containing diazirine photocrosslinkers. Further examples include target identification of the psychoactive agent $\Delta^{8/9}$ -Tetrahydrocannabinol (THC),⁹⁹ ramariolide natural products,¹⁸⁰ photoreactive anticancer inhibitors,¹⁸⁴ oxysterol compounds,¹⁸⁵ and they have also been used to profile the binding landscape of sialic acid binding proteins,¹⁰⁰ histone deacetylase inhibitors,¹⁸⁶ and a suite of so-called “fully functionalised fragments” to uncover new druggable targets in a live cell system.^{187,188}

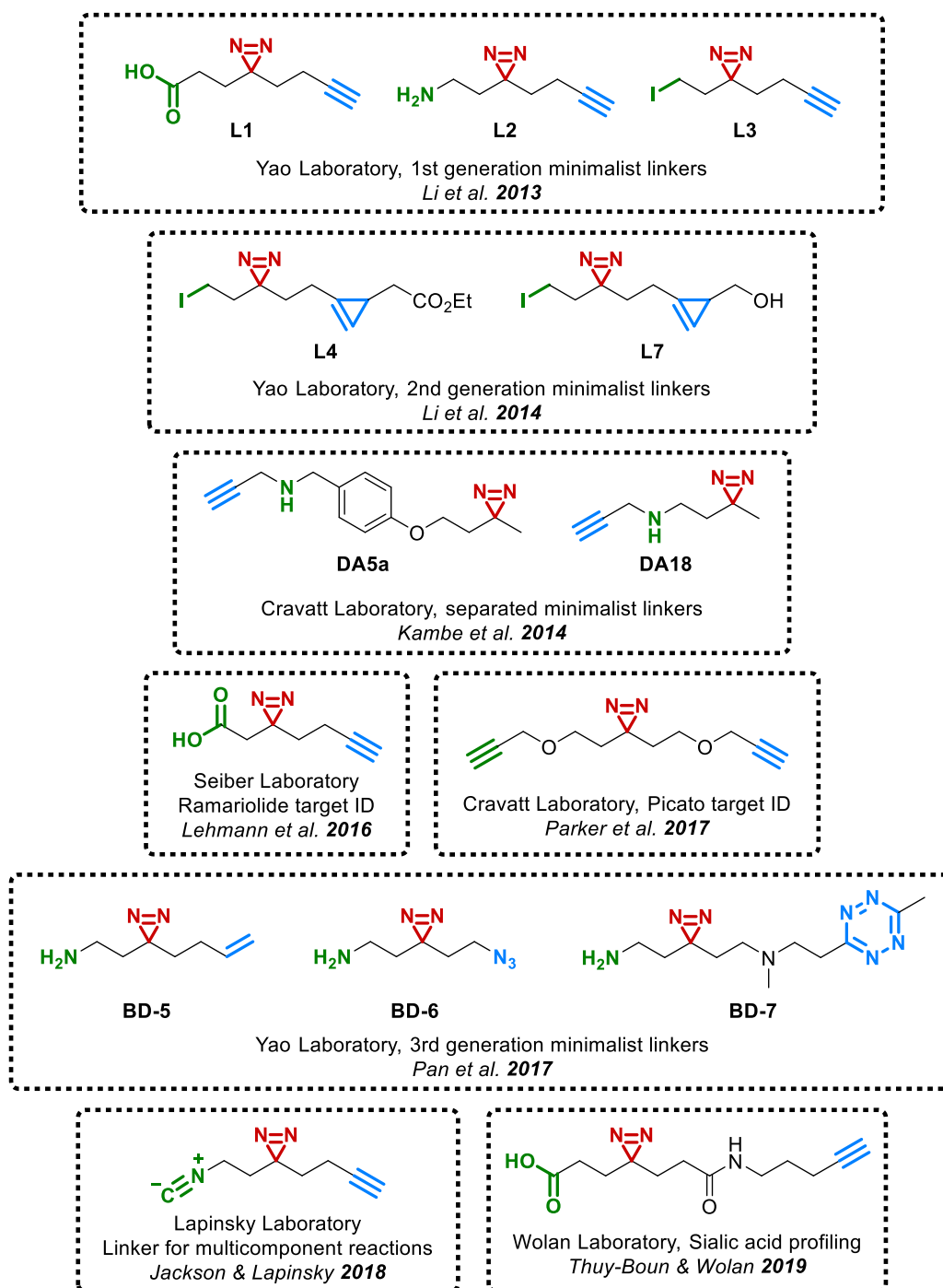
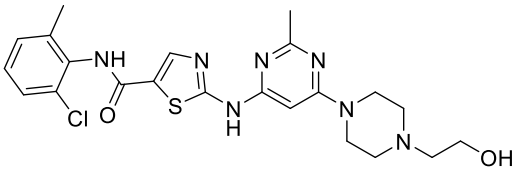
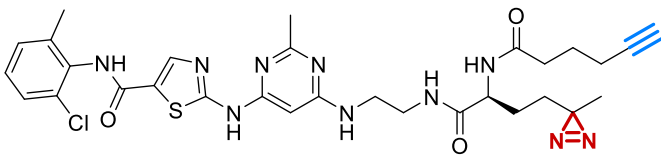
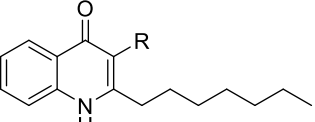
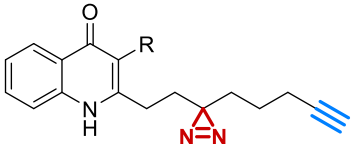
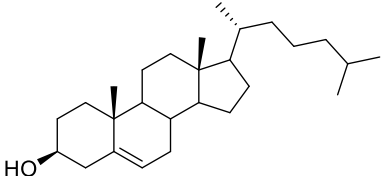
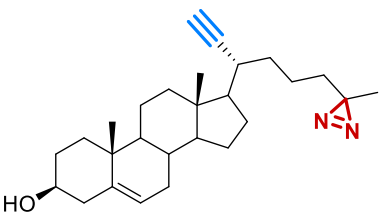
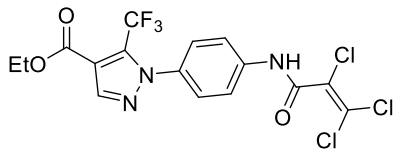
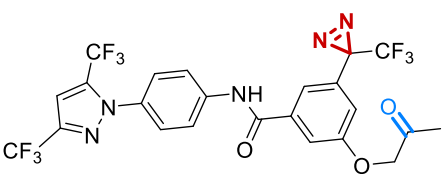
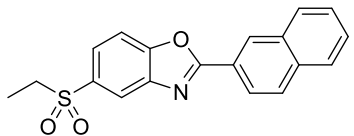
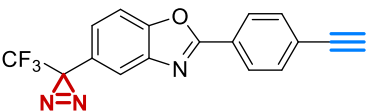
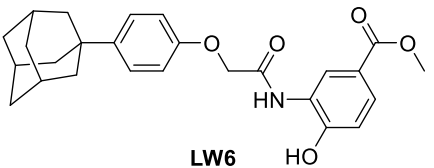
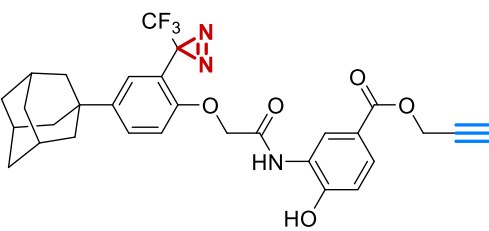
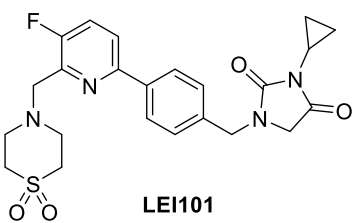
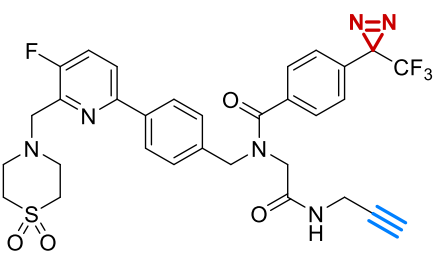
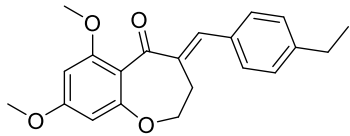
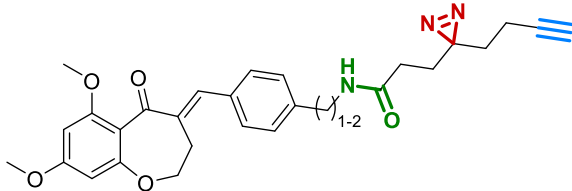
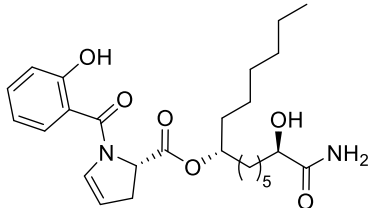
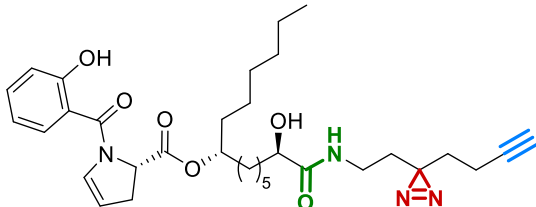
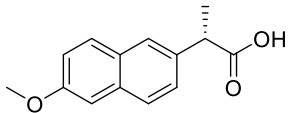
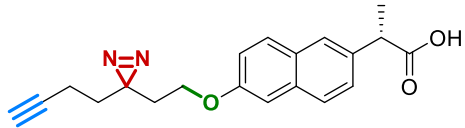
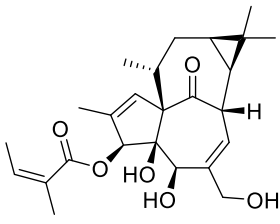
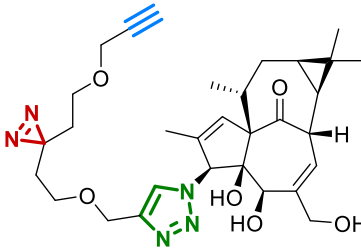


Figure 1.5 Timeline of development of various diazirine-containing “minimalist” diazirine-containing photocrosslinking groups. Green = coupling point to rest of probe, red = diazirine, blue = biorthogonal ligation handle.

Table 1.4 Representative examples of diazirine affinity-based probes for target ID/profiling studies. Red = diazirine, blue = biorthogonal ligation handle, green (minimalist class) = coupling point to rest of probe. PQS = *Pseudomonas* quinolone signal (2-heptyl-3,4-dihydroxyquinoline); HHQ = 4-hydroxy-2-heptylquinoline.

Diazirine class	Compound	Probe	Target(s) identified/profiled	Reference
Aliphatic	 <p>Dasatinib</p>		Protein kinase A (PKA) Serine/threonine-protein kinase pim-3 (PIM-3), Serine/threonine protein kinase N2 (PKN2)	96
	 <p>R = OH, PQS R = H, HHQ</p>		Various quorum sensing molecule interacting proteins	102
	 <p>Cholesterol</p>		Diverse cholesterol binding proteins	189

Aromatic	 <p>Pyr3</p>		Transient receptor potential channel 3 (TRPC3)	150
	 <p>Ezutromid</p>		Primary: Aryl hydrocarbon receptor (AHR) Selected secondary: Catalase (CAT) Arfaptin-2 (ARFIP2)	27
	 <p>LW6</p>		Malate dehydrogenase 2 (MDH2)	97
	 <p>LE1101</p>		Cannabinoid receptor type 2 (CB ₂)	98

Minimalist	 <p>Benzoxepane derivative</p>		<p>Primary: Pyruvate kinase M2 (PKM2) Selected secondary: Heterogeneous nuclear ribonucleoprotein, Actin</p>	190
	 <p>Promysalin</p>		<p>Succinate dehydrogenase C-subunit (SdhC)</p>	191
	 <p>Naproxen</p>		<p>Several members of e.g. NF-κB signalling complex and ubiquitin E3 ligase complexes</p>	34
	 <p>Picato®</p>		<p>Primary: Solute carrier family 25 member 20 (SLC25A20) Selected secondary: Paraoxonase 2 (PON2) Saccharopine dehydrogenase-like oxidoreductase (SCCPDH)</p>	183

1.4 Affinity-based protein profiling workflow

Once the AfBP has been designed and synthesised, it can be used to profile its biomolecular targets in cell lysates (*in vitro*) or in live, intact cells (*in situ*). First however, it is necessary to validate that the AfBP is a suitable chemical tool for the parent compound, and that the modifications made to the parent molecule have not severely negatively impacted on the biological activity and/or cell permeability of the compound. This usually involves testing the AfBP in the same phenotypic assays that were used to demonstrate the activity of the parent compound and, if any of the targets are already known, biophysical or enzymatic assays that measure the binding or inhibition of the AfBP with respect to the parent molecule.^{27,98} If the probe is tested and fails to elicit an acceptable level activity compared to the parent compound, then alternative probe designs should be adopted. AfBPs that are active in these phenotypic assays can be taken forward to affinity-based protein profiling experiments.

The generalised AfBPP workflow is outlined in **Figure 1.6**. Intact cells or lysates are treated with the probe (or an appropriate control) then irradiated with 365 nm UV light. This generates the hyper-reactive carbene species that crosslinks the probe to the bound protein partner. If performing this experiment *in situ*, the cells are lysed mechanically or with an appropriate buffer. After normalisation of each sample to a common protein concentration, tagged proteins are ligated to a reporter molecule through CuAAC which then allows visualisation, analysis and/or quantification of the probe-tagged proteins.¹⁹²

Exploratory AfBPP experiments assessing the labelling efficiency of the probe at several concentrations, over various incubation times and with different UV irradiation times are necessary to determine the optimal conditions to obtain significant labelling results in larger target profiling campaigns. This is most readily assessed through CuAAC (**Scheme 1.7**) to a reporter molecule containing a fluorophore that allows qualitative assessment of the labelling via in-gel techniques (**Figure 1.6**).^{36,95,186}

1.4.1 Reporter molecules

The Tate group has extensive experience in the optimisation of the CuAAC reaction for chemical biology,^{30,159,172} and as a result has several reagents that have been designed and synthesised in-house to functionalise alkyne-tagged proteins with reporter groups.^{158,193} While commercial azide-functionalised tags are available, the group have previously reported the superior labelling achieved by these hydrophilic peptide-based reporter molecules.¹⁵⁸ These azide-based reporters are functionalised either with both a 5(6)-carboxytetramethylrhodamine (TAMRA) fluorophore and a biotin enrichment handle (AzTB, **Figure 1.7**) or with a biotin group and a protease-cleavable linker between the azide and the biotin (AzRB, **Figure 1.7**).

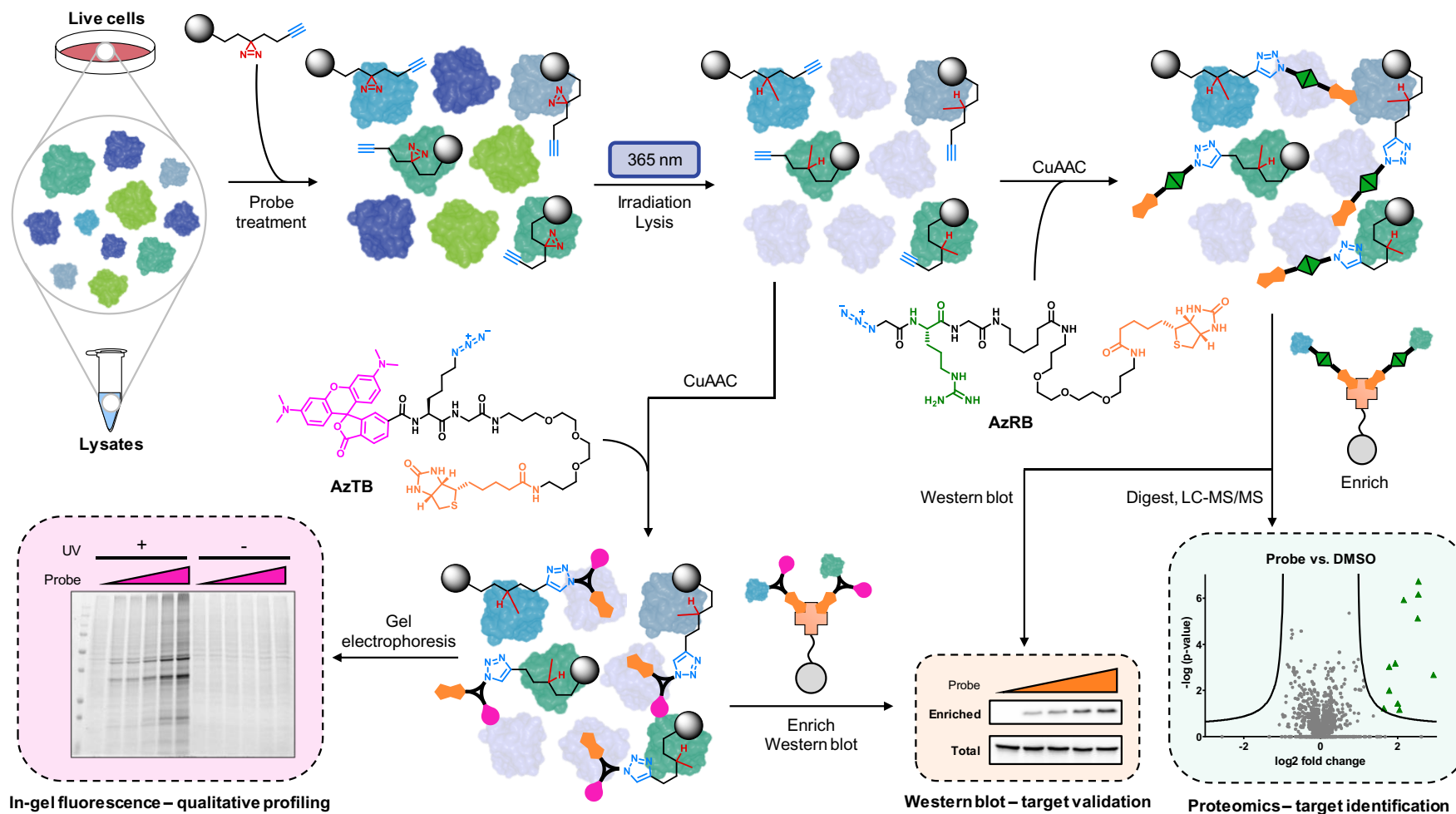


Figure 1.6 Workflow of affinity-based protein profiling (AfBPP). Live cells or cell lysates are treated with an affinity-based probe, and irradiation covalently captures the reversible probe-protein interactions. Cells are lysed if necessary then subjected to a copper catalysed azide-alkyne cycloaddition (CuAAC) with either azide-arginine-biotin (AzRB) or azide-TAMRA-biotin (AzTB). TAMRA-tagged proteins can be visualised by gel electrophoresis, and biotin-tagged proteins can be enriched on avidin beads for Western blot analysis or proteomics. Incorporation of a cleavable linker (AzRB) allows for release and analysis of the labelled peptide from the avidin beads.^{77,158}

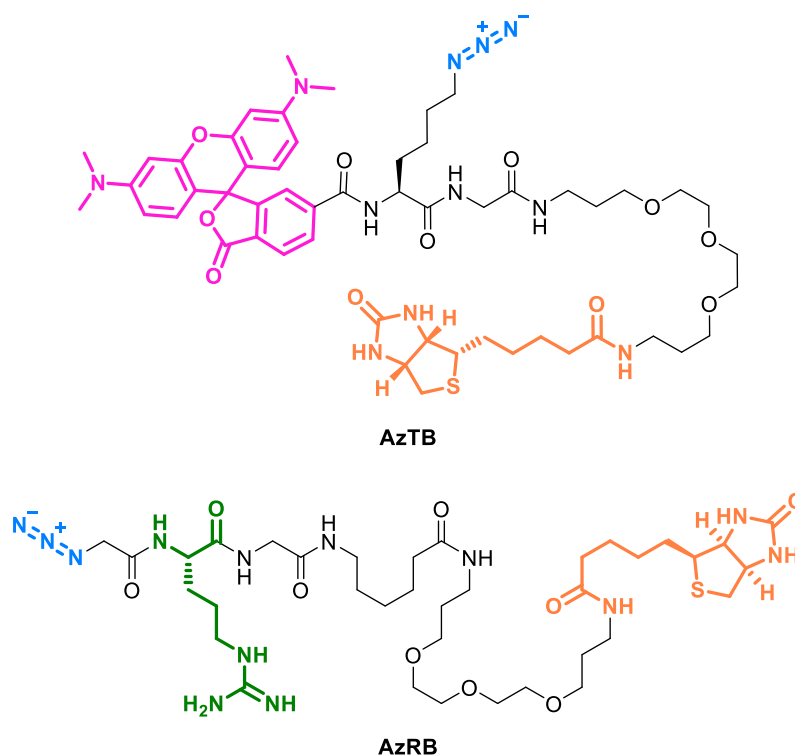


Figure 1.7 Reporter molecules designed and synthesised in the Tate group. Blue = azide (biorthogonal ligation handle), orange = biotin, pink = TAMRA fluorophore, green = arginine (trypsin cleavable linker).¹⁵⁸

1.4.2 Analysis techniques

Once proteins have been labelled and functionalised with the appropriate reporter molecule through CuAAC, the excess click reagents can be removed by precipitation of the proteins with, for example, a mixture of chloroform and methanol. The proteins can then be redissolved in an appropriate buffer to give the final functionalised protein sample.¹⁹⁴ The proteins can then be analysed by gel- or proteomics-based methodologies.

1.4.2.1 In-gel fluorescence

Functionalisation of alkyne-tagged proteins with AzTB allows for the detection of labelled proteins through the appended TAMRA fluorophore. Proteins can be loaded onto a polyacrylamide gel and separated by size using gel electrophoresis. The separated, functionalised proteins can then be visualised by exciting the gel with 532 nm light and reading the emitted fluorescence at 610 nm.¹⁷² The fluorescent bands indicate proteins that have been labelled by the AfBP, and analysis of the labelling pattern across various concentrations of the probe can give a qualitative indication of the labelling efficiency of the probe.

Further information can be gleaned from this technique by performing a “competition experiment” (**Figure 1.8**).^{20,195} In this type of experiment, samples are treated with vehicle control, AfBP only, or AfBP *and* the parent molecule at the same time. In the latter case, probe-tagged proteins that are targets of the parent molecule as well should exhibit a lower level of labelling since the parent compound will

blockade the binding site of the protein and prevent the probe from photocrosslinking to the protein upon irradiation. This competition experiment is essential to determine which protein bands on the gel represent true targets and which are products of non-specific background labelling brought about through binding of the newly added diazirine and alkyne groups; in this case no decrease in labelling would be expected upon co-treatment of the sample with the parent molecule. Such common background binders to widely used photocrosslinking warheads have been profiled by the Sieber group, and is a valuable resource for identifying potential false positive hits identified through AfBPP.¹¹⁷

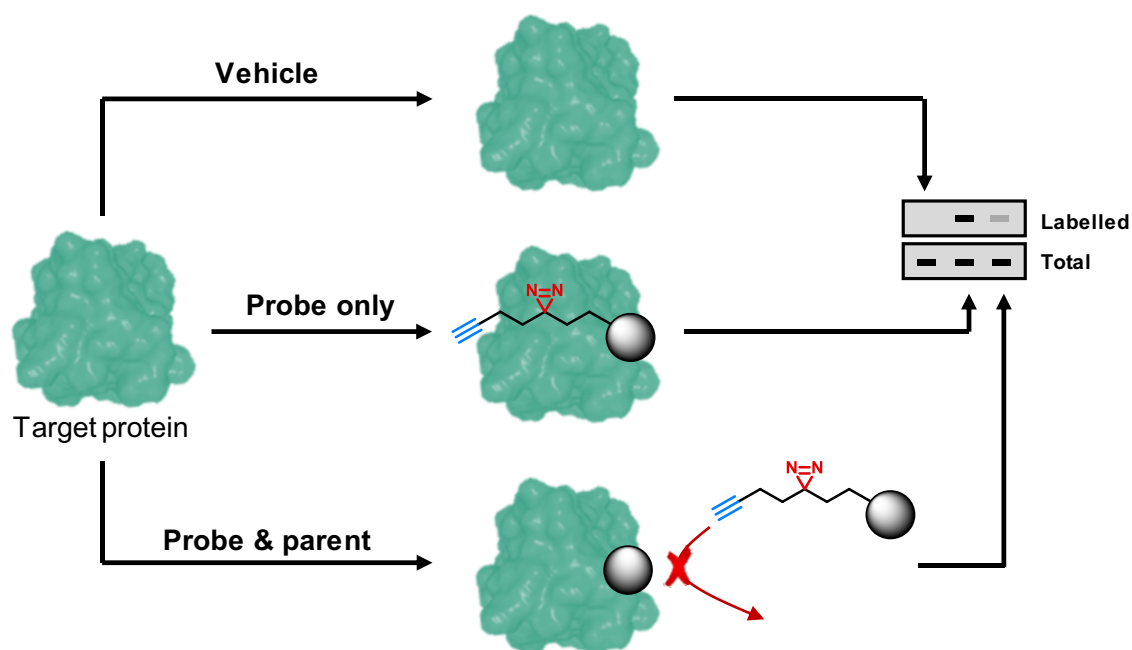


Figure 1.8 The principle of competition experiments. The total protein remains constant across all samples, but competition-treated samples demonstrate a decrease in labelling of a true target due to parental blockade of the probe’s binding site.

Excision of the labelled bands on the gel and analysis by mass spectrometry can be performed to identify the targets of the probe, however this “top-down” approach is a relatively time-consuming process if each band is excised. This would also neglect proteins that do not separate well on polyacrylamide gel electrophoresis such as those with extreme isoelectric points or more hydrophobic proteins, and would bias towards high abundance proteins.^{196,197} Instead, an unbiased, whole proteome approach (“bottom up” **Section 1.4.2.3**) is more often taken.

1.4.2.2 Western blot

Both AzTB and AzRB contain a biotin group which allows for avidin-based enrichment of tagged proteins from the background proteome. Biotin has an extremely strong binding affinity ($\sim 10^{-14}$ M) to avidin proteins (streptavidin, NeutrAvidin).¹⁹⁸ Attachment of this protein to a solid support such as

magnetic or agarose beads allows for enrichment of the biotin-labelled proteome: after elution from the beads and separation on-gel, the enriched fraction can be analysed either by in-gel fluorescence again and/or by transfer to nitrocellulose membrane and Western blotting. The latter technique can be used to confirm probe enrichment of a specific protein of interest by using an antibody raised against that protein.

1.4.2.3 Chemical proteomics

Proteomics analysis of the enriched proteome is the most comprehensive methodology for *de novo* target identification and quantification. Rather than eluting the enriched sample directly from the beads, samples are subjected to on-bead digestion into their constituent peptides with a protease such as trypsin.^{199,200} Ligation of the tagged proteins to AzRB rather than AzTB incorporates a trypsin cleavable linker into the probe-protein tag which means the biotin group will be cleaved from the labelled peptide, liberating a peptide modification that is smaller, more hydrophilic and therefore more able to be detected by liquid-chromatography (LC) and tandem mass spectrometry (MS/MS) techniques (**Figure 1.9**).^{158,175} This increases the chance that the modified peptide can be identified and therefore data such as binding site information can be obtained from these AfBPP experiments.

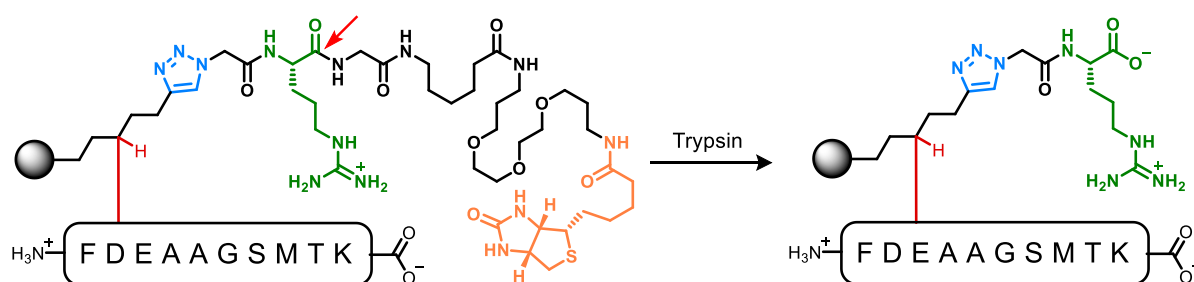


Figure 1.9 Trypsin processing of a probe-modified peptide. Trypsin cleavage is specific for lysine (K) and arginine (R) residues and cleaves towards the C-terminal end of these residues (red arrow).¹⁵⁸

Once the peptides have been generated, they are separated by nano-liquid chromatography (nanoLC), ionised, and the ions separated by their mass-to-charge ratio at the first mass spectrometer (MS^1). The most abundant peptides are then fragmented and the resulting ions undergo separation by a second mass spectrometer (MS^2): this scan pattern is used to deconvolute the sequence of the fragmented peptide.^{201,202} Matching against annotated genomic databases of the organism in question then allows identification of the source protein by mapping of the peptide sequence to a known protein.²⁰³ Such identification of peptides from a complex mixture of proteins is a “bottom-up” technique and is referred to as shotgun proteomics.²⁰⁴

Peptides from each sample can be run and analysed individually and their MS^1 ion intensities compared across samples to perform relative quantification. This type of quantification is known as label-free quantification (LFQ) and is the simplest and cheapest type of proteomics experiment that can be performed, and due to the analysis of one sample at a time has a large dynamic range.²⁰⁵ However,

keeping samples separate at every stage of the experiment can reduce reproducibility due to variation in sample preparation across different conditions.^{77,206} Techniques to pool different samples together allows for sample multiplexing and can reduce cross-sample variability, however some type of labelling methodology is required to distinguish peptides from different conditions pooled into the same sample.

One approach to this is metabolic labelling methodologies such as stable isotope labelling by/with amino acids in cell culture (SILAC) whereby cells of different experimental conditions (e.g. vehicle treated, probe treated) are cultured in a medium containing differentially heavy-, medium-, or light-labelled amino acids.²⁰⁷⁻²⁰⁹ The proteins from each condition will then be labelled with different isotopes from the outset and can be pooled immediately, reducing variation in sample preparation from the start; relative quantification across samples is then performed at the MS¹ level by comparing the abundance of heavy-, medium- and light-labelled peptides. A drawback of this methodology is the time and effort required to set up and maintain cell lines with the corresponding isotope label, the reagents for which can be costly. Furthermore, simpler SILAC experiments are generally limited to three isotope conditions, and SILAC is only possible for organisms and samples that readily incorporate such labels.

Alternatively, chemical labelling methodologies have emerged as a method of labelling proteins or peptides from different samples with a unique chemical tag that allows them to be distinguished once pooled together. Many such labelling reagents are available, including dimethyl labelling reagents²¹⁰ and isobaric tags for relative and absolute quantitation (iTRAQ),²¹¹ however the chemical labels most commonly used in-house are the tandem mass tag (TMT) reagents (**Figure 1.10**).^{159,172,212} In TMT labelling, the peptides of each sample are labelled with a unique isobaric TMT reagent, meaning the mass addition from each TMT reagent is the same at the MS¹ level.^{213,214} Upon fragmentation however the TMT-label fragments along with the peptide in a predictable manner, and each label sheds a unique isotopically coded reporter ion which can be detected and quantified at the MS² level alongside the fragment peptide ions. The relative levels of each of these reporter ions is then used to quantify the amount of this peptide that comes from each sample. Commercially available kits like the ThermoFisher TMT10plex™ reagents can allow the multiplexing of up to 10 samples into one MS run, reducing processing time and running costs, however this amount of information requires a longer chromatographic gradient to separate the large number of peptides.²¹⁵ Additionally, each multiplexed sample can be fractionated by high pH reverse phase or ion exchange methods prior to LC-MS/MS analysis to increase the depth and coverage of the experiment.²¹⁶ While TMT reagents are expensive and ion contamination at the MS² level can suppress quantification, it has been reported that TMT labelling is more precise than LFQ, and can detect more statistically significant changes between samples.^{217,218}

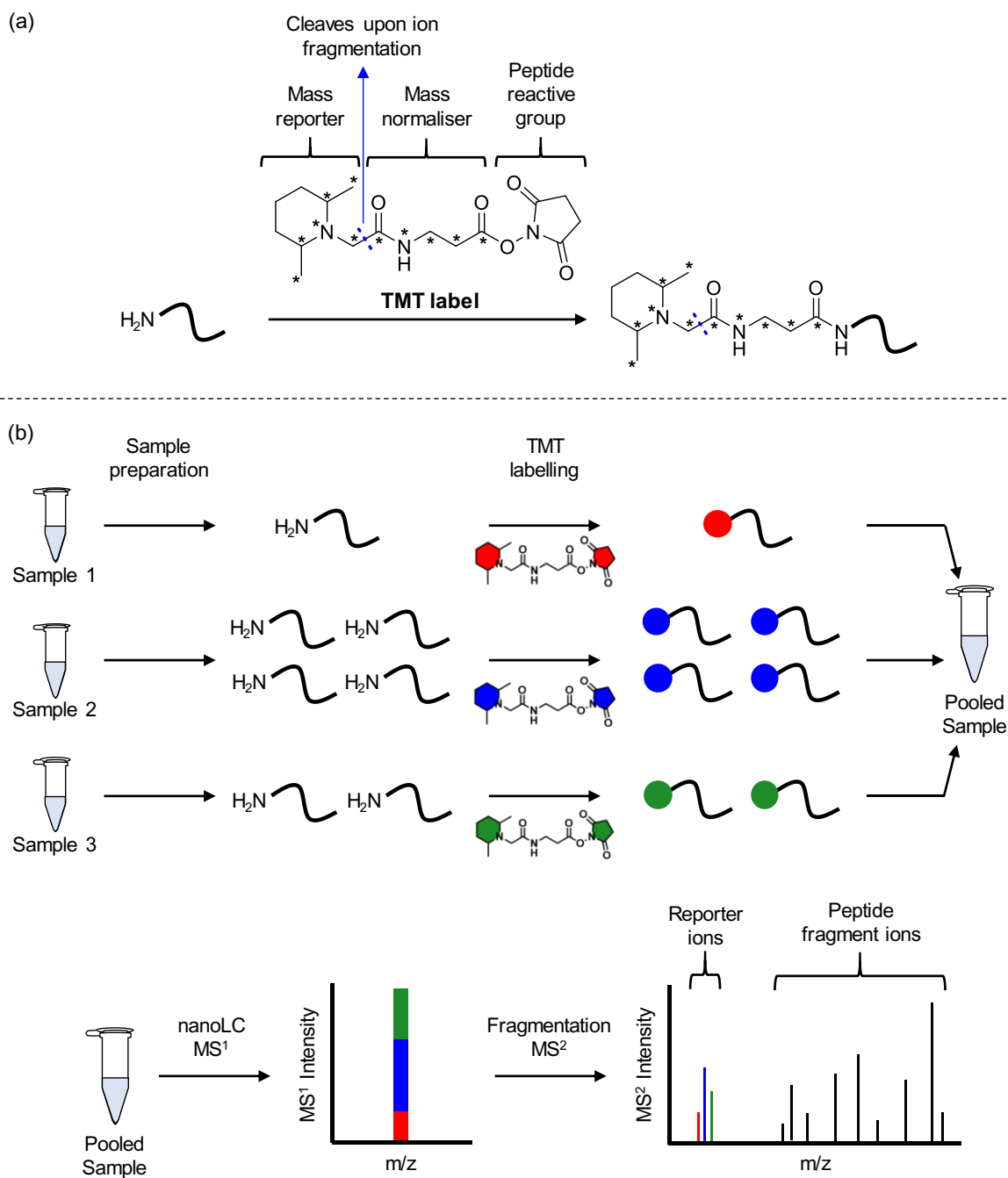


Figure 1.10 Peptide labelling with TMT10plex™ reagents. (a) Structure of the generic TMT10plex isobaric labelling reagent and its attachment to the N-termini (and lysine residues) of peptides to generate the isobarically tagged peptides. Asterisks represent positions that are variably isotopically encoded (¹³C/¹⁵N) across the 10 different reagents – the mass normalising spacer is also isotopically encoded to balance out the mass difference in the mass reporter so the overall mass remains the same until MS² fragmentation. (b) Up to 10 samples can be labelled with different TMT10plex reagents at which point the samples can be pooled and run on nLC-MS/MS. The same peptides from different samples co-elute at MS¹ and are fragmented together; the reporter ions fragment predictably and the different amounts of each reporter can be detected by their different MS² masses and the intensity of each used for quantification.

1.5 Thesis aims

Target profiling of small molecule drugs is essential to achieve a better understanding of how they interact with biological systems. The technologies described above can determine the molecular mechanism of action of a pharmacological molecule and the cause of any undesired toxicity, helping to shape a compound's development into a clinical molecule. Affinity-based protein profiling (AfBPP) linked with chemical proteomics provides a robust strategy with which to perform this task in a living system and is the methodology of choice used to profile the molecules under investigation in this Thesis. Given their favourable properties and extensive literature precedent discussed above, the diazirine group was chosen as the photo-reactive warhead, and the alkyne as the ligation handle. Alkynes were also selected due to the experience within the Tate group of alkyne-based Click chemistry, and the availability of suitable in-house reporter molecules.

The overall aim of this Thesis is to undertake two AfBPP campaigns to profile the biomolecular interactome of (1) novel and existing poly(ADP-ribose) polymerase (PARP) inhibitors and (2) new inhibitors of necroptosis through the development and application of diazirine-alkyne AfBPs.

The aims of Chapter Two are:

- Establish the current literature precedent for PARP enzymes, their relevance to disease, and their inhibition, including any existing protein profiling campaigns and the chemical matter upon which the PARP AfBP used herein (**PARPYnD**) is based.
- Undertake photocrosslinking experiments to evaluate AfBP **PARPYnD** (previously synthesised in *Ryan Howard, MRes Chemical Biology, 2017*)²¹⁹ in live cells and establish its ability to profile PARP enzymes.
- Generate a complete target profile for **PARPYnD** using chemical proteomics and use competition experiments to profile other PARP inhibitors.
- Validate the mechanism of action of the parent compounds of **PARPYnD** in live cells.

The aims of Chapter Three are:

- Review the existing literature on the inflammatory process known as necroptosis, its relevance to disease, and current efforts to inhibit the pathway by small molecules.
- Design, synthesise and validate AfBPs based upon a new pharmacophore that inhibits necroptosis, discovered through a recent high content screen of an AstraZeneca library of compounds.
- Generate a complete target profile for the AfBP and utilise competition experiments to identify the molecular targets of the parent pharmacophore.
- Use orthogonal techniques to identify the key biomolecular interaction(s) that drives the mechanism of action of this novel anti-necroptosis agent.

Chapter 2 Target profiling of novel and existing poly(ADP-ribose) polymerase inhibitors

2.1 Poly(ADP-ribose) polymerases (PARPs)

Poly(ADP-ribose) polymerases (PARPs) are a family of seventeen enzymes that catalyse a reversible post-translational modification (PTM) known as ADP-ribosylation.^{220–222} This involves the transfer of one (mono-ADP-ribosylation; MARylation) or more (poly-ADP-ribosylation; PARylation) units of ADP-ribose (ADPr) from a nicotinamide adenine dinucleotide (NAD⁺) cofactor to a substrate protein (**Figure 2.1**), nucleic acid or small molecule, leading to diverse biological consequences. The involvement of PARPs in various disease states has made them the subject of many drug discovery campaigns, resulting in several PARP inhibitors (PARPi) successfully entering the clinic. This chapter will discuss the PARPs and their relevance to mammalian physiology and disease before addressing the key PARPi relevant to this work, highlighting the need for robust tools to profile the interactions of PARPi with the PARPs and other proteins in living systems. The results then describe the development and application of a novel affinity-based probe to investigate the action of PARPi in a live-cell setting, uncovering new information about how PARPi interact with the cellular proteome.

2.1.1 PARPs and ADP-ribosylation

PARPs belong to a larger superfamily of proteins known as ADP-ribosyltransferases (ARTs). PARPs are classified as “ART diphtheria toxin like” proteins (ARTDs) due to the structural homology of their ADP-ribosyltransferase domain to the bacterial diphtheria toxin protein produced by *C. diphtheriae*.^{223,224} The bacterial protein has a specific fold in its catalytic ADPr transferase domain that appears to be evolutionarily conserved in mammalian PARPs. This has led to the suggestion of an updated nomenclature from “PARP” proteins to “ARTD” proteins to distinguish them from another mammalian family of ADP-ribosylating proteins, the “ART cholera toxin like” proteins (ARTCs).²²⁴

Importantly, this ARTD-fold of the C-terminal PARP catalytic domain is largely conserved across the family, with the key catalytic motif assembled as a triad of histidine, tyrosine and glutamic acid (H-Y-E).^{224,225} Every PARP protein contains this H-Y-E motif, or some slight variant, and is key for the catalytic activity of the enzyme. The crystal structure of PARP1 with a non-hydrolysable analogue of its NAD⁺ cofactor bound into the active site was recently solved, and along with previous studies provided key insights into the mechanism of ADP-ribosylation by the PARP family of proteins (**Figure 2.1**).²²⁶

NAD⁺ binds into its cofactor pocket in a compact conformation (**Figure 2.1**, inset) that promotes the lengthening and weakening of the C1'–N bond connecting nicotinamide to the furanose ring, stabilised by the formation of a furanosyl oxocarbenium cation (**Figure 2.1**).^{227,228} In an almost S_N1-type manner, this bond is nearly severed before nucleophilic attack from a residue on the substrate protein generates

the MARylated product.²²⁹ Once the substrate protein is MARylated, certain members of the family can then extend this modification with further units of ADPr from multiple NAD⁺ cofactors, transferring them onto the free hydroxyl groups of the initial ADPr modification to generate linear or branched chains of poly(ADP-ribose) (Figure 2.1).²³⁰ ADP-ribosylation is also a dynamic, reversible modification and can be removed upon hydrolysis by specific ADP-ribosylhydrolases such as PAR degrading enzymes poly-ADP-ribose glycohydrolase (PARG)²³¹ and ADP-ribosyl-acceptor hydrolase 3 (ARH3),²³² and various MAR hydrolases.²³³

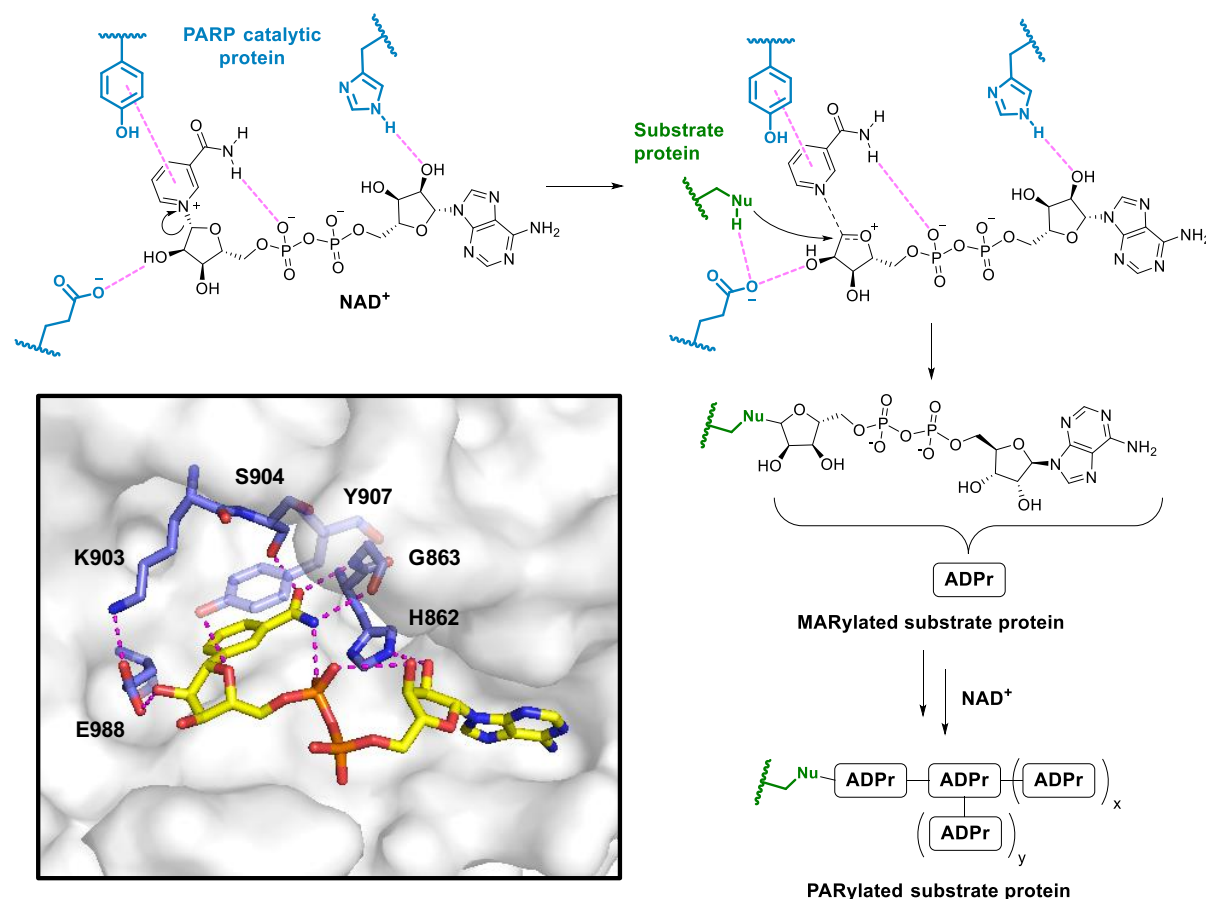


Figure 2.1 PARPs and ADP-ribosylation. Main figure: mechanism of MARylation and PARylation of a substrate protein. Key contacts of NAD⁺ with the PARP1 H-Y-E domain are highlighted in pink, x = number of linear ADPr units, y = number of branched ADPr units. Inset: crystal structure of non-hydrolysable NAD⁺ analogue (yellow) bound into the active site of PARP1 (grey); key interacting residues, including the H-Y-E domain, are highlighted in blue and polar contacts are highlighted in pink [PDB ID: 6BHV].^{222,226}

Across the family of 17 PARPs, four are able to catalyse PARylation, with the majority of the remaining family members only able to catalyse MARylation of the target protein; one (PARP13) is not currently reported to be catalytically active (Table 2.1).^{225,234} This is largely due to variations in the H-Y-E triad; mutagenesis studies in the structurally related diphtheria toxin have shown that all three residues are essential for NAD⁺ binding, but glutamic acid in particular was found to be important for the transfer of ADPr units onto the substrate (Figure 2.1).^{235–237} The majority of human PARPs that only catalyse

MARylation vary in this glutamate residue (**Table 2.1**) with, most commonly, an isoleucine/leucine in its place, suggesting glutamate is key for chain extension and PARylation.²²⁵ Accordingly, mutagenesis experiments on E988 in the PARP1 active site abolished PARylation activity but not MARylation activity, though PARP3/4 do contain a glutamate without any associated PARylation activity.²³⁸

Table 2.1 Activity and catalytic motifs of the PARP family of enzymes.

Activity	Catalytic motif	PARPs
PARylation	H-Y-E	1, 2, 5a, 5b
	H-Y-E	3, 4
	H-Y-I	6–8, 10–12
MARylation	H-Y-L	14, 15
	H-Y-Y	16
	Q-Y-T	9
Inactive	Y-Y-V	13

While catalytic activity is governed by the conserved ARTD fold, the substrate specificity and therefore biological action of each PARP is determined by the remainder of the protein sequence. To date, ADPr modifications have been detected on aspartate, glutamate, lysine, arginine, cysteine, serine, and asparagine residues,^{224,239–241} and no robust consensus sequences have been determined for ADP-ribosylation.^{242,243} Therefore, the unique domains that exist N-terminal to the ARTD catalytic domain for each PARP are thought to direct PARP-protein interactions, and the overall structure of the various PARP-substrate complexes determine which residue is modified by the PARP.^{244–247}

2.1.2 ADP-ribosylation in biology and disease

Like most PTMs, ADPr can significantly alter the structure and/or function of the substrate protein. PARylation in particular is a large, negatively charged modification, and this can lead to dissociation of the modified protein from DNA, RNA, or any other negatively charged binding partners.²⁴⁸ Addition of the large polymer can also represent a gain-of-function modification by acting as a scaffold to recruit proteins with known PAR interaction motifs.²⁴⁹ More generally, and like many other PTMs, ADPr can alter the topology of the modified protein and therefore its ability to participate in substrate-protein or protein-protein interactions.²⁵⁰ Also, the PARP proteins are all universally expressed across a wide variety of tissues, although this expression level can be altered in various disease states for individual family members.^{220,221} As a result, PARPs and ADP-ribosylation have been implicated in a variety of biological networks.

2.1.2.1 PARylation

PARylation can be catalysed by PARP1, PARP2, PARP5a and PARP5b, however PARP1 is by far the best studied member of the family, and the primary role of PARP1 is DNA damage repair (DDR) (**Figure 2.2**). PARP1 is known to recognise and bind to both single-stranded breaks (SSBs) and double-

stranded breaks (DSBs) in nuclear DNA through its zinc finger domains.²⁵¹ This binding causes an allosteric modification that activates the catalytic site, and PARP1 is auto-modified with linear and branched chains of ADPr.²⁴⁴ Binding of histone PARylation factor 1 (HPF1) to PARP1 limits this auto-ADP-ribosylation and shifts PARylation activity to neighbouring histone proteins.²⁴⁵ For SSBs, these PAR scaffolds cooperate to recruit DDR proteins such as X-ray repair cross-complementing protein 1 (XRCC1), DNA polymerase beta (Pol β), and DNA ligase III α (Lig3 α) to the affected lesion to repair the DNA and maintain genomic integrity.²²²

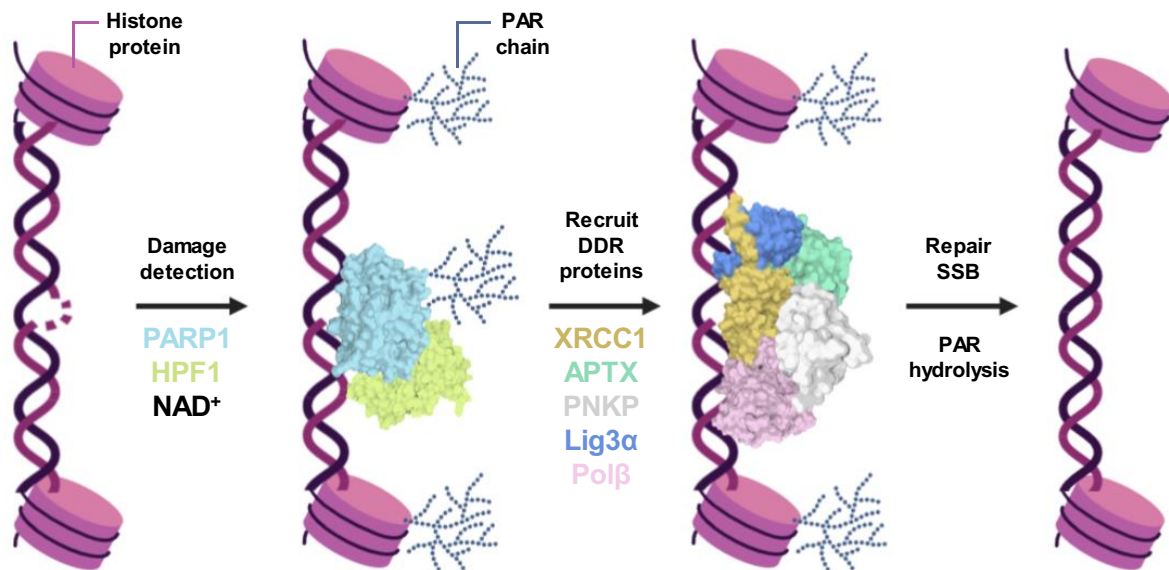


Figure 2.2 Schematic of the DNA-damage repair (DDR) mechanism mediated by PARP1. A single strand break (SSB) is detected by PARP1 which modifies itself with chains of poly-ADP-ribose (PAR). HPF1 binds and switches PARP1 from auto-PARylation to trans-PARylation of adjacent histones. Together these PAR scaffolds recruit the DDR complex: aprataxin (APTX) and bifunctional polynucleotide phosphatase/kinase (PNKP) to process DNA blunt ends, Pol β to extend the gap, and Lig3 α to ligate the nick. The complex dissociates and ADPr hydrolysis enzymes regenerate the histone proteins.

PARP1 has also been implicated in the regulation of transcription due to its reported association with chromatin and various gene promoters.^{252,253} It has been associated with the integrity and function of the nucleolus,^{254,255} and contributes to the faithful inheritance of silent ribosomal DNA.²⁵⁶ Lack of PARP1 has also been linked to amplification of centrosomes, part of the cellular machinery involved in mitosis.²⁵⁷ PARP1 is also a target for cleavage by caspases 3 and 7 in order to preserve the cellular stocks of NAD⁺ and its precursor adenosine triphosphate (ATP) necessary to execute apoptosis.^{258,259} Incidentally, protein-free chains of poly-ADP-ribose have themselves been reported to play a role in cell death pathways by activating another form of regulated cell death referred to as parthanatos.^{260,261} PAR chains are released from their sites of modification by ADP-ribosylhydrolase enzymes such as PARG, and upon accumulation in the cytosol are targeted to the mitochondria.²⁶² Here, they stimulate the proteolysis and release of apoptosis-inducing factor (AIF) which dimerises with migration inhibitory

factor (MIF). This complex translocates to the nucleus where MIF cleaves and degrades genomic DNA, leading to a form of regulated necrotic cell death (see also **Section 3.1.1**).^{263,264}

PARP2 is also reported to assist in DDR and is responsible for the majority of the remaining 10% of cellular PARylation observed upon knockout of PARP1; double knockout of both PARP1 and PARP2 was shown to be lethal in mouse embryos.²⁶⁵ PARP2 has been reported to localise with PARP1 to chromosomal centromeres during metaphase, suggesting a joint role in cell division.²⁶⁶ PARP2, but not PARP1, interacts with the transcription factor forkhead box protein A1 (FOXA1), promoting the expression of various androgen receptor driven oncogenes, making it a novel prostate cancer target.²⁶⁷ The remaining PARylating PARPs, PARP5a and PARP5b, annotated together as the tankyrases, have been associated with the regulation of telomeres²⁶⁸ and are known to disrupt the Wnt signalling pathway, leading to the activation of the cancer-associated transcription factor β -catenin and making the tankyrases attractive anti-cancer targets in their own right.^{269,270}

2.1.2.2 MARYlation

While PARylation endows a large PTM onto a protein, mono-ADP-ribosylation is more subtle. MARYlation is much less well studied, however it has been possible to link almost every MARYlating PARP to some biological function or disease indication. Several have been implicated in RNA metabolism and recognition of pathogenic nucleic acids, with PARPs 7, 12 and 13 containing CCCH zinc finger domains, and PARPs 10 and 14 containing RNA recognition motifs.²²¹ PARP13, the catalytically inactive protein, demonstrates clear binding to viral RNA,²⁷¹ and PARP4 is localised within the vault ribonucleoprotein complex.²⁷² PARPs 10, 12 and 14 have also shown increased expression levels in human monocytes when infected with *Borrelia burgdorferi* bacteria,²⁷³ and PARPs 10 and 14 are induced in response to upon viral infection.^{274,275}

Other MARYlating PARPs have been implicated in various stress responses; PARP3 is also involved in DDR and the activation of PARP1,²⁷⁶ as well as being found to directly MARYlate DNA SSBs.²⁷⁷ PARP9, which until recently was thought to be catalytically inactive, specifically MARYlates the C-terminus of ubiquitin when dimerised with the E3 ubiquitin-protein ligase DTX3L, and this activity was shown to be associated with DDR.²³⁴ PARP16, a single-pass endoplasmic reticulum (ER) protein, has been found to MARYlate and activate proteins involved in the ER-associated unfolded protein response,²⁷⁸ and PARP10 is implicated in immune regulation through its interaction with the NF- κ B signalling pathway.²⁷⁹

Finally, MARYlation is thought to modulate various transcription factors, reinforcing the PARPs as promising anti-cancer targets. PARP10 is known to interact with the proto-oncogene c-Myc,²⁸⁰ and is thought to be an oncogene in its own right,²⁸¹ whereas PARP6 seems to act as a tumour suppressor gene in the development of colorectal cancer.^{282,283} Inhibiting the MARYlation of glycogen synthase kinase

3 beta (GSK3 β) by PARP3 has been shown to reduce the survival of triple negative breast cancer (TNBC) cells deficient in breast cancer type 1 susceptibility protein (BRCA1; **Section 2.1.3.1**).²⁸⁴

2.1.3 PARP inhibition

Given the implication of PARP proteins in various cellular and disease networks, PARPs have become clinical targets of interest. Several drug discovery campaigns have been undertaken against the PARP enzyme family, the most successful of which have led to clinical trials and approval of PARPi for various types of cancer, and there is mounting pre-clinical evidence to suggest that PARPi may also be useful in other indications.

2.1.3.1 PARP and BRCA: Synthetic lethality

PARPi have been most successful in their application to *BRCA1* or *BRCA2* mutated (*BRCAm*) cancers (**Figure 2.3**). Breast cancer associated proteins 1 and 2 (*BRCA1/2*) are key proteins involved in the homologous recombination (HR) mechanism of repair for double strand breaks in DNA.²⁸⁵ HR repairs the DSB using the homologous sequence of the sister chromosome as a template to extend and repair the breaks in the DNA with high fidelity.²⁸⁶ Patients with an inherited germline deficiency in either *BRCA1* or *BRCA2* must rely on more error-prone pathways such as non-homologous end joining (NHEJ) to repair DSBs.²⁸⁷ *BRCA1/2* are therefore both considered to be tumour suppressor genes and *BRCAm* patients are more susceptible to the development of cancer.²⁸⁸

This inability to activate HR however is also passed onto the resulting tumour. Since all cancerous cells replicate at a faster rate than normal tissue, they accumulate more single- and double-stranded breaks, relying solely on PARP1 to repair SSBs (**Figure 2.2**) and error-prone NHEJ pathways to repair any DSBs.^{285,288} If PARP1 fails to repair DNA SSBs, subsequent DNA replication results in an accumulation of DNA DSBs which, in the absence of HR, are not efficiently repaired. This reliance on PARP1 leads to a *synthetic lethal* relationship between PARP1 and BRCA, where inhibition or genetic abrogation of one protein is not sufficient to cause cell death alone, but when both proteins are modulated, the combination is lethal to the cell (**Figure 2.3**).^{289,290} Chemical inhibition of PARP1 has therefore become a viable therapeutic strategy in *BRCAm* cancers.

Compound binding into the PARP1 NAD⁺-binding site inhibits the PARylation of PARP1 and associated histone proteins. This prevents the recruitment of DNA repair proteins for nucleotide excision repair (NER) or base excision repair (BER) and subsequent DNA replication generates a DSB. Alternatively, PARP1 inhibition can also generate a DSB by directly “trapping” PARP1 onto the affected DNA lesion and inhibiting the progress of the replication fork (**Figure 2.3**).^{289,291} PARP1 is also involved in various NHEJ pathways, so inhibition of PARP1 activity in these pathways also promotes cancer cell cytotoxicity through the further accumulation of DNA DSBs.²⁹² This mechanism has resulted in the approval of various clinical PARPi, the first of which was olaparib.

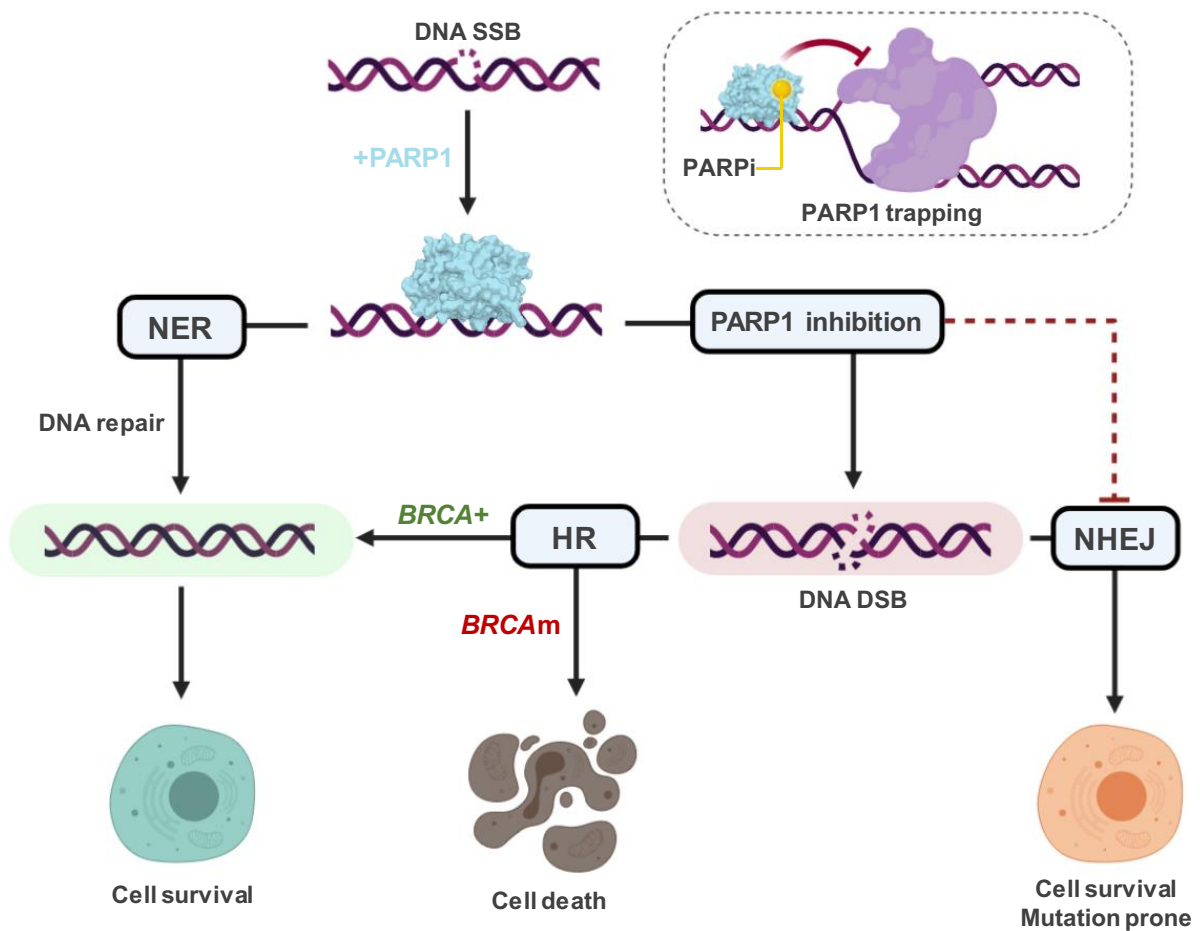


Figure 2.3 Synthetic lethality between BRCA and PARP1. PARP1 inhibition prevents the repair of DNA SSBs and a DSB is formed either through failed repair and subsequent replication, or by PARP trapping (top right). In wild type cells, BRCA proteins repair this DSB through homologous recombination (HR), however in BRCAm cancers this DSB is often unresolved and the cells die. Non-homologous end joining (NHEJ) can repair DSBs in a less efficient manner, however this pathway is also susceptible to PARPi. NER = nucleotide excision repair.

2.1.3.1.1 Olaparib and other PARP1 inhibitors

Olaparib (**Figure 2.4**) is a first-in-class phthalazinone-based PARPi; marketed jointly by AstraZeneca and Merck as Lynparza®, it was first approved in 2014 as a fourth line treatment for germline deleterious *BRCAm* ovarian cancer.²⁹³ It has since been approved for various other cancers including peritoneal, pancreatic and breast cancer either as a treatment or as maintenance therapy,²⁹⁴ and is in clinical trials for prostate cancer (preregistration), non-small cell lung cancer (Phase III), squamous cell cancer (Phase III) and many others.²⁹⁵ It works as an NAD⁺ mimetic, binding into the NAD⁺ binding site with olaparib's phthalazinone group mimicking the key hydrogen bonding interactions that the benzamide moiety of NAD⁺ makes with ARTD site residues, preventing the binding of the natural cofactor.²⁴⁴

Other NAD⁺-mimicking PARP1 inhibitors have reached the market (**Figure 2.4**), including rucaparib and niraparib for platinum sensitive ovarian, fallopian, and peritoneal cancers, and talazoparib for advanced *BRCAM* breast cancer, with all of these also in various clinical trials alone or in combination with other molecules.^{294,296} Veliparib has yet to reach the market but is currently in Phase III clinical trials for breast and ovarian cancer.^{295,296}

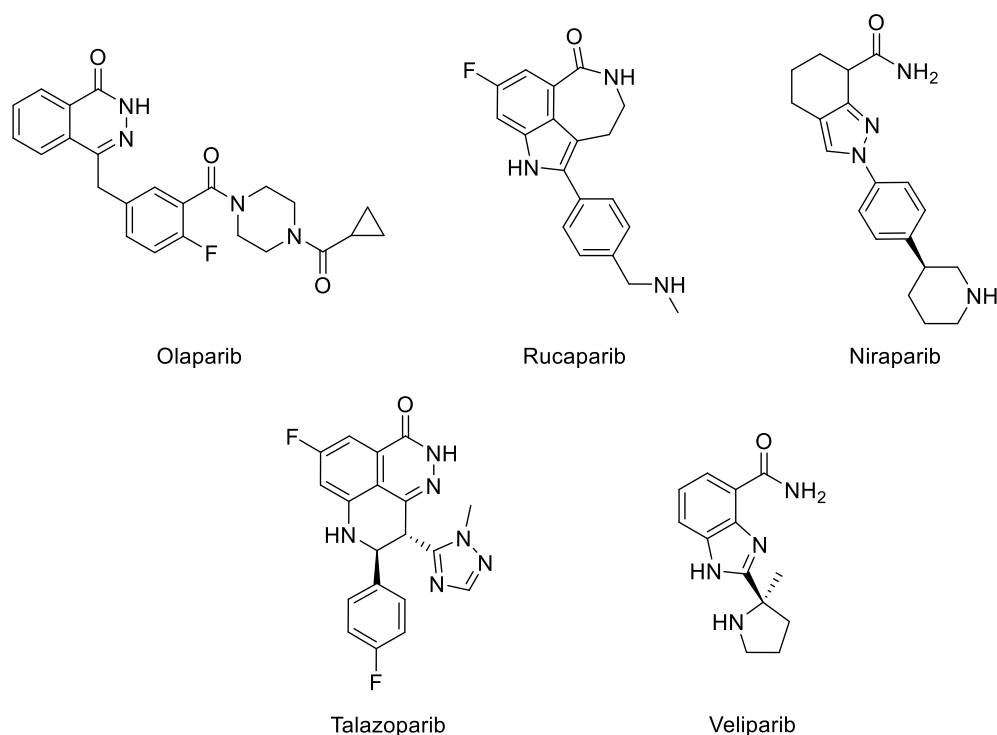


Figure 2.4 PARPi developed to combat cancers with deficiencies in *BRCA* and homologous recombination.

Since synthetic lethality between PARP inhibition and *BRCAM* was first demonstrated in 2005,^{297,298} these PARPi have enjoyed rapid success with development and clinical application achieved within a decade.²⁹¹ Accordingly, there are still many gaps in knowledge surrounding PARPi that require further investigation. NAD⁺ mimicking PARPi display polypharmacology within the PARP family, which is unsurprising given the structural conservation of the ARTD fold (**Section 2.1.1**).²⁹⁹ The PARPi in **Figure 2.4** are known to inhibit PARP2 as well as PARP1, all but veliparib have demonstrated strong PARP3 binding, and talazoparib and rucaparib inhibit the tankyrases.^{300,301} The contributions of inhibition of the various PARPs to the clinical response of each molecule in each indication remains an understudied area.

Additionally, PARP1/2 trapping (**Figure 2.3**) as well as inhibition of PARylation, is known to contribute to the formation of DSBs,³⁰² however the relative contributions of each mechanism to the efficacy and safety of each drug is under debate. Biomolecular studies have been able to dissect trapping potency from catalytic inhibition;^{301–303} talazoparib is universally the most potent trapper while veliparib is the weakest, and the remaining inhibitors are intermediate in their trapping potency.^{301,304} While the

exact rank order varies between experiments, PARP trapping potency does not seem to correlate with catalytic inhibition of PARP1. Many studies have demonstrated that PARP trapping can be key in achieving significant cancer cell death,^{291,305} while other work has suggested that superior PARP trapping ability does not remarkably improve the therapeutic index, and may even contribute to off-target cytotoxicity.^{301,304,306}

2.1.3.2 PARPi beyond PARP1 and cancer

Clinical application of PARPi beyond DDR in cancer has yet to be realised, however preclinical evidence has suggested that PARPi would be beneficial for ischaemia reperfusion injury (IRI) after cardiovascular trauma, and for neurodegenerative disorders.²²¹ Specific inhibitors of other members of the PARP family are under development; selective PARP2 inhibitors have demonstrated promising results in prostate cancer,²⁶⁷ and tankyrase-selective inhibitors are promising anti-cancer inhibitors via non-DDR mechanisms.^{307–309} The development of selective inhibitors of the MARYlating PARPs and genetic studies have also demonstrated the clinical potential of these targets including PARP3,^{284,310} PARP6,^{282,283,311} PARP10,^{281,312,313} PARP11,³¹⁴ PARP12,³¹⁵ and PARP14.^{246,316–319}

2.1.4 Previous PARP profiling campaigns

PARP inhibitor development for various members of the PARP family is increasing and there are still questions regarding the polypharmacology and mechanism of action of novel and existing agents in living systems. Accordingly, there have been several attempts to profile the binding and activity of PARPi using various techniques. To measure direct PARP inhibition, several different *in vitro* binding/inhibition assays exist for the PARP enzymes, and these have been used to generate IC₅₀ values for various PARPi.^{320–322} These methods however only measure the interaction with one PARP at a time, and outside of the native biological system.

2.1.4.1 Label-free PARP profiling

The cellular thermal shift assay (CETSA) has been used to profile the cellular interactions of PARPi (**Section 1.2**). In one study, cell lysates were incubated with or without either known PARPi olaparib, or alleged PARPi iniparib. These lysates were then subjected to a heat challenge and the soluble, folded protein fraction for each temperature analysed using Western blot (**Section 1.4.2.2**) for the amount of remaining PARP1.³²³ It was found that when the lysates were treated with olaparib, PARP1 unfolded at higher temperatures than in the vehicle treated samples, demonstrating stabilisation of PARP1 by olaparib and clear target engagement. However, treatment with iniparib did not stabilise PARP1, reinforcing that iniparib was not an authentic PARPi.³²⁴

These CETSA experiments have since been extended to live, intact cells to profile the engagement of over 6,000 compounds with PARP1.³²⁵ Comparisons of this data with biophysical binding data for purified PARP1 were used to highlight clear outliers that demonstrate potent *in vitro* inhibition but fail to engage PARP1 in cells. This suggested that cell permeability or metabolic instability may prevent

certain compounds from reaching PARP1 in cells, highlighting the need to assess target engagement early in the drug discovery pipeline. Label-free methodologies could be further applied to PARPi through combination with proteomics to assess engagement with other proteins outside of PARP1.

2.1.4.2 Label-assisted PARP profiling

In an alternative approach, a BODIPY-tagged analogue of olaparib, PARPi-FL (**Figure 2.5**), used fluorescence anisotropy (FA) measurements to show binding of PARPi-FL to total cellular PARP1–3 using live-cell imaging and flow cytometry. Competition of PARPi-FL with the various PARPi in **Figure 2.4** resulted in differential depletion of the FA signal, allowing for quantification of the cellular occupancy of each PARPi.^{326,327} Taking this further, Carney *et al.* also used an ¹⁸F analogue of olaparib, [¹⁸F]PARPi (**Figure 2.5**), to demonstrate occupancy across all of PARP1–3 in an *in vivo* mouse model using positron emission tomography (PET).³²⁷ Similar PARP PET radiotracers have been developed for human use and are currently under clinical review.^{328–330}

While valuable pharmacological and clinical data can be achieved by monitoring drug target occupancy with these imaging probes, the exact identity of the bound proteins cannot typically be elucidated. However very recently, Wigle *et al.* have developed a methodology to measure the occupancy of a drug for a particular PARP family member using a fluorescent PARP probe and a nano-luciferase-tagged version of the specific PARP enzyme ectopically overexpressed in human cells.³³¹ The bioluminescence resonance energy transfer (BRET) signal generated in this assay is suppressed by competition of the bound probe away from the overexpressed PARP of choice by the co-treated PARPi, and this is used to measure target engagement. While this successfully measured drug target occupancy of specific target PARPs *in situ*, the system requires overexpression of each PARP protein, altering the system away from basal expression levels. Furthermore, the probes can only assess engagement of the different PARPs in discrete assays and is unable to measure on- and off-target occupancy simultaneously across the whole cellular proteome.

The first such experiment to interrogate the complete, unbiased interactome of a PARPi utilised an olaparib-*trans*-cyclooctene (olaparib-TCO1, **Figure 2.5**) probe and an affinity-based protein profiling approach.³³² Olaparib-TCO1 was incubated with live cells to allow binding to target proteins, the cells were then lysed and incubated with tetrazine-conjugated beads, capturing non-covalently tagged proteins with an inverse-electron demand Diels-Alder cycloaddition (IED-DAC) reaction (**Table 1.3**).

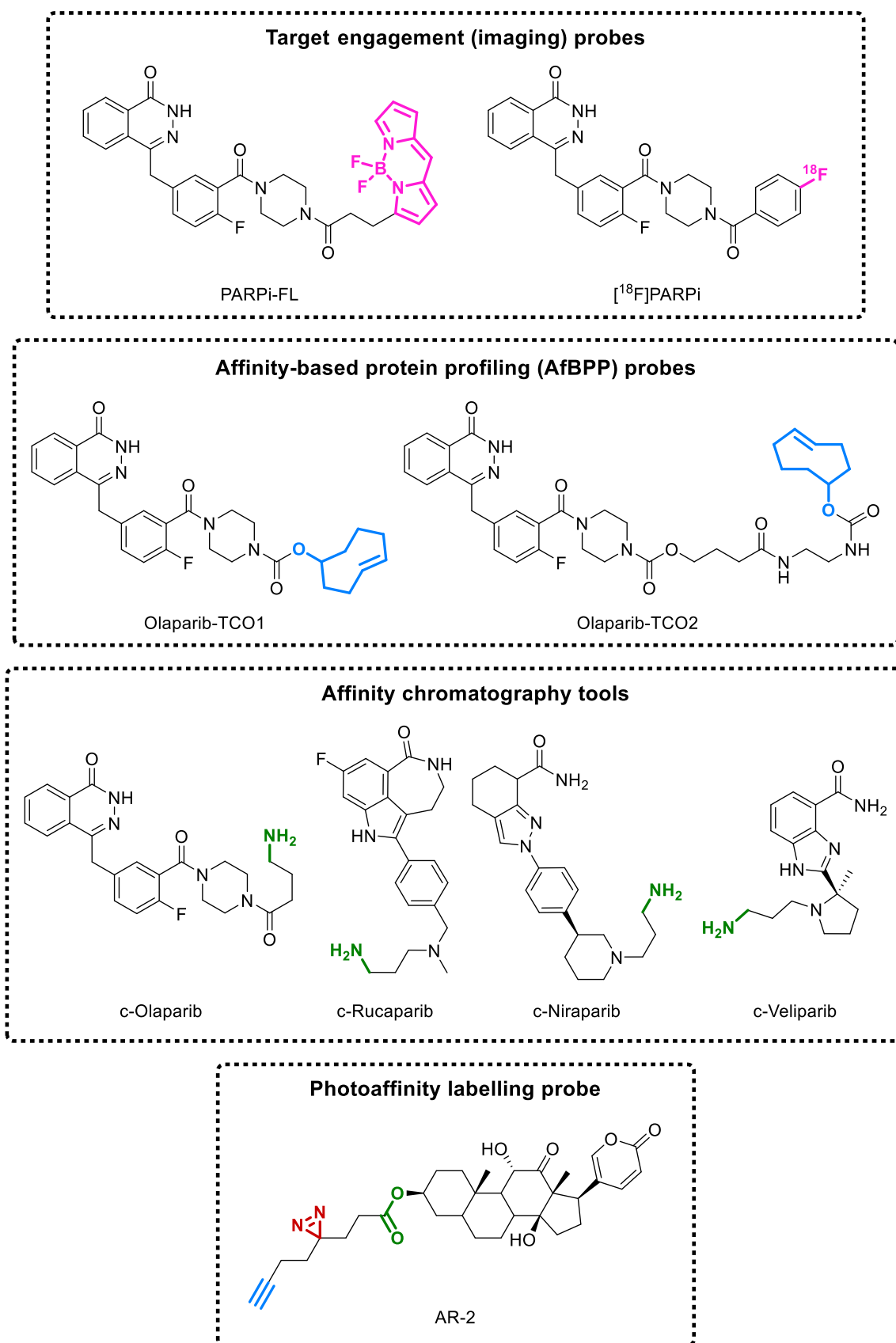


Figure 2.5 Target profiling probes for PARP enzymes and PARPi. Pink = imaging group, blue = biorthogonal ligation handle, green = coupling handle, red = diazirine.

Several high-confidence hits were identified, including DNA topoisomerase 2A (TOP2A), however no competition studies were performed with the parent olaparib to rule out non-specific probe enrichment, limiting the validity of these results.

Cellzome also profiled the targets of olaparib using an AfBPP approach, synthesising a range of olaparib probes with different biorthogonal ligation handles and assessing their efficiency in target identification and live-cell visualisation assays.⁸⁷ Their most successful probe was an improved olaparib-TCO probe (olaparib-TCO2, **Figure 2.5**) with a longer spacer between the drug and the TCO handle. Olaparib-TCO2 was similarly incubated in live cells but this time co-treated with parent unmodified olaparib as a competitor. Cells were lysed, incubated with tetrazine beads and the enriched proteins analysed by proteomics. These experiments were the first to demonstrate efficient engagement of PARP1, PARP2 and PARP16 by olaparib in live cells using a label-assisted AfBPP approach. The mild lysis conditions were able to allow enrichment of a PARP1 complex protein (XRCC5) and one potential off-target, inosine-5'-monophosphate dehydrogenase 2 (IMPDH2).

Finally, affinity chromatography (**Section 1.2.1**) was employed by the Rix group, generating so-called “coupleable” analogues of olaparib, rucaparib, niraparib and veliparib (**Figure 2.5**).⁷³ Each drug was modified with an alkyl amine and conjugated to *N*-hydroxysuccinimide (NHS) sepharose beads. A major drawback of affinity chromatography is that it is not compatible with live cells, so native TNBC lysates were pre-treated with DMSO or parent unmodified drug then incubated with the drug-derivatised beads; enriched proteins were analysed by LC-MS/MS. Engagement of all drugs with PARP1/2 was confirmed, weak binding to the tankyrases for all but veliparib was observed, and engagement with PARP4 could be seen for olaparib and rucaparib. IMPDH2 was once again enriched by all drugs, however this work demonstrated that this was in fact as part of a complex with PARP1/2; other PARP1-interacting proteins were also enriched including Lig3a, XRCC1, XRCC5 and XRCC6. Crucially, new *bona fide* drug-protein interactions were observed: deoxycytidine kinase (DCK) was identified as a target of niraparib, and rucaparib was found to bind to hexose-6-phosphate dehydrogenase (H6PD). No novel binders were observed for olaparib or rucaparib.

2.2 Research objectives

The aforementioned PARP profiling campaigns represent a significant step forward in understanding the molecular interactome of PARPi in living systems, however they rely solely on the non-covalent interactions of probe molecules with their binding partners (**Section 1.2.1**). These transient interactions may fail to capture weaker, secondary binders that could have real physiological ramifications. To date, one recently published photoreactive AfBP, AR-2 (**Figure 2.5**), was found serendipitously to enrich PARP1 as a compound specific secondary target of the parent anticancer molecule arenobufagin in photoaffinity labelling studies, however this compound was not designed specifically to profile PARPi, and its utility in this setting remains to be explored.¹⁸⁴

The work herein describes the design, synthesis and application of the first photoreactive AfBP developed specifically for the PARP enzyme family. This probe was developed with the view to generate a novel chemical tool to assess PARP engagement by PARPi in living systems, and to profile weaker, off-target binders of novel and existing PARPi that previous protein profiling campaigns may have failed to enrich. This work builds upon initial findings described in *Ryan Howard, MRes Chemical Biology, 2017*,³³³ and further describes data that was ultimately published in *ACS Chemical Biology*.³³⁴

2.3 Results and Discussion

2.3.1 Background: AstraZeneca and PARPi

Olaparib was originally developed by KuDOS Pharmaceuticals which, in 2006, was acquired by AstraZeneca (AZ).³³⁵ This acquisition allowed AZ to obtain a large library of phthalazinone and quinazolinone based compounds that were developed around olaparib. Given AZ's experience with PARPi and their polypharmacology within the PARP family, they began to turn their attention to other disease indications that this library of PARP-inhibiting compounds could be useful for.

2.3.1.1 Discovery of AZ0108

As discussed above, PARP1/2 have been implicated in cell division. PAR formation by TNKS1 (PARP5a) has been shown to be important for centrosome function,³³⁶ and genetic knockdown of the *D. melanogaster* homologues of PARP5a and PARP16 induced an aberrant multipolar spindle (MPS) phenotype in dividing cells (**Figure 2.6a**).³³⁷ PARP inhibition in general has been shown to disrupt the formation of a normal bipolar spindle, and this strategy has shown promise in the treatment of cancer.^{338,339}

With this knowledge, AZ screened their library of phthalazinone and quinazolinone PARPi in a high content microscopy assay for the MPS phenotype in HeLa cells, counting the number of spindle poles per mitotic cell.³⁴⁰ One compound in particular, **AZ9482 (Figure 2.6b)**, was found to increase the number of spindle poles per mitotic cell (MPS induction) in a single concentration screen, then in a dose-response manner to give the most promising MPS induction EC₅₀ of <18 nM, and this was shown to be selective for cancer cells. This behaviour was not phenocopied using the parent phthalazinone compound olaparib, and so the mechanism of action was reasoned to be through inhibition of a PARP enzyme other than PARP1–3; *in vitro* enzyme screens suggested potent inhibition of PARP5a could be responsible for the MPS phenotype.

AZ9482 however displayed poor aqueous solubility and drug metabolism and pharmacokinetic (DMPK) properties, so efficacy could not be assessed *in vivo*. A lead optimisation campaign was undertaken to optimise these properties, resulting in compound **AZ0108 (Figure 2.6b)**, which displayed superior DMPK properties and was also able to induce MPS formation in cancer cells. Despite this, the strong inhibitory potency of PARP5a had been lost (**Figure 2.6b**), suggesting that PARP5a inhibition

was not the true mechanism of action of these compounds and that further work was required to elucidate this.

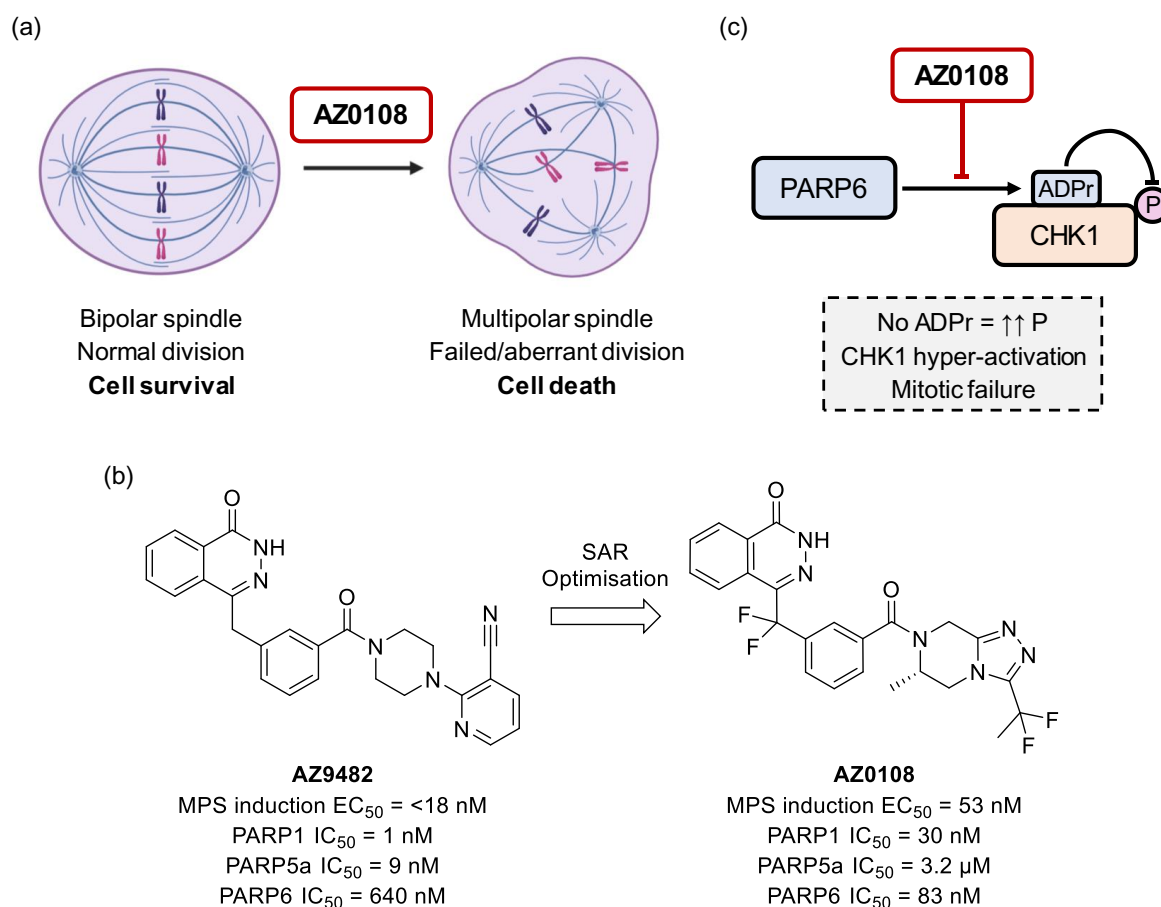


Figure 2.6 PARP inhibition as a mechanism to induce a cytotoxic multipolar spindle (MPS) phenotype in cancer. (a) Schematic of the MPS phenotype. (b) MPS inducing PARPi developed by AZ and associated parameters; SAR = structure-activity relationship.³⁴⁰ (c) Proposed mechanism of MPS induction by PARP6 inhibition by Wang *et al.*^{341,342}

2.3.1.2 Mechanism of action

In order to more fully understand the mechanism of MPS formation by **AZ0108**, further work was performed to identify the molecular interactions responsible.³⁴¹ In light of the poor inhibitory potency of **AZ0108** for PARP5a, regression analysis was performed on the EC_{50} of all MPS inducing compounds generated by AZ, plotting the values for each compound against their corresponding IC_{50} for each PARP enzyme. The strongest correlation was observed for PARP6, and knockdown of PARP6, but not PARP1, resulted in the formation of an MPS phenotype, suggesting PARP6i was driving MPS induction.

To investigate potential substrates of PARP6 that could contribute to MPS formation upon PARP6i, AZ performed a high-density protein microarray to characterise PARP6 substrates *in vitro*. Checkpoint kinase 1 (CHK1), a key regulator of mitotic entry, was found to be a specific target of PARP6, and its

MARylation was inhibited by **AZ0108**. Further work was undertaken with two particularly **AZ0108**-sensitive TNBC cell lines, MDA-MB-468 and HCC1806. Inhibition of CHK1 MARylation by **AZ0108** was confirmed in MDA-MB-468 cells, as was the observed concomitant hyper-phosphorylation of CHK1 upon **AZ0108** treatment. It was proposed that MARylation regulates the phosphorylation status of CHK1, and **AZ0108** disrupts this mechanism, altering the tightly regulated pathways that control mitosis to induce cytotoxic MPS formation (**Figure 2.6c**).

In vivo studies were promising, with breast cancer xenograft models of both MDA-MB-468 and HCC1806 demonstrating an excellent response to **AZ0108** dosing, and MPS formation could clearly be observed upon immunohistochemistry analysis of the treated tissues. Despite these results, **AZ0108** failed to be nominated for clinical trials due to significant toxicity upon treatment in preclinical studies (proprietary data). Questions also remained as to why **AZ0108** displayed differential cytotoxicity across a panel of breast cancer cell lines with no clear pattern, and *bona fide* engagement of PARP6 by **AZ0108** had not been confirmed.

To this end, a collaboration between AZ and the Tate group was initiated to design a photoreactive AfBP based on the molecular scaffold of MPS-inducing PARPi. Not only would this facilitate target engagement studies to validate PARP6 target engagement, but off-target profiling might be useful when investigating the cytotoxicity of these molecules *in vivo*. Furthermore, given that **AZ0108** and **AZ9482** bind to both PARP1/2 and various MARylating PARPs, they were envisaged as idealised structures upon which to base the first NAD⁺-mimicking photoreactive AfBP for PARPs in general, able to quantify the engagement of novel and existing PARPi in a live cell setting. Therefore, it was decided that a novel PARP photoaffinity probe would be synthesised based on these MPS-inducing PARPi.

2.3.2 Probe design and synthesis

In the absence of any structural information for PARP6, including the binding mode of **AZ9482** and **AZ0108**, the design of the probe was based around SAR data developed during the course of the optimisation of **AZ0108** into a candidate molecule, and structural data of the compounds bound to other members of the PARP family. Given the synthetic route to **AZ0108** was more complex, it was decided that the AfBP would be based on the more synthetically tractable **AZ9482**. All phthalazinone-based PARPi bind by mimicking the adenosine group of NAD⁺, therefore this phthalazinone group and the associated benzyl group were retained when designing the probe (**Figure 2.7**).

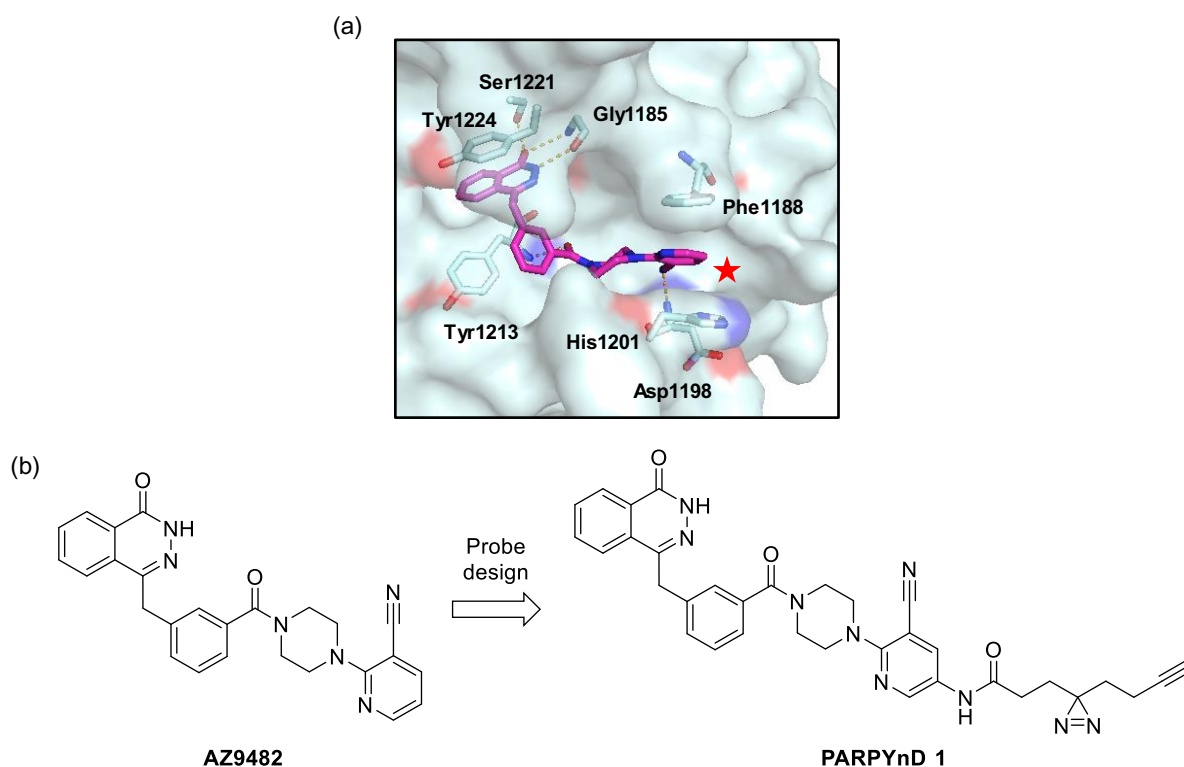
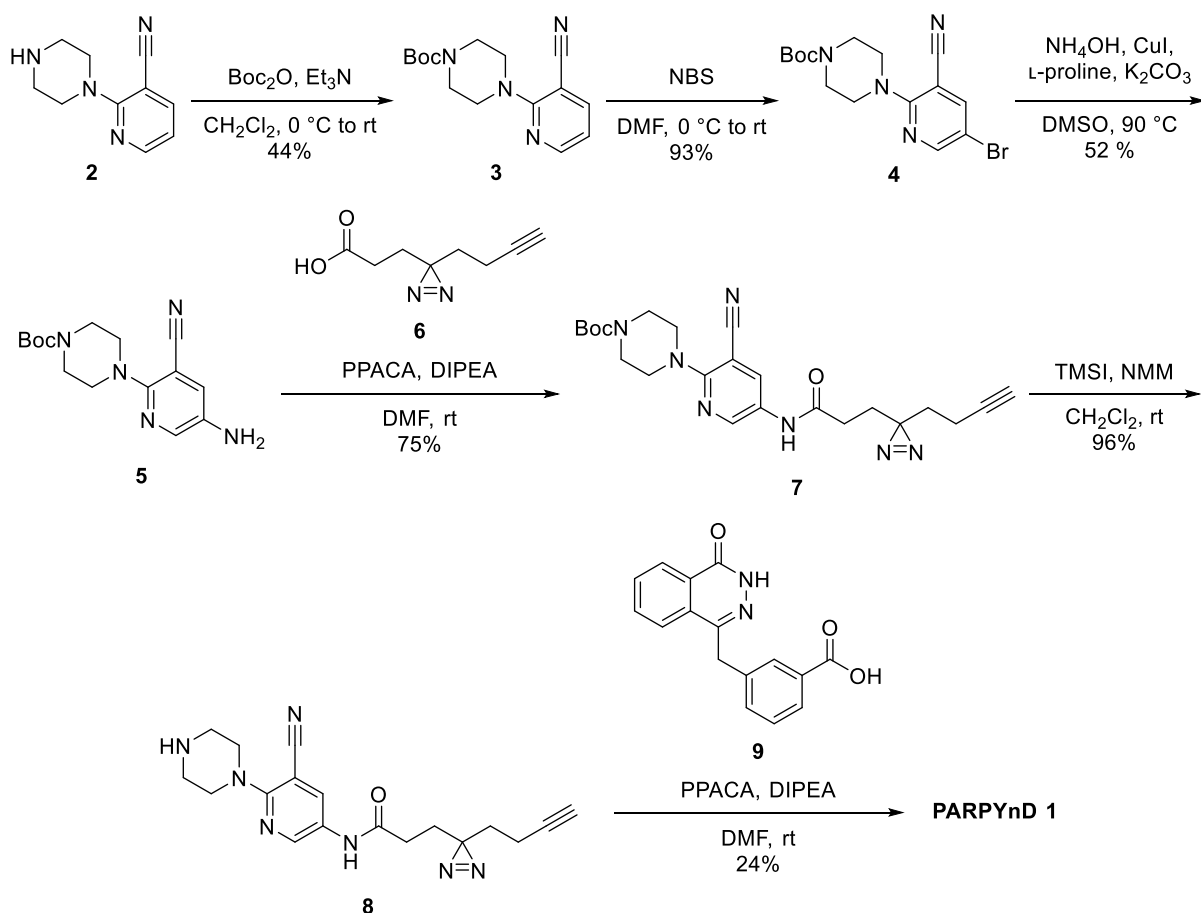


Figure 2.7 Design of probe **PARPYnD**. (a) Crystal structure of **AZ9482** bound in the NAD⁺-binding site of PARP5a (PDB: 5ECE),³⁴⁰ key interactions highlighted in orange, red star indicates position for building out into the solvent channel. (b) **PARPYnD** design from parent molecule **AZ9482**. Adapted from Howard *et al.* 2020.³³⁴

AZ9482 had been previously crystallised in the NAD⁺ binding pocket of PARP5a (**Figure 2.7a**), and while the 3-nitrile is a key backbone hydrogen bond acceptor, it can be seen from the crystal structure that the 5-position of the pyridine ring lies adjacent to a solvent channel, suggesting that this position may be a potential modification site. SAR data provided by AZ indicated further that modification at this position did not disrupt induction of MPS formation. Taken together, this prompted the design of photoaffinity probe **PARPYnD** (**1**, **Figure 2.7b**), with a minimal “photoclickable” group appended to the core structure of **AZ9482** via the 5-position of the pyridine ring.

Synthesis of **PARPYnD** has previously been reported (Ryan Howard, *MRes Chemical Biology, 2017*),³³³ however the synthetic scheme is outlined in **Scheme 2.1**.³³⁴ Briefly, 2-(piperazin-1-yl)pyridine-3-carbonitrile **2** was boc-protected (**3**), brominated (**4**), and underwent a copper-catalysed amination, installing the key amine in **5** for introduction of the minimal “photoclickable” group **6** to generate coupled product **7**. Boc deprotection to generate free amine **8** and coupling to the central phthalazinone core **9** yielded **PARPYnD** (**1**).



Scheme 2.1 The synthetic route to **PARPYnD**. Previously reported in *Ryan Howard, MRes Chemical Biology, 2017* and updated in/adapted from *Howard et al. 2020*.^{333,334}

2.3.3 Probe validation

2.3.3.1 Biophysical characterisation

Once the probe was in hand, it was necessary to test whether the modifications made to the structure of **AZ9482** were tolerated. First, the probe was sent to AZ where it was tested in their in-house fluorescence anisotropy binding assays for PARP1, PARP2, PARP3, PARP5a, and PARP6. Briefly, a fluorescent substrate that binds into the NAD^+ binding site of the PARP enzymes was incubated with the PARP enzyme and exposed to increasing concentrations of **PARPYnD**; a decrease in anisotropy signal would be indicative of the probe binding to the enzyme and competing the fluorescent substrate away from the PARP protein. From this assay, **PARPYnD** was shown to bind to all the tested enzymes suggesting that **PARPYnD** has a similar selectivity profile to the parent compounds (**Figure 2.8, Table 2.2**).

The effect of the minimal “photoclickable” moiety can be seen in the perturbations in the IC_{50} values for each protein measured using this assay (**Table 2.2**). For PARP1/2, **PARPYnD** displays IC_{50} values similar to all parent molecules, suggesting that this modification is tolerated for binding to these enzymes. While **PARPYnD** is able to bind to PARP3 and PARP5a, it appears that the modification

made to the structure of **AZ9482** results in a reduced binding affinity towards both enzymes. Importantly however, **PARPYnD** displays an improved IC_{50} value of $0.23 \mu\text{M}$ for PARP6 compared to $0.64 \mu\text{M}$ for **AZ9482**. Taken together, the biophysical assessment of **PARPYnD** suggests that it should be an effective PARP1/2/6 profiling probe.

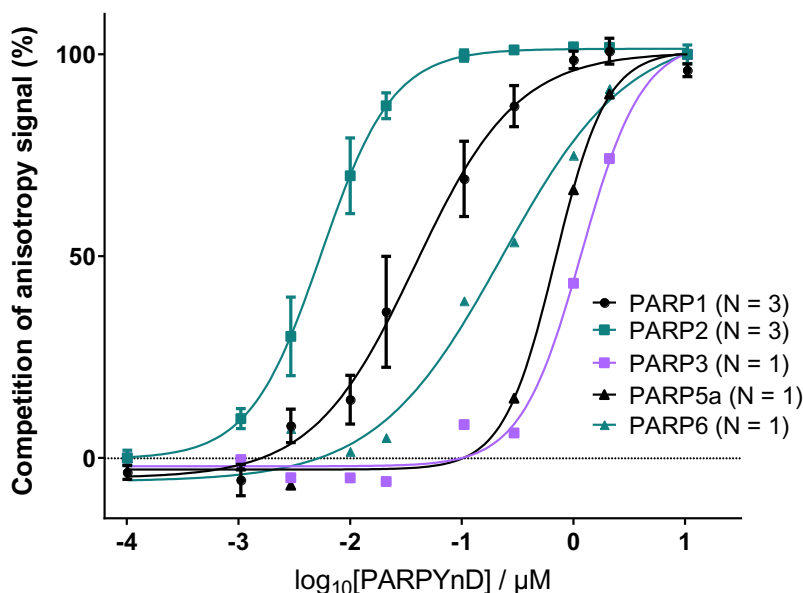


Figure 2.8 Fluorescence anisotropy competition dose-response curves for **PARPYnD**. Inhibition curves for PARP1, PARP2, PARP3, PARP5a and PARP6 each fit to a four-parameter dose-response function; y axis values calculated as a percentage of the maximum competition. N = number of biological replicates – data displayed \pm SEM. Adapted from Howard *et al.* 2020.³³⁴

Table 2.2 Biochemical/biophysical parameters associated with olaparib, **AZ9482**, **AZ0108** and **PARPYnD**. ^aData generated in this work, ^bGI₅₀ value previously generated in MDA-MB-468 cells,^{340,341} MPS = multipolar spindle. Adapted from Howard *et al.* 2020.³³⁴

Molecule	AZ9482	AZ0108	Olaparib	PARPYnD
PARP1 IC_{50} (μM)	0.001	0.03	0.001	0.038 ^a
PARP2 IC_{50} (μM)	0.001	<0.03	0.003	0.006 ^a
PARP3 IC_{50} (μM)	0.046	2.8	0.046	1.2 ^a
PARP5a IC_{50} (μM)	0.009	3.2	1.9	0.69 ^a
PARP6 IC_{50} (μM)	0.64	0.083	1.8	0.23 ^a
MPS EC_{50} (μM)	0.018	0.053	>11	0.012 ^a
Cytotoxicity EC_{50} (μM)	0.024 ^a	0.14 ^a	8.6 ^b	0.30 ^a

2.3.3.2 Phenotypic characterization

For **PARPYnD** to be a suitable probe to profile the biomolecular interactions of parent molecules **AZ9482** and **AZ0108**, it must be able to recapitulate the biological effects of these compounds,

therefore AZ applied **PARPYnD** in their high content MPS assay. HeLa cells were treated with varying concentrations of the compound, fixed and imaged via automated immunofluorescence analysis. For each compound treatment, the number of spindle poles (pericentrin stain) are counted per mitotic cell (cyclin D stain) and a percentage calculated of those mitotic cells that contain >2 spindle poles. **PARPYnD** was found to significantly induce MPS formation, displaying the most potent EC₅₀ of the tested molecules (**Table 2.2**) and demonstrating a comparable degree of MPS induction to the parent compound **AZ9482** at the same concentration (**Figure 2.9a**).

The parent molecules had also been shown to induce cytotoxicity in TNBC cell line MDA-MB-468, and studies linking PARP6 inhibition to CHK1 inhibition and MPS formation were performed in this cell line. A cell viability study of **PARPYnD** and the parent molecules was therefore performed in MDA-MB-468 cells using the MTS assay (**Figure 2.9b**, **Table 2.2**). After three days of treatment, **PARPYnD** was also found to induce cytotoxicity of this cell line with comparable potency to **AZ9482** and **AZ0108**.

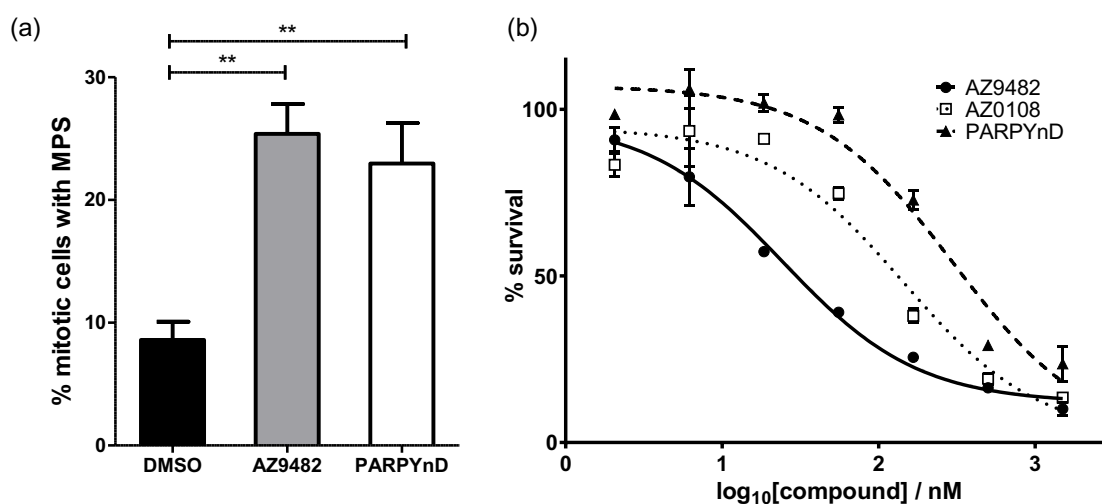


Figure 2.9 Phenotypic validation of **PARPYnD**. (a) Percentage of cells with multipolar spindle (MPS) phenotype after treatment with DMSO (N = 4), **AZ9482** (41 nM, N = 2) and **PARPYnD** (41 nM, N = 2). Data plotted \pm SEM of biological replicates; significance between treatments was calculated using an ordinary one-way ANOVA; ** = p-value < 0.01. (b) MDA-MB-468 cell survival \pm SD of technical replicates as determined by MTS assay after three days treatment with the compounds indicated. Adapted from Howard *et al.* 2020.³³⁴

2.3.3.3 Assessment of photocrosslinking efficiency

Given that **PARPYnD** had displayed a positive readout in the cell based MPS and MTS assays, this was strongly suggestive that the cell permeability of the probe had been retained. To confirm whether **PARPYnD** would be able to label proteins in live cells in a UV-dependent manner, pilot labelling experiments were performed and reported in Ryan Howard, *MRes Chemical Biology, 2017*.³³³ Briefly, live TNBC cells (MDA-MB-231) were treated with varying concentrations of **PARPYnD** over varying time periods and either irradiated with 365 nm UV light or kept in the dark. Cells were then lysed,

ligated to AzTB (**Figure 1.7**) via a CuAAC reaction and the proteins run on an SDS-PAGE gel and scanned for TAMRA fluorescence (**Figure 2.10**).

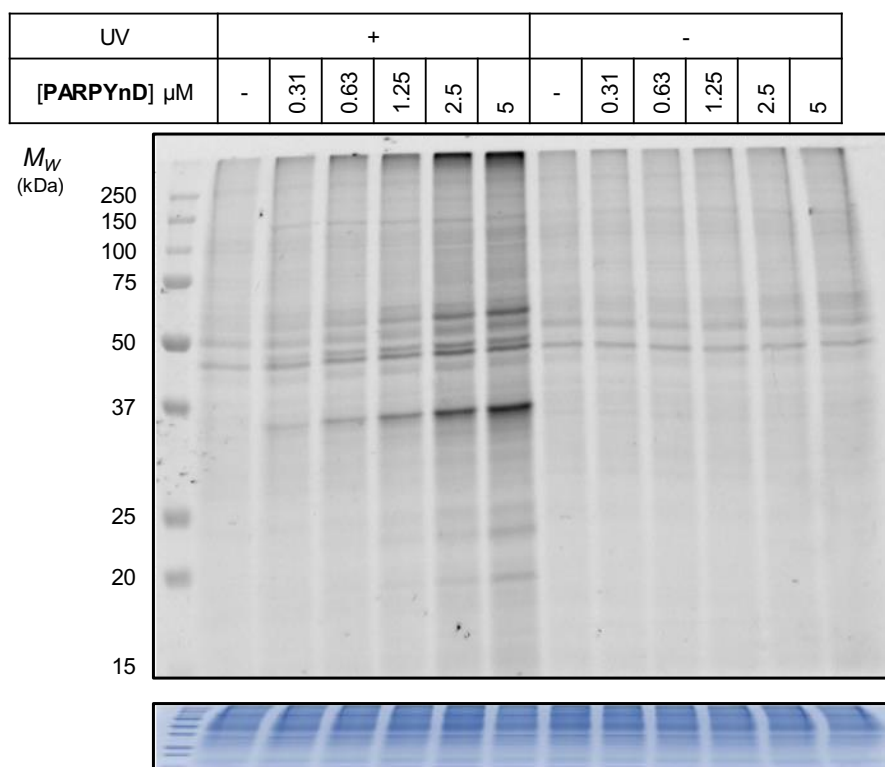


Figure 2.10 Optimisation of **PARPYnD** photocrosslinking in MDA-MB-231 cells. Cells were treated with **PARPYnD** for 3 h, irradiated, lysed and clicked to AzTB. Top: TAMRA fluorescence, bottom: Coomassie Brilliant Blue (CBB) staining. Adapted from *Ryan Howard, MRes Chemical Biology, 2017*.³³³

The presence of several bands increasing in a dose-dependent manner in the UV-irradiated samples demonstrated that **PARPYnD** was able to successfully label proteins in a UV-dependent manner with minimal background labelling. The alkyne was able to successfully link the probe-tagged proteins to the TAMRA-containing reporter molecule, and negligible labelling of the remaining proteome with AzTB (vehicle treated lanes) was in-line with what had previously been reported.^{30,159} The results displayed in **Figure 2.10** are after a probe incubation time of 3 h, the optimisation of which was described in *Ryan Howard, MRes Chemical Biology, 2017*.³³³

Given that **PARPYnD** was able to bind to PARP1/2/6 in biophysical assays, displays comparable phenotypic properties to the parent compounds and is able to label proteins in a model cell system, this suggested that it would be a suitable AfBP to profile PARP enzymes in live cells and would be able to aid in linking the biomolecular interactions of these compounds to their biological outcomes, assisting in their target validation and off-target identification.

2.3.4 Affinity-based protein profiling

2.3.4.1 Gel-based analysis

To profile the PARP enzymes in a live-cell system, MDA-MB-468 cells were treated with DMSO vehicle, **PARPYnD**, or **PARPYnD** and either **AZ9482**, **AZ0108** or olaparib at various concentrations. Cells were then irradiated with 365 nm UV light, lysed and ligated to AzTB via CuAAC reaction. Gel based analysis of the streptavidin-enriched proteomes is shown in **Figure 2.11** (top). Once again, **PARPYnD** is shown to label several different protein bands (lanes 1–3) demonstrating robust labelling efficiency and cell permeability, and indicating that phthalazinone-based PARPi appear to bind several protein targets. Co-treatment of the cells with **AZ9482**, **AZ0108** or olaparib and the probe **PARPYnD** was also performed in order to determine whether **PARPYnD** was labelling any true targets of these molecules; this would be demonstrated by the observation of any dose-dependent reduction in probe labelling as a result of competitive blockade of the probe binding site (**Figure 1.8**).

While the labelling profile of the competition samples appears to remain largely unchanged upon treatment with the various parent molecules, one band is clearly out-competed by **AZ9482** and, to a lesser extent, **AZ0108** (>, **Figure 2.11**). This band has a molecular weight around 110 kDa and was also out-competed by known PARP1 inhibitor olaparib. Therefore, to test whether this band was PARP1, the enriched samples were separated on SDS-PAGE, transferred to nitrocellulose membrane and immunoblotted against PARP1. While the total amount of PARP1 remained consistent across the lysates, it can be seen in **Figure 2.11** that **PARPYnD** was able to enrich PARP1 in a dose-dependent manner. This enrichment was depleted by competition with **AZ9482** and olaparib, and the lower level of competition observed on-gel for **AZ0108** was also recapitulated. These results demonstrate that **PARPYnD** is the first cell-active photocrosslinking AfBP for the PARP enzyme family and is able to assess the engagement of NAD⁺-mimicking inhibitors for PARP enzymes in living systems.

Given that induction of MPS formation by these molecules in MDA-MB-468 cells had been reported to work through the cellular engagement of PARP6, the enriched fraction was also immunoblotted for PARP6 (**Figure 2.11**) to validate this target engagement in a live-cell setting. While the protein could be detected in the cellular lysate, it was not present in any of the lanes of the enriched samples, suggesting PARP6 was not being engaged by **PARPYnD**. This was a surprising result given that **PARPYnD** had been shown to bind to PARP6 in *in vitro* assays and was also able to induce MPS formation.

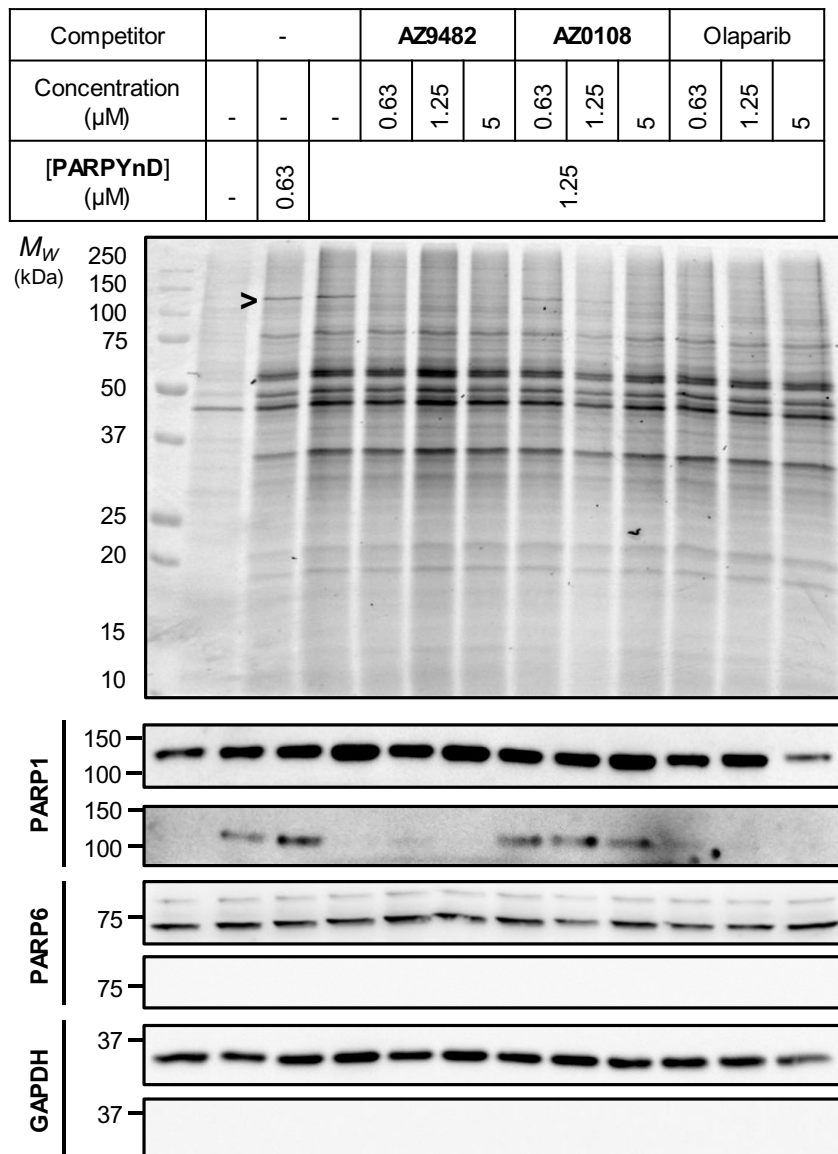


Figure 2.11 Gel and Western blot analysis of the binding profile of **PARPYnD** and its parent molecules. MDA-MB-468 cells were treated as indicated, irradiated and lysed. Tagged proteins were ligated to AzTB and enriched on streptavidin beads. Top: TAMRA fluorescence (enriched fractions), bottom: immunoblot analysis before (I = input) and after (P = pull down) enrichment, > = competition observed on-gel, GAPDH = glyceraldehyde-3-phosphate dehydrogenase (loading control). Adapted from Howard *et al.* 2020.³³⁴

To investigate this further, MDA-MB-468 cells were treated with up to 10 μM **PARPYnD** in an effort to label endogenous PARP6, a concentration more than 10 times greater than its IC₅₀ for PARP6 as determined by fluorescence anisotropy. After irradiation and lysis, labelled proteins were once again ligated to AzTB, enriched and analysed by gel and Western blot (**Figure 2.12**).

No PARP6 was detected in the enriched fractions even at 10 μM of **PARPYnD**, which was once again unexpected given that binding to PARP6 was predicted for **PARPYnD**. It was thought that poor antibody efficiency and/or low levels of endogenous PARP6 expression may render detection by gel

and Western blot methods too insensitive to detect the protein. As such, **PARPYnD** was taken on to proteomics-based studies.

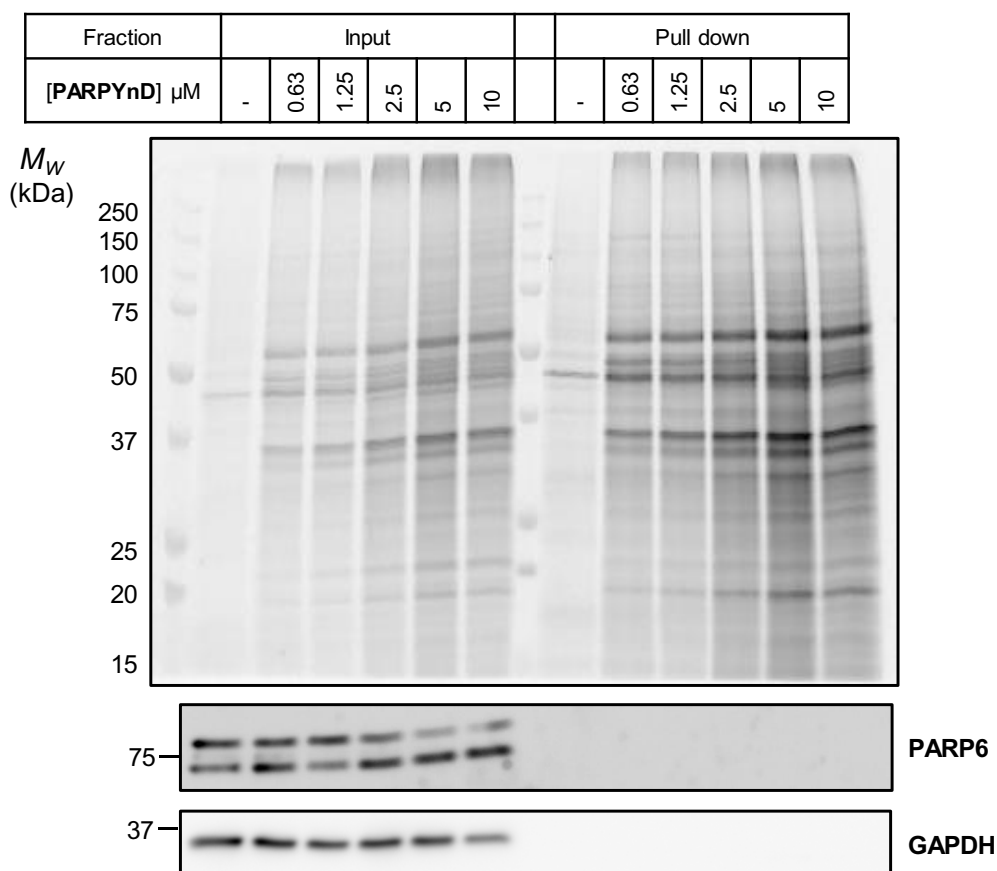


Figure 2.12 Gel and Western blot analysis of the binding profile of **PARPYnD** at higher concentrations. MDA-MB-468 cells were treated as indicated, irradiated and lysed. Tagged proteins were ligated to AzTB, enriched on streptavidin beads, and both lysate and enriched fractions were separated on SDS-PAGE. Top: TAMRA fluorescence, bottom: immunoblot analysis, GAPDH = loading control. Adapted from Howard *et al.* 2020.³³⁴

2.3.4.2 Chemical proteomics

Proteomics analysis of the biomolecular interactome of **PARPYnD** in MDA-MB-468 cells was necessary to assist in the identification of the remainder of the protein bands observed in the gel-based experiments and robustly quantify any differences in labelling upon competition. It also allowed the entire proteome to be profiled at once without immunoblotting for each member of the PARP family individually and permitted the profiling of other off-target proteins. Furthermore, it was anticipated that the sensitivity of shotgun proteomics may facilitate the detection of weaker binders and low abundance proteins.

MDA-MB-468 cells were treated in triplicate with vehicle (DMSO), **PARPYnD** (1 μ M), or co-treated with **PARPYnD** (1 μ M) and either **AZ9482** (5 μ M), **AZ0108** (5 μ M) or olaparib (5 μ M). Dishes were irradiated with UV light, cells were lysed and tagged proteins were ligated to AzRB (**Figure 1.7**) via CuAAC. Biotin-labelled proteins were enriched on NeutrAvidin agarose beads, reduced and alkylated,

and digested into their constituent peptides with trypsin. Given that tandem mass tag (TMT) labelling has been reported to boost the identification of lower abundance proteins,²¹⁸ peptides were TMT labelled for quantification. The samples were combined, fractionated six times to enhance proteome coverage, and then analysed by nanoLC-MS/MS.

2.3.4.2.1 Protein labelling profile of PARPYnD

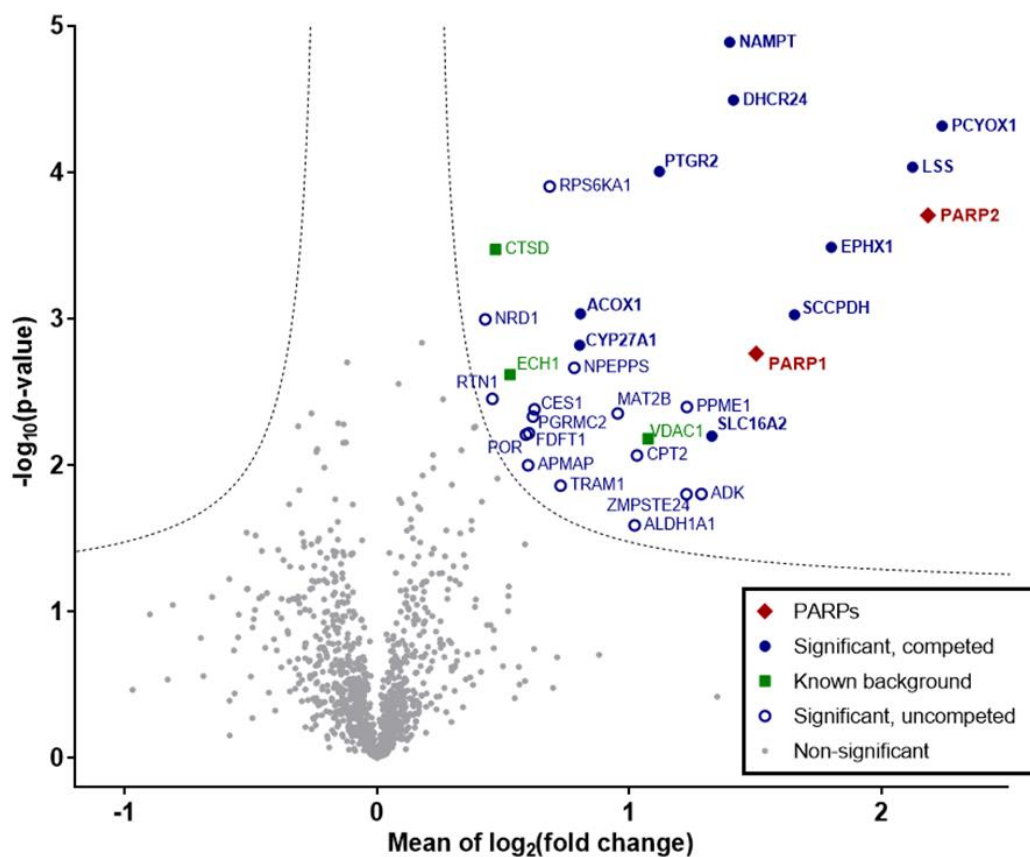


Figure 2.13 Labelling profile of **PARPYnD** in MDA-MB-468 cells. Cells were treated in triplicate with **PARPYnD** (1 μ M) or DMSO, irradiated, lysed, and tagged proteins clicked to AzRB. Proteins were enriched on NeutrAvidin agarose, digested into peptides, and TMT labelled for analysis by LC-MS/MS. Volcano plot demonstrates enrichment between probe- and DMSO-treated conditions (x axis) and the associated significance (y axis) determined by pairwise Student's T-test ($S_0 = 0.1$, false discovery rate (FDR) = 5%). Adapted from Howard *et al.* 2020.³³⁴

Comparing **PARPYnD**-treated samples to the vehicle control allowed for the generation of a volcano plot that depicts the protein targets engaged by **PARPYnD** at 1 μ M (**Figure 2.13**). PARP1 is shown to be labelled by the probe, reconfirming the results obtained by Western blotting, and PARP2 is also shown to be enriched as was originally expected from the recombinant protein binding assay data. Given that **PARPYnD** can provide engagement data on both PARP1 and PARP2, this expands the utility of this AfBP as the first photocrosslinking probe for the PARP family.

Expected binders of the diazirine moiety were also found to be labelled by **PARPYnD**; these are found to be enriched in AfBPP studies with diazirine AfBPs regardless of the core probe scaffold, and include here cathepsin D (CTSD), voltage dependent anion-gated channel 1 (VDAC1) and enoyl-CoA hydratase 1 (ECH1).¹¹⁷ While these proteins are not targets of the parent molecules as demonstrated by the lack of depletion in competition volcano plots (see below, **Figure 2.15a–c**), they provide a useful internal standard for indication of a successful photoaffinity labelling experiment. The remainder of the proteins labelled by **PARPYnD** represent novel binders for the phthalazinone class of PARPi, and the complete list of labelled proteins is detailed in **Table 2.3**.

Table 2.3 Proteins identified through AfBPP experiments with **PARPYnD**. Data from the competition experiments (**Figure 2.15**) were used to populate the competition columns.

Grouping	Gene	Protein	Competed by		
			AZ9482	AZ0108	Olaparib
PARPs	PARP1	Poly(ADP-ribose) polymerase 1	+	+	+
	PARP2	Poly(ADP-ribose) polymerase 2	+	+	+
Background	CTSD	Cathepsin D	-	-	-
	ECH1	Enoyl-CoA hydratase 1	-	-	-
	VDAC1	Voltage dependent anion-gated channel 1	-	-	-
Enriched, competed	CYP27A1	Mitochondrial sterol 26-hydroxylase	-	+	-
	DHCR24	$\Delta(24)$ -sterol reductase	-	+	+
	EPHX1	Epoxide hydrolase 1	-	+	-
	LSS	Lanosterol synthase	-	+	+
	NAMPT	Nicotinamide phosphoribosyl-transferase	-	+	+
	PCYOX1	Prenylcysteine oxidase 1	-	+	+
	PTGR2	Prostaglandin reductase 2	-	+	-
	SCCPDH	Saccharopine dehydrogenase-like oxidoreductase	-	+	-
SLC16A2	Monocarboxylate transporter 8	-	-	+	
Enriched, non-competed	ADK	Adenosine kinase	-	-	-
	ALDH1A1	Aldehyde dehydrogenase 1 family member A1	-	-	-
	APMAP	Adipocyte plasma membrane-associated protein	-	-	-
	CES1	Carboxylesterase 1	-	-	-
	CPT2	Carnitine O-palmitoyltransferase 2, mitochondrial	-	-	-
	FDFT1	Squalene synthase	-	-	-
	MAT2B	Methionine adenosyltransferase 2 subunit beta	-	-	-
	NPEPPS	Puromycin-sensitive aminopeptidase	-	-	-
	NRD1	Nardilysin	-	-	-
	PGRMC2	Membrane-assoc. progesterone receptor component 2	-	-	-
	POR	NADPH-cytochrome P450 reductase	-	-	-
	PPME1	Protein phosphatase methylesterase 1	-	-	-
	RPS6KA1	Ribosomal protein S6 kinase alpha-1	-	-	-
	RTN1	Reticulon-1	-	-	-
	TRAM1	Translocating chain-associated membrane protein 1	-	-	-
	ZMPSTE24	CAAX prenyl protease 1 homolog	-	-	-

It was also important to demonstrate that this labelling profile of **PARPYnD** was dependent upon UV irradiation, so MDA-MB-468 cells were once again treated in triplicate with vehicle (DMSO) or **PARPYnD** (1 μ M) but kept in the dark. Cells were lysed and tagged proteins were ligated to AzRB via

CuAAC and enriched on NeutrAvidin agarose. Peptides were generated and analysed as described above. Comparison of non-irradiated **PARPYnD** treated samples with DMSO samples showed almost no significant enrichment of any proteins, indicating that UV irradiation was necessary to label and enrich the proteins identified by **PARPYnD** (Figure 2.14).

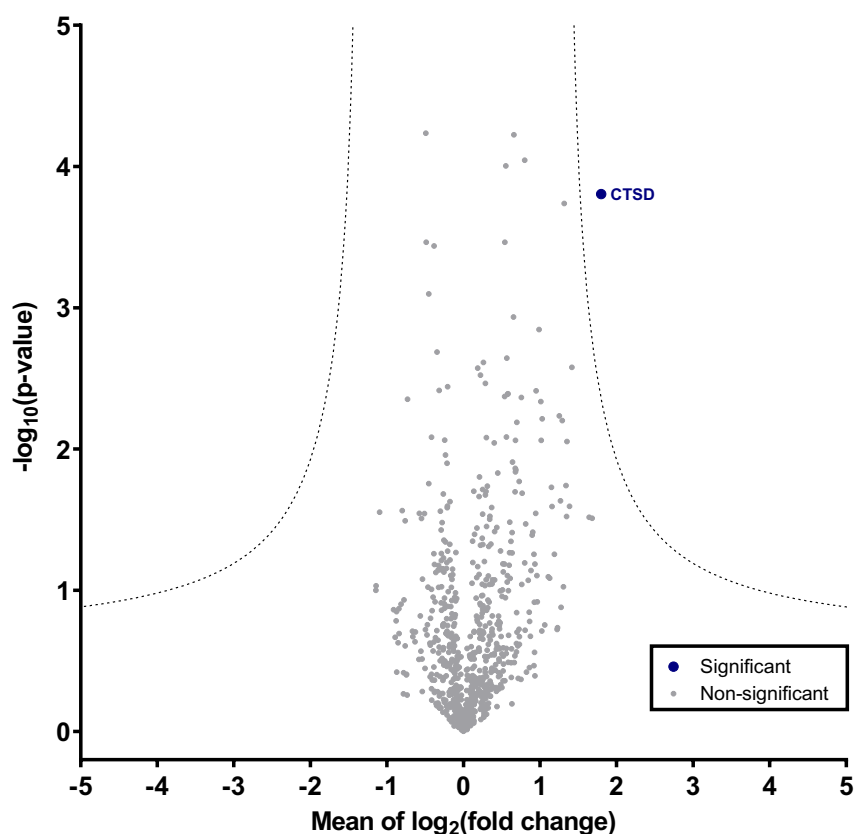


Figure 2.14 Labelling profile of **PARPYnD** in MDA-MB-468 cells without UV irradiation. Cells were treated in triplicate with **PARPYnD** (1 μ M) or DMSO, lysed and tagged proteins clicked to AzRB. Proteins were enriched on NeutrAvidin agarose, digested into peptides, and TMT labelled for analysis by LC-MS/MS. Volcano plot demonstrates enrichment between probe- and DMSO-treated conditions (x axis) and the associated significance (y axis) determined by pairwise Student's T-test ($S_0 = 1.0$, false discovery rate (FDR) = 1%). Adapted from Howard *et al.* 2020.³³⁴

2.3.4.2.2 Competition experiments

To investigate which of the **PARPYnD** enriched proteins were also targets of the parent molecules, comparison of the probe-labelled samples with those also treated with each parent compound was performed (Figure 2.15). Competition experiments with all the parent molecules resulted in depletion of PARP1 and PARP2, confirming that all of these molecules engage PARP1/2 in a live-cell setting, and demonstrating once again that **PARPYnD** is an effective AfBPP to assay the engagement of PARP enzymes by small molecules in intact cells. Aside from demonstrating on-target engagement, these

competition experiments were also able to identify several other interacting proteins for both **AZ0108** and olaparib (**Table 2.3**) which represent potentially novel off-target proteins for both molecules.

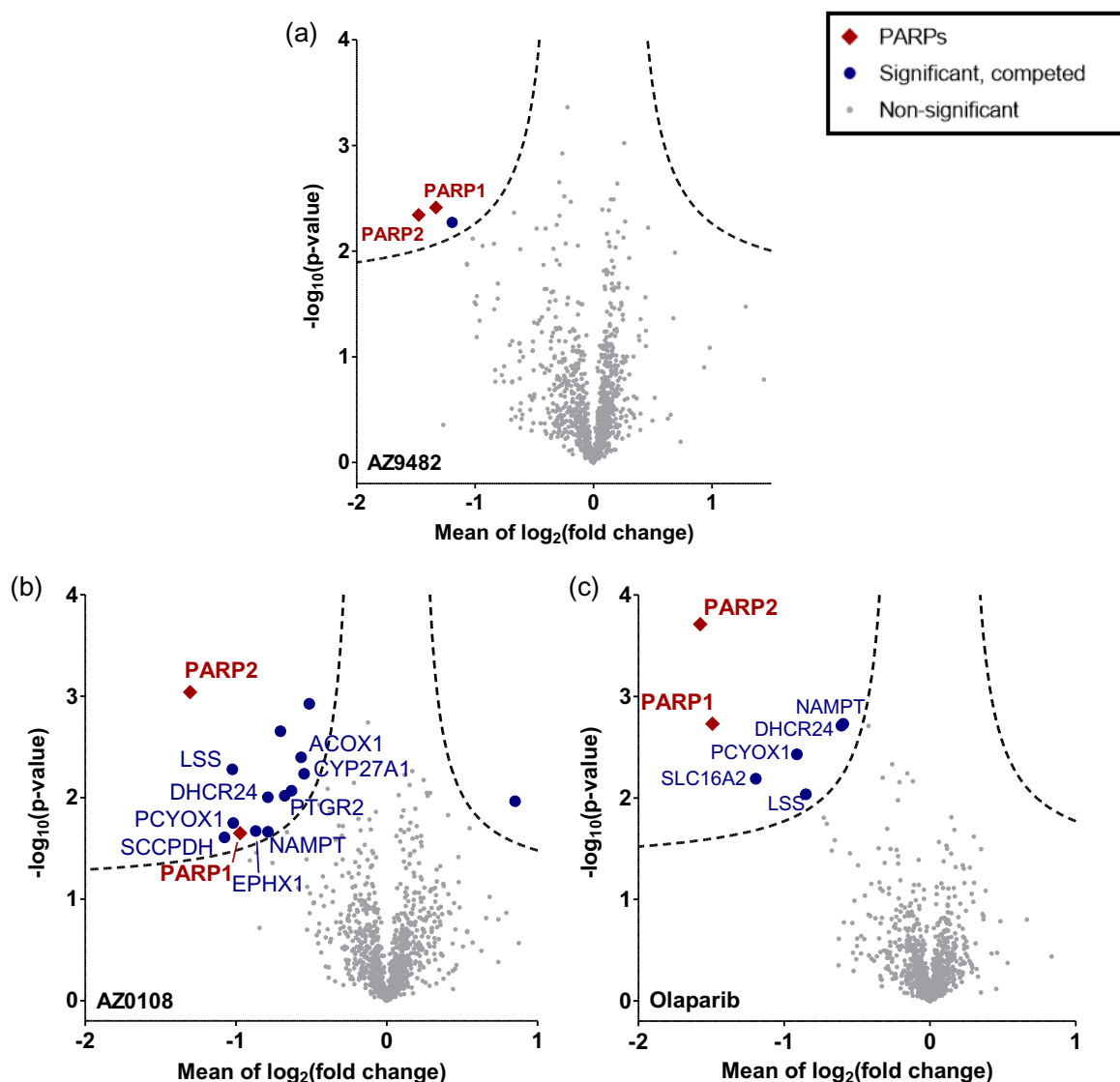


Figure 2.15 Volcano plots for **PARPYnD** competition experiments. Cells were treated with **PARPYnD** (1 μ M) or co-treated with **PARPYnD** (1 μ M) and either (a) **AZ9482** (5 μ M), (b) **AZ0108** (5 μ M) or (c) olaparib (5 μ M), irradiated, lysed and the tagged proteins clicked to AzRB. Proteins were enriched on NeutrAvidin agarose, digested into peptides, and TMT labelled for analysed by LC-MS/MS. Volcano plot demonstrates enrichment between probe- and probe/competitor-treated conditions (x axis) and the associated significance (y axis) determined by pairwise Student's T-test ($S_0 = 0.1$, false discovery rate (FDR) = 15%). Significantly depleted proteins were only labelled with their gene name if they also appear enriched in **PARPYnD** (1 μ M) vs. DMSO experiments (**Figure 2.13**). Adapted from Howard *et al.* 2020.³³⁴

Among these proteins, NAMPT is of interest since it catalyses the condensation of nicotinamide with 5-phosphoribosyl-1-pyrophosphate to yield nicotinamide mononucleotide, a key intermediate in the biosynthesis of NAD^+ . Since phthalazinone PARPi are known to mimic the adenine of NAD^+ , it is not

surprising that these molecules interact with proteins such as NAMPT, however this is the first time any such engagement has been experimentally detected. Novel off-targets involved in sterol biosynthesis and metabolism were also identified, including LSS, NADP⁺-dependent reductase DHCR24, and NAD(P)-independent oxidase CYP27A1, all of which are annotated together as a functional network by the Search Tool for the Retrieval of Interacting Genes/Proteins (STRING) (Figure 2.16).

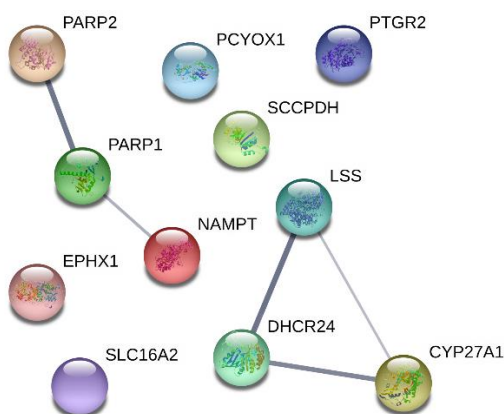


Figure 2.16 STRING molecular interaction analysis of proteins enriched by **PARPYnD** and competed by the parent molecules. Edge width is proportional to confidence in the relationship (minimum required interaction score: 0.4 (maximum 1)).³⁴³

The remainder of the competed proteins seem to be functionally independent, but do include an NADH-dependent reductase prostaglandin reductase 2 (PTGR2), again indicating that these inhibitors have the potential to interact with other proteins that use NAD(P)⁺/NAD(P)H as a cofactor. Other competed proteins include NAD(P)⁺-independent oxidase prenylcysteine oxidase 1 (PCYOX1), putative oxidoreductase saccharopine dehydrogenase-like oxidoreductase (SCCPDH), and epoxide hydrolase 1 (EPHX1). Monocarboxylate transporter 8 (SLC16A2), a member of the solute carrier protein family, was also identified as a binder for **AZ0108** and is of particular interest since recent research has highlighted the importance of the SLC family of proteins in transporting drugs across cellular membranes,³⁴⁴ and identification of SLC16A2 may suggest a role for protein in the cellular trafficking of PARPi. All of these identified targets for **AZ0108** and olaparib may be of significance when considering the use of these molecules *in vivo* or in the clinic and may lead to a greater understanding of their off-target toxicity or their use in novel indications.

2.3.4.2.3 Non-competed proteins

PARPYnD also enriches several proteins that are not competed by any of the inhibitors tested, meaning that this AfBP may be a potential chemical tool to profile these proteins and their interactions with other binders outside the PARPi family. These include other NAD(P) binding proteins, and proteins that bind other adenosine containing cofactors:

- NAD(P) binding proteins
 - NADPH-cytochrome P450 reductase (POR)
 - Squalene synthase (FDFT1)
 - Retinal dehydrogenase (ALDH1A1)
- Coenzyme A binding proteins
 - Peroxisomal acyl-coenzyme A oxidase 1 (ACOX1)
 - Carnitine *O*-palmitoyltransferase 2, mitochondrial (CPT2)
- ATP binding proteins
 - Adenosine kinase (ADK)
 - Methionine adenosyltransferase 2 subunit beta (MAT2B)
 - Ribosomal protein S6 kinase alpha-1 (RPS6KA1)

Once again, STRING functional analysis of these proteins was performed (**Figure 2.17**).

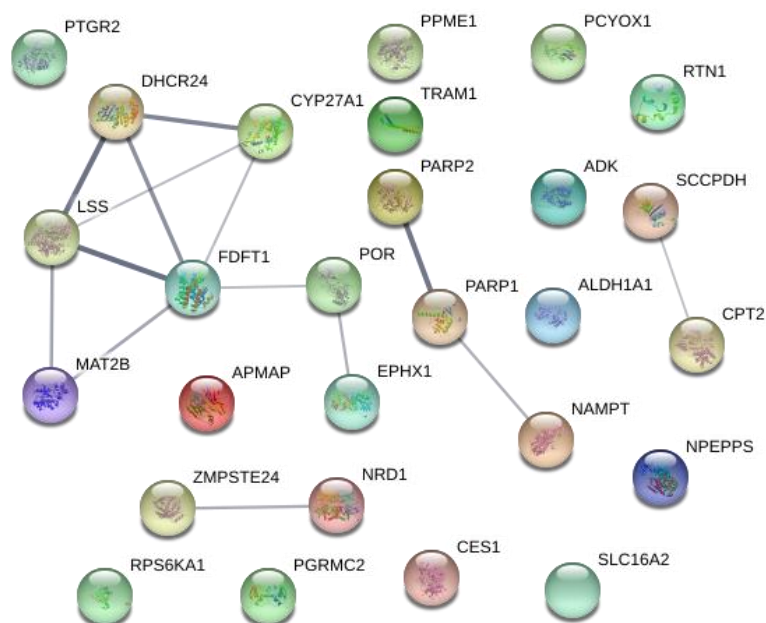


Figure 2.17 STRING molecular interaction analysis of all proteins enriched by **PARPYnD** excluding known background diazirine binders. Edge width is proportional to confidence in the relationship (minimum required interaction score: 0.4 (maximum 1)).³⁴³

While most proteins were functionally independent, inclusion of the proteins enriched by **PARPYnD** but not competed by parent molecules resulted in an extension of the previously identified sterol biosynthesis/metabolism network to include squalene synthase (FDFT1) and other associated proteins, highlighting the potential utility of **PARPYnD** to profile this family of proteins.

2.3.4.3 Overexpression of FLAG-PARP6

It was hypothesised that low endogenous expression levels of PARP6 in MDA-MB-468 cells may preclude the detection of the interaction with **PARPYnD** and therefore **AZ0108**. In order to overcome this, AZ were able to provide an N-terminally FLAG-tagged fusion of PARP6 in a mammalian expression vector (plasmid map in **Appendix I**). This would allow for the transient overexpression of PARP6, overcoming any issues with a low endogenous expression level, and the N-terminal FLAG tag would facilitate detection of the protein by immunoblot with the well-validated anti-FLAG antibody, addressing any concerns regarding PARP6 antibody efficiency. The transfection efficiency of the plasmid containing FLAG-PARP6 was assessed in MDA-MB-468 cells by varying the amount of vector and Lipofectamine™ transfection reagent (**Figure 2.18**).

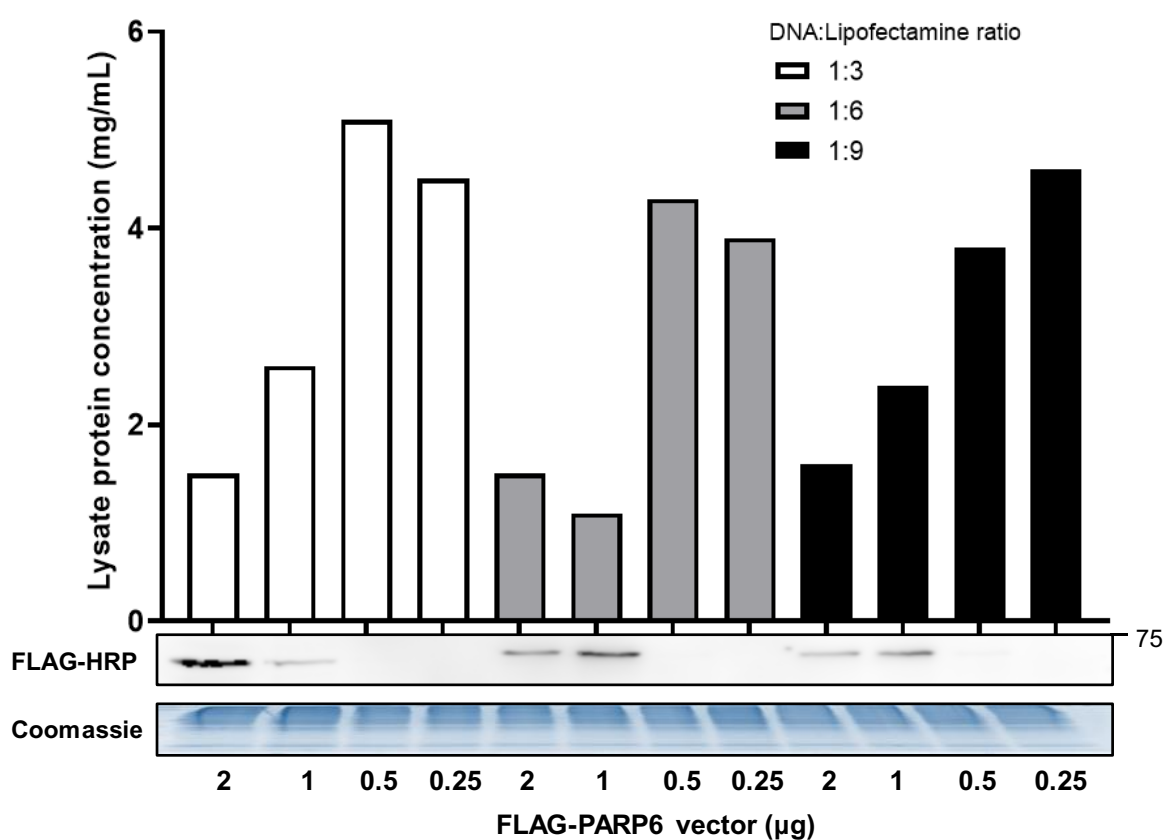


Figure 2.18 Optimisation of FLAG-PARP6 transfection conditions in MDA-MB-468 cells. Cells were treated with varying amounts of vector containing the PARP-FLAG6 gene and Lipofectamine (DNA:Lipofectamine ratio x:y is x µg DNA to y µL Lipofectamine) in 6-well plates as shown and lysed after 24 h, all in the same volume. Protein concentrations were measured (top) and lysates immunoblotted against the FLAG epitope with CBB staining performed for protein loading (bottom).

Detection of FLAG-PARP6 was possible by Western blot, and while varying the amount of Lipofectamine reagent did not largely alter the expression of FLAG-PARP6, higher amounts of DNA were required to detect the protein. Transfection with more DNA was however cytotoxic to MDA-MB-

468 cells, represented by a decreased protein yield in each lysate when exposed to higher amounts of DNA (**Figure 2.18**). While it is known that increased DNA concentration during transfection causes cytotoxicity,³⁴⁵ in this case higher amounts of DNA also leads to increased expression of the constitutively active PARP enzyme which has been shown to be toxic due to uncontrolled depletion of the cellular stocks of NAD⁺.²⁴⁴

Nevertheless, MDA-MB-468 cells were seeded to confluency in 6-well plates and transfected with 2 μ g DNA and a 1:3 ratio of DNA (μ g) to Lipofectamine (μ L). The cells were then treated with DMSO vehicle, **PARPYnD**, or **PARPYnD** and either **AZ9482**, **AZ0108** or olaparib at the same concentrations as in previous experiments. Cells were irradiated, lysed and the labelled proteins ligated to AzTB. Biotin-tagged proteins were enriched over streptavidin and the lysate and enriched fractions immunoblotted for the presence of the FLAG epitope (**Figure 2.19**). Once again, PARP6 was not enriched by **PARPYnD**, as shown by the lack of signal in the FLAG western blot for the enriched fractions (lanes 2–3), and therefore competition to investigate engagement of PARP6 by **AZ0108** was not possible.

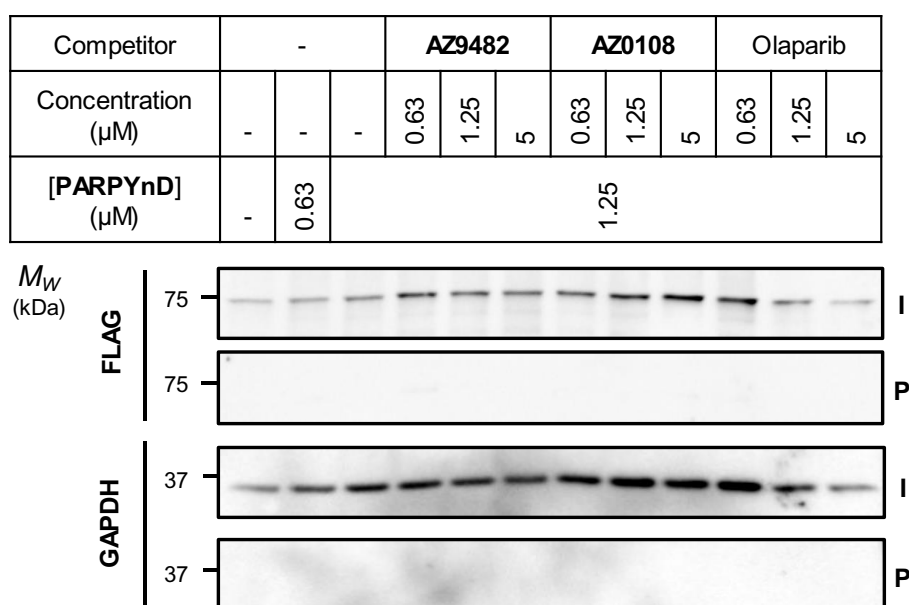


Figure 2.19 Attempted enrichment of overexpressed FLAG-PARP6 by **PARPYnD**. MDA-MB-468 cells were transfected to express FLAG-PARP6 and treated as indicated, irradiated, lysed, and tagged proteins ligated to AzTB. Displayed is the immunoblot analysis before (I = input) and after (P = pull down) enrichment, GAPDH = loading control. Adapted from Howard *et al.* 2020.³³⁴

2.3.4.4 Recombinant PARP6

The failure to enrich FLAG-PARP6 when overexpressed in live cells was once again surprising, and was suggestive of **PARPYnD** being unable to bind and/or photocrosslink to PARP6. However as discussed, **PARPYnD** has clearly demonstrated that it can induce MPS formation and bind to recombinant PARP6 with an IC₅₀ of 0.23 μ M. Given the lack of structural information on PARP6, it

was possible that **PARPYnD** was binding to the protein but the diazirine was in an unfavourable orientation such that it could not effectively label PARP6, explaining why PARP6 had not been enriched by **PARPYnD** in AfBPP experiments. In order to help resolve this, AZ provided the recombinant form of PARP6 used in their fluorescence anisotropy assays. With this protein in hand, it was possible to perform experiments with the aim of confirming whether or not **PARPYnD** was both binding and crosslinking to PARP6 *in vitro*. The construct contained full-length PARP6 with an N-terminal glutathione *S*-transferase (GST) fusion protein attached (**Figure 2.20**, sequence in **Appendix II**).

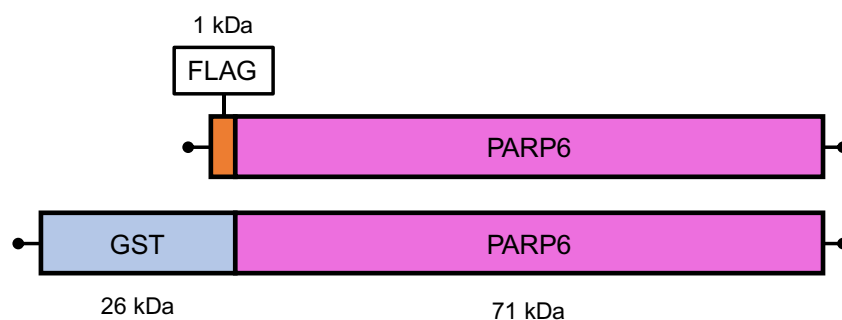


Figure 2.20 PARP6 protein constructs used in this work. FLAG-PARP6 (top) was the protein product of the expression construct after transfection in mammalian cells. GST-PARP6 (bottom) was produced as a recombinant fusion protein in *E. coli* cells.

It was first necessary to confirm whether this GST-PARP6 protein was active. PARP6 is able to undergo auto-modification to generate mono(ADP-ribosyl)PARP6 in the presence of a suitable NAD^+ substrate,²²⁵ so GST-PARP6 was incubated *in vitro* with biotinylated NAD^+ , resolved on an SDS-PAGE gel, and immunoblotted for biotin using NeutrAvidin-horseradish peroxidase (HRP) (**Figure 2.21**). GST-PARP6 was active as shown via the detection of an HRP signal when treated with NAD^+ -biotin. Importantly, it could be shown that this modification could be inhibited in a dose-dependent fashion with the addition of increasing concentrations of **PARPYnD**. This once again confirmed that **PARPYnD** does bind to GST-PARP6, and that this binding inhibits the catalytic activity of the enzyme.

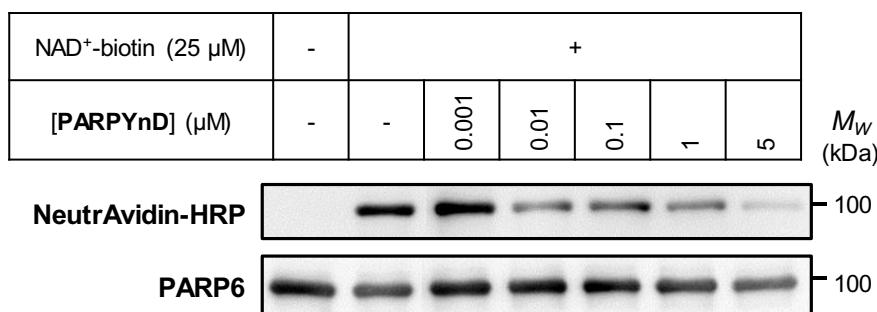


Figure 2.21 GST-PARP6 auto-modification assay. GST-PARP6 was incubated with NAD^+ -biotin and increasing concentrations of **PARPYnD**. Reactions were diluted in gel loading buffer, boiled, separated on SDS-PAGE, and immunoblotted using NeutrAvidin-HRP (signal) and anti-PARP6 (protein loading). Adapted from Howard *et al.* 2020.³³⁴

2.3.4.4.1 Solution-based photocrosslinking

With confirmation that **PARPYnD** was able to bind to the catalytically active GST-PARP6, it was then possible to investigate whether **PARPYnD** could photocrosslink to the protein. **PARPYnD** was incubated with GST-PARP6, irradiated with 365 nm UV light, and co-precipitated with bovine serum albumin (BSA) to remove the tris(hydroxy-methyl)aminomethane (Tris) present in the GST-PARP6 storage buffer which would otherwise inhibit the click reaction.¹⁴⁶ The proteins were ligated to AzTB via CuAAC, precipitated again to remove excess click reagent and analysed by SDS-PAGE (**Figure 2.22**).

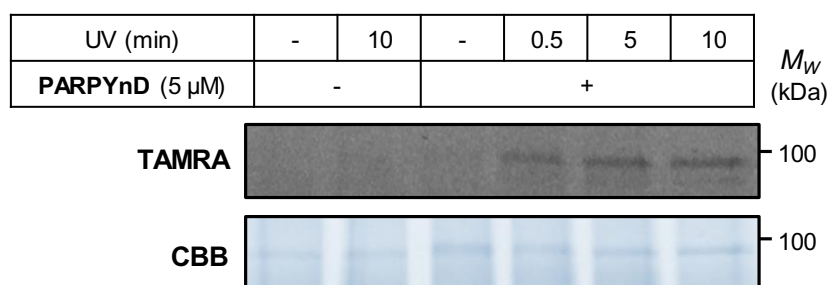


Figure 2.22 GST-PARP6 labelling by **PARPYnD** *in vitro*. GST-PARP6 and PARPYnD or vehicle control were incubated together, irradiated, precipitated, ligated to AzTB, and analysed by SDS-PAGE. Top: TAMRA fluorescence, bottom: CBB.

Labelling of GST-PARP6 was observed upon UV irradiation in the presence of the probe, suggesting that **PARPYnD** was able to effectively label the recombinant protein, something not observed for endogenous PARP6. However, this experiment was conducted outside of a native biological environment, and with **PARPYnD** and GST-PARP6 being the only components of the mixture; labelling could be driven by non-specific association of the two molecules, especially over longer irradiation times.

2.3.4.4.2 Lysate-based photocrosslinking

In order to address this, a competition experiment was devised with parent molecule **AZ0108**. If labelling by **PARPYnD** is representative of specific binding to PARP6 through, for example, interactions with the NAD⁺ binding pocket, then this should be effectively competed by **AZ0108** blockading the binding site. Furthermore, labelling achieved in cellular lysates would be more representative of a true binding interaction between probe and protein as it would be in the presence of the surrounding biological milieu and subject to various opportunities for off-target binding.

Therefore, native MDA-MB-468 cellular lysates were spiked with GST-PARP6 or vehicle control to investigate the labelling of *endogenous* PARP6 present in the lysates. The samples were treated with DMSO vehicle, **PARPYnD** (1 μ M), or **PARPYnD** (1 μ M) and **AZ0108** (1 μ M or 5 μ M), irradiated, precipitated to remove Tris, ligated to AzTB, and enriched on streptavidin beads. The whole lysate,

supernatant and enriched fractions were all analysed by in-gel fluorescence and Western blot (**Figure 2.23**).

In both the presence and absence of GST-PARP6, **PARPYnD** is able to label multiple endogenous proteins in the lysate, though the binding profile observed by in-gel fluorescence was somewhat different to that observed by labelling achieved *in situ* (**Figure 2.11**). Nonetheless, a faint band could be detected at the same height as the band identified as PARP1 via *in situ* labelling (>, **Figure 2.11**), and competition with **AZ0108** could be observed (**Figure 2.23**, “- GST-PARP6” gel, pull down fractions), indicating that labelling in the lysate was at least partially able to recapitulate cell-based labelling.

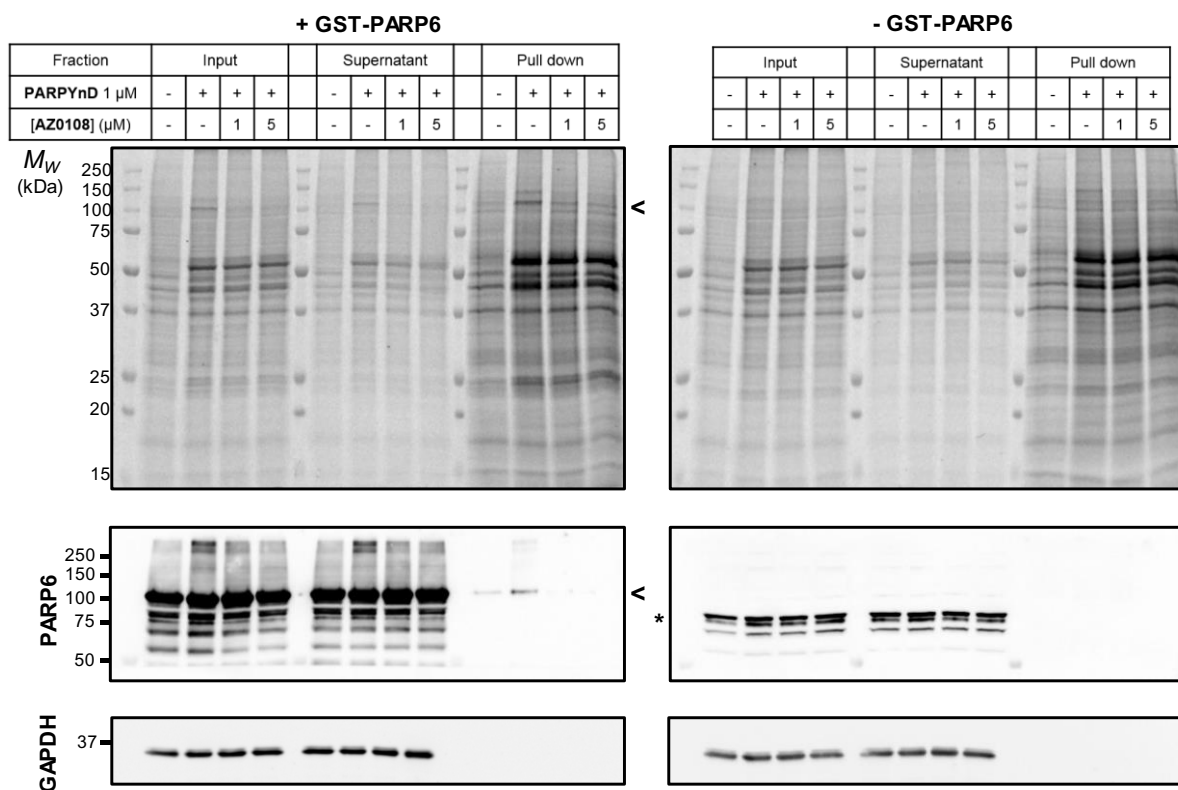


Figure 2.23 **PARPYnD** crosslinking to GST-PARP6 in lysates. MDA-MB-468 lysates were spiked with GST-PARP6 or vehicle control and treated as indicated, irradiated, precipitated, and tagged proteins clicked to AzTB. Samples were enriched on streptavidin and the whole lysate (input), supernatant and enriched (pull down) fractions analysed by in-gel fluorescence and Western blot; < = GST-PARP6, * = endogenous PARP6. Adapted from Howard *et al.* 2020.³³⁴

Importantly, a clear band could be detected in the **PARPYnD** treated lanes at around 100 kDa (<, **Figure 2.23**) in the whole lysate and enriched fractions when GST-PARP6 (98 kDa) had been spiked in to the lysates. This band was not present without spiked-in GST-PARP6 and could be effectively out-competed by **AZ0108**. This suggested that **PARPYnD** could bind and crosslink to GST-PARP6 in a complex biological background and this was out-competed by a known PARP6 inhibitor, indicating

that this labelling was specific. Interrogating the enriched fractions via immunoblotting against PARP6 reinforced that the band visualised on in-gel fluorescence was the spiked-in GST-PARP6 (<, **Figure 2.23**). The intensity of the band in the **PARPYnD** treated sample was greater than in the DMSO sample, and this enrichment could be effectively out-competed by **AZ0108**. Despite this, **PARPYnD** was still not able to enrich *endogenous* PARP6 from the lysate (*, **Figure 2.23**); this is demonstrated from the lack of any signal in the enriched fraction on either PARP6 immunoblot at 71 kDa.

These data demonstrate that **PARPYnD** is able to both bind and crosslink to the recombinant, GST-tagged PARP6, but not to the endogenous PARP6 present in MDA-MB-468 cells, suggesting that there is a biomolecular disparity between the recombinant and endogenous proteins that precludes binding of **PARPYnD** to the endogenous version. This raises significant questions about the proposed mechanism of action of MPS-inducing PARPi; PARP6 inhibition is the expected molecular mechanism of action that induces the MPS phenotype, yet these experiments demonstrate that endogenous PARP6 is not a substrate for **PARPYnD**, suggesting that **PARPYnD** induces MPS formation through an alternative mechanism. However, the N-terminal GST fusion tag does make recombinant PARP6 structurally distinct from the endogenous protein, and it cannot be ruled out that the GST-tag is somehow promoting the photocrosslinking of **PARPYnD** to the recombinant protein, accounting for the differences in labelling observed.

2.3.4.4.3 GST-tag influence on photocrosslinking

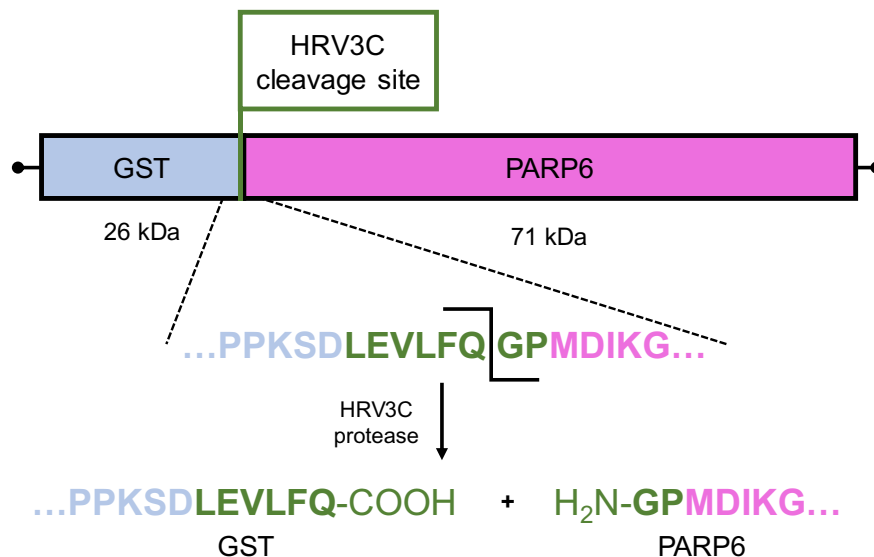


Figure 2.24 Location of the HRV3C cleavage site in GST-PARP6. The recognition sequence (LEVL FQ|GP) is highlighted in green and the resulting reaction products shown.

In order to investigate this, it was possible to make use of an internal human rhinovirus 3C (HRV3C) protease cleavage site that connects the GST-tag to the PARP6 protein (**Figure 2.24**). Cleavage at this position would remove the large GST-tag that might be in some way responsible for influencing the

binding of **PARPYnD** to recombinant GST-PARP6. MDA-MB-468 lysates were once again spiked with GST-PARP6 protein and crosslinked to **PARPYnD** in the presence or absence of competitor **AZ0108**. The protein was left intact or cleaved either before or after the crosslinking had been performed. The lysates were then processed as previously described and the results analysed by in-gel fluorescence (Figure 2.25).

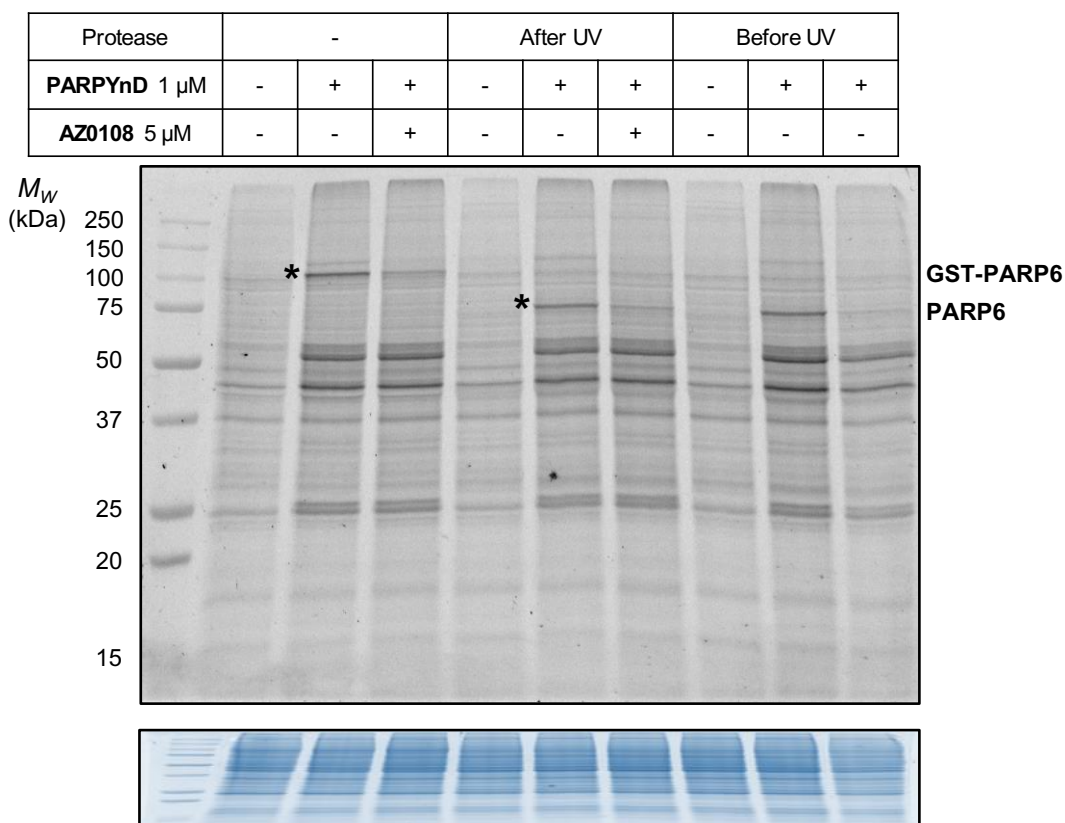


Figure 2.25 **PARPYnD** crosslinking to protease-cleaved GST-PARP6 in MDA-MB-468 lysates. Lysates were spiked with GST-PARP6, treated as shown, irradiated, precipitated, and tagged proteins clicked to AzTB and analysed by in-gel fluorescence. Top: TAMRA fluorescence, bottom: CBB, * = labelled GST-PARP6/cleaved-PARP6. Adapted from Howard *et al.* 2020.³³⁴

Once again, the full-length GST-PARP6 was labelled in lysates by **PARPYnD**, and this labelling could be competed by parent molecule **AZ0108**. Crosslinking to GST-PARP6 and then cleaving off the GST-tag resulted in a decrease in the molecular weight of the labelled and competed band to the weight corresponding to the 71 kDa PARP6 portion of the protein. This indicated that the binding site for **PARPYnD** was on the PARP6 section of the protein and not on the 26 kDa GST-tag. Finally, cleaving the GST tag off *first* then performing photocrosslinking also resulted in labelling of the PARP6 portion of the protein, indicating that the GST-tag was likely not influencing the full-length protein structure and promoting labelling by **PARPYnD**.

These data suggest that **PARPYnD** is able to bind and label recombinant PARP6 produced in *E. coli* but not endogenous mammalian PARP6. This implies that access to the NAD⁺ binding site may be

regulated in the endogenous protein by complex formation with another biomolecule or some post-translational modification. It cannot be entirely ruled out that the two remaining N-terminal amino acid residues resulting from the HRV3C protease cleavage of GST-PARP6 (**Figure 2.24**) promote the binding and/or photocrosslinking of **PARPYnD** and **AZ0108** to the recombinant protein since this remains a structural distinction between this protein and endogenous PARP6. Nonetheless, **PARPYnD** has uncovered a clear disparity in the binding of phthalazinone-based PARPi to the two proteins which raises interesting questions surrounding the molecular mechanism of action of **AZ0108**. Further work will be required to uncover the molecular basis for this discrepancy and **PARPYnD** will be an invaluable tool with which to investigate this question.

2.4 Conclusions and future work

This work details the design, synthesis and application of the first photoreactive affinity-based probe for the PARP enzyme family. **PARPYnD** is able to bind to and label PARP1 in live cells, and Western blot can be used to measure enrichment of PARP1 by **PARPYnD**. PARP2 as well as PARP1 can be detected after enrichment through chemical proteomics, and together these methods can be used to quantify the engagement of novel PARPi **AZ9482** and **AZ0108**, and existing PARPi olaparib, with these PARP enzymes. This validates **PARPYnD** as a tool to measure engagement of NAD⁺-mimicking PARPi in live-cells and could be further applied to different cell types and inhibitors to demonstrate target engagement and selectivity in other systems. Further work should be undertaken in different cell lines to assess binding to PARP enzymes that may be under-represented in MDA-MB-468 cells, potentially extending the utility of **PARPYnD**.

Chemical proteomics highlighted unexpected and novel targets for both **AZ0108** and olaparib. Previous work with non-covalent affinity-based probes and affinity chromatography handles (**Figure 2.5**) failed to enrich any of the secondary targets found for olaparib in this work.^{73,87,332} This highlights the importance of photoreactive warheads in AfBPP and their ability to capture weaker, secondary binders. Further work is required to validate these hits by competitive enrichment and Western blot experiments, but engagement of these targets may lead to deeper understanding of the compounds' toxicity or utility in novel indications. STRING molecular interaction analysis was able to demonstrate that proteins involved in sterol metabolism were interactors of **PARPYnD** and its parent molecules, which could have implications for the safety and efficacy of these compounds. **PARPYnD** was also able to enrich a further 16 proteins that were not found to be competed by any parent compound. These could represent further novel interactions for phthalazinone-based compounds and expands the utility of **PARPYnD** to profiling protein interactions for drugs outside of the PARPi family.

PARPYnD was also used to address the validity of the mechanism of action of multipolar spindle induction by PARPi such as **AZ0108**, reported to be via PARP6 inhibition. Surprisingly **PARPYnD**, which displayed PARP6 binding *in vitro* and clear MPS induction potency, was not able to enrich

PARP6 from MDA-MB-468 cells or lysates, even when transiently overexpressed with an epitope tag. Conversely, binding and photocrosslinking to the GST-tagged version of PARP6 used in *in vitro* experiments was demonstrated both in solution and in lysates, and this labelling was found to be independent of the N-terminal GST-tag. Demonstrating this difference in engagement between the recombinant and endogenous forms of the protein may highlight a biomolecular disparity that regulates access to the NAD⁺ binding site in the endogenous protein, raising questions about the original mechanism of action proposed for MPS-inducing PARPi. While genetic silencing of PARP6 was indeed shown to generate an MPS phenotype,³⁴¹ the results described herein suggest that these phthalazinone-based PARPi do not directly inhibit PARP6 in live cells even though they still induce MPS formation, highlighting a potential alternative mechanism of action that requires further investigation. Endogenous expression of the full-length GST-PARP6 in live cells and subsequent photocrosslinking experiments would help to reinforce these results, and more details around the structure and activity of endogenous PARP6 would assist further investigations. Unfortunately, very little is known about PARP6 beyond its role as a tumour suppressor in colorectal cancer and as a regulator of hippocampal dendrite morphogenesis,^{282,283,311} and any structural information is currently lacking. Nonetheless, *in vitro* and *in situ* investigation of PARP6 was made possible by **PARPYnD**, and once again showcases the value of photoreactive chemical tools in the investigation of target profiling.

Proceeding the publication of **PARPYnD** as a photoaffinity probe for the PARP enzyme family, the van der Stelt group published two further photoreactive AfBPs that were also able to label PARP1 in live cells (**Figure 2.26**).³⁴⁶ Taken together with **PARPYnD**, these tool molecules will be of great value for any researcher wishing to assess the target engagement of PARP1/2 *in situ*. In an effort to profile further the inter-family PARP selectivity of PARPi, AZ have also generated a phthalazinone-based scaffold that is reported to enrich all PARP family members (except PARP6) from cellular lysates as an affinity chromatography handle (structure and data proprietary). Adaptation of this scaffold into a photoreactive AfBP would allow PARPi selectivity profiling to be performed in intact cells, potentially constituting a superior AfBP to the probes discussed herein. This remains a future collaboration to be undertaken between AZ and the Tate group.

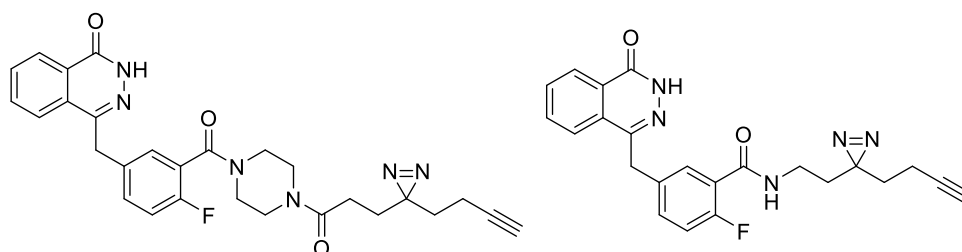


Figure 2.26 Olaparib-based photoreactive AfBPs developed by the van der Stelt group.

Chapter 3 Target profiling of novel necroptosis inhibitors

3.1 Necroptosis and inflammatory cell death

Necroptosis is an inflammatory form of regulated cell death that is initiated by mammalian cells experiencing cellular stresses such as infection.³⁴⁷ The dysregulation of this biochemical pathway has been implicated in various disease states, and there have been growing efforts to develop chemical inhibitors of this pathway to treat these pathologies.³⁴⁸ This chapter will outline the cellular mechanism of necroptosis and its association with disease before summarising existing efforts to drug the pathway, including the molecules relevant to this study that were found to inhibit necroptosis through novel mechanisms of action. The results then describe the development and application of an affinity-based probe to profile the cellular targets of one of these series of molecules. Five key proteins are identified from protein-profiling studies as the potential molecular mechanism of action of these molecules, and preliminary functional validation experiments are described that may link specific inhibitor-protein interactions to necroptosis inhibition.

3.1.1 Cell death in mammalian cells

Discrete cellular death is a natural consequence of life for all living organisms.³⁴⁹ For cells of multicellular life forms, those exposed to mechanical or other environmental forces that damage the physical integrity of the cell experience a type of cell death known as accidental cell death (ACD).³⁵⁰ ACD is rapid, unpredictable and the consequences can be severe or even fatal for a multicellular organism, depending on the number and type of cells affected.³⁵¹ ACD is largely insensitive to any clinical interventions and treatment of such traumatic injuries is carried out at the systemic level after cellular death has occurred.

Cells of multicellular life forms also experience regulated cell death (RCD) which is essential for the development and homeostasis of the organism (**Figure 3.1**).²⁶¹ RCD occurs when an individual cell of the organism receives an endogenous or exogenous signal that initiates a cellular signalling cascade, ultimately leading to the death of the cell.³⁵² This signal can be built into the cell as a result of physiological programming (programmed cell death – PCD), which is a key process that ensures faithful embryonic and foetal development and, postnatally, the proper turnover of various tissues.³⁵⁰ PCD is distinct from other forms of RCD that occur as a result of intrinsic or extrinsic promoters of cellular stress; these RCD pathways can, for example, eliminate potentially cancerous cells and those infected with pathogens, and play a vital role in the inflammatory response by signalling immune cells to an affected locus.^{353,354}

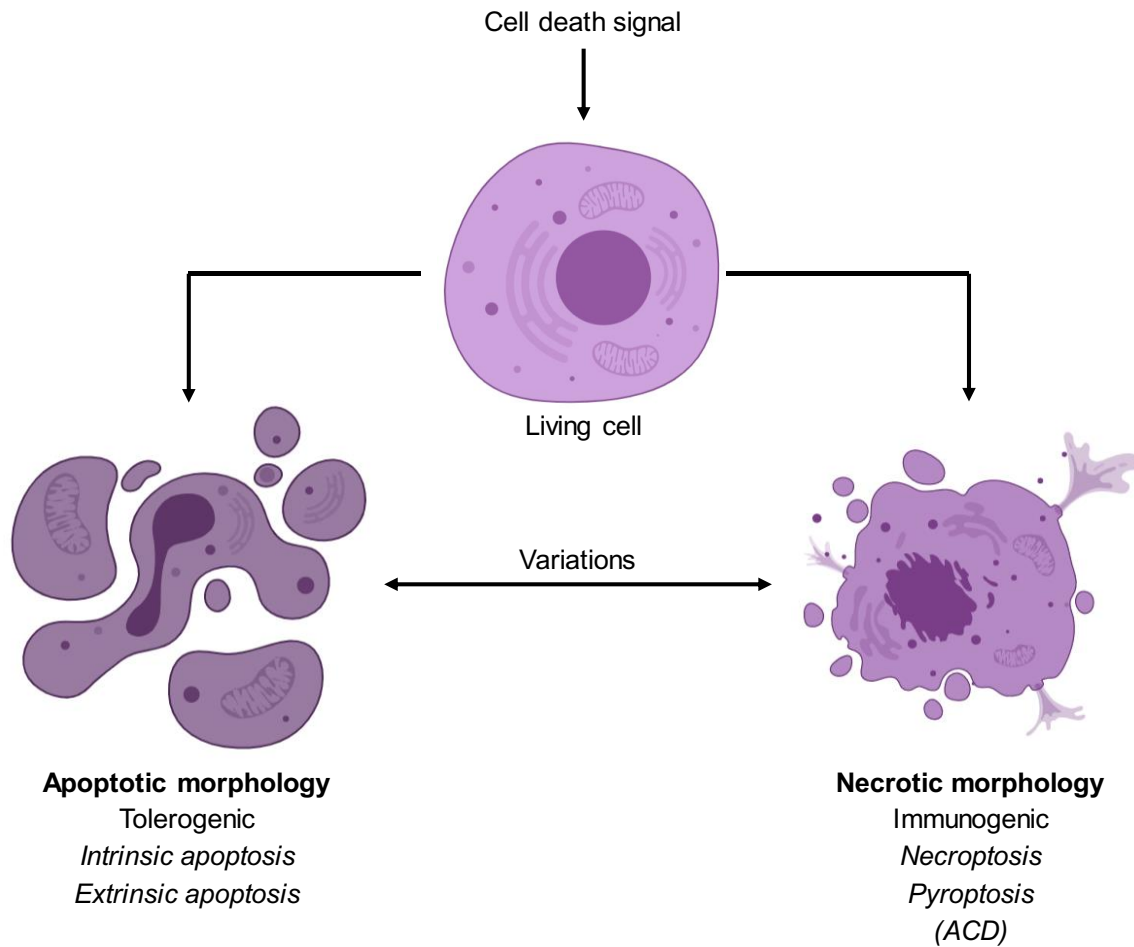


Figure 3.1 Types of regulated cell death (RCD). An internal or external signal triggers a signalling cascade that results in cell death with apoptotic features (membrane blebbing, vesicle formation) that is usually anti-inflammatory, with necrotic features (membrane rupture, loss of internal contents) that is usually pro-inflammatory, or with features somewhere in between. Accidental cell death (ACD) while a result of physical disruption and not a cell death signal, usually displays the morphological features of necrosis. Adapted from Galluzzi *et al.* 2018.²⁶¹

For a considerable period, it was thought that cell death could be simply divided into accidental necrotic cell death, and a programmed form of cell death known as apoptosis.³⁵⁵ Apoptosis is characterised by shrinkage of the cytoplasm and blebbing of the plasma membrane to form compact vesicles that are consumed by surrounding phagocytic cells in a largely immunologically silent (tolerogenic) manner (**Figure 3.1**).³⁵² In the 1990s, much research was devoted to the characterisation of the molecular components of apoptosis, such as the caspase proteases that feature as one of the primary biomarkers of apoptotic cell death.³⁵⁶ Activation of the caspase cascade was often achieved by cellular stimulation with the inflammatory cytokine tumour necrosis factor alpha (TNF α), however it was noted that alongside the traditional morphological hallmarks of apoptosis, cells stimulated with TNF α could also display type of a lytic cell death reminiscent of accidental necrosis (**Figure 3.1**).^{357,358} It was concluded after further research that this was a distinct form of RCD caused by an intrinsic signalling cascade that

could be intentionally activated by mammalian cells.³⁵⁹ This process was defined as necroptosis, and over the subsequent years would be characterised as an inflammatory form of RCD with genetically encoded molecular machinery, predominantly receptor-interacting serine/threonine-protein kinase 1 (RIPK1),³⁶⁰ receptor-interacting serine/threonine-protein kinase 3 (RIPK3),^{361–363} and mixed-lineage kinase domain-like protein (MLKL).^{364,365} Since the discovery of necroptosis, several RCD pathways have been uncovered including pyroptosis, autophagy, parthanatos (**Section 2.1.2.1**), ferroptosis, and many more.²⁶¹ This work has revealed not only novel mechanisms of cell death, but also a level of interconnectivity and redundancy that still requires further research. The remainder of the introduction to this chapter will focus solely on necroptosis, including its molecular features, its association with disease, and its druggability.

3.1.2 Necroptosis

3.1.2.1 Cellular mechanism

Necroptosis is a lytic, inflammatory form of regulated cell death that occurs upon cellular stimulation with inflammatory cytokines or by infection with pathogens, and therefore plays a role in the host immune response.^{347,366} It is activated primarily through exogenous signalling molecules ligating to their cognate death receptor (DR) proteins on the cell surface i.e. tumour necrosis factor alpha (TNF α) binding to tumour necrosis factor receptor 1 (TNFR1),³⁵⁸ Fas-ligand (FASL) binding to Fas-receptor (FASR),³⁶⁷ or TNF α -related apoptosis-inducing ligand (TRAIL) binding to the TRAIL-receptor (TRAILR).³⁵⁸ By far the best studied mechanism of necroptosis is that induced by TNF α , described in **Figure 3.2**.

TNF α causes the trimerisation and activation of TNFR1, which promotes the recruitment of TNFR1-associated death domain protein (TRADD), RIPK1, and then the ubiquitin ligases cellular inhibitors of apoptosis (cIAPs) and linear ubiquitin chain assembly complex (LUBAC) that ubiquitinate RIPK1 and form membrane complex I.^{368,369} This results initially in the activation of NF- κ B and its translocation to the nucleus, where it acts as a transcription factor upregulating survival-, proliferation-, and inflammation-associated genes. Upon continued activation of TNFR1, RIPK1 becomes deubiquitinated and along with TRADD dissociates from complex I and recruits Fas-associated death domain protein (FADD).³⁷⁰ This new cytosolic complex II is primed to activate the apoptosis pathway, dimerising and activating caspase 8, which in turn initiates apoptosis through cleavage of caspase 3/7 which cleave multiple other apoptotic substrates that lead to the cellular shrinkage and compartmentalisation described above. However, in situations where the cell is unable to execute apoptosis, such as genetic ablation or depletion of caspase 8, or through inhibition of cellular caspase activity, RIPK1 dissociates from complex II and recruits RIPK3.^{361–363} Auto-phosphorylation leads to recruitment of mixed-lineage kinase domain-like protein (MLKL) which is dual-phosphorylated to form the “necrosome”.^{364,365} MLKL can then oligomerise and translocate to the cell membrane which it ruptures, leading to the

release of damage-associated molecular patterns (DAMPs) that stimulate inflammation in the surrounding tissue.^{371,372} This RIPK1-RIPK3-MLKL axis has become known as the canonical pathway of necroptosis, and MLKL is ultimately the defining biomarker for necroptosis, distinguishing it from other forms of necrotic cell death.³⁷³

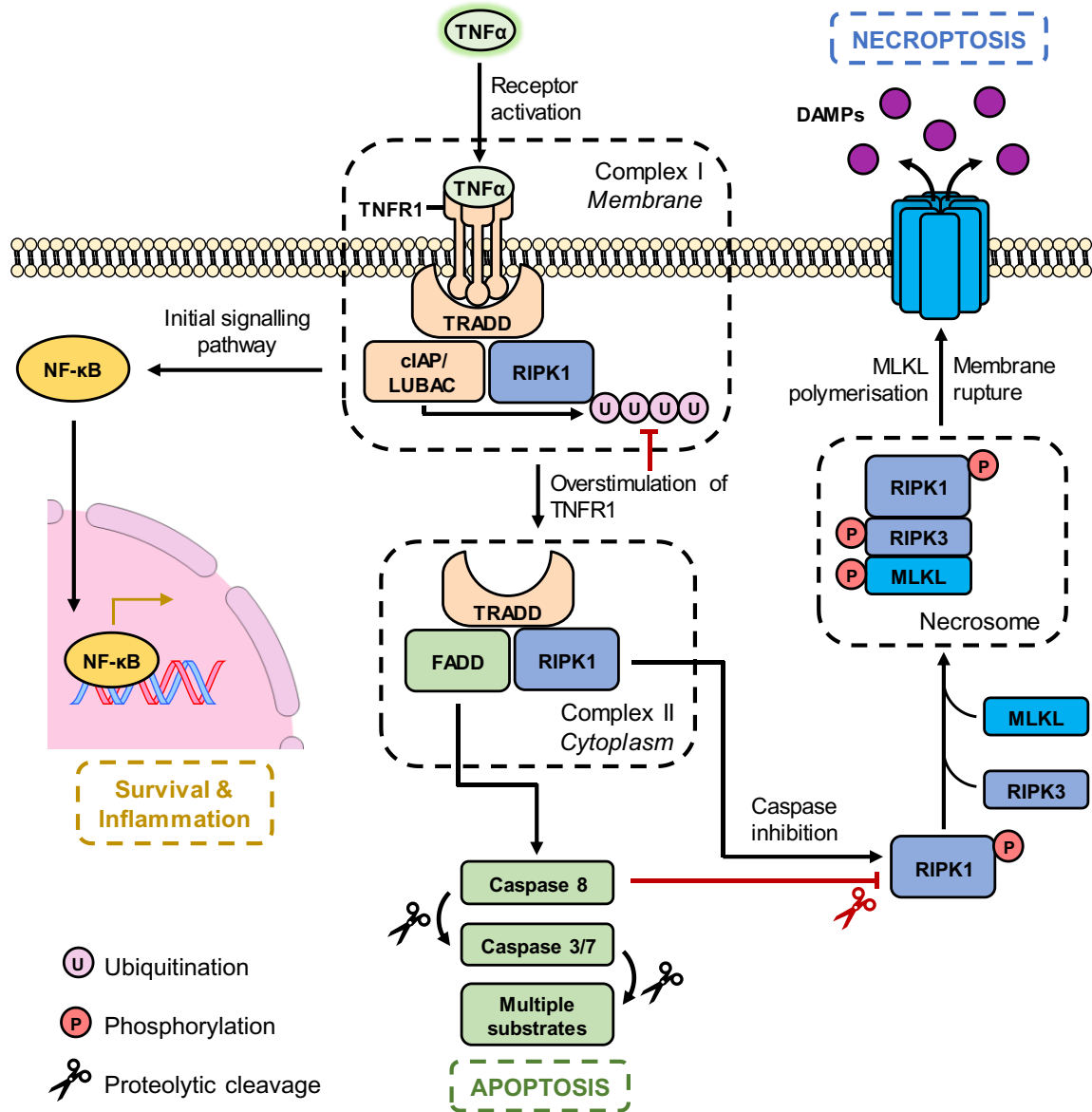


Figure 3.2 TNF α induction of apoptosis, necroptosis and the inflammatory response. The mechanism is described in full in the text. Briefly, TNF α binding to TNFR1 initiates a cellular signalling cascade that initially results in NF- κ B upregulation of survival and pro-inflammatory genes. Overstimulation with TNF α results in cell death, usually via apoptosis, however in situations where cellular caspase activity is deficient, phosphorylated RIPK1 recruits RIPK3 and MLKL to execute necroptosis. Adapted from Weinlich *et al.* 2017³⁴⁷ and Zhuang & Chen 2020.³⁴⁸

This canonical pathway is the most studied mechanism by which necroptosis is induced, however the system is far more complicated than this. Aside from the various other DR ligations that can stimulate

this pathway, RIPK3 can also execute necroptosis independently of complexation with RIPK1. Activation of toll-like receptors 3 and 4 (TLR3/4) and stimulation with the viral-defence proteins interferons (IFNs) can lead to the activation of RIPK3 and subsequent necroptosis.³⁷⁴⁻³⁷⁶ RIPK3 can also be recruited by active DNA-dependent activator of IFN-regulatory factors (DAI), a protein that recognises viral DNA.³⁷⁷ Furthermore, viruses often carry caspase inhibitors that, upon infection, will prevent the host cell from executing apoptosis.³⁶⁶ Taken together, this suggests a physiological role for necroptosis in the killing of virally infected cells when apoptosis is not available, and subsequent inflammatory signalling to local tissue and the wider immune system.

Beyond this, there is also a significant amount of crosstalk with other mechanisms of regulated cell death. **Figure 3.2** outlines already how interconnected both apoptosis and necroptosis are, as they share cytosolic complex II, also known as the “rioptosome”, responsible for initiating both forms of RIPK-dependent cell death.^{347,378} It has also been shown that ripoosome-member caspase 8 is a key suppressor of necroptosis through the cellular cleavage of RIPK1, and that caspase 8 cleavage of the gasdermin (GSDM) pore-forming proteins can lead to an alternative necrotic PCD pathway known as pyroptosis.^{379,380} This activity has led to caspase 8 being defined as the “molecular switch” between apoptosis, necroptosis and pyroptosis.³⁸¹ While the distinct molecular mechanisms that lead to these different forms of cell death and the crosstalk between them are beyond the scope of this work, it is important to appreciate that stimulation of necroptosis is not a linear pathway, and system interconnectivity must be carefully considered when interpreting results for “necroptosis-specific” inhibitors.

Looking in more detail at the molecular mechanism of necroptosis, several recent studies have uncovered novel protein elements of the pathway that have expanded our understanding beyond RIPK1, RIPK3, and MLKL (**Figure 3.3**). While it was known that MLKL phosphorylation drives oligomerisation, translocation to the membrane, association with phospholipids and subsequent cell membrane rupture, it was further shown that this phosphorylation event is promoted by chaperone protein heat shock protein 90 kDa (HSP90) and its co-chaperone CDC37.³⁸² This HSP90-CDC37 complex also physically associates with both RIPK3 and MLKL and stabilises these proteins against degradation.^{383,384} Another heat shock protein (HSP70) has also been implicated in the formation of MLKL polymers from MLKL tetramers by promoting the formation of disulphide bridges that connect the tetramers.³⁸⁵ Most recently, the casein kinase 1 (CK1) family of proteins including CK1 α , CK1 δ , and CK1 ϵ were found to be components of the necrosome, and perform the key serine 227 phosphorylation of RIPK3, originally thought to be an auto-phosphorylation event, that leads to the association of MLKL to the necrosome and its subsequent phosphorylation.³⁸⁶

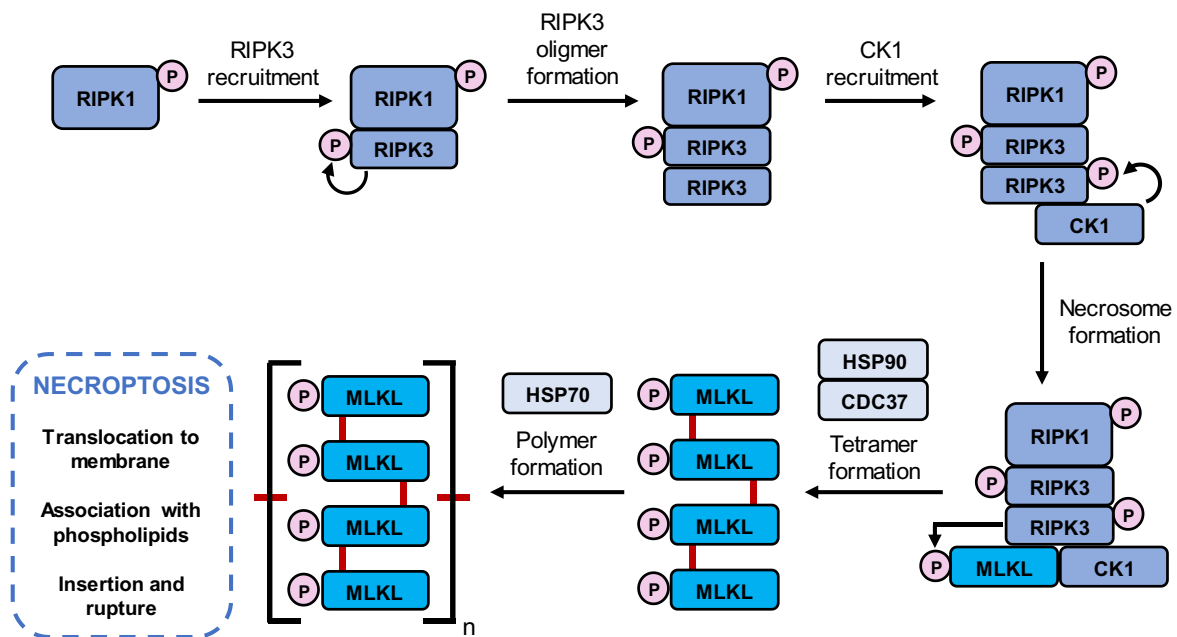


Figure 3.3 Biomolecular pathway of RIPK1-induced necroptosis.^{383,385,386} Phosphorylated RIPK1 recruits RIPK3, and auto-phosphorylation of RIPK3 switches the preference from hetero-oligomerisation to homo-oligomerisation. CK1 proteins bind to homo-oligomers of RIPK3 and phosphorylate RIPK3 at an alternative site which primes it to recruit and phosphorylate MLKL with the help of the HSP90-CDC37 complex. MLKL then forms tetramers through disulphide bridges (red connections), and these tetramers are polymerised with the help of HSP70. The MLKL polymers then translocate to the cell membrane and rupture the bilayer by unknown mechanisms. P = phosphorylation.

Taken together, these studies have led to a greater understanding of the molecular detail of necroptosis, however there are still several unanswered questions. It has been shown that the terminal 4-helix bundle (4HB) domain of MLKL is essential for membrane trafficking,³⁸⁷ but it is not known which factors associate with the 4HB to allow membrane trafficking of MLKL, or whether MLKL associates with anything at the membrane other than phospholipids.³⁸⁵ Furthermore, how MLKL polymers actually rupture the membrane is under debate: some studies have suggested the 4HB may directly form pores in the membrane, whereas others have suggested MLKL associates with and dysregulates membrane ion channels.³⁷³ Given these unanswered questions and that novel necrosome components can still be uncovered as recently as this year (2020),³⁸⁶ this suggests that the full target catalogue of proteins involved in necroptosis has yet to be completed.

3.1.2.2 Association with disease

Like many cellular signalling pathways, dysregulation of necroptosis has been associated with the pathophysiology of various diseases, therefore chemical inhibition of necroptosis could be a viable strategy to ameliorate these conditions. While primarily implicated in *protection* against viral and bacterial infections, there is growing evidence that hyper-active necroptosis results in exacerbated inflammatory responses in infections such as influenza,³⁸⁸ and contributes to the development of

systemic pathogenic sepsis.³⁸⁹ Necroptosis has also been demonstrated to be a mechanism of undesirable cytopathic depletion for CD4⁺ T-lymphocytes in human immunodeficiency virus (HIV) infections, and RIPK1 inhibition potently restricted this cytopathy.³⁹⁰ Necroptosis has been strongly associated with cell death experienced upon ischaemia-reperfusion injury (IRI), a where an organ or body part suffers oxidative tissue damage upon re-oxygenation after a period of traumatic hypoxia.³⁹¹ This has been shown to be relevant following myocardial infarction,³⁹² and after organ transplantation,³⁹³ indicating that necroptosis inhibition could be a viable strategy to reduce tissue damage following IRI in these cases.

Unsurprisingly, dysregulation of necroptosis has been associated with various inflammatory disorders,³⁹⁴ including rheumatoid arthritis,³⁹⁵ systemic inflammatory response syndrome (SIRS),³⁹⁶ atherosclerosis,³⁹⁷ and psoriasis.³⁹⁸ This extends to neuro-inflammatory and neurodegenerative disorders,^{399,400} with necroptosis implicated in amyotrophic lateral sclerosis (ALS),⁴⁰¹ Alzheimer's disease,^{402,403} Huntington's disease,⁴⁰⁴ and retinitis pigmentosa.⁴⁰⁵ A role for necroptosis in the progression of cancer has also been proposed, however the reports are conflicted, with some clearly suggesting a role for necroptosis in tumour metastasis,^{406,407} while other work has shown RIPK1 inhibition fails to prevent, or even promotes, tumour growth and metastasis.^{395,408} The current understanding is that the role of necroptosis in cancer is context dependent, and likely depends on the type of cancer.⁴⁰⁹

3.1.3 Pharmacological inhibition of necroptosis

Given the association of necroptosis with various disease states, there has been a concerted effort to develop novel inhibitors of the pathway in an effort to treat these diseases.³⁴⁸ Since HSP70, HSP90/CDC37, and the CK1 proteins have only been discovered to be involved in necroptosis relatively recently, the main efforts towards drugging the necroptosis pathway have focussed upon developing chemical inhibitors of RIPK1, RIPK3, and MLKL.

3.1.3.1 RIPK1 inhibitors

Receptor-interacting serine/threonine-protein kinase 1 (RIPK1) is a protein kinase that catalyses the phosphorylation of target proteins on serine or threonine residues, transferred from the terminal phosphate group of the essential co-factor adenosine triphosphate (ATP).⁴¹⁰ Through this phosphorylation of target proteins it transduces signalling along a biochemical pathway, and is most often involved in cell death signalling. RIPK1 is the enzyme in the necroptosis axis with the richest history of drug development, not only due to its role in necroptosis, but also it is unique among the RIPK family (RIPK1–7) as it possesses a C-terminal “death domain” that recruits it to various signalling complexes associated with other forms of clinically relevant RCD and inflammatory processes.⁴¹¹

The human “kinome” represents one of the most heavily drugged family of enzymes due to their involvement in a broad range of signalling pathways and disease pathologies. Furthermore, the shared

ATP-binding site is well characterised and strategies to develop inhibitors that bind into this pocket are well established.^{412,413} As a result, inhibitors of the RIPK family can be subdivided into various classes depending on their mode of kinase inhibition, a generally applicable classification for inhibitors of kinases across the human kinome:⁴¹⁴

- Class I – Competitive inhibitor for the ATP-binding site of the active protein,
- Class II – Competitive inhibitor for the ATP-binding site of the inactive protein,
- Class III – Reversible allosteric inhibitor that binds just next to the ATP-binding site with ATP bound.

The most successful inhibitors of RIPK1 and therefore of necroptosis are Class III, largely because Class III inhibitors bind to an allosteric portion of the protein that is unique for each protein kinase. Class I/II inhibitors by comparison bind to the ATP-binding site which is largely conserved across the kinases, making these inhibitors more susceptible to polypharmacology and resulting off-target effects.⁴¹³ The first Class III RIPK1 inhibitor identified was necrostatin-1 (Nec-1, **Figure 3.4**), a tryptophan-type inhibitor that exhibited an EC₅₀ of 0.49 μM against necroptosis.³⁵⁹ Nec-1 was however found to have an off-target interaction through inhibition of the immunomodulatory enzyme indoleamine 2,3-dioxygenase 1 (IDO1).⁴¹⁵ Derivatisation to Nec-1s (**Figure 3.4**) ablated this off-target activity, improved the anti-necroptosis EC₅₀ to 0.23 μM, and through its Class III binding mode demonstrated excellent selectivity toward RIPK1 across a panel of human kinases.⁴¹⁶ While these “necrostatins” were not progressed clinically, they remain key chemical probes utilised in fundamental necroptosis research.^{417,418}

Currently, the most clinically promising anti-necroptosis RIPK1 inhibitors are the benzoxazepine class of molecules discovered by GlaxoSmithKline (GSK) via a DNA-encoded library screening platform.⁴¹⁹ After medicinal chemistry optimisation of the original hit molecule, GSK2982772 (GSK’772, **Figure 3.4**) was found to be a highly selective Class III inhibitor of RIPK1 with an IC₅₀ of 1.0 nM and a corresponding cellular anti-necroptosis EC₅₀ of 6.3 nM.⁴²⁰ In the same study, a dosing of 50 mg kg⁻¹ was found to provide 93% protection against TNFα-induced inflammatory shock in a mouse model and this, along with viable pharmacokinetic (PK) characteristics, has resulted in GSK’772 being the most promising clinical anti-necroptosis candidate. It is currently in Phase II trials for various inflammatory disorders: ulcerative colitis (NCT02903966), psoriasis (NCT02776033) and rheumatoid arthritis (NCT02858492),⁴²¹ all currently suspended due to the ongoing situation with COVID-19.⁴²² A similar derivative, GSK3145095 (GSK’095, **Figure 3.4**), was developed for oncological indications and was shown to be active against pancreatic ductal adenocarcinoma (PDAC) in organ cultures, highlighting for the first time the clinical potential of treating cancer using necroptosis inhibitors.⁴²³ GSK’095 was progressed to a Phase I clinical trial (NCT03681951) to be evaluated for use in PDAC and other solid

tumours,⁴²⁴ but this has since been discontinued following in internal review of GSK's research and development portfolio.⁴²⁵

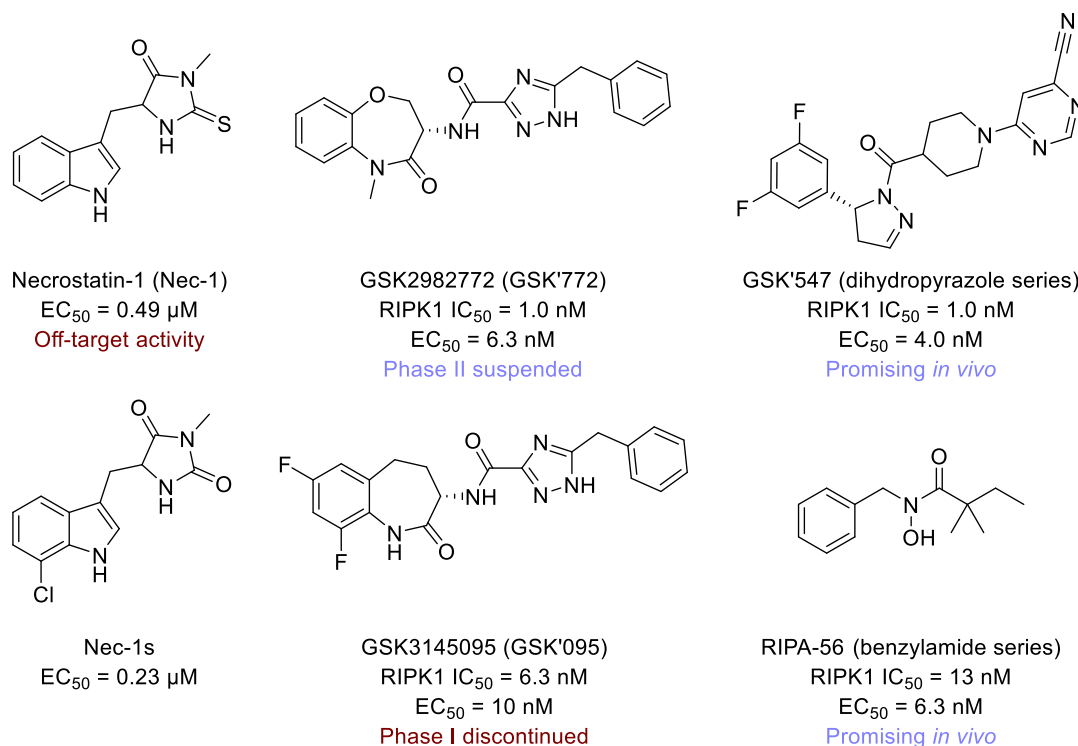


Figure 3.4 Previously reported RIPK1 inhibitors as potential necroptosis modulators.

Other notable RIPK1 inhibitors include DNL747, a brain-penetrating RIPK1 inhibitor with an undisclosed structure that is currently being evaluated in Phase I clinical trials for both Alzheimer's Disease (NCT03757325) and ALS (NCT03757351).⁴²⁶ Two other pharmacophores have also shown promise as novel allosteric RIPK1 inhibitors: the dihydropyrazole series and the benzylamide series.³⁴⁸ GSK'547 (**Figure 3.4**) represents the most promising of the dihydropyrazole compounds, with a RIPK1 IC₅₀ of 1.0 nM, an anti-necroptosis EC₅₀ of 4.0 nM, good PK properties and promising growth and metastasis inhibition in PDAC models *in vivo*.^{427,428} The Class III RIPK1 inhibitor RIPA-56 (**Figure 3.4**) with a benzylamide core also showed promising *in vivo* anti-necroptosis behaviour in a TNF α -induced inflammatory shock model.⁴²⁹

3.1.3.2 RIPK3 inhibitors

While inhibition of RIPK1 has shown the most clinical promise as an anti-necroptosis strategy, it is a protein found upstream in the necroptosis pathway and is involved in other forms of RCD, therefore RIPK1 inhibition may have unanticipated off-pathway effects that may impact the desired therapeutic result.⁴¹¹ Receptor interacting serine/threonine-protein kinase 3 (RIPK3) is a protein kinase in the same family as RIPK1, but is downstream of RIPK1 in the necroptosis pathway (**Figure 3.2**) and can also activate necroptosis in a RIPK1-independent fashion.³⁴⁷ While inhibition of RIPK3 would therefore be

expected to be more targeted towards necroptosis inhibition, the development of RIPK3 inhibitors has been much less successful than for RIPK1.³⁴⁸

From the GSK DNA-encoded library screen that identified the benzoxazepine class of RIPK1 inhibitors, GSK'840 (**Figure 3.5**) was also identified as a modulator of necroptosis that was a potent inhibitor of RIPK3 ($IC_{50} = 0.9$ nM), however this molecule was also found to induce RIPK3-dependent apoptosis.⁴³⁰ Given that the goal of necroptosis inhibitors was to prevent cellular death, exacerbation of an alternative RCD pathway was not desirable, and this facet of pharmacological modulation of RIPK3 has generally hampered the development of RIPK3 inhibitors in the context of necroptosis.³⁴⁸ It has been suggested that RIPK3 inhibition without the induction of apoptosis is possible, and a derivative of an inhibitor of the RAF-kinase family (**Figure 3.5**) showed promise as a necroptosis inhibitor through modulation of RIPK3, however the polypharmacology shared with the RAF family remains a challenge for the development of this compound.⁴³¹

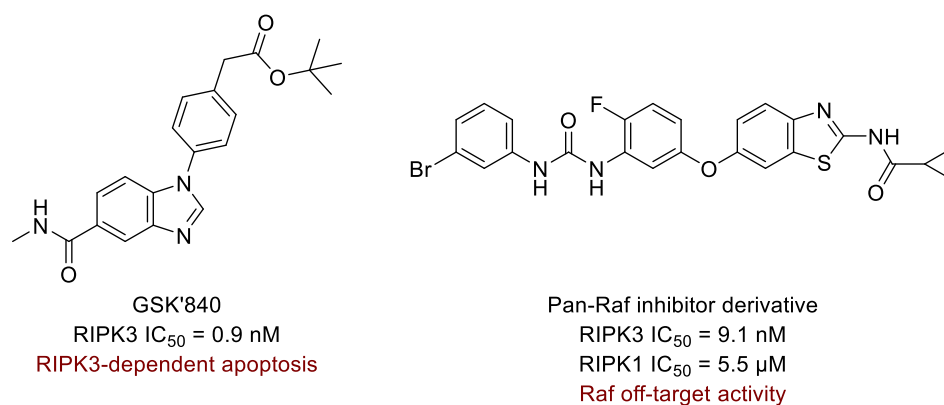


Figure 3.5 Previously reported RIPK3 inhibitors as potential necroptosis modulators.

3.1.3.3 MLKL inhibitors

Mixed lineage kinase domain-like protein (MLKL) is a pseudokinase, a catalytically-deficient kinase, which is now known to be the key pore-forming protein that causes the final membrane destabilisation and rupture characteristic of necroptosis.⁴³² While RIPK1/3 have been known as mediators of necroptosis from the 2000s, it was not until 2012 that MLKL was implicated in necroptosis,³⁶⁴ therefore drug discovery efforts are not as developed for this protein. Incidentally, MLKL was first identified through a target profiling campaign; the small molecule necrosulfonamide (NSA, **Figure 3.6**) was found to block necroptosis downstream of RIPK3 by an unknown mechanism of action.^{364,433} To investigate this, an affinity chromatography methodology using biotin-labelled NSA conjugated to streptavidin beads allowed for enrichment of the target of NSA from lysates, identified by Western blot as MLKL. Unfortunately, the covalent inhibitor NSA displayed only moderate potency against necroptosis ($EC_{50} = 200$ nM) and the structure-activity relationship (SAR) data was too narrow to improve upon this molecule for preclinical evaluation.

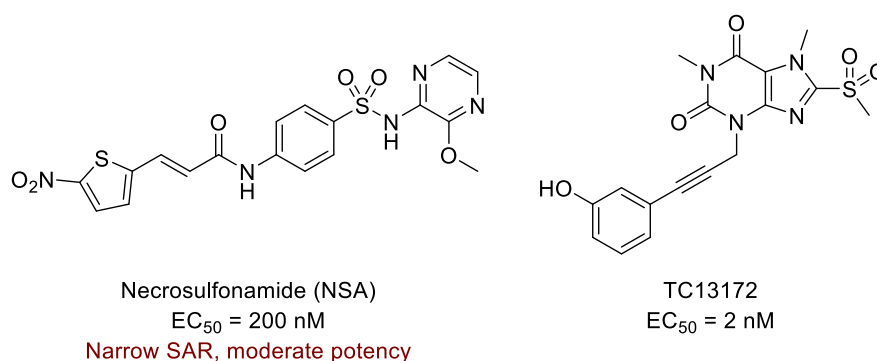


Figure 3.6 Previously reported MLKL inhibitors as potential necroptosis modulators.

Other efforts to drug necroptosis through MLKL inhibition have been investigated; an optimised heterocyclic inhibitor of MLKL, TC13172 (**Figure 3.6**), showed promise as a necroptosis inhibitor ($EC_{50} = 2 \text{ nM}$), however no further development of this compound has been reported.⁴³⁴ It is likely that many drug discovery campaigns are in their infancy with respect to MLKL, and recent insights into the molecular mechanism of MLKL in necroptosis will help to focus these efforts, including the discovery of novel protein components of the necrosome and their interaction with MLKL,^{385,386} insights into the structure of MLKL tetramers and polymers,^{384,432} and emerging details regarding MLKL membrane translocation, association and rupture.^{387,435,436}

3.1.4 Discovery of novel necroptosis inhibitors

Despite the above examples of necroptosis inhibition via targeting of RIPK1, RIPK3 or MLKL, efforts are still underway to develop new modulators of necroptosis that can be used as an effective clinical therapy, something that has not yet been realised despite the clinical potential of such molecules. To attempt to discover novel chemotypes that inhibit necroptosis without focussing on inhibition of a specific target, the University of Lisbon, in collaboration with AstraZeneca (AZ), designed a phenotypic high-throughput screen (HTS) that evaluated the anti-necroptosis potential of a diverse AZ compound library of over 250,000 compounds (**Figure 3.7**).^{437,438} The molecules were initially screened at a single concentration ($31.7 \mu\text{M}$) for their ability to inhibit $\text{TNF}\alpha$ -induced necroptosis in mouse fibroblast (L929) cells. 3,353 compounds (1.4% hit rate) were found to inhibit necroptosis by greater than 30% and were analysed in a dose-response version of the same assay; 1,438 displayed dose-dependent inhibition of necroptosis with an $EC_{50} < 10 \mu\text{M}$ in both L929 cells and a human $FADD^{-/-}$ acute T-cell lymphoblastic leukaemia (Jurkat) cell line (I2.1). Finally, these compounds were tested for their ability to modulate (negatively or positively) cycloheximide-stimulated apoptosis over a four-point concentration range ($0.03\text{--}30 \mu\text{M}$) and any such modulators were excluded, resulting in 356 compounds that solely inhibited necroptosis.

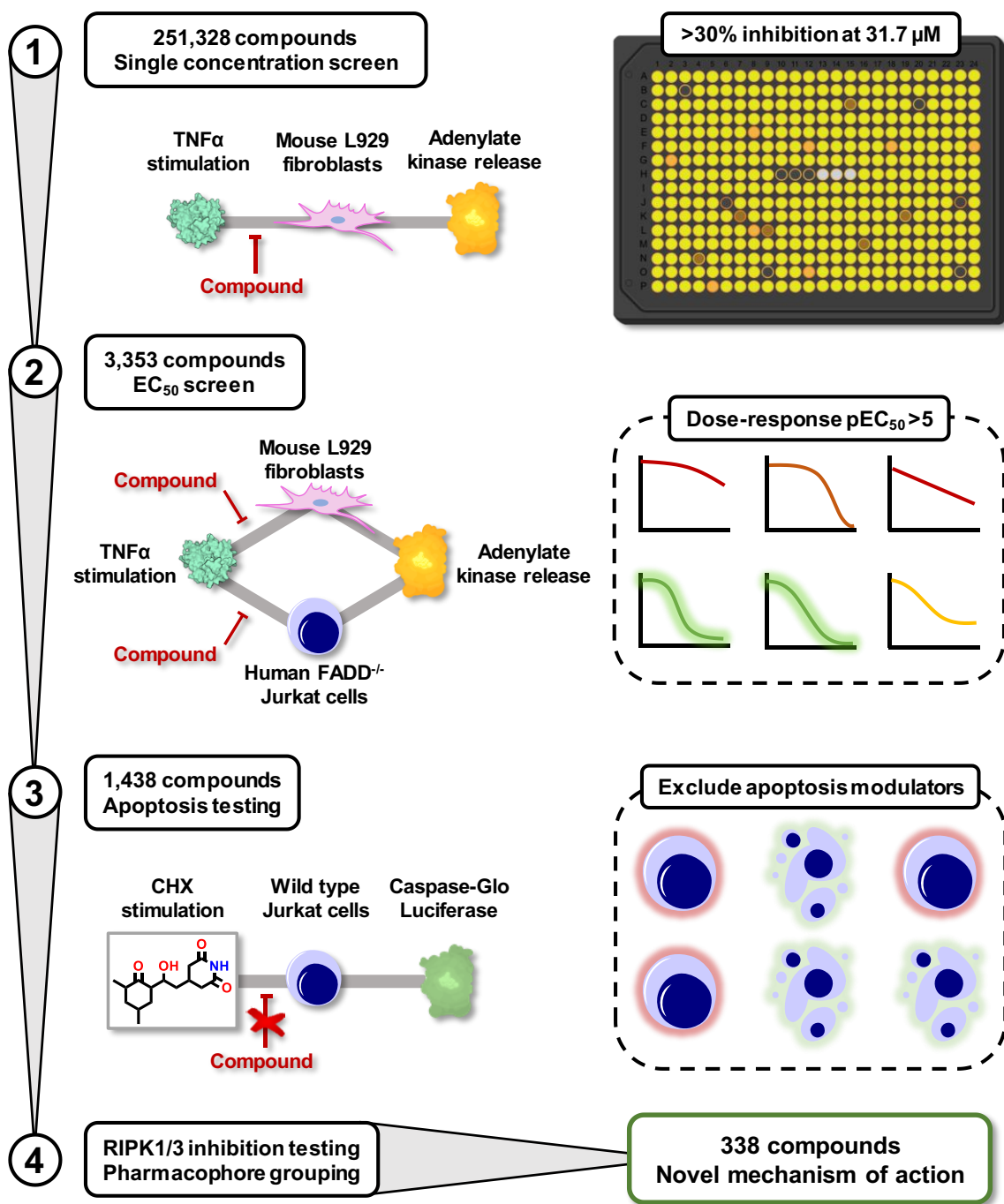


Figure 3.7 High throughput screening pipeline for new necroptosis inhibitors performed by Brito *et al.*⁴³⁸ 1 – Compounds were screened in 384-well plate format for their ability to inhibit TNF α -stimulated necroptosis in L929 cells, using adenylate kinase release as the readout for necroptosis. 2 – Hits from step 1 were tested in a dose-response version of the same adenylate kinase necroptosis assay in both L929 cells and I2.1 cells. 3 – Those compounds with good dose-response profiles were tested to exclude those that inhibited or promoted cycloheximide (CHX) stimulated apoptosis, an RCD modality with similar molecular players to necroptosis (Figure 3.2). 4 – *Bona fide* necroptosis inhibitors were tested for RIPK activity and grouped into common pharmacophores.

Some of the hit compounds were found to inhibit RIPK1 or RIPK3 in *in vitro* assays, so these were presumed to inhibit necroptosis through this molecular mechanism of action; Brito *et al.* discussed further the development of one of these RIPK1 inhibitors as a novel anti-necroptosis agent.⁴³⁸ Of the remaining compounds, 338 were found not to inhibit RIPK1 or RIPK3 in *in vitro* assays, leaving open the possibility that they work through novel mechanisms of action. Many of these compounds could be broadly classified into three major pharmacophore series (**Figure 3.8**): thiazole, benzimidazole, and 7-phenylquinoline (7PQ). The discovery of the molecular targets of any member of this series may open up new drug discovery campaigns and provide new insights into the biomolecular pathway of necroptosis, thus leaving key target profiling work still to be undertaken on this project.

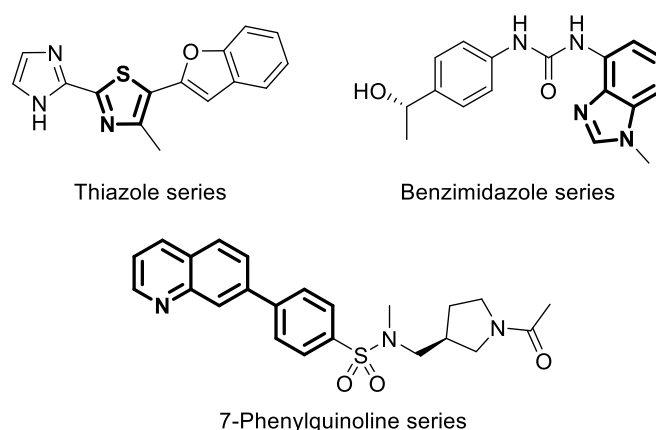


Figure 3.8 Novel pharmacophores uncovered from HTS with unknown mechanisms of action. Common scaffold properties are highlighted in bold.

3.2 Research objectives

The compound series presented in **Figure 3.8** represent novel prospects to pharmacologically inhibit necroptosis, and the target profiling strategy of affinity-based protein profiling outlined in Chapter 1 is an ideal strategy with which to profile the targets of these molecules. The overall aim of this project is to discover the target(s) of the 7PQ class of anti-necroptosis compounds. This pharmacophore was selected due to the wealth of available structure-activity relationship data on this series from the EC₅₀ screen (**Figure 3.7**), increasing the chance of developing a successful AfBP that can effectively profile this class of compounds. Furthermore, AfBPP has recently been applied to a novel polyaromatic class of necroptosis inhibitors, discovering that the compounds worked through multimodal inhibition of RIPK1, RIPK3, and MLKL, demonstrating that photoaffinity labelling can successfully identify targets of necroptosis modulators.⁴³⁹

The work herein describes the design and synthesis of two novel AfBPs for the 7PQ series. One of these compounds was taken forward to probe validation in a novel live-cell necroptosis assay developed here for this project. The AfBP was then advanced to target profiling studies to uncover the biomolecular

interactome of this compound series, and preliminary functional validation of these protein hits was undertaken.

3.3 Results and discussion

3.3.1 Probe design and synthesis

To design an effective AfBP for the 7PQ series, proprietary structure-activity relationship (SAR) data was provided by the University of Lisbon. Thirteen compounds were discovered from the HTS with a 7PQ core, and these could be ranked by their anti-necroptosis EC_{50} in murine L929 fibrosarcoma cells (**Figure 3.9**).

The 7PQ series could broadly be classified as having either an amide or a sulphonamide linkage that connects the phenyl ring to the remaining “right hand side” (RHS) of the molecule, and the amide compounds were generally less potent in EC_{50} when compared to the sulphonamide compounds. When considering the RHS portion of the molecules, they exhibit a range of structural features: mono- or di-substitution on the sulphonamide or amide nitrogen, ring sizes of 3–6 atoms with various heteroatoms and substitution patterns, and variations in stereochemistry. In the absence of any perceived pattern in the SAR data for the RHS of the molecules, it was reasoned that while the 7PQ core was indispensable for activity, the remainder could be modified, within reason, with minimal impact on the SAR.

The RHS was therefore a viable modification site to include both a photoreactive warhead and a bio-orthogonal ligation handle. Given that the SAR provided no robust consensus on the best modifications to optimise the activity of this series, it seemed sensible to incorporate these key chemical functionalities as one minimalist “photoclickable” group (**Section 1.3.4**) since these groups at least have reported, reproducible synthetic routes. Most of the molecules in **Figure 3.9** are di-substituted at the amide or sulphonamide nitrogen, so it seemed reasonable to utilise a separated minimalist linker, such as those described by the Cravatt group (**Figure 1.5**), so a tertiary sulphonamide or amide could be retained.¹⁸² From these considerations, two probes **7PQYnD1 (10)** and **7PQYnD2 (11)**, were designed to generate AfBPs based on both the sulphonamide and amide linkages respectively (**Figure 3.10**).

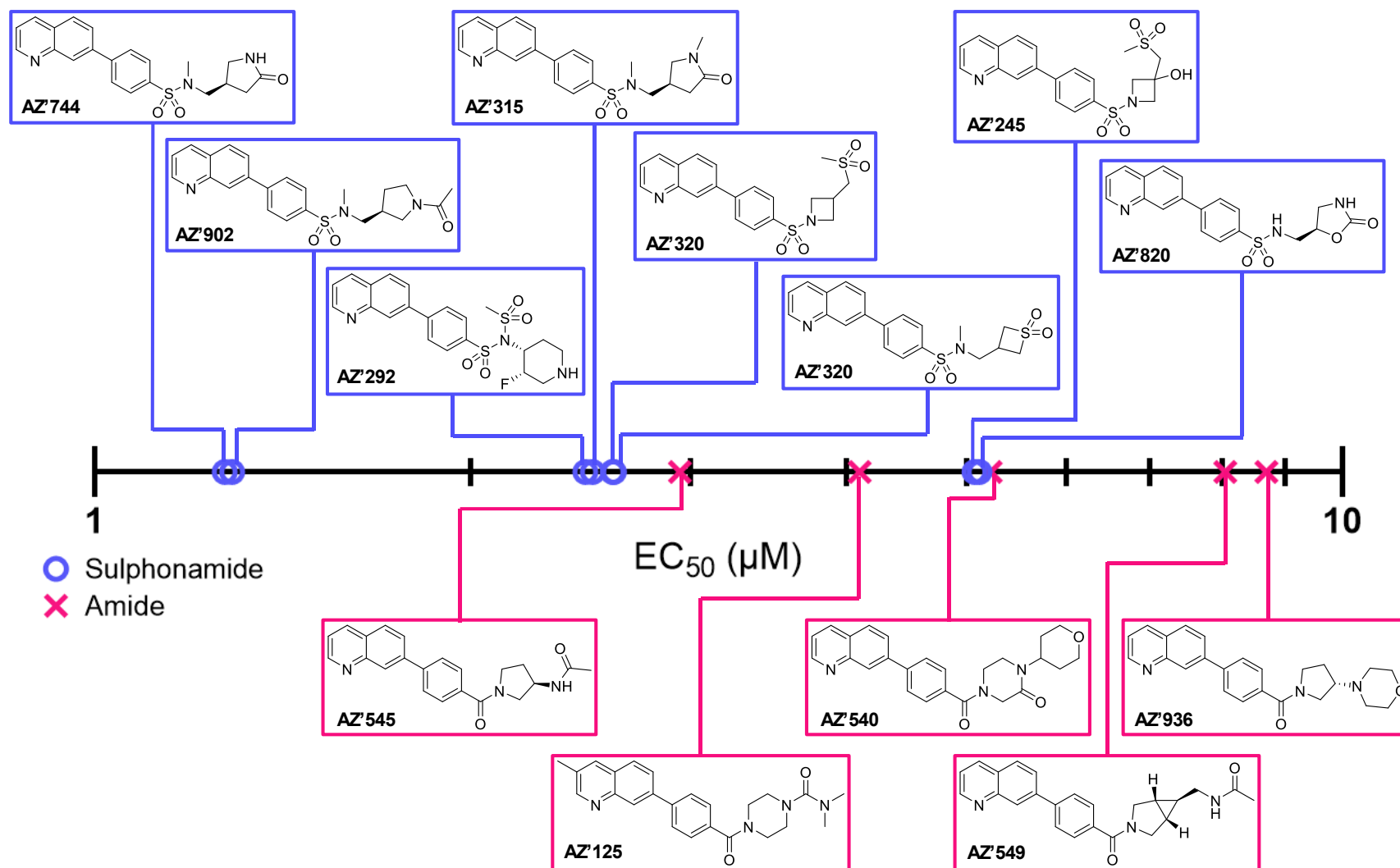


Figure 3.9 Structure-activity relationship data of the 7PQ analogues from the HTS.

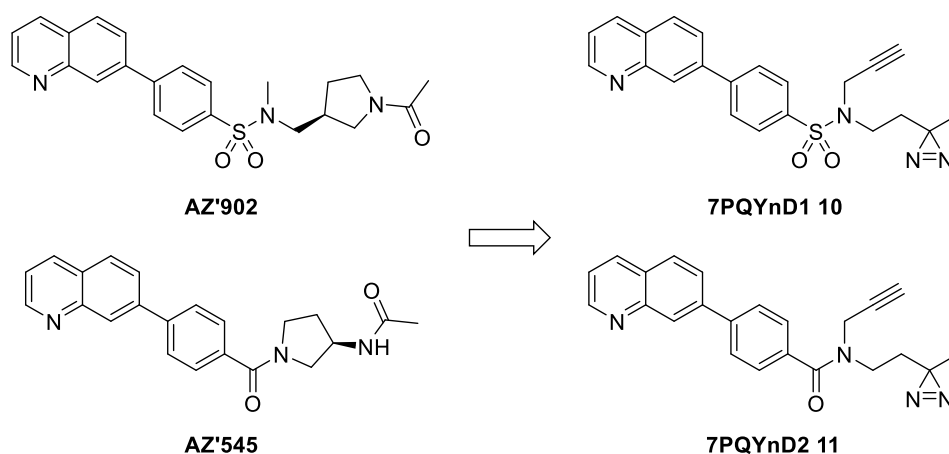
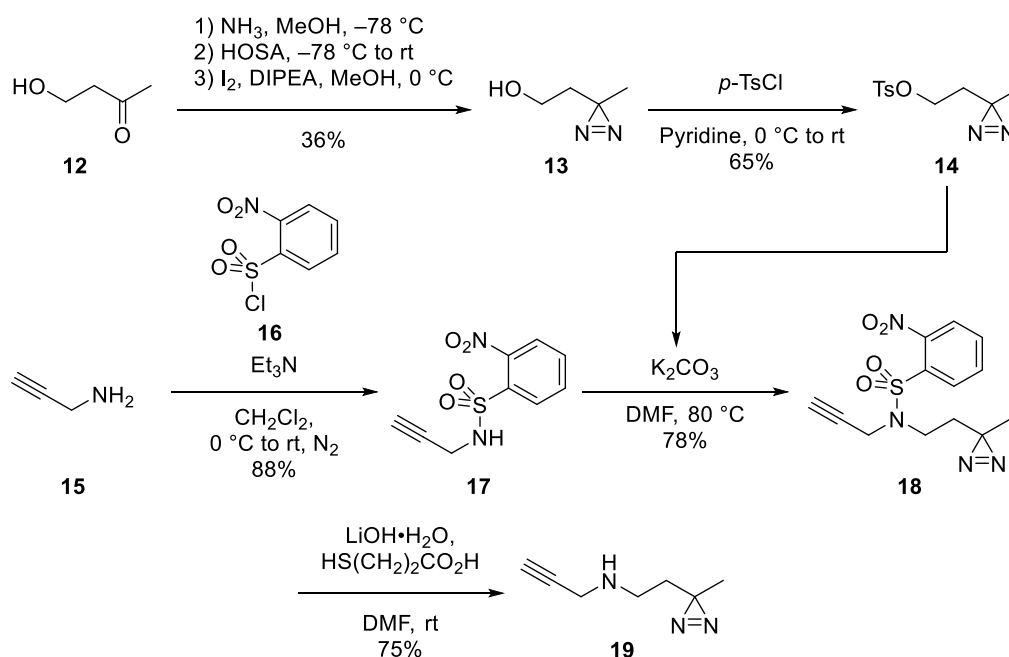


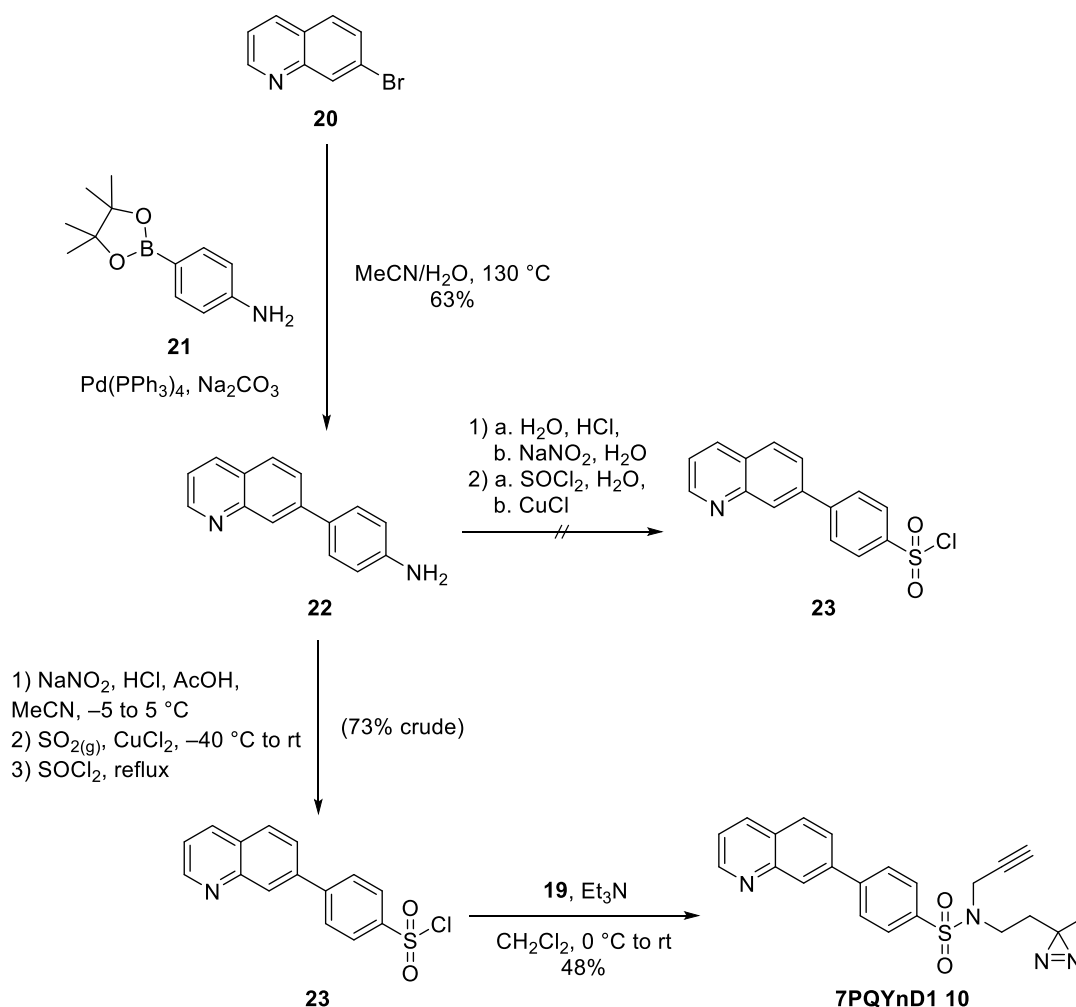
Figure 3.10 Probe designs for 7PQ pharmacophore.

In order to synthesise these probes, it was first necessary to synthesise the minimalist “photoclickable” group, as it was not commercially available. The molecule **19** was synthesised as reported by Kambe *et al.* with few modifications to the original procedure (**Scheme 3.1**).¹⁸² Briefly, 4-hydroxybutanone **12** was diazirinylated (**13**) and tosylated (**14**), then coupled to nosylated propargylamine **17** to generate **18**, which was finally deprotected to generate ~500 mg of the “minimalist photoclickable” group **19** sufficient for the synthesis of both AfBPs.



Scheme 3.1 Synthesis of minimalist “photoclickable” group.

3.3.1.1 Synthesis of 7PQYnD1



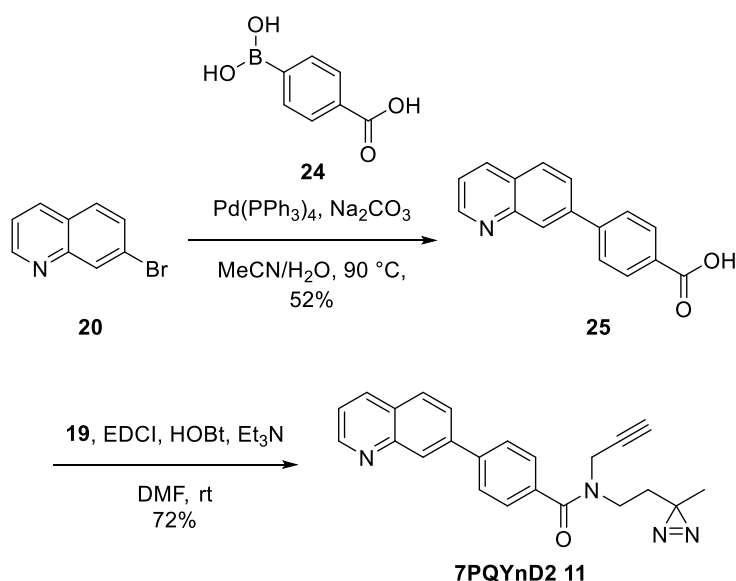
Scheme 3.2 Synthesis of 7PQYnD1. The first attempted Sandmeyer reaction in aqueous conditions failed (hashed arrow); alternative organic conditions (below) yielded the desired sulphonyl chloride necessary for probe synthesis.

With the minimalist group in hand, synthesis of the core of probe 7PQYnD1 was undertaken. The 7PQ core was made by a Suzuki coupling between commercially available 7-bromoquinoline **20** and the corresponding *para*-pinacolborane aniline **21** using a previously reported methodology for similar heteroaromatic substrates (**Scheme 3.2**).⁴⁴⁰ The resulting aromatic amine **22** was then available for diazotisation and displacement via a modified Sandmeyer reaction to incorporate a sulphonyl chloride moiety for transformation to the corresponding sulphonamide.⁴⁴¹ An initial attempt to perform this reaction with the aqueous acidic reaction conditions reported by Hogan and Cox⁴⁴² did not yield the desired product **23**, potentially due to the apparent insolubility of the starting material in H₂O. Using alternative reported conditions with acetic acid as a co-solvent and using gaseous SO₂,^{441,443} a crude version of the product could be isolated that was unstable on silica gel. The crude product was therefore

coupled directly with the minimalist “photoclickable” group **19** (Scheme 3.1) to successfully yield over 100 mg of **7PQYnD1** (**10**).

3.3.1.2 Synthesis of **7PQYnD2**

Synthesis of the amide probe **7PQYnD2** appeared simpler than for **7PQYnD1** since the core structure required for coupling of the “minimalist photoclickable” group could be synthesised in one step (Scheme 3.3). This Suzuki coupling was performed once again with 7-bromoquinoline **20** and boronic acid **24** using the conditions of Gong and Paul,⁴⁴⁴ allowing the pure product **25** to be collected as a precipitate from the reaction mixture after concentration and acidification. Coupling of benzoic acid **25** and minimalist amine **19** (Scheme 3.1) using traditional amide coupling conditions was then attempted.



Scheme 3.3 Attempted synthesis of **7PQYnD2**.

This appeared to generate 58 mg of the amide product **7PQYnD2**, detected as a single, pure spot on thin layer chromatography (TLC). However dissolution of this product in deuterated chloroform for NMR analysis resulted in the apparent and unexpected decomposition of **7PQYnD2**, as demonstrated by the appearance of multiple new spots by TLC (Figure 3.11). When the NMR was analysed, clear broadening of peaks corresponding to several of the aliphatic protons and the aromatic protons *ortho* to the amide linkage was observed (Figure 3.11). Both reaction repetition and chromatographic purification of the fraction corresponding to the desired R_f failed to isolate the pure product. While it was not possible to exclude the possibility of amide rotamers contributing to the broadening of the NMR peaks,⁴⁴⁵ two rotamers could not account for the multiple spots observed by TLC.

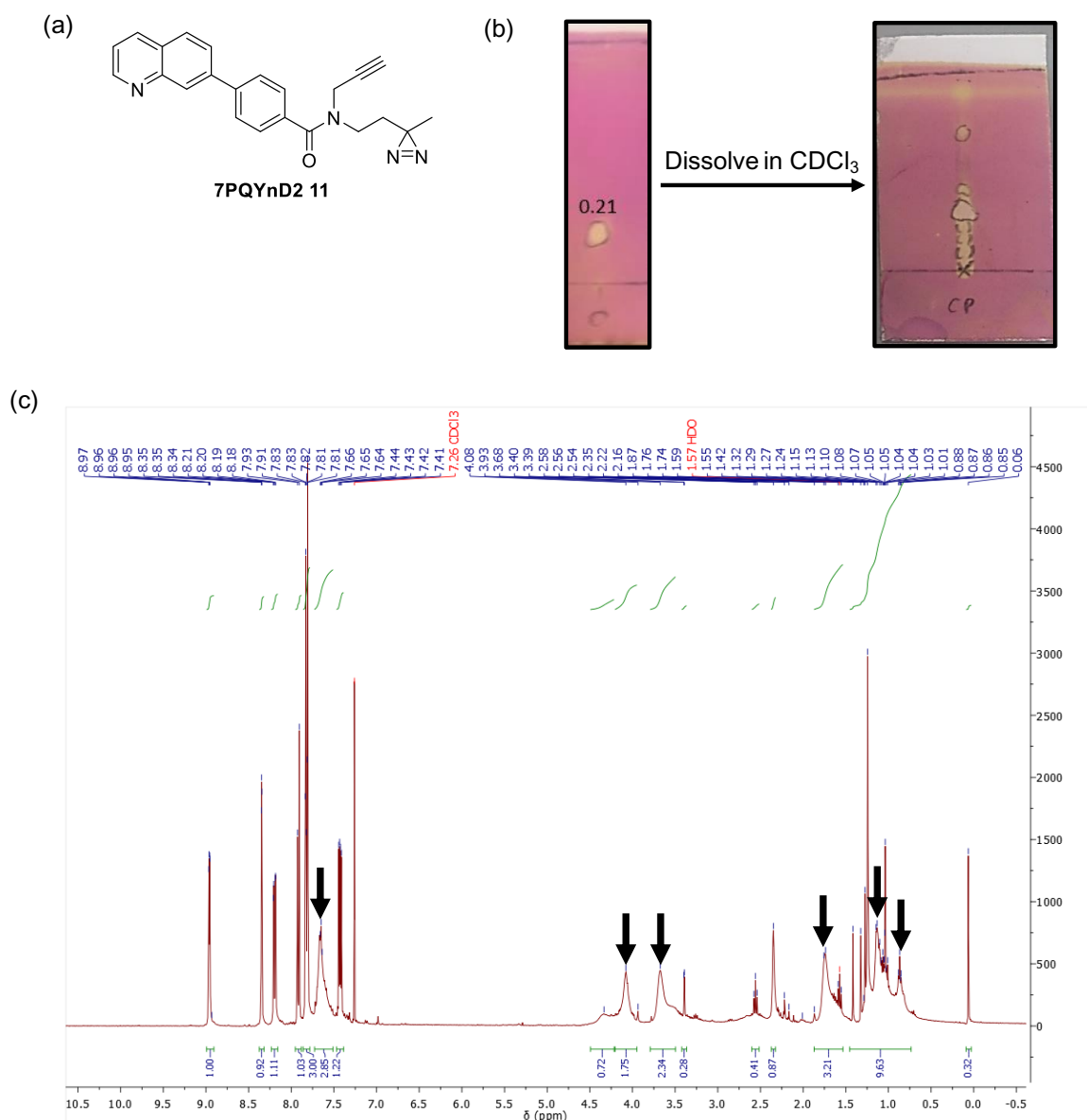


Figure 3.11 Apparent instability of **7PQYnD2**. (a) Structure of **7PQYnD2**. (b) TLC analysis of **7PQYnD2** after immediate isolation from the aqueous work-up (left) and after dissolution in CDCl₃ (right); 10% acetone in CH₂Cl₂. (c) 400 MHz NMR of **7PQYnD2** in CDCl₃, arrows indicate broadened areas of the NMR spectrum.

Unfortunately, further investigation of this unexpected problem was limited by the time constraints of the project, and discovery of the potential instability of **7PQYnD2** raised questions about its utility as a probe intended for a living system. It was therefore decided to continue with **7PQYnD1** as the lead probe.

3.3.2 Probe validation

3.3.2.1 Necroptosis assay development

With **7PQYnD1** now in hand, it was necessary to evaluate its utility as a probe by assessing whether it could inhibit necroptosis in a similar manner to the parent compounds. This required the development of a novel in-house necroptosis assay as no assay to demonstrate the anti-necroptosis activity of a chemical compound was available at Imperial College London.

First, an appropriate cellular system was required. Human *FADD*-deficient (*FADD*^{-/-}) acute T-cell lymphoblastic leukaemia (Jurkat) cells (I2.1) were used by Brito *et al.* in the dose-response necroptosis assay of their HTS campaign (**Figure 3.7**).⁴³⁸ Due to this deficiency in FAS-associated death domain protein (FADD), canonical apoptosis mechanisms are unavailable to these cells and so continuous activation of tumour necrosis factor receptor 1 (TNFR1) results solely in necroptosis (**Figure 3.2**). This is convenient since treatment simply with tumour necrosis factor alpha (TNF α) is sufficient to induce necroptosis without needing to co-treat with cellular inhibitors of apoptosis, therefore these cells were selected as the appropriate biological system.

The recent acquisition of an IncuCyte® S3 Live Cell Analysis System⁴⁴⁶ within the Tate group permitted the use of live-cell fluorescence microscopy in the analysis of cellular necroptosis. While endpoint assays that measure total necroptosis as a single readout at a specific time-point have been used previously to quantify necroptosis, live-cell monitoring in a 96-well plate format allows for analysis of the cellular kinetics of necroptosis across multiple treatment conditions. Combination of fluorescence analysis with phase contrast microscopy further permits the analysis of discrete cellular behaviours not possible through a heterogeneous endpoint assay.

It was also necessary to have a primary assay readout with which the IncuCyte could measure necroptosis. Since I2.1 cells can only undergo necroptosis upon TNFR1 stimulation, any cell death as a result of TNF α treatment was reasoned to be solely attributable to the necroptosis pathway. Therefore, a generic cell viability dye would provide an indirect measure of necroptosis through the cell permeability achieved upon cell death. Sytox™ Green (SG) is a well-validated, cell-impermeable dye that becomes fluorescent ($\lambda_{\text{ex}} = 504 \text{ nm}$, $\lambda_{\text{em}} = 523 \text{ nm}$) when binding to nucleic acids, so only dead or dying cells with leaky membranes emit fluorescence;⁴⁴⁷ SG is also compatible with the fluorescence parameters of the IncuCyte.

3.3.2.1.1 Optimisation of Sytox Green

To determine the appropriate concentrations of SG and TNF α to use, I2.1 cells were seeded in a 96-well plate and incubated overnight before being treated in an array with varying concentrations of SG (0.03–2 μM) along one array axis and varying concentrations of TNF α (0.01–5 nM) along the other

axis. Appropriate untreated (TNF α -) controls were employed to determine the background fluorescence and cytotoxicity of all concentrations of SG. Unstained (SG-) controls and cell permeabilising detergent treatment (Triton X-100) were used to provide minimum and maximum green fluorescence responses respectively: necessary controls for accurate and reproducible image analysis. Wells were imaged once per hour (10 \times zoom, 4 images) over 24 h using both green fluorescence and phase contrast imaging. For each image, the background corrected green integrated fluorescence intensity per image divided by the total phase area per image was plotted as a measure of necroptosis against time and represented as a microplate graph (**Figure 3.12a**).

As expected, increasing both [TNF α] and [SG] gave a higher overall cell death signal. Below 0.13 μ M SG, no necroptosis could be detected, therefore requiring that the assay should use a concentration of SG higher than this. For TNF α , the cell death signal appeared to plateau at concentrations above 0.63 nM (**Figure 3.12a**, columns 8–11). In order to determine which [SG] would be appropriate for future assays, the G_p values (mean \pm SD across all four images per well) at 0.63 nM TNF α for each concentration of SG were all plotted on the same graph against time; wells treated with these concentrations of SG but untreated with respect to TNF α were also plotted to assess background SG cytotoxicity (**Figure 3.12b**).

Once again, cell death signals were enhanced in magnitude with increasing [SG], and this did not correspond to an increase in background cytotoxicity of SG. Extracting the cumulative cell death signal at 0.63 nM TNF α over 24 h for each of these curves (represented by the area under the curve) allowed these data to be represented as a histogram (**Figure 3.12c**). Only moderate background cytotoxicity was attributable to SG across all concentrations of the reagent, each of which could clearly be differentiated from the cell death signal in the corresponding TNF α treated sample. This demonstrated that I2.1 cells were largely unaffected by SG treatment and across SG all concentrations an appreciable signal window was observed. In order to select the optimal SG concentration, it was therefore necessary to assess the ability of each [SG] to facilitate the generation of dose-response relationship data.

The initial necroptosis response demonstrated a linear relationship with time within the first eight hours (**Figure 3.12b**), allowing linear regression to be performed on these data and generating a first order rate constant for the rate of necroptosis in each well. Plotting these values (mean \pm SD across all four images per well) against TNF α concentration for each concentration of SG generated the dose-response profiles seen in **Figure 3.13**.

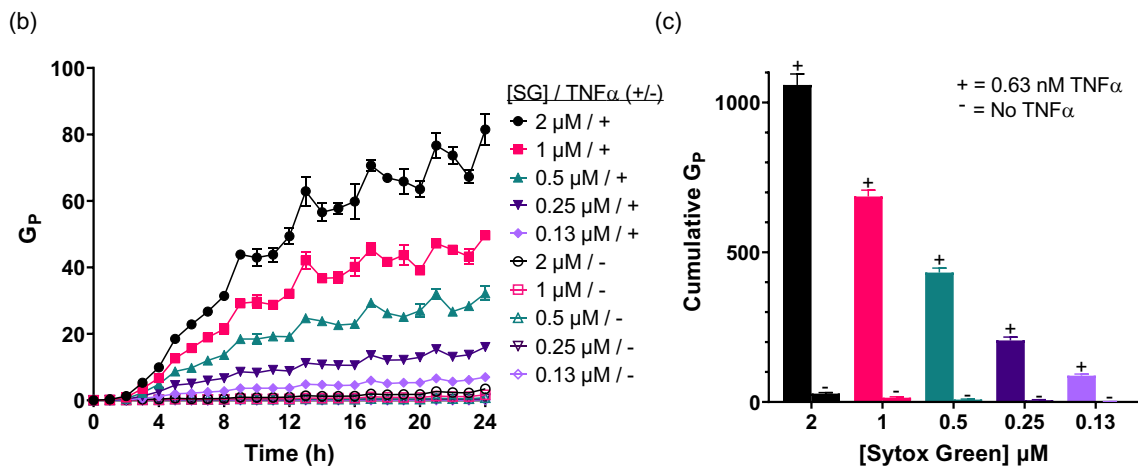
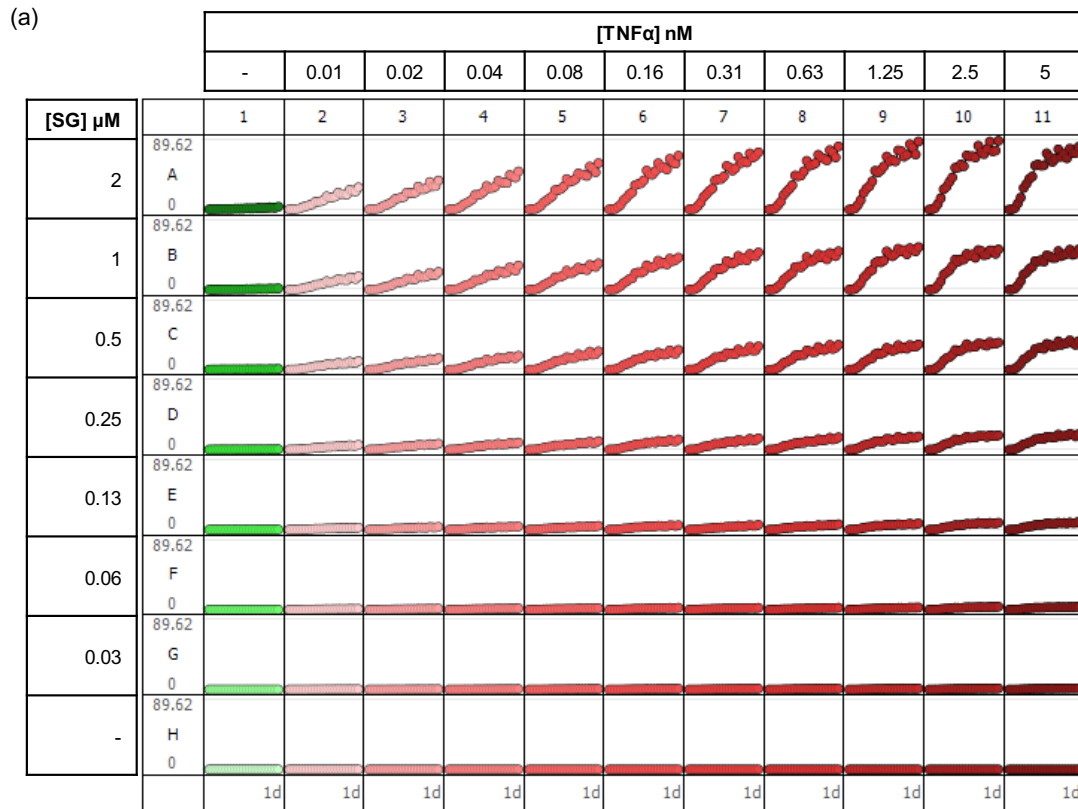


Figure 3.12 Optimisation of Sytox Green treatment in the necroptosis assay. (a) The well of each condition was imaged four times every hour using both green fluorescence and phase contrast imaging over 24 h. The total green integrated fluorescence intensity for each image was divided by the total phase area per image and averaged across the four images. This value was plotted against time for each well to generate a graph for each well. (b) The values for graphs A–E1 and A–E8 were background corrected to time 0 to generate the “G_p” parameter and were plotted \pm SD across four images against time. (c) Cumulative cell death over 24 h was calculated as area under the curve (AUC) values from the graphs of individual images representing the data in (b) and plotted \pm SD as a histogram grouped according to [SG]. SG = Sytox Green, TNF α = Tumour necrosis factor alpha.

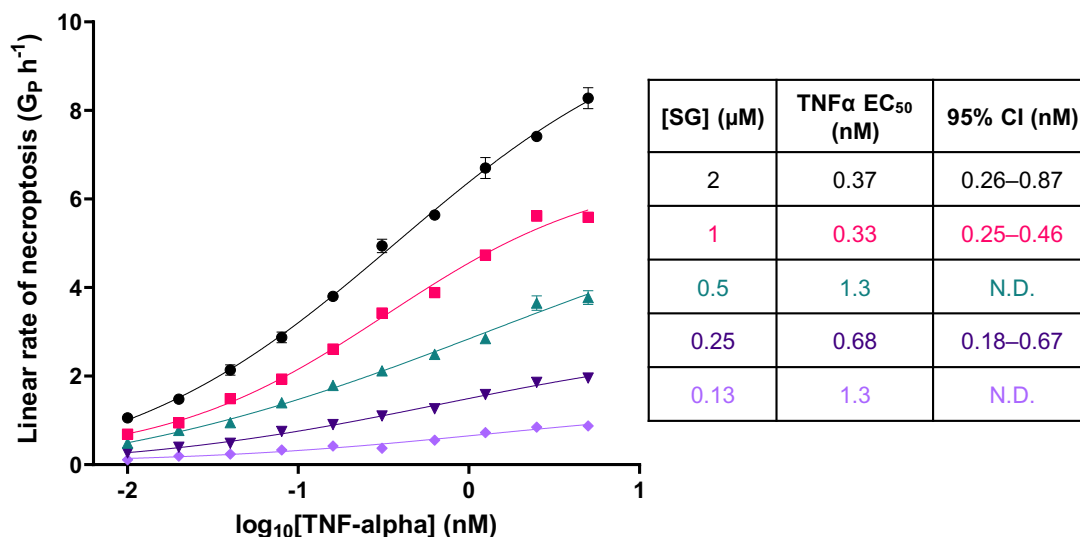


Figure 3.13 TNF α dose-response in necroptosis assay. The well representing each condition was imaged four times every hour using both green fluorescence and phase contrast imaging. The total green integrated fluorescence intensity for each image was divided by the total phase area per image, background corrected to time 0 (G_p), and the rate (slope – $G_p \text{ h}^{-1}$) derived for the linear change in death rate observed within the first 8 h of treatment for each image. The average slope value \pm SD across all four images for each condition was plotted against $\log_{10}[\text{TNF}\alpha]$ for each concentration of SG. The data were fitted to a four-parameter dose-response function generating an EC₅₀ value for TNF α for each [SG] presented along with the 95% confidence interval (CI). N.D. = Not determined, SG = Sytox Green, TNF α = Tumour necrosis factor alpha.

As expected, the absolute change in cell death signal is greater with higher [SG] across each concentration of TNF α as more DNA-binding fluorophore increases the sensitivity of the assay. The data were fit using non-linear regression to a four-parameter dose-response function due to the non-binary relationship between TNF α -binding and the necroptosis response. EC₅₀ values were extracted for all [SG], however due to the linear, non-sigmoidal nature of the curves generated at $[\text{SG}] \leq 0.5 \mu\text{M}$ and the failed interpolation of the 95% confidence intervals (CIs) for some of these curves, it was decided that these were not appropriate [SG] to use in the necroptosis assay. Instead, 1 μM SG appeared to provide an appropriate trade-off between conservation of reagent and ability to extract an EC₅₀ from the dose-response curve.ⁱ

ⁱ At the conclusion of the project, it was discovered that there was significant variability between different batches of SG, and that the trade-off between cytotoxicity and signal-to-noise ratio often varied between batches. For future experiments, care should be taken to monitor and correct for individual SG batch effects.

3.3.2.1.2 Optimisation of TNF α

In order to produce an assay that was able to effectively quantify the inhibition of necroptosis by a chemical antagonist, it was necessary to optimise the concentration of TNF α in the presence of a known inhibitor of necroptosis and assess the ability of the assay to extract dose-response inhibition data. Once again, I2.1 cells were seeded in a 96-well plate and incubated overnight before being treated in an array with varying concentrations of Nec-1 (**Figure 3.4**, 0.16–10 μ M) along one array axis and varying concentrations of TNF α (0.01–5 nM) along the other axis. Green fluorescence and phase contrast images were once again taken for each well every hour (10 \times zoom, 4 images) over 24 h and the resulting G_P parameter plotted against time for each well and represented as a microplate graph (**Figure 3.14a**).

Once again, increased TNF α generated a stronger necroptosis signal, and concentrations of TNF α above 0.16 nM generated an appreciable signal window between maximum Nec-1 treatment (row A) and Nec-1 untreated cells (row H). To further investigate which of the concentrations of TNF α was most suitable to investigate the dose-response inhibition of necroptosis by Nec-1, the linear rate of necroptosis was extracted per well as described in **Section 3.3.2.1.1** and the resulting values (mean \pm SD across all four images per well) plotted against Nec-1 concentration for each concentration of TNF α (**Figure 3.14b**).

These data show again that the signal window of the assay can be increased by increasing [TNF α], however fitting these data as before to a four-parameter dose-response function resulted in EC₅₀ values that were broadly unchanged over 0.31–5 nM TNF α . Therefore, it was envisaged that a 0.6 nM concentration of TNF α would allow conservation of reagent while also providing promising conditions to efficiently extract dose-response necroptosis inhibition data. Furthermore, this concentration of TNF α (0.6 nM \approx 10 ng mL⁻¹) corresponds to concentrations widely reported in other literature necroptosis assays using I2.1 cells, so this appeared to be the optimal choice for this reagent.^{363,438,448}

Finally, to test the reproducibility of these assay conditions, I2.1 cells were plated overnight in 96-well plates and treated in triplicate with a serial dilution of Nec-1, 0.6 nM TNF α , and 1 μ M Sytox Green. The cells were imaged as described above, and the linear rate of necroptosis for each well extracted as previously demonstrated and averaged among technical replicates. This was repeated for three independent biological experiments, and the averaged linear rates from each experiment normalised to the maximum (TNF α and SG treated) and minimum (SG-only treated) necroptosis controls within each plate. These were then averaged and plotted \pm standard error of the mean (SEM) against log₁₀[Nec-1] to generate the dose-response profile in **Figure 3.15**.

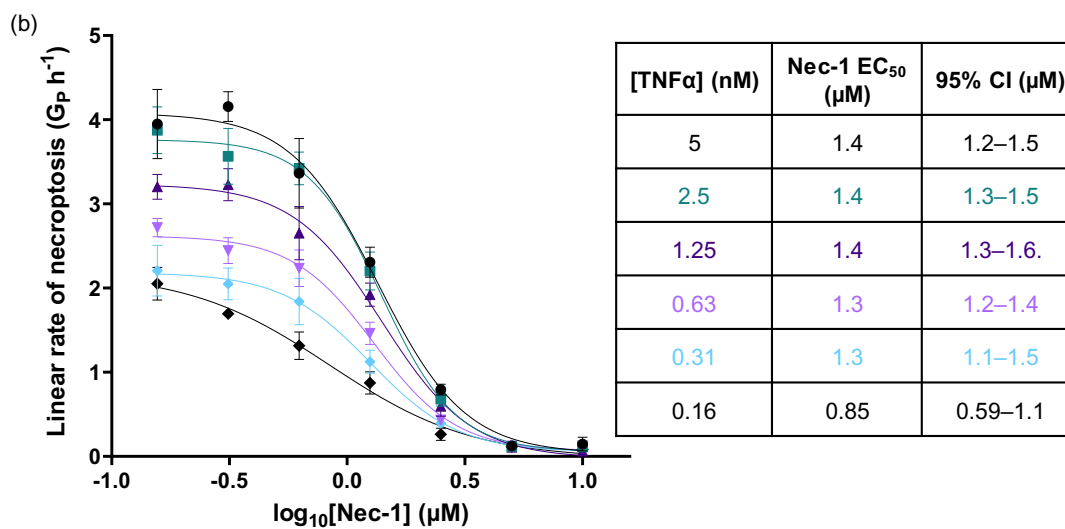
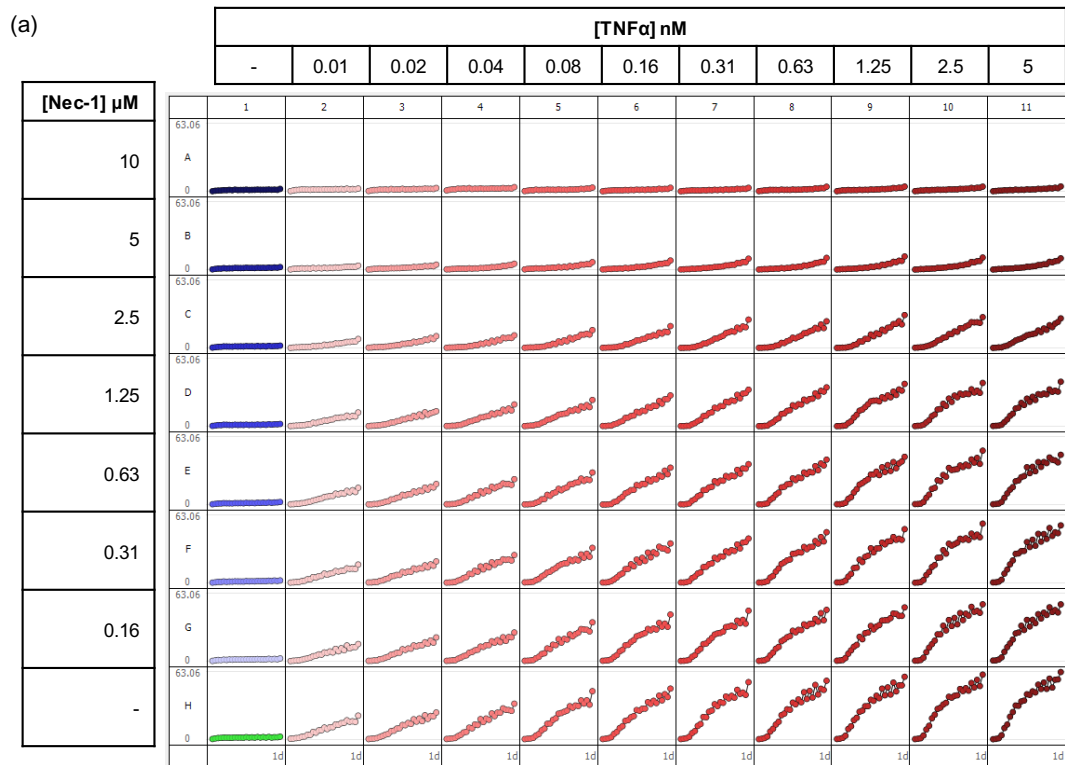


Figure 3.14 Optimisation of TNF α in necroptosis assay. (a) The well of each condition was imaged four times every hour using both green fluorescence and phase contrast imaging. The total green integrated fluorescence intensity for each image was divided by the total phase area per image and averaged across the four images. This value was plotted against time for each well to generate a graph for each well. (b) The values from wells A–G across columns 6–11 in (a) were background corrected to time 0 (G_P), and the rate (slope – $G_P \text{ h}^{-1}$) derived for the linear change in death rate observed within the first 8 h of treatment for each image. The average slope value \pm SD across all four images for each condition was plotted against $\log_{10}[\text{Nec-1}]$ for each concentration of TNF α . The data were fitted to a four-parameter dose-response function generating an EC₅₀ value for Nec-1 for each [TNF α] presented along with the 95% confidence interval (CI). TNF α = Tumour necrosis factor alpha.

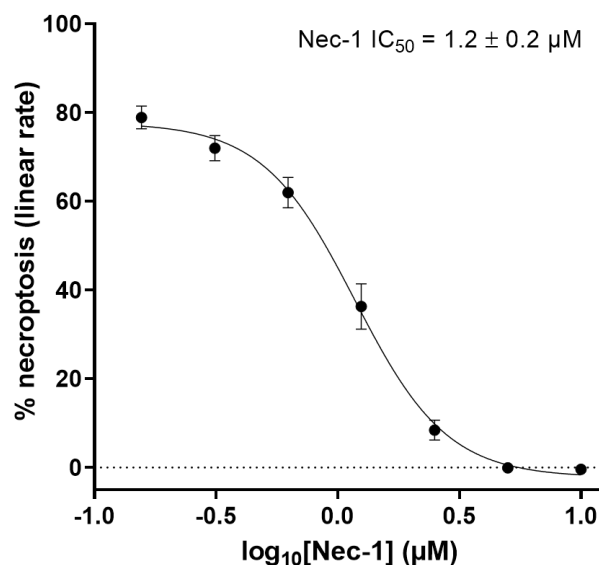


Figure 3.15 Nec-1 inhibition of necroptosis. I2.1 cells were treated in triplicate with indicated concentrations of Nec-1, and with TNF α (0.6 nM) and SG (1 μM). Cells were imaged every hour for 24 h (phase contrast and green fluorescence) and the resulting background corrected G_P values plotted against time for each well. The linear phase of necroptosis was taken from each well and linear regression performed to extract individual slope values that were normalised to the average slopes for TNF α +SG+ wells (100%) and TNF α -/SG+ wells (0%) within each experiment. The normalised linear rates for each compound concentration were averaged within each experiment and plotted \pm SEM of biological replicates (N = 3) against $\log_{10}[\text{Nec-1}]$. The data was fit to a four-parameter dose-response function generating an IC_{50} value for Nec-1 presented \pm 95% CI.

This necroptosis assay was able to reliably extract dose-response inhibition data for necroptosis using an established chemical inhibitor of necroptosis, Nec-1, over several independent experiments. The minimal variability between biological replicates, evidenced by a narrow SEM at each tested concentration and a small 95% CI around the IC_{50} value, demonstrates the reproducibility of this assay. The IC_{50} value presented here is greater than the literature IC_{50} value (0.49 μM), however this kinetic analysis of necroptosis and its inhibition is a novel way of extracting dose-response relationship data compared to the endpoint analysis that is typical of traditional necroptosis assays.³⁴⁸ In order to scrutinise necroptosis inhibition parameters derived from this assay and compare them to those resulting from traditional endpoint assays, a more thorough analysis of established necroptosis inhibitors should be conducted. However, this successfully developed assay was taken forward within the context of this project to evaluate the compounds of the 7PQ pharmacophore series.

3.3.2.1.3 Probe and inhibitor testing

To test the compounds in the newly developed assay, 96-well plates were seeded with I2.1 cells and incubated overnight. Cells were then treated in triplicate with various concentrations of the inhibitor,

vehicle control (DMSO), and with both TNF α and SG. The G_P value for each well was plotted against time and linear regression analysis was performed on the initial linear response as described above. The slope value for each inhibitor concentration was normalised and plotted \pm SD against log₁₀ concentration and fitted to a dose-response curve (**Figure 3.16a**).

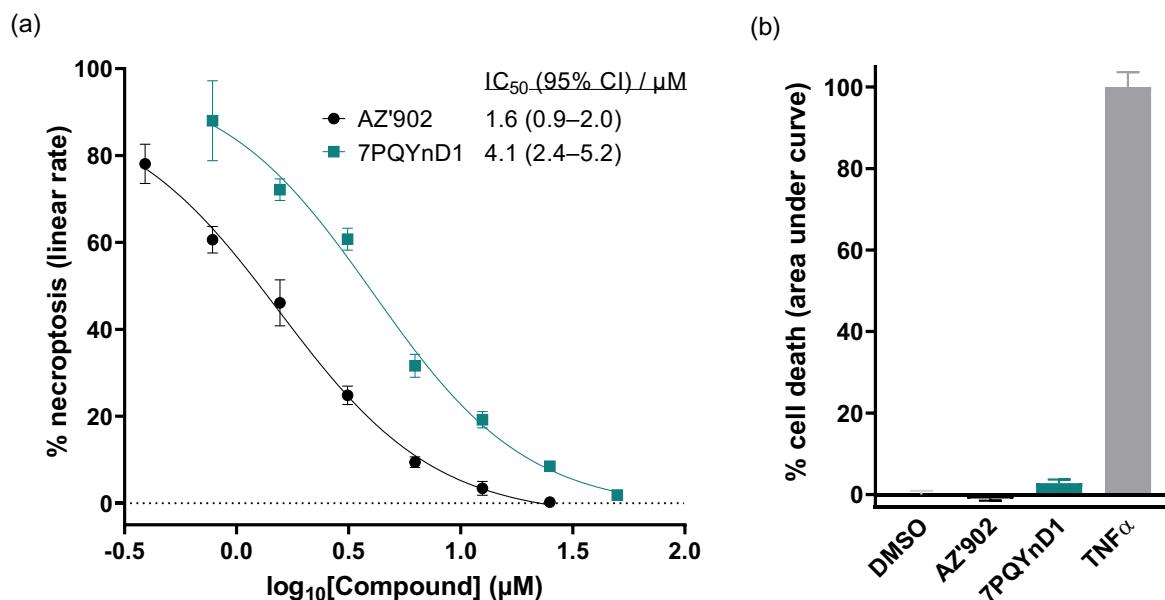


Figure 3.16 Testing of **AZ'902** and **7PQYnD1** in necroptosis assay. I2.1 cells were treated \pm TNF α (0.6 nM), SG (1 μ M) and varying amounts of either **7PQYnD1** or **AZ'902**. Cells were imaged every hour for 24 h (green/phase) and the resulting background corrected G_P values plotted against time for each well. (a) Necroptosis assay – the linear phase of necroptosis was taken from each well and linear regression performed to extract individual slope values that were normalised to the average slopes for TNF α +/SG+ wells (100%) and TNF α -/SG+ wells (0%). The normalised slope values were plotted \pm SD of technical replicates against log₁₀ compound concentration. The data were fitted to a four-parameter dose-response function generating IC₅₀ values presented alongside the associated 95% CI. (b) Cytotoxicity assay – cumulative necroptosis over 24 h was extracted as AUC values for each well treatment and normalised to the average AUC for TNF α +/SG+ wells (100%) and TNF α -/SG+ wells (0%). The normalised AUC values were plotted \pm SD of technical replicates as a histogram. Compound treatments refer to maximum concentrations used in necroptosis assays: **AZ'902** = 25 μ M, **7PQYnD1** = 50 μ M.

It could be demonstrated that both **7PQYnD1** and the parent compound **AZ'902** inhibited necroptosis in a dose-dependent fashion. The IC₅₀ value determined for **AZ'902** of 1.6 μ M (95% CI: 0.9–2.0 μ M) aligned well with the IC₅₀ value of 1.29 μ M from the original HTS campaign in murine fibrosarcoma cells. This provided confidence that this novel assay was able to recapitulate results from necroptosis assays performed in Lisbon, however analysis of further compounds and biological replicates would allow more effective comparisons between the values derived from this assay and the assay developed by Brito *et al.*, representing further work for this project.

Nonetheless, the probe **7PQYnD1** was also tested and found to inhibit necroptosis with an IC_{50} of 4.1 μ M (95% confidence interval: 2.4–5.2 μ M). While this was less potent than **AZ'902**, it was still within the 1–10 μ M range of EC_{50} values displayed by members of the 7PQ series (**Figure 3.9**). Given that all members of the series are assumed to inhibit necroptosis via the same molecular mechanism of action, the ability of **7PQYnD1** to inhibit necroptosis suggested that it was able to bind to the same biomolecular substrates as the rest of the series *in situ* and would be an effective AfBP.

In the same assay, it was also possible to assess whether the compounds were cytotoxic to I2.1 cells over 24 h of treatment. For I2.1 cells treated with maximal concentrations of each compound but not treated with $TNF\alpha$, the G_p value for each well was once again plotted against time and this time the AUC values for each graph were extracted. The values were normalised to 0% (DMSO) and 100% ($TNF\alpha$) cell death and plotted \pm SD alongside the normalisation controls (**Figure 3.16b**). It could be shown that over the course of 24 h of treatment, neither compound caused significant excess cell death that would antagonise their cytoprotective effect. This also demonstrated that I2.1 cells could tolerate treatment of these compounds for at least 24 h and could be confidently used in future cell-based experiments.

3.3.2.2 Optimisation of photocrosslinking

Having shown that **7PQYnD1** is active against necroptosis, it was next necessary to assess its ability to label proteins in live cells. While activity in the above cell-based assay is suggestive of **7PQYnD1** being cell permeable, it cannot be ruled out that the probe and the parent molecules exert their biomolecular effect by binding to a substrate on the cell surface. In order to assess both the cell permeability of **7PQYnD1**, and to find the optimal conditions for cellular protein labelling, preliminary photocrosslinking experiments were undertaken.

I2.1 cells were treated with varying concentrations of **7PQYnD1** for 3 h or 24 h. The cells were either irradiated with 365 nm UV light or kept in the dark, washed and lysed, and the tagged proteins ligated to azide-TAMRA-biotin (AzTB, **Figure 1.7**) via a copper(I)-catalysed azide-alkyne cycloaddition (CuAAC) reaction. The proteins were separated by polyacrylamide gel electrophoresis and the gel scanned for TAMRA fluorescence to highlight the labelled protein bands (**Figure 3.17**).

It can be seen for both incubation times that the probe is able to label several protein bands with labelling only observed in the UV-irradiated samples, indicating that the probe does not participate in background labelling reactions through some unanticipated covalent reactivity. The alkyne group was able to successfully ligate the tagged proteins to the reporter molecule, and background labelling of the reporter in the click reaction (vehicle treated lanes) is low and in line with previously published data for AzTB.^{30,159,334} In both cases, probe labelling showed a dose-dependent relationship, indicating that the

extent of labelling is proportional to the concentration of **7PQYnD1** and this labelling appeared to saturate around 5 μM . Incubation for 24 h over 3 h did not appear to dramatically alter the labelling profile, therefore it was deemed that 3 h was sufficient to achieve adequate probe labelling.

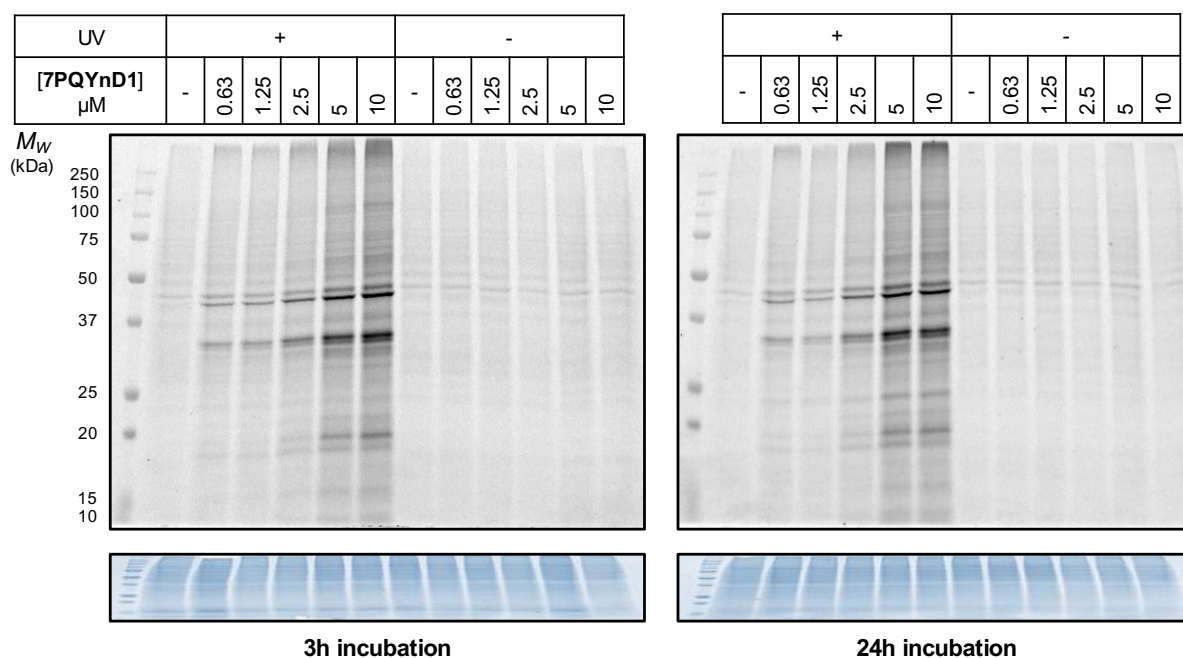


Figure 3.17 Optimisation of **7PQYnD1** photocrosslinking in I2.1 cells. Cells were treated with **7PQYnD1** as shown for 3 h (left) or 24 h (right), irradiated, lysed and clicked to AzTB. Top: TAMRA fluorescence, bottom: Coomassie Brilliant Blue (CBB) staining (protein loading).

3.3.3 Target profiling

3.3.3.1 In-gel fluorescence

Probe **7PQYnD1** inhibits necroptosis within the same range of potency as the parent compounds and displays dose- and UV-dependent protein labelling in live cells. This suggests that **7PQYnD1** is an effective tool molecule with which to interrogate the protein profile of the 7PQ series of anti-necroptosis compounds. Chemical proteomics techniques are required to identify the probe-labelled proteins, however it was first necessary to perform simpler gel-based competition analysis (**Figure 1.8**) to determine the optimal concentrations of both probe and parent compound before undertaking more complex proteomics experiments.

I2.1 cells were once again treated with DMSO vehicle, **7PQYnD1**, or **7PQYnD1** and parent compound **AZ'902** (**Figure 3.9**) at various concentrations for 3 h. 2.5 μM was selected as the highest **7PQYnD1** concentration as optimisations in **Figure 3.17** demonstrated labelling of all available bands without achieving full saturation, giving competition with the parent compound the best chance of demonstrating dose-dependent reduction in band labelling. 1 h before irradiation, cells were treated

either with TNF α or vehicle control to assess any difference in the labelling profile upon induction of necroptosis. Cells were irradiated with 365 nm UV light, washed and lysed, and the tagged proteins ligated to AzTB via a CuAAC reaction and analysed by in-gel fluorescence (**Figure 3.18**).

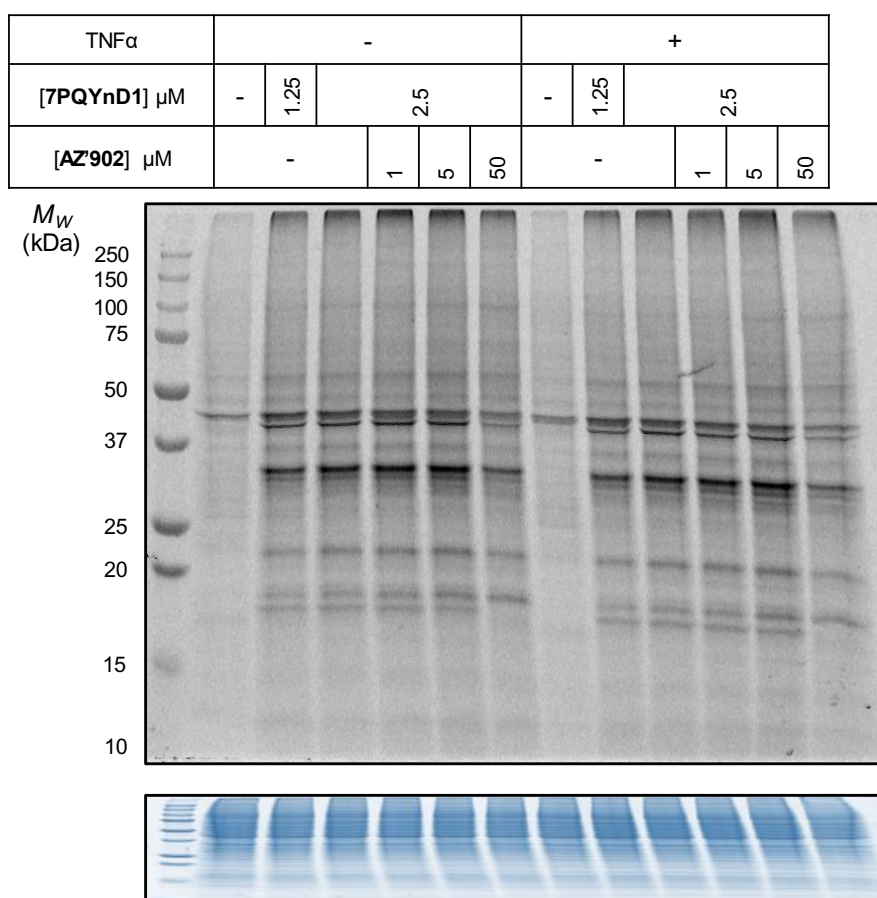


Figure 3.18 Competition profile of **7PQYnD1** by in-gel fluorescence. I2.1 cells were treated as indicated, irradiated, lysed and tagged proteins were ligated to AzTB. Top: TAMRA fluorescence, bottom: CBB staining.

As before, **7PQYnD1** was able to label proteins in a dose-dependent manner (lanes 1–3 and 7–9). At the highest concentration of parent compound **AZ'902** (lanes 6 and 12), loss of labelling of several protein bands could be observed, indicating that the probe was likely labelling the same protein targets as the parent compounds, and this could be assessed through competition experiments. Surprisingly, no difference in band labelling could be seen upon induction of necroptosis (lanes 7–12 versus 1–6), indicating potentially that the protein target responsible for anti-necroptosis activity may be present and druggable in cells regardless of whether necroptosis had been induced. However, it could not be ruled out that some protein labelling is undetectable by gel-based methods, either due to low expression levels or poor resolution by gel electrophoresis. Nevertheless, the positive result in this competition experiment provided confidence that proteomics experiments to identify true protein targets of the 7PQ series would yield useful results.

3.3.3.2 Chemical proteomics

With the generation of stable isotope-labelled cell lines being a costly and arduous task, two quantification methodologies remain available to perform chemical proteomics experiments with **7PQYnD1**, namely label free quantification (LFQ) and tandem mass tag (TMT) labelling. As discussed in **Section 1.4.2.3**, LFQ is the cheaper and simpler option and has a greater dynamic range owing to the analysis of one sample at a time. TMT labelling on the other hand is more costly, and sample multiplexing increases complexity, however it also reduces inter-sample variation and increases sensitivity towards lower abundance proteins.^{217,218} Therefore, LFQ proteomics was chosen to perform pilot experiments to assess probe labelling and quantification, and TMT labelling was envisaged as a follow-up experiment to more thoroughly analyse the labelled proteome once initial conditions had been optimised. Together, these experiments assisted in the identification of key compound-protein interactions that are potentially responsible for the anti-necroptosis activity of these compounds

3.3.3.2.1 Label-free quantification

For LFQ proteomics experiments, I2.1 cells were treated in triplicate with vehicle (DMSO), **7PQYnD1** (1 μ M, 2.5 μ M), or co-treated with **7PQYnD1** (1 μ M) and 10 \times parent compound **AZ'902** (10 μ M). Necroptosis was induced at least 1 h before dishes were irradiated with 365 nm UV light, and cells were washed, lysed and the tagged proteins ligated to azide-arginine-biotin (AzRB, **Figure 1.7**) via CuAAC. The biotin-labelled proteome was enriched over NeutrAvidin beads, reduced and alkylated, and digested on-bead into peptides with trypsin. The peptides were desalted and analysed by nanoLC-MS/MS to identify and quantify the proteins present in each sample. Pairwise comparisons between LFQ ion intensities in separate triplicate conditions were performed to highlight the proteins with significant changes in abundance across samples, represented by the volcano plots presented in **Figure 3.19**.

Only three proteins were significantly enriched at either probe concentration (**Figure 3.19a–b**), which is surprising since at least seven protein bands can be clearly identified by gel-based analysis (**Figure 3.18**). Nonetheless, all three enriched proteins exhibit a dose-dependent profile with **7PQYnD1** treatment as demonstrated by the rightward shift in the fold change for all hits upon increasing the probe concentration. Two of these proteins were voltage dependent anion-gated channels 1 and 2 (VDAC1, VDAC2), which as previously highlighted in **Section 2.3.4.2.1** are known background binders of diazirine-containing AfBPs,¹¹⁷ and suggested **7PQYnD1** was entering cells and photocrosslinking to proteins in a predictable manner. The remaining protein, adenosine deaminase (ADA), is an enzyme involved in purine nucleotide metabolism and potentially represents a novel target for the 7PQ class of compounds. Unfortunately, no competition could be observed at 1 μ M **7PQYnD1** with 10 \times parent

compound **AZ'902** (Figure 3.19c) for any of the proteins, though this would be expected of the background binders VDAC1/2.

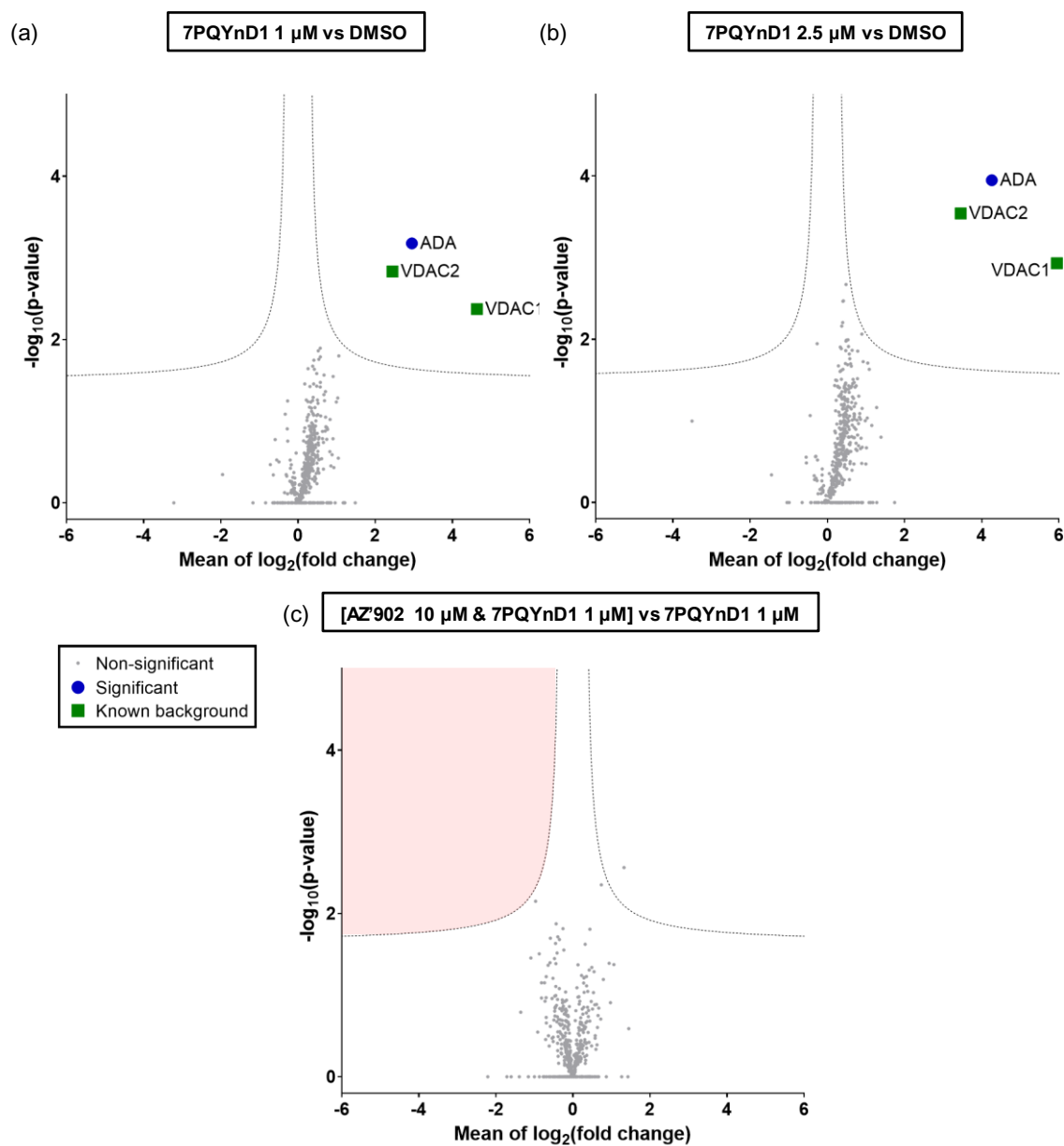


Figure 3.19 Label-free quantification target profiling of **7PQYnD1** and **AZ'902**. I2.1 cells were treated in triplicate with DMSO, **7PQYnD1** (1 μ M, 2.5 μ M) or co-treated with **7PQYnD1** (1 μ M) and **AZ'902** (10 μ M). Cells were treated with TNF α , irradiated, lysed and the tagged proteins clicked to AzRB. Proteins were enriched on NeutrAvidin agarose, digested into peptides, and analysed by LC-MS/MS. Volcano plots demonstrate enrichment (x axis) between (a) 1 μ M **7PQYnD1** and DMSO samples, (b) 2.5 μ M **7PQYnD1** and DMSO samples, and (c) 10 μ M **AZ'902**/1 μ M **7PQYnD1** versus 1 μ M **7PQYnD1** samples. The associated significance (y axis) was determined by pairwise Student's t-test (cut offs: $S_0 = 0.1$, false discovery rate (FDR) = 5%). Red area in (c) represents the area in which significantly competed proteins would be expected to be found.

One of the limitations of LFQ-based analysis of affinity-enrichment experiments is that proteins clearly detectable in the LC-MS/MS runs of probe-enriched samples may not be detected at all in vehicle or competitor-treated samples. This means the proteins' LFQ intensity values in these samples will be missing and the corresponding fold change between samples cannot be calculated. To replace these missing values, it is possible to perform imputation analysis that assigns each missing value a random LFQ intensity from the normal distribution of valid values across the whole matrix.⁴⁴⁹ Since missing values are often representative of low abundance measurements, values are chosen to reflect this, however it is important to remember that such values are not real when drawing conclusions from data analysed from these numbers. Nonetheless, in order to salvage further information from this LFQ experiment, imputation analysis was performed on these data and volcano plots were once again generated to represent statistically significant changes in protein abundances across samples (**Figure 3.20**).

Imputation resulted in replacement of the missing values with low LFQ intensity values as demonstrated by the histogram in **Figure 3.20d**. Replacing these missing values resulted in a greater number of significantly enriched hits for **7PQYnD1**, more in-line with the gel labelling profile observed in **Figure 3.18**. Further background diazirine binders such as delta(3,5)-delta(2,4)-dienoyl-CoA isomerase, mitochondrial (ECH1) and cathepsin D (CTSD) are now detectable in the 2.5 μM **7PQYnD1** versus DMSO comparison, suggesting that imputation of the missing values has recovered some potentially significant data. Several more potential novel targets of the 7PQ series can also be seen in **Figure 3.20b**, however only one of these proteins, squalene synthase (FDFT1) was found to be significantly depleted in the competition volcano plot (**Figure 3.20c**).

Displaying the averaged LFQ intensities of all significant hits in **Figure 3.20a–b** across DMSO, **7PQYnD1** (1 μM) and **7PQYnD1** (1 μM)/**AZ'902** (10 μM) treated samples as a heat map revealed smaller perturbations in competitive depletion of probe labelling that were lost by the cut-offs imposed by t-test analysis (**Figure 3.21**). The averaged intensities were background corrected to a uniform DMSO LFQ intensity and, since not all hits from **Figure 3.20a–b** displayed sensible labelling patterns across the four total conditions, these were excluded from the heat map. Those that did display sensible labelling are depicted in **Figure 3.21**. They include protein populations that are unchanged upon co-treatment with the parent compound (non-competed), which is expected for known background proteins such as VDAC1/2 and ECH1. Also in this category are the cell surface complex protein and T-cell marker: T-cell surface glycoprotein CD3 epsilon chain (CD3 ϵ), and citric acid cycle enzyme isocitrate dehydrogenase [NADP], mitochondrial (IDH2). While these proteins are non-competed, it is possible higher concentrations of **AZ'902** are required to observe significant depletion of probe labelling. Proteins that did exhibit depleted labelling upon **AZ'902** treatment (competed) include ADA and

FDFT1, and also sterol biosynthesis enzyme delta(14)-sterol reductase (LBR). Putative oxidoreductase saccharopine dehydrogenase-like oxidoreductase (SCCPDH) was also tentatively included, however the LFQ intensity of SCCPDH in the parent-competed samples was unusually lower than in vehicle treated samples.

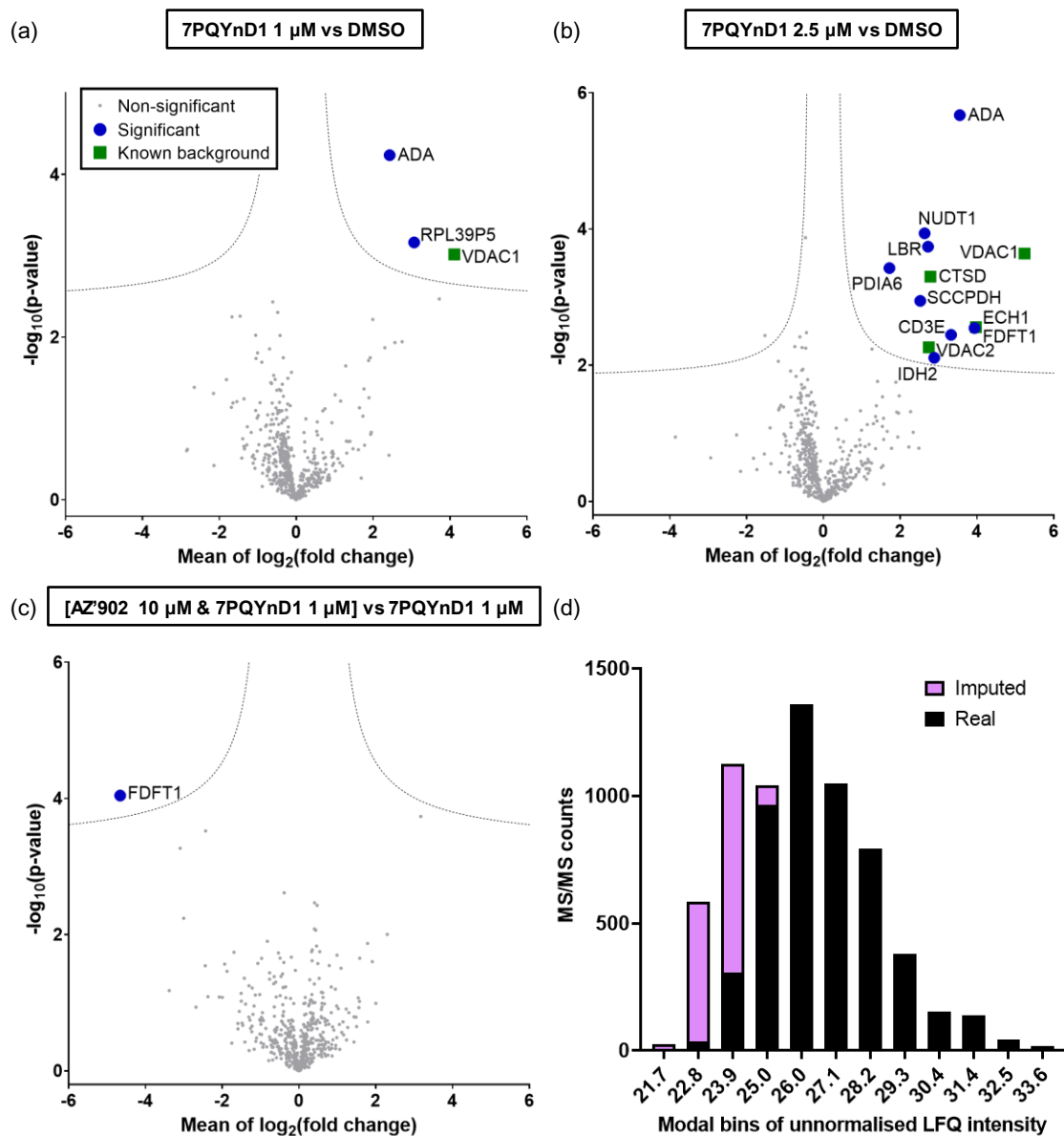


Figure 3.20 Label-free quantification target profiling of **7PQYnD1** and **AZ'902** with missing values imputed. Averaged LFQ intensities were collected as described in **Figure 3.19**, however additionally, missing LFQ intensity values were imputed from the normal distribution of valid values across the whole matrix. (a–c) Volcano plots demonstrate enrichment (x axis) between (a) 1 μM **7PQYnD1** and DMSO samples, (b) 2.5 μM **7PQYnD1** and DMSO samples, and (c) 10 μM **AZ'902**/1 μM **7PQYnD1** versus 1 μM **7PQYnD1** samples. The associated significance (y axis) was determined by pairwise Student's t-test (cut offs: $S_0 = 0.1$, FDR = 10%). (d) Histogram demonstrating the position in the normal distribution of LFQ intensities that imputed values were generated from.

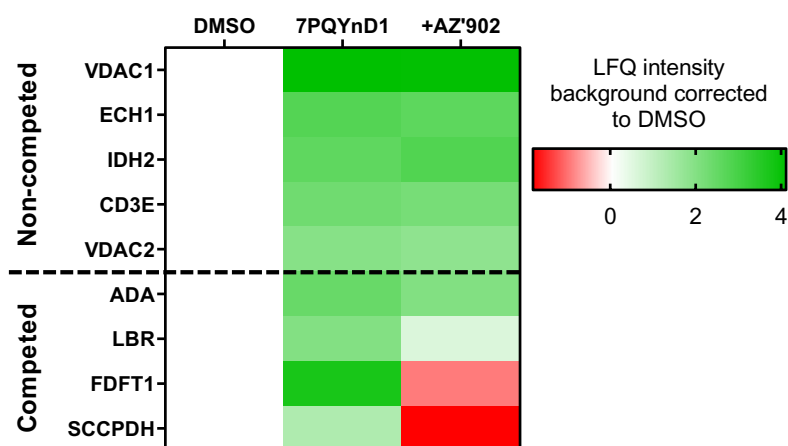


Figure 3.21 Heat map of key proteins identified through LFQ proteomic profiling of **7PQYnD1**. Averaged LFQ intensities were collected from experiments described in **Figure 3.20**. Proteins significantly enriched in **Figure 3.20a–b** with sensible labelling patterns across all conditions were background corrected to their DMSO value and displayed in the heat map. Top: unchanged upon **AZ'902** treatment (non-competed); bottom: depleted upon **AZ'902** treatment (competed).

While these data begin to highlight proteins that may be true targets of the 7PQ class of compounds, many of the values are imputed, and therefore not real. Furthermore, exhibition of a dose-dependent relationship in competitive AfBPP would provide more confidence in the assignment of proteins as real targets of the molecules. With this in mind, the data generated in these pilot LFQ experiments laid the foundation for more in-depth experiments by TMT labelling.

3.3.3.2.2 Tandem mass tag quantification

TMT proteomics is more costly than LFQ experiments, mainly due to the cost of the labelling reagents themselves, however labelling each sample condition with a unique isobaric tag allows the multiplexing of several sample conditions in to one LC-MS/MS run, saving on both equipment running costs and time.²¹³ Furthermore, the LFQ analysis above suffered from missing values in the analysis of DMSO- and competitor-treated conditions as a result of peptide MS¹ intensities not reaching the detection threshold in these channels. Multiplexing in TMT-based analysis mitigates this problem as quantification of peptides across different conditions is performed at the MS²-level by measurement of TMT reporter ion intensities.²¹⁸ This means that even if very few peptides of a particular protein are present in, for example, vehicle-treated samples, they will co-elute and be detected with the much larger proportion of corresponding peptides present in the probe-treated sample(s), and their reporter ion intensities will be detected and recorded, reducing the number of missing values.

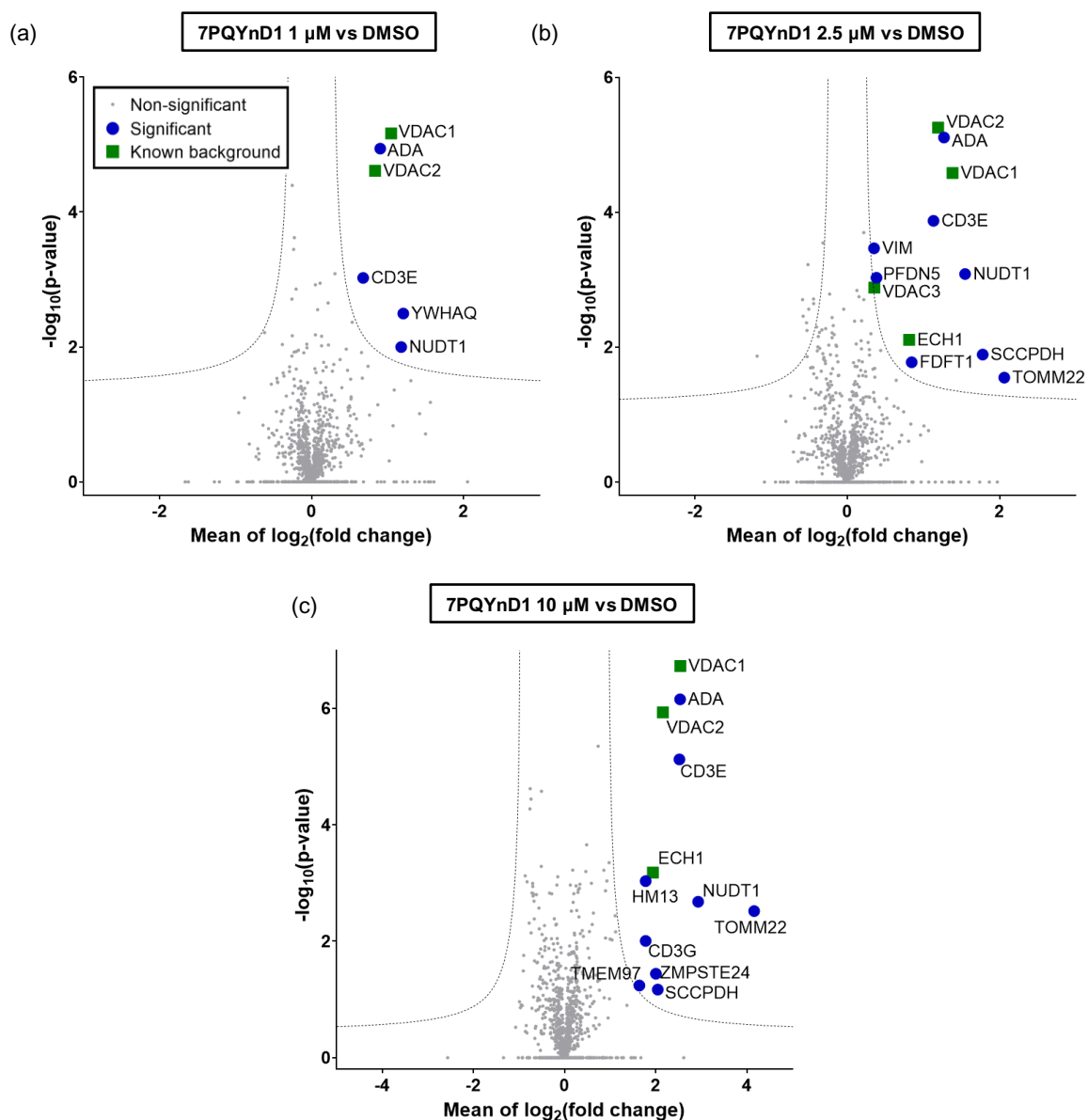


Figure 3.22 Tandem mass tag target profiling of **7PQYnD1**. I2.1 cells were treated in triplicate with **7PQYnD1** (1 μ M, 2.5 μ M, 10 μ M) or DMSO. Cells were treated with TNF α , irradiated, lysed and tagged proteins clicked to AzRB. Proteins were enriched on NeutrAvidin agarose, digested into peptides, and TMT labelled for analysis by LC-MS/MS. Volcano plots demonstrate enrichment (x axis) between (a) 1 μ M **7PQYnD1** and DMSO samples, (b) 2.5 μ M **7PQYnD1** and DMSO samples, and (c) 10 μ M **7PQYnD1** and DMSO samples. The associated significance (y axis) was determined by pairwise Student's t-test (cut offs: $S_0 = 0.1$, FDR = 5%).

For TMT-based proteomics experiments (**Figure 3.22**), I2.1 cells were once again treated in triplicate with vehicle (DMSO), **7PQYnD1** (1 μ M, 2.5 μ M, 10 μ M), or co-treated with **7PQYnD1** (2.5 μ M) and parent compound **AZ'902** (2.5 μ M, 10 μ M, 50 μ M). Necroptosis was induced at least 1 h before dishes were irradiated with 365 nm UV light, and cells were washed, lysed and the tagged proteins ligated to AzRB via CuAAC. The biotin-labelled proteome was enriched over NeutrAvidin beads, reduced and

alkylated, and digested on-bead into peptides with trypsin. The peptides were TMT labelled, combined appropriately, fractionated three times to reduce sample complexity and analysed by nanoLC-MS/MS. Pairwise comparisons between TMT reporter ion intensities in the probe-treated samples versus DMSO-treated samples generated the volcano plots in **Figure 3.22**.

Across these comparisons, many more significantly enriched proteins are found in the probe-enriched samples than found in LFQ experiments, even when considering those found after imputation of missing values, reinforcing that TMT analysis can detect more statistically significant changes in protein enrichment than LFQ. However, the fold change values of proteins calculated between different sample conditions is different in TMT analysis; ADA for example exhibits a $\log_2(\text{fold change})$ of ~ 4 (fold change = 16) with 2.5 μM probe enrichment compared to DMSO in LFQ data (**Figure 3.18b**) compared to a suppressed $\log_2(\text{fold change})$ of < 2 (fold change = < 4) for similar treatments in TMT data (**Figure 3.22b**). This is likely due to ratio compression experienced by TMT-labelling as discussed in **Section 1.4.2.3**, meaning the fold-change values obtained through all TMT-based experiments herein are likely underestimations.

Nonetheless, expected diazirine binders VDAC1/2 and ECH1 were identified, along with newly identified VDAC3, another known background protein.¹¹⁷ The remainder of the proteins identified in these volcano plots include potential hits identified in LFQ experiments including ADA, CD3 ϵ , FDFT1 and SCCPDH, reinforcing that these proteins may be targets of the 7PQ series. The other hits represent potentially novel target proteins for these molecules, however analysis of the competitor treated samples was necessary to confirm each protein as a true target.

Given that this experiment was performed with three concentrations of parent molecule at co-treated with 2.5 μM **7PQYnD1**, it was possible to generate a more comprehensive heat map for these data that would be able to reveal any dose-dependent depletion of probe labelling upon competitor treatment. Once again, all significant hits from the volcano plots in **Figure 3.22** were analysed individually for a sensible labelling patterns across replicates and conditions, and those with anomalous behaviours were excluded. The remaining TMT reporter values were averaged within replicates, background corrected to DMSO and displayed as a heat map in **Figure 3.23**.

From this analysis, thirteen proteins show clear dose-dependent enrichment over increasing probe concentrations. Three of these are the known background proteins VDAC1/2 and ECH1 and remain non-competed by parent molecule **AZ'902**. Five proteins clearly exhibit competition: FDFT1 and a newly identified protein, sigma intracellular receptor 2 (TMEM97) exhibit a clear dose-dependent depletion with **AZ'902** treatment starting from the lowest concentration of 2.5 μM . SCCPDH is also

competed from 10 μM **AZ'902**, and CD3 ϵ (previously non-competed in the LFQ experiments) and ADA are both depleted at the highest concentration of 50 μM parent molecule.

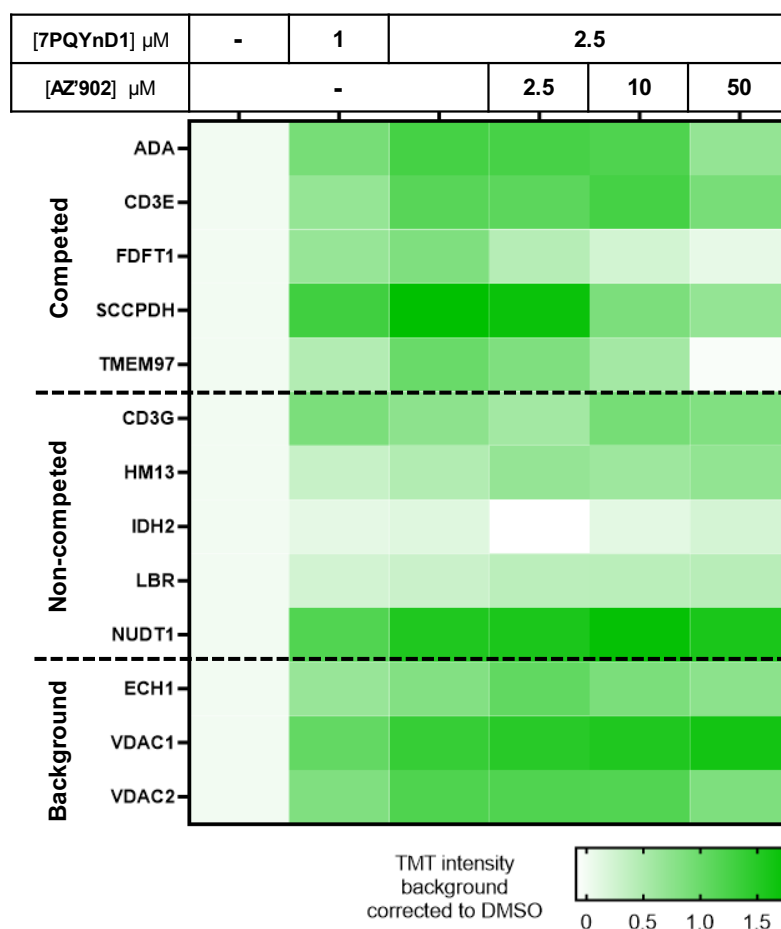


Figure 3.23 Heat map of key proteins identified through TMT proteomic profiling of **7PQYnD1**. Averaged TMT reporter ion intensities were collected in experiments described in **Figure 3.22**. Proteins significantly enriched in **Figure 3.22** with sensible labelling patterns across all conditions were background corrected to their DMSO value and displayed in the heat map. Top: depleted upon **AZ'902** treatment (competed); middle: unchanged upon **AZ'902** treatment (non-competed); bottom: unchanged upon **AZ'902** treatment and known as a diazirine binder (background).

The remaining protein hits enriched by **7PQYnD1** appeared not to be depleted by parent compound treatment. These include protein hit T-cell surface glycoprotein CD3 gamma chain (CD3 γ) which may be enriched as a result of it being in the same membrane complex as CD3 ϵ ,⁴⁵⁰ for which there is more robust evidence of enrichment and competition in this data. LBR, previously shown to be competed in LFQ experiments, shows no evidence of depletion and IDH2 also remains non-competed at the highest concentrations of **AZ'902** as in the LFQ experiments. Two newly non-competed hits were also identified: 7,8-dihydro-8-oxoguanine triphosphatase (NUDT1), involved in the recycling of oxidised

nucleotide triphosphates, and minor histocompatibility antigen H13 (HM13), a proteolytic enzyme involved in signal transduction. As previously highlighted, these proteins may require higher concentrations of parent compound to effectively compete against **7PQYnD1**. Alternatively, they may represent interactions unique to the probe's overall structure that are not shared by the parent molecule and would therefore be irrelevant to the target profile of the 7PQ series. Further experiments with higher concentrations of **AZ'902** and with different parent molecules represent future work to resolve the status of these non-competed hits. Nonetheless, the five competed hits (**Figure 3.23**) are the most promising candidates responsible for the anti-necroptosis activity of the 7PQ series, and were taken forward to target validation studies.

3.3.4 Target validation

With several protein hits identified in the proteomics experiment, it was next necessary to validate both the probe-based enrichment of the individual proteins and their corresponding competition in an orthogonal experiment. Western blot analysis of the enriched proteins allows for simpler and more facile interrogation of individual protein profiles across various conditions compared to large scale proteomics experiments (**Section 1.4.2.2**). I2.1 cells were again treated with DMSO vehicle, **7PQYnD1**, or **7PQYnD1** and **AZ'902** at various concentrations for 3 h. Necroptosis was induced with TNF α and cells were irradiated with 365 nm UV light, washed and lysed, and the tagged proteins ligated to AzTB via a CuAAC reaction. The biotin-labelled proteins were enriched on streptavidin magnetic beads and both the total lysate (input) and enriched fractions (pull down) were analysed by immunoblot (**Figure 3.24**).

All probed proteins were detectable in the total lysate fractions and expressed largely uniformly across all samples, indicating that **7PQYnD1** and/or **AZ'902** treatment does not alter the total expression level of any of the proteins, including that of the loading control heat shock protein 90 kDa (HSP90). HSP90 was also not detected in the enriched fractions, indicating that, at least for this control, the enrichment procedure was successful in excluding unlabelled proteins; this was particularly important to establish for this loading control given its association with the necroptosis pathway.³⁸³

Every protein target identified in proteomics experiments demonstrated dose dependent enrichment when labelled with increasing concentrations of the probe, and this was competed by co-treatment with the parent molecule **AZ'902**. In line with the TMT proteomics data, FDFT1 and SCCPDH were competed in a dose-dependent fashion by **AZ'902** from the lowest concentration, and ADA and CD3 ϵ were competed at the highest (50 μ M) concentration of parent compound, validating all of these proteins as true targets of **AZ'902**. TMEM97 was also enriched by **7PQYnD1** and competed by **AZ'902** in the immunoblot analysis, indicating it is also a target of these molecules, surprisingly however the enriched band appeared at a lower molecular weight than the protein detected in the total lysate. This could

potentially be explained by the antibody being polyclonal, or by different TMEM97 isoforms being present in the lysate, and the probe selectively enriching the smaller of the two. Indeed, the National Center for Biotechnology Information (NCBI) reference sequence (RefSeq) database registers two transcriptional variations of TMEM97, the experimentally verified 20.8 kDa protein (NCBI reference sequence: NP_055388.2) and a longer 24.5 kDa transcriptional variant, isoform X1 (NCBI reference sequence: XP_005258022.1), so this offers a potential explanation.⁴⁵¹ However, epitope tagged constructs of the shorter isoform *only* have been expressed in mammalian cells, and Western blots against the epitope in these lysates have similarly exhibited two bands, suggesting instead that post-translational modification of the protein may be the cause of the two detected proteoforms.⁴⁵²

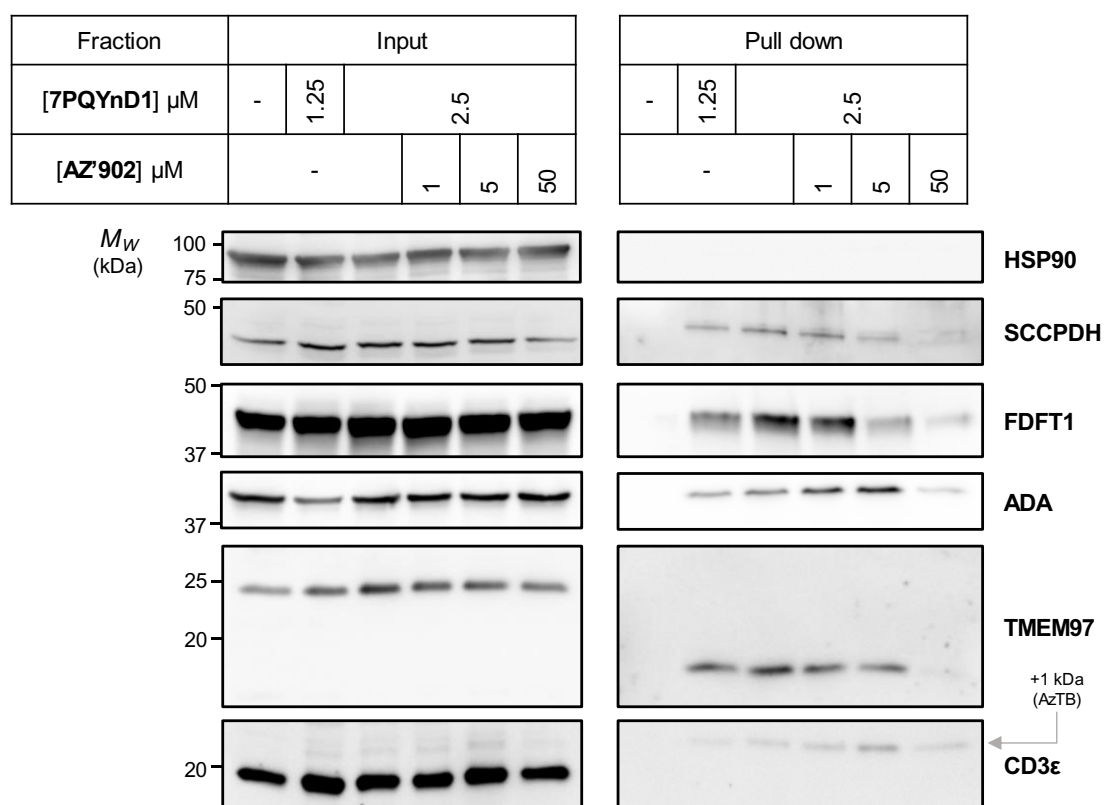


Figure 3.24 Western blot analysis of the 7PQYnD1 enriched proteome. I2.1 cells were treated as indicated, irradiated, lysed and tagged proteins were ligated to AzTB. Displayed is the immunoblot analysis before (input) and after (pull down) enrichment on streptavidin beads. A shift in molecular weight can be observed in both the input and pull down for the lower molecular weight protein CD3ε due to the ligation of the ~1 kDa molecule of AzTB. HSP90 = heat shock protein 90 kDa (HSP90) – loading control.

Five potential hits have been identified from the proteomics data, all of which have been experimentally verified by Western blot. Taken together, this represents a key milestone in the project; one of the main objectives was to generate a cellular protein profile for the 7PQ series, and these data are a significant step towards this goal. Further target profiling experiments using other parent molecules such as those

depicted in **Figure 3.9**, or generation of further affinity-based probes around these molecules such as **7PQYnD2**, would help to corroborate these results and generate overlapping profiles that could help to prioritise the protein targets that may be responsible for the molecular mechanism of action of these compounds. In particular, generation of an inactive analogue of either the probe and/or the parent molecules could help towards this goal, and all of these tasks represent further work that could be undertaken on this project. However, the remainder of the work herein focusses on the functional evaluation of the targets found through the above protein profiling campaign and their potential contributions to the anti-necroptosis behaviour of these molecules.

3.3.5 Functional evaluation of targets

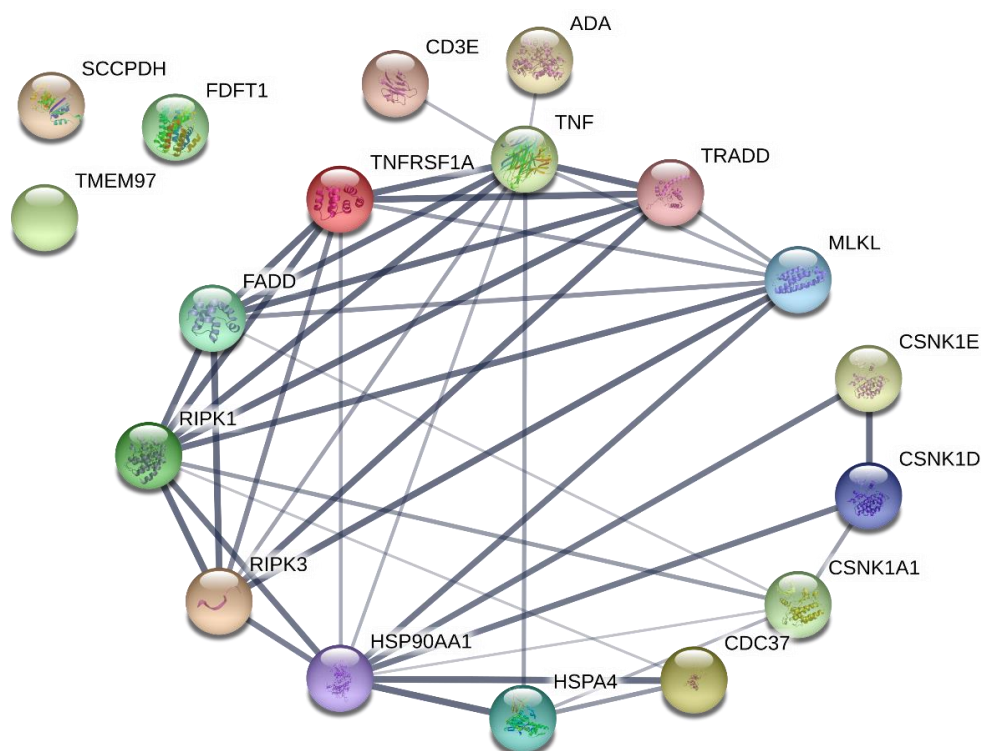


Figure 3.25 STRING molecular interaction analysis of proteins involved in necroptosis (from **Figure 3.2**, **Figure 3.3**) and including those identified in **7PQYnD1** competitive AfBPP experiments. Edge width is proportional to confidence in the relationship (minimum required interaction score: 0.4 (maximum 1)).³⁴³ TNFRSF1A = TNFR1, HSP90AA1 = HSP90, HSPA4 = HSP70, CSNK1A1 = CK1 α , CSNK1D = CK1 δ , CSNK1E = CK1 ϵ .

The five targets ADA, CD3 ϵ , FDFT1, SCCPDH, TMEM97 have not been implicated in necroptosis in previous studies. The Kyoto Encyclopaedia of Genes and Genomes (KEGG) database does not register any of these proteins as involved in the pathway of necroptosis (pathway: hsa04217) or indeed any other regulated cell death pathway.⁴⁵³ STRING molecular interaction analysis was performed on all proteins involved in the linear pathway of necroptosis induced upon TNF α activation (from **Figure 3.2** and **Figure 3.3**) and the five hits from **7PQYnD1** AfBPP experiments (**Figure 3.25**).³⁴³ The highly

interactive network of physical and functional protein-protein interactions involved in necroptosis can be seen as clearly distinct from the five hits highlighted in this study. FDFT1, SCCPDH and TMEM97 have no recorded associations with any of the major players in necroptosis. ADA has demonstrated weak co-expression data with TNF α , and both ADA and CD3 ϵ have been co-mentioned with TNF α in various abstracts in the NCBI's PubMed database, however no other genetic correlations were found (e.g. similar genetic loci), no pairwise associations were identified in any curated databases, and importantly no experimental data exists to corroborate a physical or functional association between these proteins and TNF α .

Nothing currently existing in curated databases suggests that any of the five hit proteins are involved in necroptosis or interact with any key necroptosis proteins. This may indicate that the 7PQ class of molecules modulate necroptosis via a previously unknown mechanism of action, facilitated by their interaction with one of these five novel targets. However, this makes it more difficult to identify which of these interactions is responsible for this phenotypic behaviour. To begin addressing this question, it was envisaged that an unbiased approach such as genetic knockdown of each of these targets would help to assign which compound-protein interaction was of importance for the molecules' anti-necroptosis activity. First however, the proteomics data generated for ADA stood out since it was the protein that had the highest number of peptide spectral counts recorded for any of the five hits by a considerable margin (**Table 3.1**). Such a high abundance of this one particular protein prompted a deeper investigation into this target.

Table 3.1 Peptide spectral counts and sequence coverage for top **7PQYnD1** protein profiling hits from TMT-proteomics data. Known background diazirine binders are included for comparison; ^anumber of spectra recorded for all peptides identified for this protein.

Category	Gene name	Sequence coverage (%)	MS/MS count ^a
Competed hit	ADA	65.0	154
	CD3 ϵ	22.4	11
	FDFT1	22.2	20
	SCCPDH	17.2	8
	TMEM97	25	5
Background binder	VDAC1	43.7	133
	VDAC2	71.7	57
	ECH1	19.8	29

3.3.5.1 Adenosine deaminase (ADA)

Adenosine deaminase (ADA) is an enzyme involved in the metabolism of purine nucleotide bases, and therefore in the recycling pathway for DNA, RNA and other nucleic acid-based biomolecules.⁴⁵⁴ It is a

41 kDa enzyme that catalyses the deamination of both adenosine and deoxyadenosine into inosine and deoxyinosine respectively (**Figure 3.26a**), and mutations that inactivate ADA are directly linked to autosomal recessive severe combined immunodeficiency (SCID) indicating that ADA is essential for proper functioning of the immune system. Through this discovery, inhibitors of ADA were developed to combat lymphoid malignancies and as immunosuppressive agents, the most potent of which is pentostatin (brand name: Nipent®, **Figure 3.26b**).⁴⁵⁵ This drug is most widely employed in the treatment of leukaemia, particularly hairy cell leukaemia, in which it is acutely potent.⁴⁵⁶

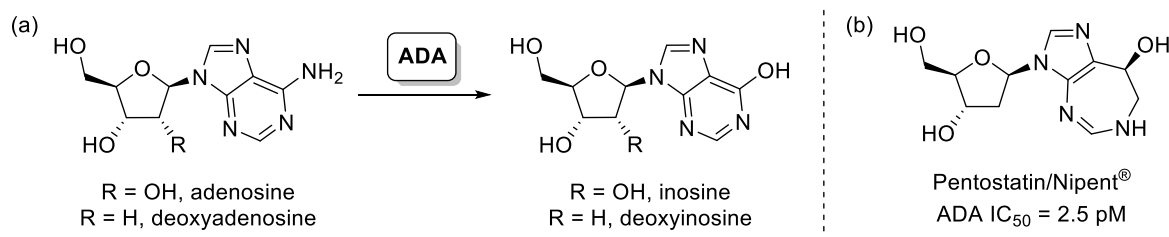


Figure 3.26 Adenosine deaminase function and inhibition. (a) Metabolic reaction catalysed by ADA. (b) Structure of ADA inhibitor pentostatin.

Given the high enrichment levels and sequence coverage of ADA in the above chemical proteomics experiments with **7PQYnD1**, the TMT proteomics data (**Section 3.3.3.2.2**) was run through PEAKS analysis software to generate complete peptide coverage maps for the enriched proteins and identify any modifications, including probe-modified peptides (**Figure 1.9**). For ADA, this coverage map is displayed in **Figure 3.27a**, and remarkably it was possible to identify probe-modified peptides of ADA from the complex mixture of enriched peptides characteristic of whole proteome enrichment data. This appeared to suggest that probe **7PQYnD1** covalently modifies ADA at one of two aspartic acid residues (D295/D296). Examining the crystal structure of ADA bound to its substrate adenosine (**Figure 3.27b–c**), these two amino acid residues are buried deep into the substrate binding pocket. This suggests that **7PQYnD1** and therefore parent molecule **AZ'902** bind into this same substrate binding site.

To validate this experimentally, competitive labelling experiments were performed with pentostatin which is known to mimic the transition state of the transformation of adenosine to inosine and therefore also binds into the same substrate binding site.⁴⁵⁷ I2.1 cells were treated with DMSO vehicle, **7PQYnD1**, or **7PQYnD1** and pentostatin at various concentrations for 3 h. Necroptosis was induced and cells were irradiated with 365 nm UV light, washed and lysed, and the tagged proteins ligated to AzTB via a CuAAC reaction. The biotin-labelled proteins were enriched on streptavidin and analysed by in-gel fluorescence and Western blot (**Figure 3.28**).

In-gel fluorescence analysis of both the total lysate and enriched samples shows one of the enriched bands around 40 kDa being clearly depleted upon treatment with pentostatin. Immunoblot analysis of

the enriched fractions demonstrates that this band corresponds to ADA, reinforcing that **7PQYnD1** and therefore **AZ'902** bind into the substrate binding pocket of ADA. The shared binding site of pentostatin and the 7PQ series suggests that if ADA inhibition is the molecular mechanism of action of these anti-necroptosis compounds, then treatment with pentostatin should phenocopy this effect in I2.1 cells.

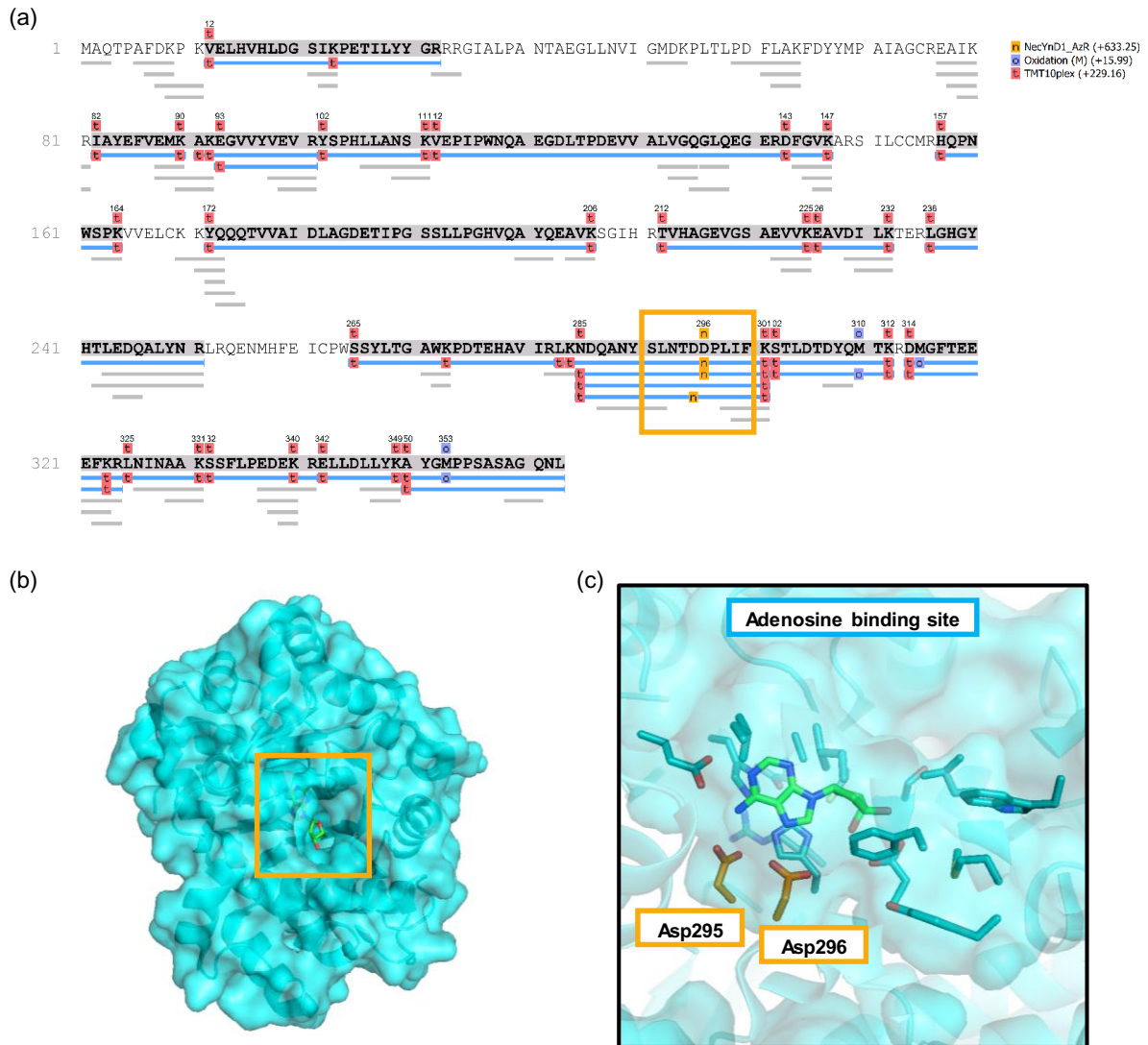


Figure 3.27 **7PQYnD1** binding site analysis of adenosine deaminase. (a) PEAKS coverage map of ADA peptides identified via TMT proteomics data of the **7PQYnD1**-enriched proteome matched against the ADA primary sequence; orange box = modified peptides. (b–c) Crystal structure of adenosine (green) bound to adenosine deaminase (cyan) [PDB ID: 3IAR]:⁴⁵⁸ (b) whole protein with adenosine binding site highlighted (orange box); (c) adenosine binding site with key aspartic acid residues that were found to be modified by **7PQYnD1** highlighted in orange.

To test this, I2.1 cells were seeded in a 96-well plate and incubated overnight. The cells were then treated with varying concentrations of pentostatin in triplicate, treated either with TNF α or vehicle

(growth medium) control, and finally with Sytox™ Green (SG). Cells were imaged with green fluorescence and phase contrast imaging in an IncuCyte live-cell analysis system every hour for 24 h. Background corrected green integrated fluorescence intensity divided by phase area over each well (G_P) was plotted \pm SD of technical replicates over the 24 hour period (necroptosis assay), or at the final time-point for non-TNF α -treated samples (cytotoxicity assay) for each pentostatin concentration (**Figure 3.29a**).

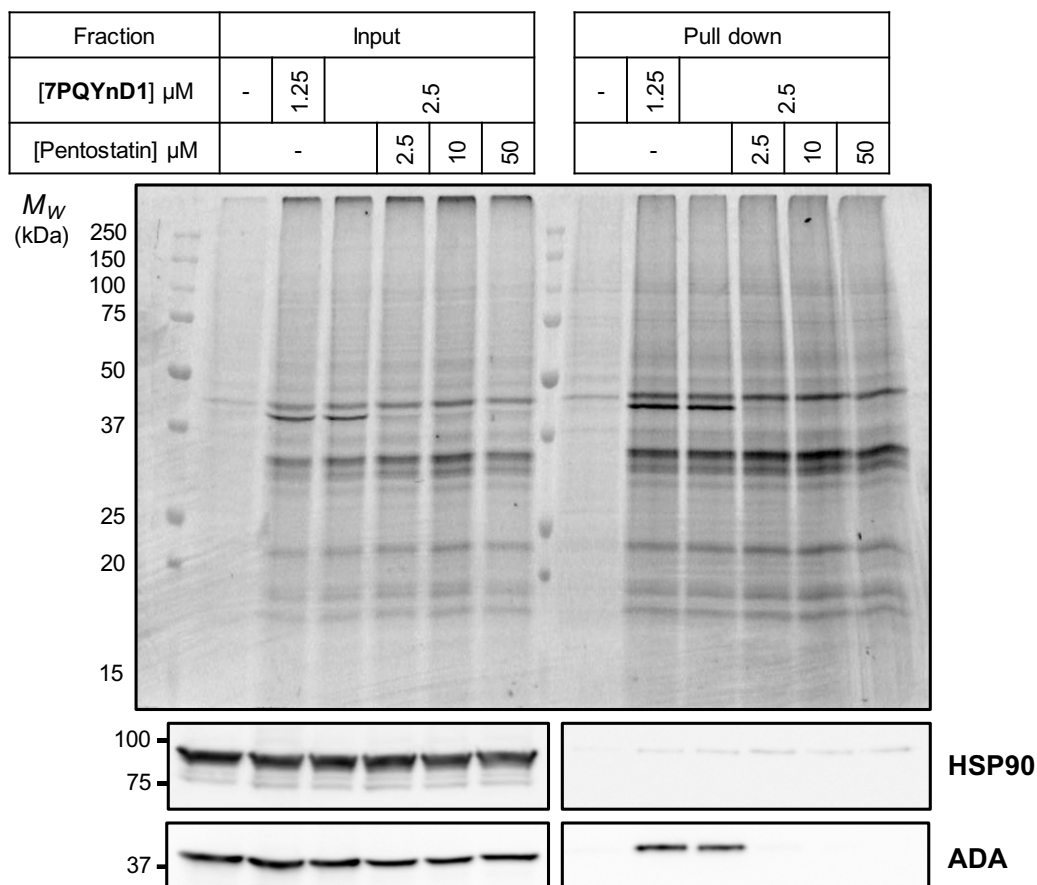


Figure 3.28 7PQYnD1 competition at ADA binding site with pentostatin. I2.1 cells were treated as indicated, irradiated, lysed and tagged proteins were ligated to AzTB. Displayed is the TAMRA fluorescence (top) immunoblot (bottom) analysis before (input) and after (pull down) enrichment on streptavidin beads. HSP90 = loading control.

Treatment of I2.1 cells with up to 50 μ M pentostatin did not appear to markedly protect them from necroptosis induction with TNF α . The linear portion of the necroptosis graph (**Figure 3.29a**, left, hours 2–5) did not change appreciably enough to extract dose-response behaviour from the associated linear rate constants from each concentration as with the 7PQ compounds (**Figure 3.16**). While the highest concentrations of pentostatin did show a slight reduction in total necroptosis at the final time points, this was not comparable to the maximal inhibitory response displayed by AZ'902, 7PQYnD1, and

Nec-1: all proven to completely suppress necroptosis in the same assay. Pentostatin was also not cytotoxic to I2.1 cells even at 50 μM (**Figure 3.29a**, right), so it was unlikely that this was causing undue cell death that negatively influenced the necroptosis assay results. Given that pentostatin fails to appreciably inhibit necroptosis, yet it is able to compete **7PQYnD1** away from the substrate binding site of ADA at the lowest tested concentration (2.5 μM , **Figure 3.28**) and is known to have picomolar affinity for ADA, it seemed unlikely that chemical inhibition of ADA was responsible for the anti-necroptosis activity of the 7PQ series.

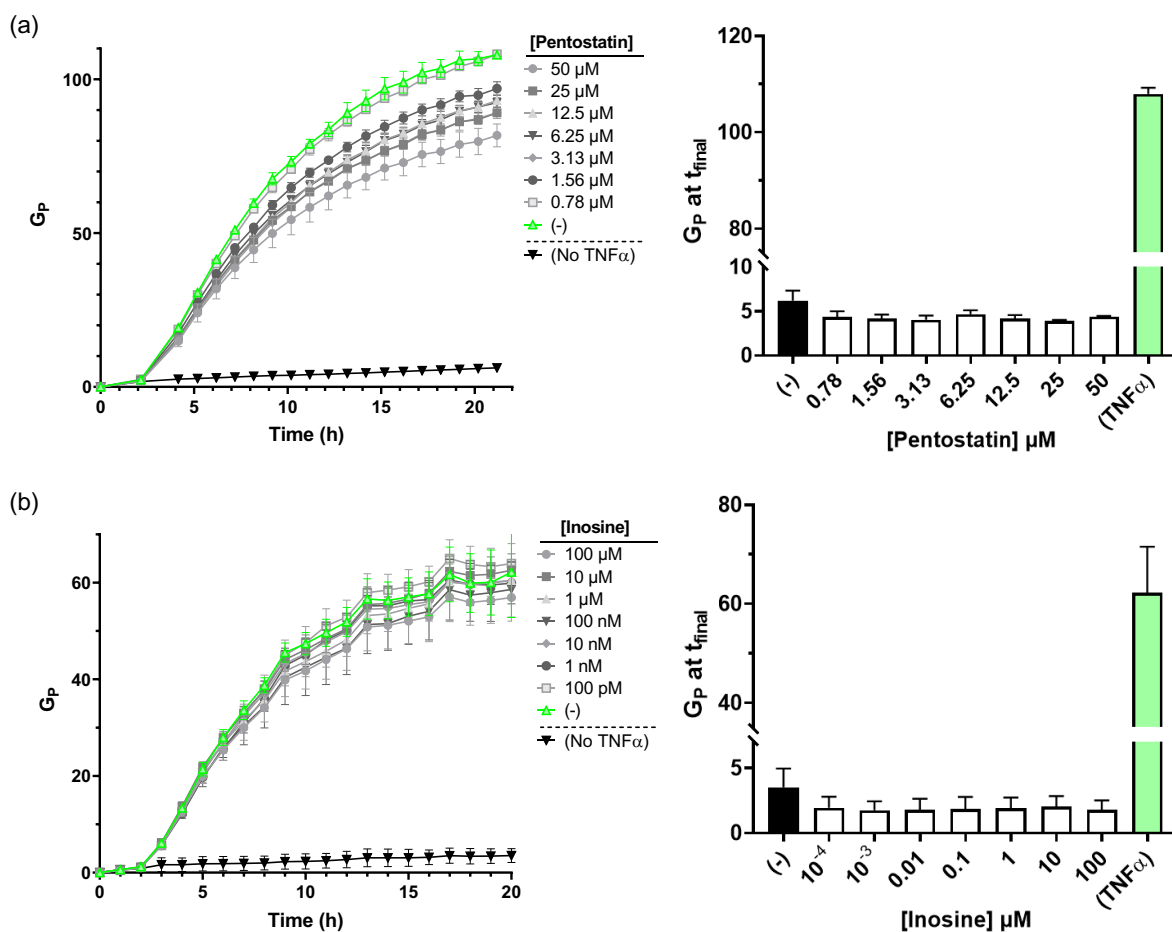


Figure 3.29 Necroptosis and cytotoxicity assays with (a) pentostatin and (b) inosine. I2.1 cells were treated with $\text{TNF}\alpha$ or vehicle, SG, and varying amounts of the molecule under investigation in triplicate. Total green integrated intensity divided by phase contrast area (G_P) was measured on an IncuCyte for each well for 24 h and the results plotted $\pm\text{SD}$ against time to demonstrate necroptosis activity (left). G_P values for wells without $\text{TNF}\alpha$ treatment were plotted at the final recorded time-point as histograms $\pm\text{SD}$ alongside $\text{TNF}\alpha$ treated control wells for comparison to demonstrate cytotoxicity of the compounds (right).

It was also investigated in the same assay whether the catalytic substrate of ADA, inosine, affected necroptosis induction in any way, which would suggest that **7PQYnD1** and its parent molecules were

acting as catalytic activators of ADA rather than inhibitors (**Figure 3.29b**). This was unlikely since binding site analysis strongly suggested that these compounds blocked the catalytic pocket, and indeed treatment of I2.1 cells with concentrations of up to 100 μ M inosine did not inhibit cell death via necroptosis, and did not cause any cytotoxicity that would bias towards these results.

From these data, it was thought to be unlikely that ADA modulation was the primary molecular mechanism of action for the anti-necroptosis activity of the 7PQ series of molecules. It could not be ruled out that binding of these compounds modulates a catalysis-independent function of ADA that cannot be recapitulated by pentostatin binding. However, in order to functionally evaluate all of the targets identified from AfBPP studies simultaneously, a more unbiased approach to functional screening was required.

3.3.5.2 RNA interference

RNA interference (RNAi) is a well validated technique to block the translation of messenger RNA (mRNA) molecules into protein in a sequence specific manner.⁴⁵⁹ Small interfering RNA (siRNA) molecules are synthesised with a complementary sequence to an mRNA molecule transcribed from a particular gene of interest. The siRNA molecules are introduced into mammalian cells as a double-stranded duplex via transient transfection, whereupon the single strand of siRNA complementary to the gene's mRNA is incorporated alongside endogenous cellular proteins into the RNA-induced silencing complex (RISC). This mature RISC then binds the corresponding mRNA through siRNA sequence complementarity and the mRNA is cleaved through RISC's nuclease activity, preventing the mature, active protein from being translated and effectively silencing the expression of that gene.⁴⁶⁰

To examine the effect of gene silencing on the successful induction of necroptosis, the appropriate double stranded siRNA molecules were purchased for the five protein hits: ADA, CD3 ϵ , FDFT1, SCCPDH, and TMEM97. Three siRNA duplexes were purchased for each gene targeting a distinct region of each gene's mRNA (for full sequences see **Table 5.1**); siRNA reagents were also purchased for MLKL, the terminal protein in the necroptosis pathway to act as a positive control for necroptosis inhibition by gene silencing. First however, it was necessary to assess the efficiency of the knockdown for each gene.

3.3.5.2.1 Validation of knockdown

I2.1 cells were reverse transfected with three siRNAs for each gene separately by adding cells to a premixed solution of the corresponding siRNA and LipofectamineTM reagent in serum-free medium by the manufacturer's recommended protocol. Cells were harvested and lysed after 48 h and the lysates analysed by Western blotting for each protein to assess the knockdown efficiency of each siRNA (**Figure 3.27**). Appreciable protein depletion was observed across all three siRNA duplexes for all genes

except for SCCPDH after 48 h knockdown. Once again for TMEM97, the major band at just above 25 kDa was unaffected, and the lower band, corresponding to the experimentally determined TMEM97 isoform (Section 3.3.4),⁴⁶¹ demonstrated depletion upon siRNA treatment. Unfortunately, time restraints on the project prevented further optimisation of the knockdown of SCCPDH, therefore 48 h was taken forward as the knockdown time for future RNAi experiments. Future experiments could include the optimisation of reagent concentration and incubation times for SCCPDH silencing, and quantification of the knockdown at the mRNA level using quantitative polymerase chain reaction (qPCR) analysis.

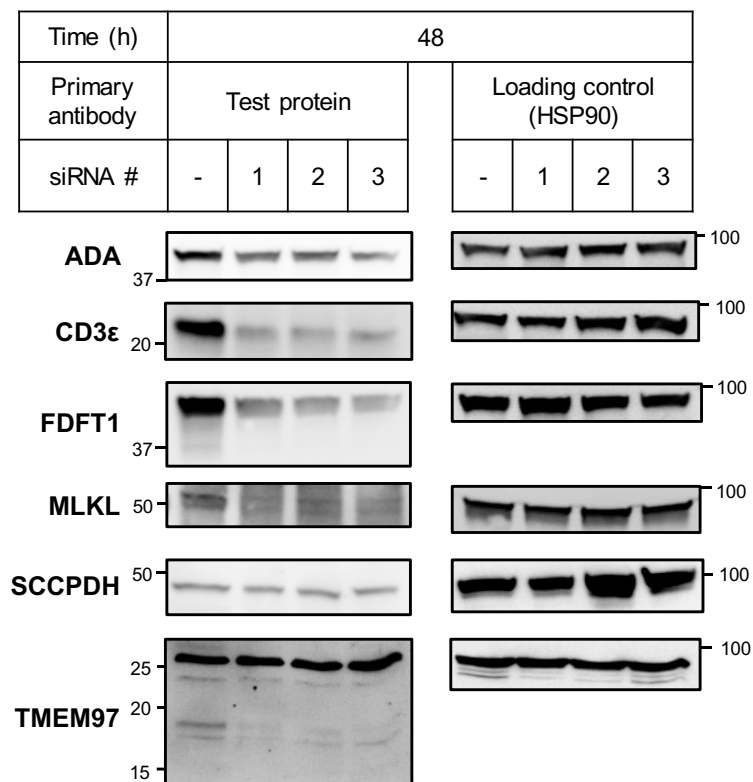


Figure 3.30 Optimisation of siRNA knockdown of indicated genes in I2.1 cells. A mixture of siRNA duplex (final 12 nM) and Lipofectamine RNAiMAX reagent (final 0.17% (v/v)) were mixed together in serum-free medium in TC plate wells. After a brief incubation, I2.1 cells in complete growth medium were added and the cells incubated for 48 h. Cells were lysed and analysed by Western blot, with the probed protein presented alongside the corresponding loading control (HSP90 = heat shock protein 90 kDa).

3.3.5.2.2 RNAi and necroptosis

In order to investigate the effect of genetic knockdown of each gene on necroptosis, transfections were performed in 6-well plates for each siRNA sequence for each gene, including a non-specific siRNA sequence as a negative control, using the general conditions described above over 48 h. The cells were then transferred as technical triplicates to 96-well plates, treated with 60 pM TNF α to induce necroptosis

and 1 μ M SG to detect cellular death. The cells were imaged in green fluorescence and phase contrast modes on an IncuCyte system every hour for 24 h and background corrected G_P values at each time point were extracted per well as previously described (**Section 3.3.2.1**). These values were plotted against time to generate a kinetic necroptosis graph for each siRNA knockdown, and area under the curve (AUC) values were calculated for each graph to represent total necroptosis. These values were normalised to the AUC values for the siRNA control treated (100%) and untreated (0%) with $TNF\alpha$ and plotted \pm SEM across three independent biological experiments over the 24 h period (**Figure 3.31**).

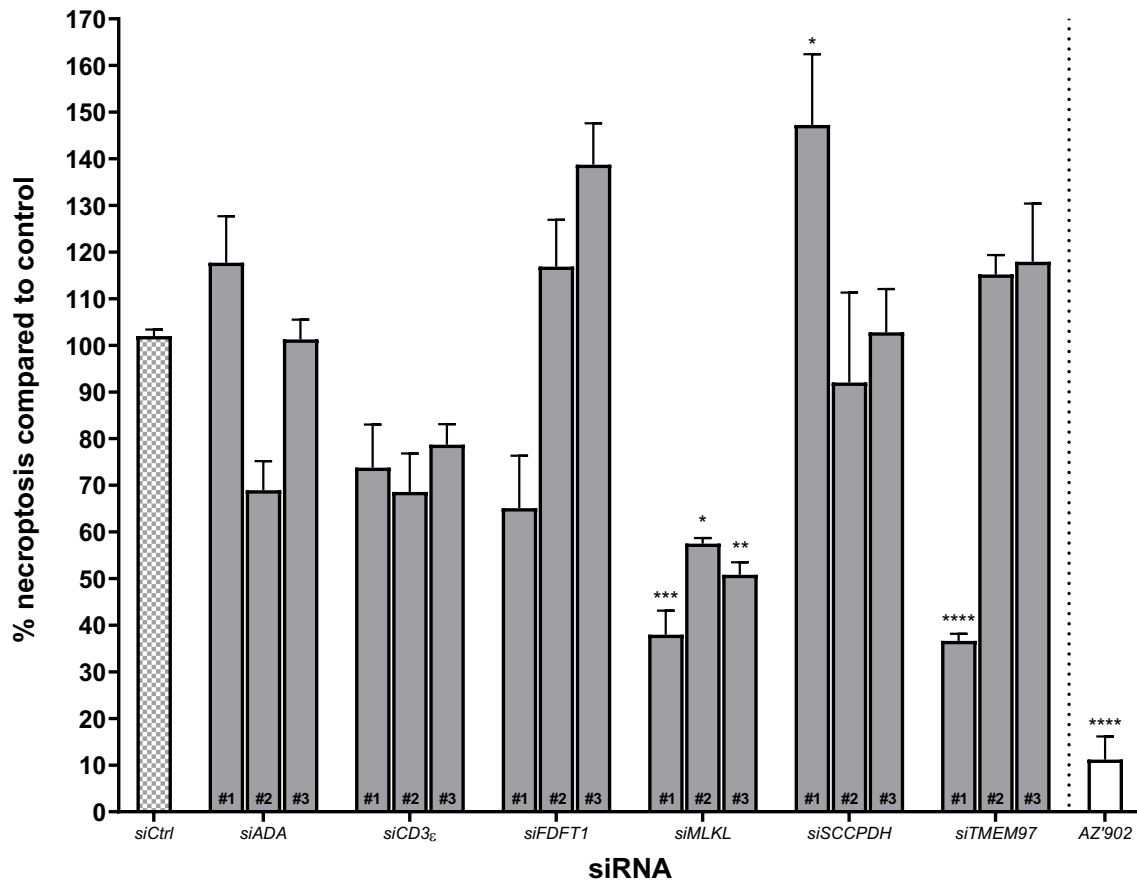


Figure 3.31 Necroptosis assays after siRNA knockdown of indicated genes in I2.1 cells. Cells were transfected with the indicated siRNA duplexes including a non-specific control siRNA sequence (*siCtrl*) for 48 h in 6-well plates. Cells from each condition were then transferred to a 96-well plate as technical triplicates and treated with $TNF\alpha$ (0.06 nM) and SG (1 μ M); an additional two triplicate sets of *siCtrl* treated cells were also transferred and one set treated with **AZ'902** (25 μ M), $TNF\alpha$ and SG, and the other set treated only with SG. Cells were imaged every hour for 24 h (phase contrast and green fluorescence) and the resulting background corrected G_P values plotted against time for each well. Total G_P was calculated by extracting AUC values for each replicate, which were normalised to the average AUC values for *siCtrl*/ $TNF\alpha$ +/ SG + wells (100%) and *siCtrl*/ $TNF\alpha$ -/ SG + wells (0%) within each experiment. These were then plotted \pm SEM of biological replicates (N = 3) and significance

between treatments and *siCtrl* were calculated using an ordinary one-way ANOVA, p-value: * = < 0.05, ** = < 0.01, *** = < 0.001, **** = < 0.0001.

Suppression of the positive control MLKL lead to a statistically significant reduction in necroptosis across all three independent siRNA sequences when compared to treatment with control siRNA. This is an expected result given that MLKL is the terminal effector in this pathway. It should be noted that the suppression of necroptosis observed by genetic knockdown did not reach the levels achieved through chemical inhibition by **AZ'902**, however it is known that transient transfection of siRNA duplexes by lipid-based reagents is not 100% efficient,⁴⁶² and subsequently treating cells with TNF α might execute necroptosis in the few cells that have retained MLKL. The resulting necrotic cell death and release of damage associated molecular patterns (DAMPs) initiated by TNF α treatment may then activate other extrinsic forms of regulated cell death in the surrounding cells independent of TNF α or even MLKL.

Unfortunately, none of the other tested genetic knockdowns led to a concomitant reduction in necroptosis across all three sequences, which does not allow any robust conclusions to be drawn about the involvement of these proteins in the necroptosis pathway, and consequently the mechanism of action of the 7PQ series of necroptosis inhibitors. However, one particular siRNA sequence, siTMEM97 #1, consistently demonstrated a significant reduction in necroptosis comparable to the reduction observed when silencing MLKL. All three siTMEM97 sequences were shown to lower the protein levels of the lower band by Western blot (**Figure 3.30**), therefore it is surprising that only one of the sequences had a reproducible necroptosis inhibition effect. Performing a BLAST alignment of the sequence against the human transcriptome indicated that the siRNA should have no off-target effects that would otherwise explain this behaviour.

In order to investigate the differential effect of the three siTMEM97 sequences, further analysis of changes in mRNA levels from each sequence by qPCR should be undertaken, in particular analysing the differential expression of the two isoforms. Additional analysis of the protein levels could also be undertaken using an N-terminally directed TMEM97 antibody that can discriminate between the two potential isoforms. To confirm the genetic phenotype of siTMEM97 #1, different siRNA sequences from other suppliers, including custom siRNA pools, could be leveraged, or alternative knockdown techniques such as short hairpin RNA-based silencing⁴⁶³ or CRISPR interference⁴⁶⁴ could be utilised. Finally, experiments with known TMEM97 ligands would improve understanding of chemical modulation of this protein and its effect on necroptosis. All of these experiments represent future work on this project, however the preliminary functional validations undertaken in this Thesis will help to guide these efforts.

3.4 Conclusions and future work

This chapter discusses the development of novel affinity-based probes to profile the biomolecular targets of a 7-phenylquinoline pharmacophore-containing series of molecules, discovered to be promising pharmacological inhibitors of necroptosis via a high-throughput screen with an unknown molecular mechanism of action. Two probes, **7PQYnD1** and **7PQYnD2**, were rationally designed from structure-activity relationship data and the successful synthesis of **7PQYnD1** is described. To validate **7PQYnD1** as an effective AfBP for the 7PQ series, it was necessary to test whether it was also able to inhibit necroptosis, and a novel live-cell necroptosis assay was developed in-house specifically for this purpose. It was confirmed that **7PQYnD1** was able to inhibit necroptosis using this assay, and so it was taken on to affinity-based protein profiling (AfBPP) studies.

Using a combination of gel- and proteomics-based AfBPP experiments with both **7PQYnD1** and a parent 7PQ competitor **AZ'902**, it was possible to profile the targets of this series of molecules for the first time via photoaffinity labelling. In particular, five proteins were identified as both significantly enriched by **7PQYnD1** and competed in a dose-dependent manner by **AZ'902**: adenosine deaminase (ADA), T-cell surface glycoprotein CD3 epsilon chain (CD3 ϵ), squalene synthase (FDFT1), saccharopine dehydrogenase-like oxidoreductase (SCCPDH) and sigma intracellular receptor 2 (TMEM97). These hits represent the first protein profile of the 7PQ series of molecules in I2.1 cells, addressing a key objective of this target identification campaign. Further AfBPP experiments with other probes and parent molecules and in other necroptosis competent cell lines would help to validate this protein profile. In particular, investigation into the apparent instability of **7PQYnD2** might help yield another probe, and it would be useful to generate a necroptosis-inactive probe that might help delineate on- and off-target protein interactions. The above identified proteins from the proteomics screening were all validated as true hits by Western blot. Also, orthogonal enrichment of different proteoforms of TMEM97 was uncovered in these experiments, a curiosity that requires further investigation.

Finally, preliminary functional validation of the hits identified through the AfBPP campaign was attempted to identify the compound-protein interaction responsible for necroptosis inhibition. While ADA initially seemed to be a promising candidate due to its high level of enrichment in proteomics analysis of **7PQYnD1** treated samples, chemical inhibition of ADA with an inhibitor that binds into the same binding site as **7PQYnD1** did not elicit the same anti-necroptosis response. Instead, genetic silencing of each of the target proteins was performed, and the cells lacking these proteins were assayed for their ability to undergo necroptosis. Intriguingly, silencing of TMEM97 was found to suppress necroptosis to the same level achieved through silencing of mixed lineage kinase domain-like protein (MLKL), the final executor of necroptosis. However, this was only achieved through with one out of the three siRNA sequences, even though all three sequences appeared to deplete the protein levels by

Western blot. Further experiments are required to address this disparity before conclusions can be reached about a potential role for TMEM97 in the execution of necroptosis. In particular, necroptosis assays and competitive AfBPP experiments with known chemical inhibitors of TMEM97 would help to assess whether pharmacological modulation of TMEM97 is able to abrogate necroptosis. Nonetheless, AfBPP experiments were able to generate a protein profile for this set of novel necroptosis inhibitors, allowing preliminary investigations into their molecular mechanism of action that were previously not possible. Using the methodology outlined in this chapter, it would also be possible to continue this work to generate similar protein profiles for the remaining pharmacophores identified in the original high-throughput screen (**Figure 3.8**).

Chapter 4 Conclusions and outlook

This section reflects on the implications and future directions of the work in this Thesis as a whole. Separate conclusions describing the individual results of each chapter have been presented previously.

4.1 The merits of target profiling in drug discovery

At the beginning of this Thesis, the roles of target profiling in drug discovery for small molecule chemical inhibitors were outlined, including target identification, target confirmation/reassignment, off-target profiling and quantification of target engagement (**Figure 1.1**). The work described herein has demonstrated the power of affinity-based protein profiling (AfBPP) to perform all of these roles, and has shown that photoaffinity labelling data can add real value to the drug discovery projects they are associated with.

In developing a first-in-class affinity-based probe (AfBP) for the profiling of novel and existing poly(ADP-ribose) polymerase (PARP) inhibitors (PARPi), this AfBPP campaign was able to demonstrate for the first time differential target engagement of both PARP1 and PARP2 in live cells.³³⁴ This could then be used to assess the selectivity of various PARPi in intact cells using proteomics-based methods. Further to cellular PARP labelling, the AfBP was also able to bind to and label several unprecedented off-target proteins for the clinical PARPi olaparib, and more widely the phthalazinone series of PARPi. Crucially, this photoaffinity labelling study was able to detect these binding events that previous studies using non-covalent AfBPs^{87,332} and affinity chromatography⁷³ had failed to identify. This reinforces that photoaffinity labelling is superior for capturing weaker, secondary binders (**Section 1.2.1**). Finally, the AfBP was shown to bind to label recombinant PARP6, yet that result was not recapitulated with endogenously produced PARP6 in mammalian cells. Given that cellular binding to PARP6 was the purported mechanism of action of anticancer parent compound **AZ0108**,³⁴¹ this raised questions about the druggability of PARP6 *in situ/vivo*. As a result of these data, AstraZeneca (AZ) has since been reassessing the mechanism by which **AZ0108** and similar compounds cause the multipolar spindle (MPS) phenotype that leads to cancer cell cytotoxicity (**Section 2.3.1**). Together with the off-target proteins uncovered by this AfBPP campaign, it may be possible to reinvigorate this series of molecules as a viable therapeutic anticancer strategy in AZ's drug discovery pipeline.

While the PARP AfBPP campaign primarily dealt with target engagement, off-target identification, and target reassignment, the second AfBPP campaign for a novel series of necroptosis inhibitors showcased the ability of photoaffinity labelling to generate *de novo* target identification data. Herein, a successful AfBP was generated for the 7-phenylquinoline (7PQ) series of necroptosis inhibitors discovered through a high-throughput screen (HTS) by our collaborators at the University of Lisbon.⁴³⁸ Through

photoaffinity labelling studies with this AfBP, five novel targets were discovered that bind the 7PQ molecules in necroptosis-competent cells. This data was even able to extract binding site information for one of these targets from the whole-proteome pull down data (**Section 3.3.5.1**), information that is typically generated by photocrosslinking studies in-solution with the recombinant protein.^{465,466} Work is currently ongoing to uncover which of the 7PQ-protein interactions is responsible for the anti-necroptosis mechanism of action of the series. Knowledge of this key therapeutic target will then assist the drug discovery campaign through more information about the biological pathway, and if the target has a known structure, will provide key structure-activity relationship (SAR) data that will help with the design and nomination of a candidate molecule that can be progressed to the clinical stages of drug development.

In conclusion, this Thesis has described successful AfBPP campaigns for two distinct biomedical applications. Together, these projects have shown how photoaffinity labelling is able to extract on- and off-target identification data, quantify cellular target engagement, and even potentially reassign the target of a drug molecule, and these data will prove invaluable in reshaping and focussing their associated ongoing drug discovery campaigns.

4.2 Future directions

The results in this Thesis contribute to the ever-growing experience within the Tate group in activity/affinity-based protein profiling, and the methods and strategies outlined here lay further groundwork that may be useful for future members of the group and the wider chemical biology community for their own target identification projects. While both projects herein are centred around two distinct biological systems, the process of design, synthesis, validation and application of the AfBPs in both cases is similar, highlighting the ease of transferability of this workflow between pharmacophores and disease models. Furthermore, the experience gained in this project has helped highlight barriers that need to be overcome for successful AfBPP campaigns, including the synthesis of the chemical probe(s), the availability of suitable assays to compare the probe to the parent compound(s), and the optimisations associated with photoaffinity labelling experiments including, but not limited to, probe incubation time, probe and parent compound concentrations, UV irradiation times, and selection of appropriate proteomic quantification methodologies.

While both projects have performed target profiling successfully, they remain limited in their conclusions due to the lack of validation through alternative techniques. Both probes were able to deliver a list of target proteins in their respective campaigns, however these data would be reinforced by orthogonal validation through further AfBPs (including inactive controls), protein profiling in multiple relevant cellular models, and even target profiling using alternative methodologies such as the

label free cellular thermal shift assay (CETSA, **Section 1.2**), representing further work for both projects. This is particularly necessary for the necroptosis project, where on-target identification is yet to be functionally confirmed, and further target profiling using alternative probes and/or cell lines might allow triaging of the list of protein hits. While all of these additions commit further time and resources, as a result of this work, addition of at least one orthogonal validation strategy is now being prioritised when undertaking new target profiling campaigns in the Tate group.

There are several further independent lines of enquiry resulting from this work that could form the basis of future individual projects, most of which have been described in the individual conclusions for each chapter. However, these are collated here for further emphasis:

- Proteomics-based target profiling of olaparib generated a whole catalogue of off-target proteins that require confirmation of their target engagement by Western blot. Once confirmed, the contribution of these interactions to known off-target toxicity and metabolism of olaparib and other PARPi could be explored.
- The identification of monocarboxylate transporter 8 (SLC16A2) as a PARPYnD target protein may implicate this transporter protein in the cellular trafficking of PARPi in and out of the cell, and association of this protein with PARPi therapy resistance in cancer should be investigated through genetic models and bioinformatics data.
- **PARPYnD** was able to uncover a biomolecular disparity between endogenous and recombinant PARP6. Further investigations into mammalian PARP6 using the biological tools and probes developed in this project should be carried out to attempt to understand the molecular basis for regulated access to the NAD⁺ binding site in mammalian PARP6.
- AstraZeneca have developed a proprietary phthalazinone-derived structure that is reported to enrich more PARP family members than just PARP1/2 from lysates through affinity chromatography. Adaptation of this structure into photoaffinity probe might generate a “best-in-class” AfBP that is able to profile these interactions in living cells and more broadly assess the inter-family selectivity of novel and existing PARPi *in situ*.
- Two pharmacophores from the HTS performed at the University of Lisbon still have unknown mechanisms of action against necroptosis, as do various other isolated molecules that could not be grouped with a common pharmacophore. AfBPP campaigns should be carried out to determine their cellular protein targets.

The prospect of discovering a new druggable target within the clinically relevant pathway of necroptosis or developing a deeper biomolecular understanding of the PARP proteins and their inhibitors is potentially of great clinical importance. This Thesis should provide future researchers with the tools and techniques with which to pursue these exciting goals and has demonstrated that photoaffinity

labelling can uncover new lines of scientific and clinical inquiry, as well as answer fundamental biochemical questions through target profiling.

Chapter 5 Materials and Methods

5.1 Materials

Chemicals were purchased from Sigma-Aldrich, Fluorochem, Acros Organics, Tokyo Chemical Industry, Alfa Aesar or Fisher Scientific and used without further purification. AzTB and AzRB (**Figure 1.7**) were synthesized in-house as previously reported.¹⁵⁸ **PARPYnD** was synthesised as previously reported.^{333,334} **AZ9482**, **AZ0108** and **AZ'902** were provided by AstraZeneca. Olaparib was purchased from VWR International. NeutrAvidin agarose resin, PreScission™ Protease and Sytox Green were purchased from Thermo Fisher Scientific. Streptavidin magnetic beads were purchased from New England BioLabs. Mammalian expression vector pcDNA3.1™ containing FLAG-PARP6 (plasmid map **Appendix I**) and recombinant GST-PARP6 protein (sequence **Appendix II**) were provided by AstraZeneca. 6-biotin-17-NAD⁺ was purchased from Bio-Techne Ltd. Recombinant human TNF α was purchased from PeproTech. The water used in all applications was ultra-pure MilliQ® water obtained using a Millipore water purification system unless otherwise stated.

Antibodies: anti-PARP1 (SantaCruz, sc-8007), anti-PARP6 (Sigma, HPA026991), anti-GAPDH (Abcam, ab9485), anti-HSP90 (SantaCruz, sc-69703), anti-FLAG-HRP [M2] (Sigma, A8592), NeutrAvidin-HRP (Invitrogen, A2664), anti-HH3 (SantaCruz, sc-10809), anti-ADA (Invitrogen, PA5-78721), anti-CD3 ϵ (Abcam, ab16044), anti-FDFT1 (SantaCruz, sc-271602), anti-MLKL (Novus, NBP1-56729), anti-SCCPDH (Invitrogen, PA5-37402), anti-TMEM97 (Invitrogen, PA5-23003), anti-mouse-HRP (Advansta, R-05071-500), anti-rabbit-HRP (Advansta, R-05072-500).

5.2 Chemical synthesis

5.2.1 General chemical methods

All anhydrous reactions were carried out in dry glassware that had been oven-dried overnight and flushed with dry nitrogen. Anhydrous solvents were dispensed from Pure Solv™ solvent drying towers (Innovative Technology Inc.) and were used unless otherwise stated. Brine refers to a saturated aqueous solution of NaCl. Yields were determined on compounds that were pure by spectroscopy and chromatography, unless otherwise stated. Reactions were monitored either by analytical liquid chromatography-mass spectrometry (LC-MS) or thin layer chromatography (TLC). For known compounds, at least 3 pieces of analytical data are provided. For those compounds previously unreported in the literature or those known but with insufficient characterisation, at least 5 pieces of analytical data are provided.

LC-MS spectra were recorded on an Agilent 1260 Infinity II high performance liquid chromatography (HPLC) system, including a G7129A vialsampler, G7112B binary pump, and G6116A multicolumn

thermostat coupled to a G7115A Diode Array Detector WR and a single quadrupole G6135B Liquid Chromatograph/Mass Selective Detector XT (LC/MSD XT) in mixed electrospray atmospheric pressure ionisation (ES-API) mode. Prior to detection, compounds were separated on a 2.1 mm × 50 mm analytical Agilent Zorbax Eclipse C₁₈ 1.8 μm column at 50 °C at a flow rate of 0.35 mL min⁻¹ over a gradient of 5–95% MeOH in H₂O. Spectra were analysed using Masshunter software.

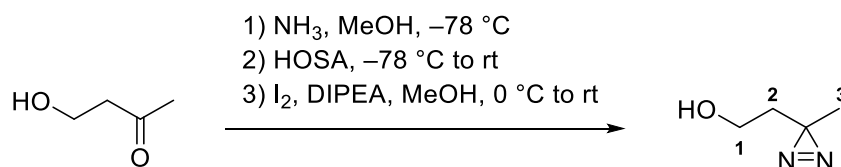
TLC was performed on Si 60, F₂₅₄ chromatography sheets (Merck) and visualised by UV absorption (254 nm) or by staining with KMnO₄, ninhydrin, vanillin, or *p*-anisaldehyde as appropriate. Purification was carried out either by manual flash column chromatography over Geduran® Si 60 (40–63 μm) silica gel (Merck) using the solvent systems indicated, or by automatic column chromatography on a Biotage Isolera™ Spektra System with ACI™ and Assist using pre-packed SNAP KP-SIL cartridges (Biotage) of appropriate weight. Purity of final compounds was calculated with raw analytical LC-MS data using GraphPad Prism 8 software by “Area under curve” analysis with an appropriate choice of baseline.

Infrared (IR) spectra were recorded neat and background corrected on a diamond ATR module using an Agilent Technologies Cary 630 FT-IR spectrometer with 4 scans per spectrum. Selected absorption maxima are reported in wavenumbers (cm⁻¹) and reported to the nearest 1 cm⁻¹.

Nuclear magnetic resonance (NMR) spectra were recorded on a Bruker AV-400 (400 MHz) instrument in the deuterated solvent stated. The field was locked using the internal deuterium resonance at ambient probe temperature with tetramethylsilane as the internal standard. ¹H NMR chemical shifts are quoted to the nearest 0.01 ppm and referenced to the residual non-deuterated solvent peak. Coupling constants (*J*) are given to the nearest 0.1 Hz. The following abbreviations are used to indicate signal multiplicity: s = singlet, d = doublet, t = triplet, and m = multiplet. ¹³C NMR spectra were recorded with broadband proton spin decoupling. The chemical shifts are quoted to the nearest 0.1 ppm and referenced to the deuterated solvent peak. NMR spectra were analysed using MestReNova© NMR software.

High-resolution mass spectrometry (HRMS) data were acquired by the Imperial Mass Spectrometry service; *m/z* values are reported in Daltons (Da) to the nearest 0.0001 Da.

5.2.2 2-(3-methyl-3H-diazirin-3-yl)ethan-1-ol (**13**)

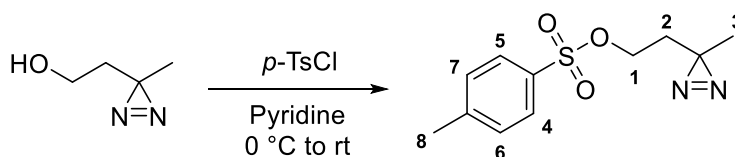


Ammonia (50 mL) was condensed at -78 °C into a 250 mL round bottom flask fitted with a cold finger of dry ice-acetone and an HCl (6 M) trap. A solution of 4-hydroxybutan-2-one **12** (95%, 6.52 g, 70.3 mmol, 1 eq.) in anhydrous MeOH (10 mL) was added and the reaction stirred at -78 °C for 5 h. A

solution of hydroxylamine-*O*-sulphonic acid (HOSA, 10.9 g, 96.5 mmol, 1.4 eq.) in anhydrous MeOH (70 mL) was added dropwise at $-78\text{ }^{\circ}\text{C}$ and the reaction stirred and allowed to warm to rt for 16 h. The reaction mixture was then filtered and the solids washed with anhydrous MeOH ($2 \times 20\text{ mL}$). The filtrate was concentrated *in vacuo* (water bath $30\text{ }^{\circ}\text{C}$) and the residue re-dissolved in anhydrous MeOH (50 mL), cooled to $0\text{ }^{\circ}\text{C}$, and *N,N*-diisopropylethylamine (DIPEA, 15.0 mL, 87.2 mmol, 1.2 eq.) was added. I_2 was added portion-wise to the stirred solution until a dark brown colour persisted for 1 h. The reaction mixture was diluted with Et_2O (150 mL) and HCl (1 M, 150 mL) and separated. The aqueous layer was extracted with Et_2O ($2 \times 100\text{ mL}$) and the combined organics washed successively with HCl (1 M, 150 mL), $\text{Na}_2\text{S}_2\text{O}_3$ (10% (w/v) aq., 150 mL) and brine (150 mL), then dried over anhydrous MgSO_4 , filtered and concentrated *in vacuo* to afford title compound **13** as a pale yellow oil (2.45 g, 24.5 mmol, 36%) that was used without further purification: $R_f = 0.53$ (1:9 MeOH/ CH_2Cl_2); δ_{H} /ppm (400 MHz, CDCl_3) 3.52 (t, $J = 6.3\text{ Hz}$, 2H, **1**), 1.62 (t, $J = 6.3\text{ Hz}$, 2H, **2**), 1.06 (s, 3H, **3**); HRMS (ESI^+) found $[\text{M}+\text{H}]^+$ 101.0720, $\text{C}_4\text{H}_9\text{N}_2\text{O}^+$ requires 101.0715.

This compound is known. ^1H NMR and HRMS data are consistent with those previously reported.¹⁸² All other data is previously unreported.

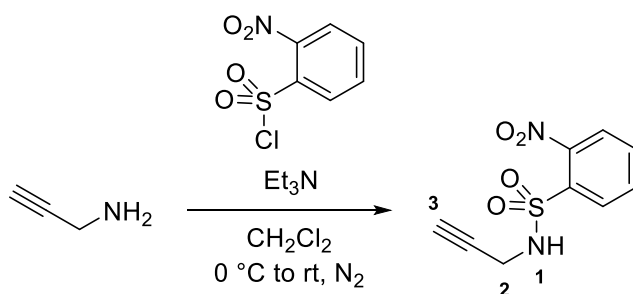
5.2.3 2-(3-methyl-3*H*-diazirin-3-yl)ethyl 4-methylbenzenesulfonate (**14**)



2-(3-methyl-3*H*-diazirin-3-yl)ethan-1-ol **13** (1.00 g, 10.0 mmol, 1 eq.) was dissolved in anhydrous pyridine (8 mL) and cooled to $0\text{ }^{\circ}\text{C}$. *Para*-toluenesulfonyl chloride (2.87 g, 15.0 mmol, 1.5 eq.) was added portion-wise and the resulting solution stirred for 3 h at rt. The reaction mixture was diluted with CH_2Cl_2 (150 mL) and HCl (1 M, 150 mL), separated, and the organic phase washed successively with HCl (1 M, 75 mL), sat. aq. NaHCO_3 (150 mL) and brine (150 mL), then dried over anhydrous MgSO_4 , filtered and concentrated *in vacuo*. The crude product was purified by automated flash column chromatography (8–66% EtOAc in *n*-hexane) to afford the title compound **14** as a colourless oil (1.65 g, 6.50 mmol, 65%): $R_f = 0.57$ (CH_2Cl_2); δ_{H} /ppm (400 MHz, CDCl_3) 7.85 – 7.77 (m, 2H, **4** and **5**), 7.36 (dd, $J = 8.6, 0.7\text{ Hz}$, 2H, **6** and **7**), 3.95 (t, $J = 6.4\text{ Hz}$, 2H, **1**), 2.45 (s, 3H, **8**), 1.67 (t, $J = 6.4\text{ Hz}$, 2H, **2**), 1.00 (s, 3H, **3**); HRMS (ESI^+) found $[\text{M}+\text{H}]^+$ 255.0814, $\text{C}_{11}\text{H}_{15}\text{N}_2\text{O}_3\text{S}^+$ requires 255.0803.

This compound is known. ^1H NMR and HRMS data are consistent with those previously reported.¹⁸² All other data is previously unreported.

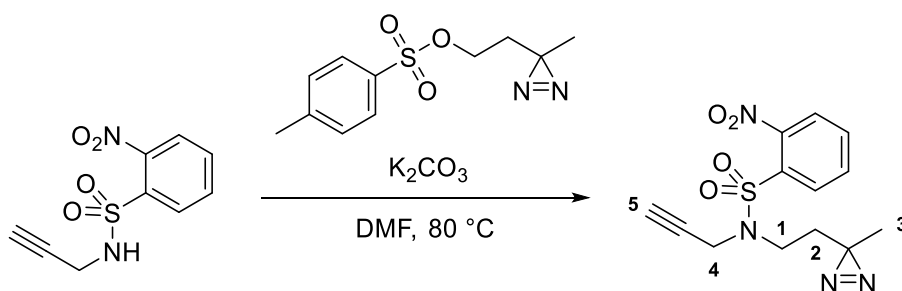
5.2.4 2-nitro-N-(prop-2-yn-1-yl)benzenesulfonamide (**17**)



Propargylamine **15** (1.00 g, 18.2 mmol, 1.06 eq.) and triethylamine (2.52 mL, 18.2 mmol, 1.06 eq.) were dissolved in CH_2Cl_2 (15 mL) and cooled to $0\text{ }^\circ\text{C}$ under N_2 . 2-Nitrobenzenesulfonyl chloride **16** (3.80 g, 17.1 mmol, 1 eq.) was added and the reaction stirred at rt for 3 h. The reaction mixture was diluted with CH_2Cl_2 (50 mL) and HCl (2 M, 50 mL) and separated. The aqueous layer was further extracted with CH_2Cl_2 (50 mL) and the combined organics were washed successively with HCl (2 M, 75 mL), H_2O (75 mL), and brine (75 mL), then dried over anhydrous Na_2SO_4 , filtered and concentrated *in vacuo* to afford the title compound **17** as a pale orange solid (3.64 g, 15.0 mmol, 88%) which was used without further purification: $R_f = 0.46$ (1:1 EtOAc/*n*-hexane); δ_{H} /ppm (400 MHz, CDCl_3) 8.23 – 8.16 (m, 1H, ArH), 7.95 – 7.88 (m, 1H, ArH), 7.80 – 7.73 (m, 2H, ArH), 5.71 (t, $J = 6.4$ Hz, 1H, **1**), 4.01 (dd, $J = 6.3, 2.5$ Hz, 2H, **2**), 1.97 (t, $J = 2.5$ Hz, 1H, **3**); HRMS (ESI⁻) found $[\text{M}-\text{H}]^-$ 239.0130, $\text{C}_9\text{H}_7\text{N}_2\text{O}_4\text{S}^-$ requires 239.0127.

This compound is known. ^1H NMR and HRMS data are consistent with those previously reported.¹⁸² All other data is previously unreported.

5.2.5 N-(2-(3-methyl-3H-diazirin-3-yl)ethyl)-2-nitro-N-(prop-2-yn-1-yl)benzenesulfonamide (**18**)

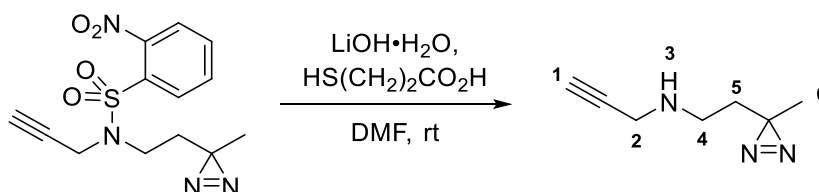


K_2CO_3 (2.69 g, 19.5 mmol, 3.33 eq.) and 2-nitro-N-(prop-2-yn-1-yl)benzenesulfonamide **17** (1.56 g, 6.50 mmol, 1 eq.) were added sequentially to a stirred solution of 2-(3-methyl-3H-diazirin-3-yl)ethyl 4-methylbenzenesulfonate **14** (1.65 g, 6.50 mmol, 1 eq.) in dimethylformamide (DMF, 13 mL) and the reaction stirred at $80\text{ }^\circ\text{C}$ for 3 h. The reaction mixture was diluted with EtOAc (75 mL) and H_2O (75 mL) and separated. The aqueous phase was further extracted with EtOAc (2×50 mL) and the

combined organics were washed successively with LiCl (5% (w/v) aq., 2×100 mL) and brine (100 mL), then dried over anhydrous MgSO_4 , filtered and concentrated *in vacuo*. The crude product was purified by automated flash column chromatography (20–100% EtOAc in *n*-hexane) to afford the title compound **18** as a pale yellow oil (1.64 g, 5.09 mmol, 78%): $R_f = 0.22$ (1:2 EtOAc/*n*-hexane); δ_{H} /ppm (400 MHz, CDCl_3) 8.08 – 7.98 (m, 1H, ArH), 7.79 – 7.65 (m, 2H, ArH), 7.65 – 7.59 (m, 1H, ArH), 4.17 (d, $J = 2.5$ Hz, 2H, **4**), 3.46 – 3.37 (m, 2H, **1**), 2.18 (t, $J = 2.5$ Hz, 1H, **5**), 1.66 – 1.56 (m, 2H, **2**), 1.05 (s, 3H, **3**); HRMS (ESI⁺) found $[\text{M}+\text{H}]^+$ 323.0815, $\text{C}_{13}\text{H}_{15}\text{N}_4\text{O}_4\text{S}^+$ requires 323.0814.

This compound is known. ¹H NMR and HRMS data are consistent with those previously reported.¹⁸² All other data is previously unreported.

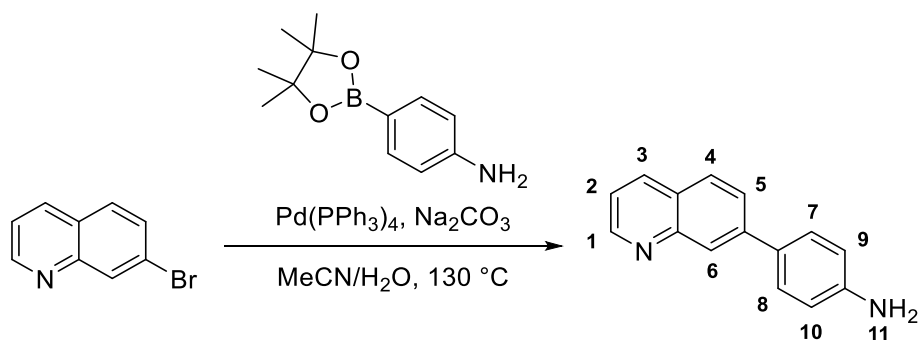
5.2.6 N-(2-(3-methyl-3H-diazirin-3-yl)ethyl)prop-2-yn-1-amine (19)



Lithium hydroxide monohydrate (857 mg, 20.4 mmol, 4 eq.) and 3-mercaptopropanoic acid (0.900 mL, 10.3 mmol, 2 eq.) were added to a stirred solution of *N*-(2-(3-methyl-3H-diazirin-3-yl)ethyl)-2-nitro-*N*-(prop-2-yn-1-yl)benzenesulfonamide **18** (1.64 g, 5.09 mmol, 1 eq.) in DMF (12.5 mL) and the reaction stirred at rt for 5 h. The reaction mixture was diluted with EtOAc (100 mL) and H_2O (100 mL) and separated. The aqueous phase was further extracted with EtOAc (2×100 mL) and the combined organics were washed successively with LiCl (5% (w/v) aq., 200 mL), sat. aq. NaHCO_3 (200 mL) and brine (100 mL), then dried over anhydrous MgSO_4 , filtered and concentrated *in vacuo*. The crude product was purified by flash column chromatography (1:1 EtOAc/*n*-hexane) to afford the title compound **19** as a yellow oil (520 mg, 3.80 mmol, 75%): $R_f = 0.22$ (1:1 EtOAc/*n*-hexane); δ_{H} /ppm (400 MHz, CDCl_3) 3.37 (d, $J = 2.4$ Hz, 2H, **2**), 2.54 (t, $J = 7.1$ Hz, 2H, **4**), 2.20 (t, $J = 2.4$ Hz, 1H, **1**), 1.55 (t, $J = 7.1$ Hz, 2H, **5**), 1.31 (s, 1H, **3**), 1.02 (s, 3H, **6**); HRMS (ESI⁺) found $[\text{M}+\text{H}]^+$ 138.1025, $\text{C}_7\text{H}_{12}\text{N}_3^+$ requires 138.1031.

This compound is known. ¹H NMR and HRMS data are consistent with those previously reported.¹⁸² All other data is previously unreported.

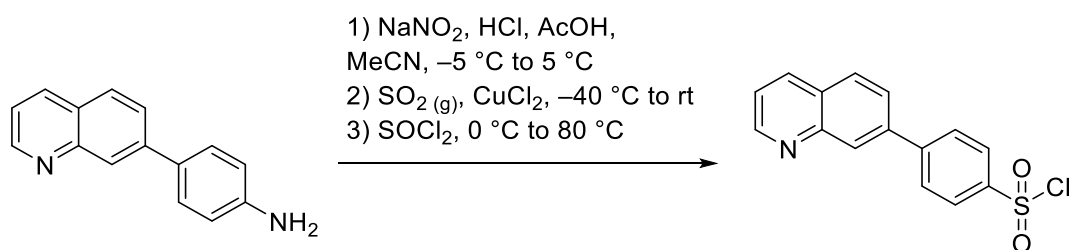
5.2.7 4-(quinolin-7-yl)aniline (22)



7-bromoquinoline **20** (2.00 g, 9.60 mmol, 1 eq.) was dissolved in MeCN (13 mL), Na₂CO₃ (509 mg, 4.80 mmol, 0.5 eq.) was dissolved in H₂O (6.5 mL) and both solutions added to solid 4-(4,4,5,5-tetramethyl-1,3,2-dioxaborolan-2-yl)aniline **21** (2.10 g, 9.59 mmol, 1 eq.). Tetrakis(triphenylphosphine)palladium(0) (336 mg, 0.290 mmol, 0.03 eq.) was added to the resulting stirred solution and the reaction refluxed at 130 °C for 18 h. The reaction was cooled to rt, diluted with EtOAc (10 mL), and filtered through a celite plug. The filtrate was concentrated *in vacuo* and the remaining aqueous component diluted with EtOAc (100 mL) and H₂O (100 mL) and separated. The aqueous phase was extracted with EtOAc (2 × 75 mL) and the combined organics were washed successively with H₂O (100 mL), brine (100 mL), then dried over anhydrous MgSO₄, filtered and concentrated *in vacuo*. The crude product was purified by automated flash column chromatography (18–100% EtOAc in *n*-hexane) to afford the title compound **22** as a yellow-gold solid (1.34 g, 6.09 mmol, 63%): *R_f* = 0.30 (4:1 EtOAc/*n*-hexane); *v*_{max}/cm⁻¹ (neat) 3412 (NH₂ antisymmetric), 3289 (NH₂ symmetric), 3200 (NH₂ bend overtone), 3015 (C-H), 1601 (NH₂ bend), 1495 (Ar C=C), 1433 (Ar C=C); *δ*_H/ppm (400 MHz, CDCl₃) 8.90 (dd, *J* = 4.3, 1.8 Hz, 1H, **1**), 8.26 (d, *J* = 1.6 Hz, 1H, **6**), 8.13 (dd, *J* = 8.2, 1.7 Hz, 1H, **3**), 7.83 (d, *J* = 8.6 Hz, 1H, **7**), 7.78 (dd, *J* = 8.5, 1.9 Hz, 1H, **8**), 7.65 – 7.53 (m, 2H, **7** and **8**), 7.34 (dd, *J* = 8.2, 4.3 Hz, 1H, **2**), 6.87 – 6.72 (m, 2H, **9** and **10**), 3.73 (s, 2H, **11**); *δ*_C/ppm (101 MHz, CDCl₃) 150.8, 148.8, 146.6, 142.3, 135.9, 130.4, 128.5 (2C), 128.1, 127.0, 126.0, 125.6, 120.6, 115.6 (2C); HRMS (ESI⁺) found [M+H]⁺ 221.1082, C₁₅H₁₃N₂⁺ requires 221.1079.

This compound is known.⁴⁶⁷ Presented data is previously unreported.

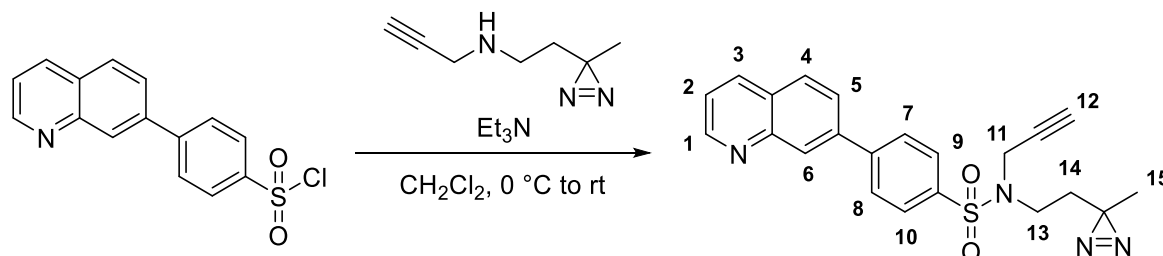
5.2.8 4-(quinolin-7-yl)benzenesulfonyl chloride (23)



Acetic acid (2 mL) was added to a stirred solution of 4-(quinolin-7-yl)aniline **22** (500 mg, 2.27 mmol, 1 eq.) in MeCN (15 mL) to yield a red solution, HCl (12.1 M, 1 mL) was added and the resulting yellow suspension was stirred vigorously and cooled to 5 °C. A solution of NaNO₂ (188 mg, 2.72 mmol, 1.2 eq.) in H₂O (0.4 mL) was added and the suspension stirred vigorously for 30 min. The reaction was then cooled to -40 °C and SO₂ gas was bubbled through the solution for 30 min after which a clear yellow solution was observed. CuCl₂ (152 mg, 1.13 mmol, 0.5 eq.) in H₂O (0.3 mL) was added and the reaction was allowed to warm to rt. The solution was degassed with N₂ and the solvent removed *in vacuo*. The crude residue was cooled to 0 °C and dissolved in SOCl₂ (10 mL). The solution was then refluxed at 80 °C for 1.5 h and the SOCl₂ removed under a stream of N₂. The crude residue was diluted in CH₂Cl₂ (250 mL) and H₂O (250 mL) and the combined phases filtered under vacuum. The filtrate was separated and the aqueous phase extracted with CH₂Cl₂ (2 × 100 mL). The combined organics were washed successively with H₂O (200 mL) and brine (200 mL), then dried over anhydrous MgSO₄, filtered and concentrated *in vacuo* to afford the title compound **23** as a crude brown solid (500 mg, 1.65 mmol) which was found to be unstable to silica-phase chromatography and was carried through to the next step without further purification.

Synthesis and characterisation previously unreported.

5.2.9 N-(2-(3-methyl-3H-diazirin-3-yl)ethyl)-N-(prop-2-yn-1-yl)-4-(quinolin-7-yl)benzenesulfonamide (**10**, 7PQYnD1)

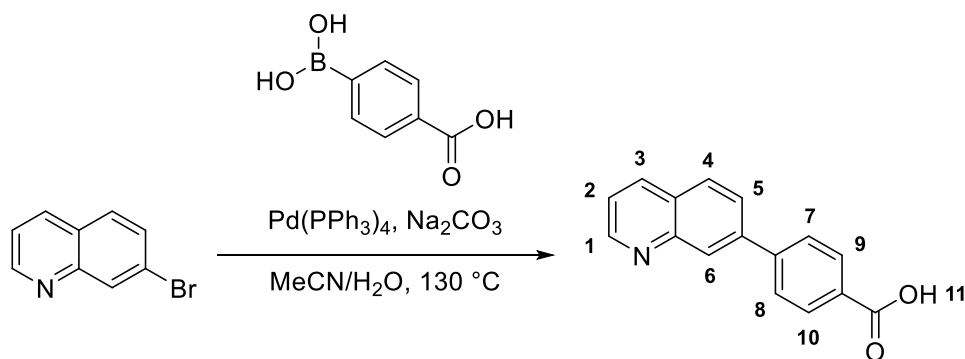


Triethylamine (0.18 mL, 1.30 mmol, 2.1 eq.) was added to a stirred solution of *N*-(2-(3-methyl-3H-diazirin-3-yl)ethyl)prop-2-yn-1-amine **19** (100 mg, 0.730 mmol, 1.2 eq.) in CH₂Cl₂ (2 mL) and the solution cooled to 0 °C. Crude 4-(quinolin-7-yl)benzenesulfonyl chloride **23** (185 mg, 0.609 mmol, 1 eq.) was added and the reaction stirred at rt for 2.5 h. The reaction mixture was diluted with CH₂Cl₂ (20 mL) and H₂O (20 mL) and separated. The aqueous phase was further extracted with CH₂Cl₂ (20 mL) and the combined organics were washed successively with H₂O (20 mL) and brine (20 mL), then dried over anhydrous MgSO₄, filtered and concentrated *in vacuo*. The crude product was purified by automated flash column chromatography (10–100% EtOAc in *n*-hexane) to afford the title compound **10** as an off-white solid (118 mg, 0.292 mmol, 48%): Purity 99% (LC-MS) R_t = 3.78 min, m/z 405.1 ([M+H]⁺); R_f = 0.31 (1:1 EtOAc/*n*-hexane); ν_{max}/cm⁻¹ (neat) 3267 (C≡C-H), 2892 (C-H), 2920 (C-H),

2887 (C-H), 2121 (C≡C), 1590 (diazirine), 1450 (Ar C=C); $\delta_{\text{H}}/\text{ppm}$ (400 MHz, CDCl_3) 8.98 (d, $J = 3.4$ Hz, 1H, **1**), 8.40 – 8.34 (m, 1H, **6**), 8.27 – 8.19 (m, 1H, **3**), 8.00 – 7.96 (m, 2H, **7** and **8**), 7.95 (d, $J = 8.1$ Hz, 1H, **4**), 7.92 – 7.87 (m, 2H, **9** and **10**), 7.83 (dd, $J = 8.5, 1.8$ Hz, 1H, **5**), 7.47 (dd, $J = 8.3, 4.2$ Hz, 1H, **2**), 4.18 (d, $J = 2.5$ Hz, 2H, **11**), 3.32 – 3.22 (m, 2H, **13**), 2.05 (t, $J = 2.5$ Hz, 1H, **12**), 1.69 – 1.60 (m, 2H, **14**), 1.09 (s, 3H, **15**); $\delta_{\text{C}}/\text{ppm}$ (101 MHz, CDCl_3) 151.2, 148.3, 145.0, 140.4, 137.7, 138.2, 136.2, 128.9, 128.6 (2C), 128.1 (2C), 127.9, 126.0, 121.8, 76.2, 74.5, 42.0, 36.8, 33.5, 24.2, 19.6; HRMS (ESI⁺) found $[\text{M}+\text{H}]^+$ 405.1381, $\text{C}_{22}\text{H}_{21}\text{N}_4\text{O}_2\text{S}^+$ requires 405.1385.

Synthesis and characterisation previously unreported.

5.2.10 4-(quinolin-7-yl)benzoic acid (**25**)



7-bromoquinoline **20** (500 mg, 2.40 mmol, 1 eq.) and 4-boronobenzoic acid **24** (398 mg, 2.40 mmol, 1 eq.) were dissolved in Na_2CO_3 (0.4 M, 12.5 mL) and MeCN (12.5 mL) and the solution degassed with N_2 for 10 min. Tetrakis(triphenylphosphine)palladium(0) (139 mg, 0.12 mmol, 0.05 eq.) was added and the reaction stirred at $90\text{ }^\circ\text{C}$ for 4 h. The hot suspension was filtered through a plug of celite and the filtrate concentrated *in vacuo*. The remaining aqueous component was washed with CH_2Cl_2 (2×20 mL) and acidified to pH 1 with HCl (2 M). The resulting precipitate was collected by vacuum filtration and washed successively with H_2O and Et_2O . The solid was dried under reduced pressure to afford the title compound **25** as a pale brown powder (357 mg, 1.43 mmol, 60%); $R_f = 0.13$ (4:1 EtOAc/*n*-hexane); $\nu_{\text{max}}/\text{cm}^{-1}$ (neat) 3356 (broad, O-H), 2892 (C-H), 2803 (C-H), 2529 (N-H), 1679 (C=O), 1567 (Ar C=C); $\delta_{\text{H}}/\text{ppm}$ (400 MHz, $\text{DMSO}-d_6$) 13.07 (s, 1H, **11**), 9.16 (dd, $J = 4.7, 1.7$ Hz, 1H, **1**), 8.81 (d, $J = 8.1$ Hz, 1H, **3**), 8.50 (s, 1H, **6**), 8.30 (d, $J = 8.6$ Hz, 1H, **4**), 8.17 (dd, $J = 8.6, 1.8$ Hz, 1H, **5**), 8.15 – 8.09 (m, 2H, **9** and **10**), 8.02 – 7.97 (m, 2H, **7** and **8**), 7.85 – 7.80 (m, 1H, **2**); $\delta_{\text{C}}/\text{ppm}$ (101 MHz, $\text{DMSO}-d_6$) 167.00, 148.81, 143.48, 142.68, 141.98, 140.56, 130.71, 130.22 (2C), 129.52, 127.83, 127.60 (2C), 127.12, 122.89, 122.11; HRMS (ESI⁺) found $[\text{M}+\text{H}]^+$ 250.0865, $\text{C}_{16}\text{H}_{12}\text{NO}_2^+$ requires 250.0868.

Synthesis and characterisation previously unreported.

5.3 Cell biology

5.3.1 Tissue Culture

All cell culturing was carried out in a sterile tissue culture cabinet sprayed with 70% (v/v) EtOH before and after use. All cell lines were cultured at 37 °C in a 5% CO₂ incubator. Mycoplasma tests were carried out monthly. Passage number was limited to 20–25 and stocks of early passages were frozen at –150 °C containing ~10⁶ cells in 1 mL FBS containing 10% (v/v) DMSO. All chemical tools were dissolved in DMSO, aliquoted and frozen at –20 °C until further use.

MDA-MB-468 cells were obtained from The Francis Crick Cell Services and were cultured in Dubecco's Modified Eagle Medium – low glucose (DMEM) supplemented with 10% (v/v) Fetal Bovine Serum (FBS). Cell harvesting was achieved by washing with Dubecco's phosphate-buffered saline (PBS) and treatment with 0.25% (w/v) Trypsin-EDTA. After 5 min incubation at 37 °C, the trypsin was quenched with DMEM to the appropriate volume for passage and aliquoted into the appropriate number of cell culture plates.

Jurkat *FADD*^{-/-} (12.1) cells were purchased from ATCC and were cultured in Roswell Park Memorial Institute 1640 (RPMI-1640) medium supplemented with 10% (v/v) FBS. Cell culturing was achieved by the transfer of the appropriate volume of parent cell suspension into subculturing flask(s) with fresh medium. Recombinant human TNF α was immediately reconstituted with water to 1 mg mL⁻¹ upon purchase, aliquoted and stored at –80 °C; working aliquots were made by diluting to 0.1 mg mL⁻¹ (57.4 nM) with RPMI-1640, stored at –80 °C.

5.3.2 Multipolar Spindle Assay

This was performed by AstraZeneca as described previously.³⁴¹ Briefly, HeLa cells were plated in 96-well plates at 7,000 cells per well and incubated at 37 °C overnight. The cells were treated with compounds in a dose-dependent manner from 0 to 11 μ M for 48 h. The cells were fixed by 4% (v/v) formaldehyde at rt for 10 min and followed by ice-cold methanol fixation for another 10 min. After washing with PBS four times, the cells were blocked in blocking buffer for 1 h at rt. The cells were labelled with primary antibodies, 1:2000 dilution of anti-cyclin B antibody (Thermo Fisher Scientific) and 1:4000 dilution of anti-pericentrin antibody (Abcam), for 16 h at 4 °C. After washing with PBS four times, the cells were labelled with secondary antibodies, 1:200 Alexa Fluor 488 anti-rabbit antibody and Alexa Fluor 594 anti-mouse antibody, for 1 h at rt. After washing with PBS twice, the nuclei were stained with 4',6-diamidino-2-phenylindole (DAPI) for 10 min at rt. The cells were washed twice with PBS and then applied to image acquisition by ImageXpress Micro High Content Screening System (Molecular Devices). The data were analysed by MetaXpress and accessed by AcuityXpress (Molecular Devices). The 16 fields in each well were acquired by ImageXpress Micro. The cyclin B

was labelled for scoring the mitotic cells and pericentrin was labelled for scoring the spindle pole number in each mitotic cell. Value output was taken as % mitotic cells with greater than 2 spindle poles.

5.3.3 Cell Viability Assay (MTS)

MDA-MB-468 cells were seeded 24 h before treatment in a sterile treated 96-well plate (Thermo Fisher Scientific) at a density of 8,000 cells per well to a final volume of 50 μ L in DMEM. PBS (100 μ L) was added to the outer wells. DMEM (50 μ L) containing the following as *the equivalent 2 \times solution* were added to the cells in triplicate:

- DMSO (0.1% (v/v), negative control),
- Puromycin (4 mM, positive control),
- Different concentrations of compound to be tested (0.1% (v/v) DMSO, prepared by serial dilution, dilution factor 3, starting from 1.5 μ M).

72 h later, a solution of MTS assay powder (3.28 mM in PBS 1 \times , Promega) and phenazine methosulfate (PMS, 3 mM in H₂O, Sigma-Aldrich) was prepared (20:1) and 20 μ L was added to each well. After 2 h, absorbance was measured 4 times per well at 490 nm (Envision Xcite plate reader, PerkinElmer) and the average absorbance taken. The average of the negative control was subtracted from every value and viability was calculated as a percentage relative to the positive control. EC₅₀ values were calculated by fitting data to a four-parameter dose-response function using GraphPad Prism 8 software.

5.3.4 Necroptosis and cytotoxicity assay

5.3.4.1 Plate treatment and image acquisition

I2.1 cells were seeded 24 h before treatment in a sterile 96-well plate (Greiner) at a density of 20,000 cells per well to a final volume of 70 μ L in RPMI-1640. The following solutions were added to the plate in 10 μ L portions as *the equivalent 10 \times solution* in the following order in triplicate according to the plate map in **Figure 5.1**:

1. Test compound(s) in a serial dilution in the desired range (final 0.1% (v/v) DMSO, vehicle added to remaining wells except the Triton X-100 wells – step 2), top concentration also added as a separate triplicate to test for cytotoxicity,
2. Triton X-100 (0.1% (v/v) in RPMI-1640),
3. TNF α (0.6 nM, RPMI-1640, vehicle added to remaining wells),
4. Sytox Green (1 μ M, 0.1% (v/v) DMSO in RPMI-1640, vehicle added to remaining wells).

	1	2	3	4	5	6	7	8	9	10	11	12
A	TNF 600 pM Compound 1 10 µM Sytox Green 1 µM			TNF 600 pM Compound 2 25 µM Sytox Green 1 µM			TNF 600 pM Compound 3 50 µM Sytox Green 1 µM			Triton 0.1% Sytox Green 1 µM		
B	TNF 600 pM Compound 1 5 µM Sytox Green 1 µM			TNF 600 pM Compound 2 12.5 µM Sytox Green 1 µM			TNF 600 pM Compound 3 25 µM Sytox Green 1 µM			Compound 1 10 µM Sytox Green 1 µM		
C	TNF 600 pM Compound 1 2.5 µM Sytox Green 1 µM			TNF 600 pM Compound 2 6.25 µM Sytox Green 1 µM			TNF 600 pM Compound 3 12.5 µM Sytox Green 1 µM			Compound 2 25 µM Sytox Green 1 µM		
D	TNF 600 pM Compound 1 1.25 µM Sytox Green 1 µM			TNF 600 pM Compound 2 3.13 µM Sytox Green 1 µM			TNF 600 pM Compound 3 6.25 µM Sytox Green 1 µM			Compound 3 50 µM Sytox Green 1 µM		
E	TNF 600 pM Compound 1 0.63 µM Sytox Green 1 µM			TNF 600 pM Compound 2 1.56 µM Sytox Green 1 µM			TNF 600 pM Compound 3 3.13 µM Sytox Green 1 µM			Sytox Green 1 µM		
F	TNF 600 pM Compound 1 0.31 µM Sytox Green 1 µM			TNF 600 pM Compound 2 0.78 µM Sytox Green 1 µM			TNF 600 pM Compound 3 1.56 µM Sytox Green 1 µM			Untreated, unstained		
G	TNF 600 pM Compound 1 0.16 µM Sytox Green 1 µM			TNF 600 pM Compound 2 0.39 µM Sytox Green 1 µM			TNF 600 pM Compound 3 0.78 µM Sytox Green 1 µM					
H	Vehicle Compound 1, TNF 600 pM, Sytox Green 1 µM			Vehicle Compound 2, TNF 600 pM, Sytox Green 1 µM			Vehicle Compound 3, TNF 600 pM, Sytox Green 1 µM					

Figure 5.1 Standard plate map for necroptosis and cytotoxicity assay.

The plate was cleared of any bubbles and agitated sufficiently to prevent the cells from clumping. The plate was transferred to an IncuCyte® S3 Live Cell Analysis System (Sartorius) where each well was imaged 4 times at 10× magnification with phase contrast and green fluorescence (λ_{ex} 440–480 nm, λ_{em} = 504–544 nm) every hour for 24 h.

5.3.4.2 Image analysis

Cell images were analysed with Incucyte 2019B Rev 2® software. At least one representative image was used to inform image machine learning software from:

- Positive control (column 11), 0 h time-point;
- Unstained control (column 2), 0 h time-point;
- Untreated control (column 10, E-G), 0 h time-point;
- The treated control (column 10, B-D), a time-point ≥ 6 h;
- Compound treated wells (columns 3-9), a time-point ≥ 6 h (at least 3 images).

The following parameters were used for most experiments but adjusted according to the cell specific parameters for each assay using the above image set as a guide:

- Phase analysis: segmentation adjustment was set to 1 and cleanup parameters were unaltered from the default settings. A minimum area filter of $70 \mu\text{m}^2$ was applied while no filters were added for eccentricity.
- Green analysis: Top-Hat segmentation was used with a radius of $13 \mu\text{m}$ and a threshold of 2 GCU. All other parameters were unchanged.

5.3.4.3 Data analysis

After complete analysis of all images, “green integrated intensity per image/phase area per image” ($(\text{GCU} \times \mu\text{m}^2/\text{Image}) / (\mu\text{m}^2/\text{Image})$), denoted “ G_P ” values were extracted for each well/image at each time-point and exported to Microsoft Excel. Background subtraction was performed for each well/image using the value from the initial time point and the data exported to GraphPad Prism 8.

Background corrected G_P values were grouped into their technical replicates and represented graphically \pm standard deviation (SD) plotted against time for each concentration. To generate EC_{50} values over a concentration range, the linear growth phase of G_P against time curves for each individual replicate well were taken and linear regression performed on each. The resultant rates (slope) were then plotted \pm SD of technical replicates against \log_{10} concentration (nM or μM depending on experiment) and fitted using a four-parameter dose-response curve to generate an EC_{50} value. For compounds with >1 biological replicate, the average rates for all concentrations were normalised to the non-TNF α (0% necroptosis) and TNF α only (100% necroptosis) within their respective biological replicate, and the resulting % response values were plotted as biological replicates \pm standard error of the mean (SEM).

Alternatively, cumulative necroptosis response was calculated by plotting G_P against time for each replicate and performing Area Under Curve (AUC) analysis over the whole experiment time. The area values were grouped into technical replicates and plotted as histograms \pm SD. For compounds with >1 biological replicate, the average AUC values for that compound treatment were normalised to the non-TNF α (0% necroptosis) and TNF α only (100% necroptosis) within their respective biological replicate, and the resulting % response values were plotted as biological replicates \pm SEM; ordinary one-way ANOVA with multiple comparisons was used to determine significant deviances from control conditions.

Cytotoxicity assay data was generated by plotting $G_P \pm$ SD for each replicate condition as a percentage of the maximum response at the experimental endpoint, or cumulative $G_P \pm$ SD from AUC data as described above.

5.3.5 Probe labelling (photocrosslinking) assays

Probe incubation was carried out in sterile treated 6-well plates (2 mL working volume) or 10 cm dishes (7 mL (MDA-MB-468) or 10 mL (I2.1) working volume). All compound treatments were performed with a pre-prepared 1000× stock of the desired concentration in DMSO and added directly to the relevant plate/well with mixing. Irradiation was performed using an in-house designed and built UV LED box (Charlie Saunders) with a monochromatic wavelength of 365 nm. Generated lysates were stored at –80 °C until further analysis (**Section 5.4**).

5.3.5.1 MDA-MB-468 cells

For each experiment, the plates/dishes were pre-seeded with MDA-MB-468 cells and the experiment carried out when cells had achieved 90–100% confluency. DMEM was replaced and the plates/dishes were incubated at 37 °C for 15 min. For competition experiments only, the relevant plates/wells were first treated with DMSO vehicle (0.1% (v/v)) or varying concentrations of competitive inhibitor in DMSO as indicated and incubated at 37 °C for 1 h before treating with probe. For all probe labelling experiments, competition or otherwise, the plates/dishes were treated with either DMSO vehicle (0.1% (v/v)) or varying concentrations of probe as required by the experiment and incubated at 37 °C for 3 h.

If irradiating the samples, the following was performed 1 plate/3 dishes at a time out of the incubator. Each plate/dish had media replaced and was irradiated with UV light for 30 s (365 nm) and placed on ice while irradiation of other samples was performed.

The cells were relieved of media, washed twice with PBS, then lysed with lysis buffer (70 µL (6-well plates), 300 µL (10 cm dishes); 1% (w/v) sodium dodecyl sulphate (SDS), 1% (v/v) Triton X-100, EDTA-free complete protease inhibitor cocktail (1×, Roche) in PBS) on ice for 10 min. The lysates were scraped and transferred to corresponding Lo-Bind Eppendorfs. Each lysate was probe sonicated (20% amplitude, 20 s (2 s pulse, 3 s rest)) to shear the nuclear DNA. Protein concentration was determined using the DC Protein Assay (Bio-Rad) in a 96-well plate as per the manufacturer's instructions.

5.3.5.2 I2.1 cells

For each experiment, the plates/dishes were pre-seeded with I2.1 cells and the experiment carried out when cells had achieved a density of $>10^6$ cells mL⁻¹. The relevant plates/wells were co-treated, first with DMSO vehicle (0.1% (v/v)) or competitive inhibitor as indicated if performing a competition experiment, then with DMSO vehicle (0.1% (v/v)) or probe as indicated; the cells were then incubated at 37 °C for 3 h. If inducing necroptosis, cells were treated with 0.5 nM TNFα (from 57.4 nM RPMI-1640 stock) 1–2 h before irradiation.

If irradiating the samples, the following was performed 1 plate/3 dishes at a time out of the incubator. Each plate/dish was irradiated with UV light for 30 s (365 nm) and placed on ice while irradiation of other samples was performed.

The cells were collected into sterile falcon tubes or 5 mL eppendorfs, pelleted for 5 min at $200 \times g$ and relieved of media. Cells were washed once with PBS, pelleted for 5 min at $200 \times g$ and relieved of PBS. The pellet was lysed with lysis buffer (70 μ L (6-well plates), 300 μ L (10 cm dishes); 0.1% or 1% (w/v) sodium dodecyl sulphate (SDS), 1% (v/v) Triton X-100, EDTA-free complete protease inhibitor cocktail (1 \times , Roche) in PBS) on ice for 10 min and the lysates were transferred to Eppendorf tubes. For lysates in 0.1% SDS lysis buffer, the lysate was cleared by centrifugation (5 min, $17,000 \times g$) and the supernatant collected into a Lo-Bind Eppendorf tube. For lysates in 1% SDS lysis buffer, each lysate was probe sonicated (20% amplitude, 20 s (2 s pulse, 3 s rest)) to shear the nuclear DNA. Protein concentration was determined using the DC Protein Assay (Bio-Rad) in a 96-well plate as per the manufacturer's instructions.

5.3.6 Transient overexpression

DNA transfections were performed either with Lipofectamine® 2000 or Lipofectamine® LTX with Plus™ Reagent according to standard manufacturer's protocol. Briefly, MDA-MB-468 cells were seeded in sterile treated 6- or 12-well plates and grown to 90–100% confluence. Optimal DNA:Lipofectamine (μ g: μ L) was determined via a titration of both DNA (0.25–2 μ g) and Lipofectamine reagent (1:3–1:9). The cells were incubated for 24 h, lysed (**Section 5.3.5.1**), and protein expression was analysed by Western blot (**Section 5.4.3**). All further transfection experiments were performed at 1:3 DNA:Lipofectamine with 2 μ g DNA, treating as indicated, incubating for 24 h and analysing by Western blot.

5.3.7 RNA interference

5.3.7.1 siRNA duplexes

All siRNA were purchased as Stealth RNAi™ siRNA duplexes (**Table 5.1**) from Thermo Fisher Scientific and reconstituted with 1 mL of RNase-free water to 20 μ M. The negative control used was the Stealth RNAi™ siRNA Negative Control, Med GC (Thermo Fisher Scientific).

5.3.7.2 Protocol

RNAi transfections were performed with Lipofectamine® RNAiMAX Transfection Reagent (Thermo Fisher Scientific), adapting the standard manufacturer's protocol for reverse transfections. Briefly, I2.1 cells were transfected in 6-well plates (100,000 cells per mL, 3 mL final volume) by preparing a master stock (1% (v/v)) of Lipofectamine in Opti-MEM™ Reduced Serum Medium (Gibco) and transferring 500 μ L to the well plates, adding 1.5 μ L of the relevant siRNA duplex (20 μ M), gently mixing, and

waiting for >10 min before adding 2.5 mL of I2.1 cell suspension gently over the top. These amounts result in final well transfection conditions of 10 nM siRNA and 0.17% (v/v) Lipofectamine. Knockdown was assessed after 48 h (or other time point) by cell lysis (**Section 5.3.5.2**) and Western blot (**Section 5.4.4**). Assessment of the phenotypic effect of RNAi on necroptosis was achieved by transferring 80 μ L of the relevant cell suspension to a 96-well plate to give a final cell density of 20,000 cells per well and adding TNF α to a final concentration of 0.06 nM and SG to a final concentration of 1 μ M with appropriate controls, performing the necroptosis assay as described in **Section 5.3.4**.

Table 5.1 siRNA molecules used in RNAi assays.

Gene targeted	siRNA number	siRNA ID	Sequence 5'–3' (sense)
<i>ADA</i>	1	HSS100159	GGGAGCUUCUCGACCUCUCUAUAA
	2	HSS100160	CGCCUUCGACAAGCCCAAAGUAGAA
	3	HSS100161	UGGCCAACUCCAAGUGGAGCCAAU
<i>CD3ϵ</i>	1	HSS101503	CCUCUGCCUCUUAUCAGUUGGCGUU
	2	HSS189979	UGGUUUUACACAGACACCAUAUAAA
	3	HSS101505	GACAUGCCUCAGUAUCCUGGAUCU
<i>FDFT1</i>	1	HSS103615	CCAGUCGCAGUUUCGCAGCUGUUAU
	2	HSS103617	GCCACUUUGGCUGCCUGUUUAUAAUA
	3	HSS176875	GAGCUCUGGACACACUGGAAGAUGA
<i>MLKL</i>	1	HSS176401	CAAGGAAACUUUGAGGCAGUAUUUA
	2	HSS136795	UCGAAUCUCCCAACAUCUGCGUAU
	3	HSS136796	GCAACGCAUGCCUGUUUCACCCAU
<i>SCCPDH</i>	1	HSS121648	CCAGUUCAGUAUGCUGCGUAUGUAA
	2	HSS121649	GGGAAGACCAACACUGUCAUCUGAA
	3	HSS121650	CCUGACUAUACAUAUCAGGACCUGAG
<i>TMEM97</i>	1	HSS120668	CCUGAGACUUUGCAUGAACGGUUAA
	2	HSS120669	CCCUACUUACUCAUCCCAUUCUAUC
	3	HSS178435	CAGUCGAGUUUAGAAACCUGCUGAA

5.4 Biochemistry

5.4.1 Click reaction

The desired amount of lysed protein from each sample was made up to 0.5–2 mg mL⁻¹ with PBS to a total volume of \leq 300 μ L. The following “click mixture” was prepared separately, preparing 6 μ L for every 100 μ L of lysate:

- Click reagent (AzTB or AzRB (**Figure 1.7**), 10 mM in DMSO, 1 vol; final concentration in reaction 0.1 mM),
- CuSO₄ (50 mM in H₂O, 2 vol; final concentration in reaction 1 mM),
- Tris(2-carboxyethyl)phosphine (TCEP, 50 mM in H₂O, 2 vol; final concentration in reaction 1 mM),

- Tris(benzyltriazolylmethyl)amine (TBTA, 10 mM in DMSO, 1 vol; final concentration in reaction 0.1 mM).

The click mixture was vortexed and incubated at rt for 2 min before 6 μ L of the mixture was added to every 100 μ L of lysate. The reaction mixtures were shaken at rt for 1 h before being quenched with EDTA (500 mM in H₂O) to a final concentration of 5 mM.

A table-top centrifuge was pre-chilled to 4 °C. Proteins were precipitated by adding H₂O (1 vol), MeOH (2 vol) and CHCl₃ (0.5 vol), vortexing briefly, then centrifuging at 17,000 \times g for 5 min. The CHCl₃ and H₂O/MeOH layers were discarded and the interface of protein pellet was retained. The pellet was washed with MeOH (300 μ L), sonicated to break up the pellet then stored at –80 °C for at least 20 min. The proteins were pelleted by centrifugation at 10,000–17000 \times g for 5–10 min or until a compact pellet was formed. The MeOH was decanted and the pellet air-dried for 5 min. The pellet was resuspended by completely dissolving in 1% (w/v) SDS in PBS (to 5 mg mL⁻¹ protein) before being made up to 1 mg mL⁻¹ protein with PBS.

5.4.2 Gel electrophoresis

Either Bio-Rad 15-well 12% Mini-PROTEAN® TGX Stain-Free™ pre-cast gels or 10-/15-well SDS-polyacrylamide gels with a 10% or 12% resolving gel and 4% stacking gel cast in house <24 h before use were used for gel electrophoresis experiments. Gel casting was performed using the following recipe (Table 5.2).

Table 5.2 SDS-PAGE gel casting recipe (makes two gels).

Reagent	Resolving gel (10%)	Resolving gel (12%)	Stacking gel (4%)
H ₂ O	4 mL	3.4 mL	3.05 mL
Resolving/Stacking Buffer (National Diagnostics)	2.5 mL	2.5 mL	1.25 mL
Protogel 30% (National Diagnostics)	3.4 mL	4 mL	0.65 mL
Ammonium Persulfate (10% (w/v) in H ₂ O)	100 μ L	100 μ L	25 μ L
<i>N,N,N',N'</i> -tetramethylethylenediamine	10 μ L	10 μ L	5 μ L

All gels were run using a Bio-Rad Mini-PROTEAN® Tetra Cell with a Bio-Rad PowerPac™ Basic power supply. In general, ~15 μ g of protein was run per well in a volume of ~15 μ L.

Samples were prepared by adding 5 μ L of 4 \times loading buffer (1:4 β -mercaptoethanol:5 \times NuPAGE LDS sample buffer) to 15 μ L of sample and boiling at 95 °C for 10 min. The samples were briefly centrifuged then 15 μ L of each sample was added to a well of the gel, with at least one well also containing Precision Plus Protein™ All Blue Prestained Protein Standard (2 μ L, Bio-Rad). The gels were run in running buffer (25 mM Tris, 192 mM glycine, 0.1% (w/v) SDS) for 10 min at 85 V then up to 1 h at 180 V for in-house cast gels, or 50 min at 180 V for pre-cast gels. Any fluorescence on the gel was detected using

a Typhoon™ FLA 9500 biomolecular imager (GE Healthcare Life Sciences) with the Cy3 ($\lambda_{\text{ex}} = 532 \text{ nm}$, $\lambda_{\text{em}} = 610 \text{ nm}$) filters to detect the TAMRA fluorophore, and the contrast normalized using Fiji (ImageJ) software. The protein loading was verified by staining with Coomassie Brilliant Blue. Coomassie stained gels were imaged using the digitisation setting (trans-illumination) on an ImageQuant LAS-4000 Imaging System (Fujifilm) and the contrast normalized in Fiji.

5.4.3 Pull down

50 μL of Pierce™ NeutrAvidin™ Agarose beads (proteomics) or 300 μL of streptavidin coated magnetic beads (New England Biolabs, Western blot) were used per 1 mg of total protein per sample to an absolute minimum of 20 μL of agarose beads or 15 μL magnetic beads. All bead washes were performed by moderate shaking for 1 min then either briefly pelleting by table-top centrifuge and vacuum aspirating the supernatant with fine-end pipette tips (agarose) or by partitioning the beads using a magnet (magnetic). The beads were pre-washed three times with 0.2% (w/v) SDS in PBS, then protein samples (1 mg mL^{-1}) were added over the beads and incubated with moderate shaking at rt for 2 h.

For Western blot analysis, the beads were washed three times with 300 μL 0.2% (w/v) SDS in PBS and captured proteins were released from the beads by boiling in 14 μL 2 \times sample loading buffer (95 °C, 10 min), briefly centrifuging and the supernatant loaded straight on to an SDS-PAGE gel. For proteomic analysis (agarose beads), the beads were treated as described below (**Section 5.5**).

5.4.4 Western Blot

SDS-PAGE gels intended for Western blot were prepared and run as outlined above. Proteins were wet transferred to nitrocellulose membrane (GE healthcare) in transfer buffer (25 mM Tris, 190 mM glycine and 20% (v/v) MeOH) at 100 V for 1 h. Successful transfer was confirmed by staining with Ponceau S. Membranes were blocked for 1 h at rt in either 5% (w/v) non-fat dried skimmed milk (NFDM) powder in TBS-T (1 \times Tris-buffered saline, 0.1% (v/v) Tween-20), 5% (w/v) bovine serum albumin (BSA) in TBS-T, or 5% (w/v) NFDM plus 1% (w/v) BSA in TBS-T (PA5-23003 only). Staining with primary antibody was performed in blocking buffer or plain TBS-T (anti-FLAG M2 only) for 1 h at rt or overnight at 4 °C. The blot was washed with TBS-T (3 \times 5 min) and, if necessary, stained with secondary antibody in blocking buffer for 1 h at rt. The blot was washed with TBS-T (3 \times 5 min) and visualized using Immobilon Crescendo Western HRP substrate, imaging using the chemiluminescence setting on an ImageQuant LAS-4000 Imaging System. To detect the ladder, Cy5 ($\lambda_{\text{ex}} = 635 \text{ nm}$, $\lambda_{\text{em}} = 670 \text{ nm}$) filters were used on the fluorescence setting.

5.4.5 *In vitro* photocrosslinking assays

5.4.5.1 In solution

In a clear 96-well plate, wells containing 1× assay buffer (**Section 5.6.1**), 1 μM GST-PARP6 (storage buffer: 25 mM Tris-HCl pH 8.0, 100 mM NaCl, 10% (v/v) glycerol, 2 mM dithiothreitol (DTT), 0.005% (w/v) Triton X-100), and 5 μM **PARPYnD** (from 100× stock (10% (v/v) DMSO) – added last) were made up to final volume with H₂O and incubated on ice for 15 min in the dark. The plate was irradiated with UV light (365 nm monochromatic) and samples were removed into Eppendorf tubes at the indicated time points. 10 μL aliquots of each sample were supplemented with BSA (1 mg/mL in PBS) to a final volume of 50 μL. The proteins were precipitated as described above (**Section 5.4.1**) to remove Tris (in GST-PARP6 storage buffer) which would otherwise inhibit the click reaction. Proteins were clicked to AzTB (**Section 5.4.1**), precipitated again, and the results analysed by in-gel fluorescence (**Section 5.4.2**).

5.4.5.2 In lysates

Native MDA-MB-468 lysates were generated by trypsination of one confluent 75 cm² flask of cells as described above (**Section 5.3.1**). Trypsin was quenched and removed by aspiration after centrifugation (200 × g, 5 min). The cells were washed similarly in PBS and resuspended in cold PBS (250 μL) supplemented with EDTA-free complete protease inhibitor cocktail (1×, Roche). Cells were lysed on ice by probe sonication (20% amplitude, 18 s (3 s pulse, 3 s rest)) and the lysate was cleared by centrifugation (5 min, 17,000 × g). Protein concentration was determined by DC protein concentration assay and the lysate snap frozen in liquid N₂ and stored at –80 °C. Lysates were thawed on ice before use.

In a clear 96-well plate, wells containing 2 mg mL⁻¹ native MDA-MB-468 lysate, 0.1 μM GST-PARP6 (or blank storage buffer), and appropriate concentration of **PARPYnD/AZ0108** (from 100× stock (10% (v/v) DMSO) – added last) were made up to final volume with PBS and incubated on ice for 30 min in the dark. The plate was irradiated with UV light for 5 min (365 nm monochromatic) and each sample transferred to Eppendorfs. The proteins were precipitated as described above to remove Tris. Proteins were clicked to AzTB and enriched as described above, and the results analysed by gel and Western blot.

5.4.5.2.1 *Variation with PreScission™ Protease*

When also treating the samples with PreScission™ Protease, samples were made up with the cleavage buffer (50 mM Tris-HCl, 150 mM NaCl, 1 mM EDTA, 1 mM DTT, pH 7.0) rather than PBS, and GST-PARP6 was added to a concentration of 0.3 μM. Cleavage was performed using 1 U of enzyme overnight with moderate shaking at 4 °C. Samples were irradiated and prepared for gel-based analysis.

5.5 Chemical proteomics

5.5.1 General methods

Lysates for all proteomics experiments were derived from cells cultured in 10 cm dishes in triplicate for each experimental condition. 600 µg of labelled protein clicked to AzRB were enriched on NeutrAvidin agarose, all as described above. All buffers were prepared fresh and filtered (0.2 µm) in ultra-pure MilliQ® water, UPLC grade solvents were used, and the work surface cleaned with 70% (v/v) EtOH before use. Dedicated tips and solutions were used to minimize cross contamination. Sample evaporation was performed in a Savant SPD1010 SpeedVac® Concentrator at 45 °C.

5.5.2 Peptide preparation

5.5.2.1 Label-free quantification

The beads were washed twice with 300 µL 1% (w/v) SDS in 50 mM ammonium bicarbonate (AMBIC). Proteins were reduced and alkylated with 5 mM TCEP and 10 mM chloroacetamide in 60 µL 50 mM AMBIC with moderate shaking for 30 min at rt. The beads were washed 3 times with 300 µL 50 mM AMBIC. Beads were resuspended in 50 µL 50 mM AMBIC and proteins were digested on-bead by treatment with 1 µL trypsin (Promega, 20 µg dissolved in 100 µL 50 mM AMBIC) with vigorous shaking at 37 °C overnight. The samples were briefly centrifuged and the supernatant transferred to new Eppendorfs. The beads were washed sequentially with 80 µL 50 mM AMBIC and 70 µL 1.5% trifluoroacetic acid in H₂O and both washed were combined with the original supernatant.

5.5.2.2 Tandem mass tag (TMT) quantification

The beads were washed twice with 300 µL 1% (w/v) SDS in 50 mM 4-(2-hydroxyethyl)-1-piperazineethanesulfonic acid (HEPES, pH 8). Proteins were reduced and alkylated with 5 mM TCEP and 10 mM chloroacetamide in 60 µL 50 mM HEPES with moderate shaking for 30 min at rt. The beads were washed 3 times with 300 µL 50 mM HEPES. Beads were resuspended in 30 µL 50 mM HEPES and proteins were digested on-bead by treatment with 1 µL trypsin (Promega, 20 µg dissolved in 100 µL 50 mM HEPES) with vigorous shaking at 37 °C overnight. The samples were briefly centrifuged and 10 µL of the supernatant from each sample was TMT-labelled by combining with 10 µL of the appropriate TMT10plex™ Isobaric Mass Tag Labelling Reagent (Thermo Fisher Scientific) dissolved in acetonitrile (8 mg mL⁻¹) with moderate shaking for 2 h at rt (see **Appendix III** for TMT labels used for samples in each experiment). TMT-labelling was quenched by the addition of 1.1 µL of 5% (w/v) hydroxylamine and the samples from each TMT set were combined into one “plex” solution. These samples were evaporated to dryness.

5.5.3 Peptide desalting

5.5.3.1 Stage tipping

Each stage tip was prepared by cutting 3× polystyrene-divinylbenzene copolymer (SDB-XC) disks (3M) and using these to plug a p200 pipette tip. The stage tip was activated with 150 μL MeOH by centrifugation (1100 × g, 3 min), then equilibrated with 150 μL H₂O by centrifugation (1100 × g, 3 min). Peptides were resuspended in ≤200 μL 0.5% trifluoroacetic acid in H₂O if not already in this solution, and each sample transferred to a stage tip. Peptides were loaded on to the SDB-XC column by centrifugation as above and desalted by centrifugation with 150 μL H₂O. The stage tips were transferred to new Eppendorfs and the peptides liberated from the column by centrifugation with 60 μL 70% (v/v) acetonitrile into Lo-Bind Eppendorfs. The peptides were evaporated to dryness and stored at –80 °C.

5.5.3.2 3-layer fractionation

Each stage tip was prepared by cutting 3× polystyrene-divinylbenzene copolymer partially modified with sulfonic acid (SDB-RPS) disks (3M) and using these to plug a p200 pipette tip. The tip was equilibrated with 150 μL H₂O by centrifugation (3000 × g, 3 min). Samples were dissolved in (or adjusted to) 1% (v/v) aqueous trifluoroacetic acid and each sample transferred to a stage tip. Peptides were loaded onto the SDB-RPS column by centrifugation as above. Peptides were desalted by centrifugation with 3× 60 μL of 0.2% (v/v) trifluoroacetic acid in H₂O. Peptides were then liberated from the column sequentially by centrifugation with 60 μL of each of the following buffers (**Table 5.3**) into separate Eppendorfs:

Table 5.3 Buffers used for three-layer fractionation.

Fraction	Buffer composition
1	100 mM ammonium formate, 40% (v/v) MeCN, 0.5% (v/v) Formic Acid
2	150 mM ammonium formate, 60% (v/v) MeCN, 0.5% (v/v) Formic Acid
3	5% (v/v) ammonium hydroxide, 80% (v/v) MeCN

All fractions of each sample were evaporated to dryness and stored at –80 °C.

5.5.3.3 6-layer fractionation

Each stage tip was prepared by cutting 3× polystyrene-divinylbenzene copolymer modified with sulfonic acid (SCX) disks (3M) and using these to plug a p200 pipette tip. The tip was activated with 150 μL MeCN by centrifugation (3000 × g, 3 min) then equilibrated with 150 μL H₂O by centrifugation (3000 × g, 3 min). Samples were dissolved in (or adjusted to) 1% (v/v) aqueous trifluoroacetic acid and each sample transferred to a stage tip. Peptides were loaded onto the SCX column by centrifugation as above. Peptides were desalted by centrifugation with 3× 60 μL of 0.2% (v/v) trifluoroacetic acid.

Peptides were then liberated from the column sequentially by centrifugation with 60 μL of each of the following buffers (**Table 5.4**) into separate Lo-Bind Eppendorfs:

Table 5.4 Buffers used for six-layer fractionation.

Fraction	Buffer composition
1	75 mM ammonium acetate, 20% (v/v) MeCN, 0.5% (v/v) Formic Acid
2	125 mM ammonium acetate, 20% (v/v) MeCN, 0.5% (v/v) Formic Acid
3	200 mM ammonium acetate, 20% (v/v) MeCN, 0.5% (v/v) Formic Acid
4	300 mM ammonium acetate, 20% (v/v) MeCN, 0.5% (v/v) Formic Acid
5	400 mM ammonium acetate, 20% (v/v) MeCN, 0.5% (v/v) Formic Acid
6	5% (v/v) ammonium hydroxide, 80% (v/v) MeCN

All fractions of each sample were evaporated to dryness and stored at $-80\text{ }^{\circ}\text{C}$.

5.5.4 LC-MS/MS methodology

Samples were rehydrated in up to 15 μL 0.5% (v/v) formic acid, 2% (v/v) MeCN in Optima™ LC-MS H₂O (Fisher Scientific) and dissolved completely by vortexing and sonication. Samples were filtered through 3 \times Durapore® membrane filters (Millipore) plugged into a p20 pipette tip by centrifuging the samples through the filters (4000 \times g, 5 min) into a mass spectrometry vial. Samples were stored at 4 $^{\circ}\text{C}$ until ready for analysis.

Up to 2 μL of the peptide solution was injected an EASY-Spray™ Acclaim PepMap C₁₈ column (50 cm \times 75 μm inner diameter, Thermo Fisher Scientific) using a 3-hour linear gradient separation of 0–100% solvent B (80% MeCN supplemented with 0.1% formic acid): solvent A (2% MeCN supplemented with 0.1% formic acid) at a flow rate of 250 nL min^{-1} . The liquid chromatography was coupled to a QExactive mass spectrometer via an easy-spray source (Thermo Fisher Scientific) which operated in data-dependent mode with survey scans acquired at a resolution of 70,000 at m/z 200. Scans were acquired from 350 to 1800 m/z . Up to 10 of the most abundant isotope patterns with charge +2 or higher from the survey scan were selected with an isolation window of 1.6 m/z and fragmented by HCD with normalized collision energy of 25. The maximum ion injection times for the survey scan and the MS/MS scans (acquired with a resolution of 35,000 at m/z 200) were 20 and 120 ms, respectively. The ion target value for MS was set to 10^6 and for MS/MS to 10^5 , and the intensity threshold was set to 8.3×10^2 .

5.5.5 Data analysis

5.5.5.1 MaxQuant and Perseus

Peptide searches were performed in MaxQuant versions 1.6.0.2–1.6.7.0. For all experiments, oxidation (M) and acetyl (protein N-term) were set as variable modifications, carbamidomethyl (C) was set as a fixed modification, trypsin/P was set as the digestion mode, re-quantify and match between runs were

selected, and up to date UniProt FASTA files for the human proteome and contaminants databases were used. For LFQ data, under group-specific parameters and label-free quantification, LFQ was selected with a min. ratio count of 2 and fast LFQ selected (min. number of neighbours: 3, average number of neighbours: 6). For TMT data, under group-specific parameters and type, reporter ion MS² was selected, and the appropriate TMT10plex™ isobaric labels selected for both lysines and N-termini.

Data analysis was performed in Perseus version 1.6.7.0. LFQ intensities (LFQ) or reporter intensity corrected values (TMT) were loaded into the matrix. Data was filtered by removing rows based on “only identified by site”, “reverse”, and “potential contaminant” columns. Data were log₂ transformed and filtered by row, retaining those that had at least 2 valid values in each triplicate condition. TMT data were normalized further by subtracting the mean of each row within each TMT “plex” (if multiple TMT sets were used) and both TMT and LFQ data were normalized for protein abundance by subtracting the median of each column. Volcano plots were generated using a pairwise Student’s t-test and the cut-offs generated using the false discovery rate (FDR) and S₀ values indicated. Imputed LFQ values were generated after filtering valid values, retaining rows that has at least 2 valid values in *at least one* condition, and replacing missing values from the normal distribution (width: 0.3, down shift: 1.8) in total matrix mode. Data were normalised and volcano plots generated as described.

5.5.5.2 PEAKS

MS raw files were processed in PEAKS version 8.0. Trypsin was selected as the digestion enzyme, allowing for a maximum of 2 missed cleavages. Deamidation, N-terminal acetylation, cysteine carbamidomethylation, methionine oxidation and photochemical **7PQYnD**-modified with cleaved AzRB adducts (**7PQYnD**-AzR, C₃₀H₃₅N₉O₅S, exact mass 633.2482) were used as variable modifications, and up to date UniProt FASTA files for the human proteome and contaminants databases were used. The peptide -log₁₀P quality score was set as ≥60 for the modified site identification analysis.

5.6 Biochemical assays

5.6.1 PARP6 auto-ADP ribosylation assay

This protocol was adapted from Hutin, Grimaldi and Matthews.⁴⁶⁸ Briefly, reaction tubes containing 1× assay buffer (20×: 1 M Tris-HCl pH 8.0, 4 mM DTT, 80 mM MgCl₂), 25 μM NAD⁺-biotin (added last), 0.3 μM GST-PARP6, appropriate concentration of inhibitor (from 10× stock (1% (v/v) DMSO)) were made up to final volume with H₂O, substituting for appropriate controls. The reactions were shaken on ice for 30 min, quenched with 4× sample loading buffer and boiled at 95 °C for 5 min. The samples were separated on to two SDS-PAGE gels and transferred to nitrocellulose. Each membrane was blotted separately using NeutrAvidin-HRP and anti-PARP6 (total protein).

5.6.2 In vitro PARP fluorescence anisotropy binding assays

These assays were performed by AstraZeneca.

5.6.2.1 Dilution of various PARP proteins and fluorescence anisotropy probe

Recombinant full length 6HIS-tagged PARP1 protein was diluted to 6 nM with 50 mM Tris pH 8, 0.001% (v/v) Triton X-100, 10 mM MgCl₂, 150 mM NaCl and incubated for four hours with an equivalent volume of 2 nM fluorescent probe diluted with 50 mM Tris pH 8, 0.001% (v/v) Triton X-100, 10 mM MgCl₂, 150 mM NaCl. The final DMSO concentration of the probe was kept below 1% (v/v).

Recombinant full length PARP2 protein was diluted to 6 nM with 50 mM Tris pH 8, 0.001% (v/v) Triton X-100, 10 mM MgCl₂, 150 mM NaCl and incubated for four hours with an equivalent volume of 2 nM fluorescent probe diluted with 50 mM Tris pH 8, 0.001% (v/v) Triton X-100, 10 mM MgCl₂, 150 mM NaCl. The final DMSO concentration of the probe was kept below 1% (v/v).

Recombinant PARP5a binding domain was diluted to 160 nM with 50 mM Tris pH 8, 0.001% (v/v) Triton X-100, 10 mM MgCl₂, 150 mM NaCl and incubated for four hours with an equivalent volume of 6 nM fluorescent probe diluted with 50 mM Tris pH 8, 0.001% (v/v) Triton X-100, 10 mM MgCl₂, 150 mM NaCl. The final DMSO concentration of the probe was kept below 1% (v/v).

Recombinant full length GST-tagged PARP6 protein was diluted to 160 nM with 50 mM Tris pH 8, 0.001% (v/v) Triton X-100, 10 mM MgCl₂, 150 mM NaCl and incubated for four hours with an equivalent volume of 6 nM fluorescent probe diluted with 50 mM Tris pH 8, 0.001% (v/v) Triton X-100, 10 mM MgCl₂, 150 mM NaCl. The final DMSO concentration of the probe was kept below 1% (v/v).

5.6.2.2 Experimental protocol

Fluorescence anisotropy of the probe when bound to the proteins was measured using a BMG Pherastar FS[®] in the presence of test compounds or solvent control and the effect on anisotropy determined. Percentage inhibition values for different test compound concentrations were calculated and fitted to a four parameter logistic plot in order to determine the IC₅₀ value.

5.7 Molecular Biology

5.7.1 General methods

All microbiology work was carried out in a work area sterilized with 70% (v/v) EtOH and in the presence of an open flame. All equipment and media were either bought sterile or sterilized by autoclave. DNA concentration was measured using a NanoDrop[™] OneC (Thermo Fisher Scientific). Sanger sequencing was performed by Genewiz.

5.7.2 Plasmid production

1 μL of pcDNATM 3.1 plasmid ($70 \text{ ng } \mu\text{L}^{-1}$) containing FLAG-PARP6 was transformed into 50 μL competent DH5 α *E. coli* cells (Invitrogen) by heat shock treatment (30 min on ice, 42 °C for 45 s, 2 min on ice). Cells were cultured in Super optimal broth with catabolite repression (S. O. C.) medium (1 h, 900 rpm, 37 °C) then 50 μL spread on lysogeny broth (LB) agar supplemented with $100 \mu\text{g } \mu\text{L}^{-1}$ ampicillin which was grown overnight at 37 °C. Individual colonies were then cultured overnight (37 °C, 170 rpm) in 15 mL LB medium supplemented with $100 \mu\text{g } \mu\text{L}^{-1}$ ampicillin. 5 mL of this culture was used to inoculate a further 150 mL LB medium supplemented with $100 \mu\text{g } \mu\text{L}^{-1}$ ampicillin and grown overnight (37 °C, 170 rpm). Plasmids were purified from the culture using the QIAGEN® Maxiprep kit and sequence identity confirmed by Sanger sequencing.

Chapter 6 References

1. Croston, G. E. The utility of target-based discovery. *Expert Opin. Drug Discov.* **12**, 427–429 (2017).
2. Moffat, J. G., Vincent, F., Lee, J. A., Eder, J. & Prunotto, M. Opportunities and challenges in phenotypic drug discovery: an industry perspective. *Nat. Rev. Drug Discov.* **16**, 531–543 (2017).
3. Aulner, N., Danckaert, A., Ihm, J. E., Shum, D. & Shorte, S. L. Next-Generation Phenotypic Screening in Early Drug Discovery for Infectious Diseases. *Trends in Parasitology* **35**, 559–570 (2019).
4. Tulloch, L. B. *et al.* Direct and indirect approaches to identify drug modes of action. *IUBMB Life* **70**, 9–22 (2018).
5. Swinney, D. C. Phenotypic vs. Target-Based Drug Discovery for First-in-Class Medicines. *Clin. Pharmacol. Ther.* **93**, 299–301 (2013).
6. Palmer, M. Phenotypic Screening. in *Small Molecule Medicinal Chemistry: Strategies and Technologies* (eds. Czechtizky, W. & Hamley, P.) 281–304 (John Wiley & Sons, Inc, 2015).
7. Hardcastle, A. *et al.* A duplexed phenotypic screen for the molecular chaperone heat shock protein 90 and modulators of cellular acetylation. *Mol. Cancer Ther.* **6**, 1112–1122 (2007).
8. Moffat, J. G., Rudolph, J. & Bailey, D. Phenotypic screening in cancer drug discovery-past, present and future. *Nat. Rev. Drug Discov.* **13**, 588–602 (2014).
9. Brown, D. G. & Wobst, H. J. Opportunities and Challenges in Phenotypic Screening for Neurodegenerative Disease Research. *J. Med. Chem.* **63**, 1823–1840 (2020).
10. Schenone, M., Dančík, V., Wagner, B. K. & Clemons, P. A. Target identification and mechanism of action in chemical biology and drug discovery. *Nat. Chem. Biol.* **9**, 232–240 (2013).
11. Hop, C. E. C. A. Attrition in the Pharmaceutical Industry. in *Attrition in the Pharmaceutical Industry: Reasons, Implications, and Pathways Forward* (eds. Alex, A. C., Harris, J. & Smith, D. A.) 46–82 (John Wiley & Sons, Inc., 2016).
12. Dowden, H. & Munro, J. Trends in clinical success rates and therapeutic focus. *Nat. Rev. Drug Discov.* **18**, 495–496 (2019).
13. Hay, M., Thomas, D. W., Craighead, J. L., Economides, C. & Rosenthal, J. Clinical development success rates for investigational drugs. *Nat. Biotechnol.* **32**, 40–51 (2014).
14. Thomas, D. W. *et al.* *Clinical Development Success Rates 2006-2015. Biotechnology Innovation Organization.* (2016).
15. Wong, C. H., Siah, K. W. & Lo, A. W. Estimation of clinical trial success rates and related parameters. *Biostatistics* **20**, 273–286 (2019).
16. Harrison, R. K. Phase II and phase III failures: 2013-2015. *Nat. Rev. Drug Discov.* **15**, 817–818 (2016).
17. Waring, M. J. *et al.* An analysis of the attrition of drug candidates from four major pharmaceutical companies. *Nat. Rev. Drug Discov.* **14**, 475–486 (2015).
18. Plowright, A. T., Mannhold, R., Buschmann, H. & Holenz, J. *Target Discovery and Validation: Methods and Strategies for Drug Discovery.* (WILEY-VCH Verlag, 2019).

19. Heal, W. P., Dang, T. H. T. & Tate, E. W. Activity-based probes: discovering new biology and new drug targets. *Chem. Soc. Rev.* **40**, 246–257 (2011).
20. Su, Y. *et al.* Target identification of biologically active small molecules via in situ methods. *Curr. Opin. Chem. Biol.* **17**, 768–775 (2013).
21. Kath, J. E. & Baranczak, A. Target engagement approaches for pharmacological evaluation in animal models. *Chem. Commun.* **55**, 9241–9250 (2019).
22. Pichler, C. M., Krysiak, J. & Breinbauer, R. Target identification of covalently binding drugs by activity-based protein profiling (ABPP). *Bioorganic Med. Chem.* **24**, 3291–3303 (2016).
23. Overington, J. P., Al-Lazikani, B. & Hopkins, A. L. How many drug targets are there? *Nat. Rev. Drug Discov.* **5**, 993–996 (2006).
24. Gregori-Puigjane, E. *et al.* Identifying mechanism-of-action targets for drugs and probes. *Proc. Natl. Acad. Sci.* **109**, 11178–11183 (2012).
25. Dominguez, E. *et al.* Integrated phenotypic and activity-based profiling links Ces3 to obesity and diabetes. *Nat. Chem. Biol.* **10**, 113–121 (2014).
26. Coll, R. C. *et al.* MCC950 directly targets the NLRP3 ATP-hydrolysis motif for inflammasome inhibition. *Nat. Chem. Biol.* **15**, 556–559 (2019).
27. Wilkinson, I. V. L. *et al.* Chemical Proteomics and Phenotypic Profiling Identifies the Aryl Hydrocarbon Receptor as a Molecular Target of the Utrophin Modulator Ezutromid. *Angew. Chemie Int. Ed.* **59**, 2420–2428 (2020).
28. Kridel, S. J., Axelrod, F., Rozenkrantz, N. & Smith, J. W. Orlistat Is a Novel Inhibitor of Fatty Acid Synthase with Antitumor Activity. *Cancer Res.* **64**, 2070–2075 (2004).
29. Dziekan, J. M. *et al.* Identifying purine nucleoside phosphorylase as the target of quinine using cellular thermal shift assay. *Sci. Transl. Med.* **11**, eaau3174 (2019).
30. Ward, J. A. *et al.* Quantitative Chemical Proteomic Profiling of Ubiquitin Specific Proteases in Intact Cancer Cells. *ACS Chem. Biol.* **11**, 3268–3272 (2016).
31. Lin, A. *et al.* Off-target toxicity is a common mechanism of action of cancer drugs undergoing clinical trials. *Sci. Transl. Med.* **11**, eaaw8412 (2019).
32. Proschak, E., Stark, H. & Merk, D. Polypharmacology by Design: A Medicinal Chemist's Perspective on Multitargeting Compounds. *J. Med. Chem.* **62**, 420–444 (2019).
33. Califf, R. M. & Slavitt, A. Lowering Cost and Increasing Access to Drugs Without Jeopardizing Innovation. *JAMA* **321**, 1571 (2019).
34. Gao, J., Mfuh, A., Amako, Y. & Woo, C. M. Small Molecule Interactome Mapping by Photoaffinity Labeling Reveals Binding Site Hotspots for the NSAIDs. *J. Am. Chem. Soc.* **140**, 4259–4268 (2018).
35. Savitski, M. M. *et al.* Tracking cancer drugs in living cells by thermal profiling of the proteome. *Science* **346**, 1255784 (2014).
36. Zuhl, A. M. *et al.* Chemoproteomic profiling reveals that cathepsin D off-target activity drives ocular toxicity of β -secretase inhibitors. *Nat. Commun.* **7**, 13042 (2016).
37. van Esbroeck, A. C. M. *et al.* Activity-based protein profiling reveals off-target proteins of the FAAH inhibitor BIA 10-2474. *Science* **356**, 1084–1087 (2017).

38. Honigberg, L. A. *et al.* The Bruton tyrosine kinase inhibitor PCI-32765 blocks B-cell activation and is efficacious in models of autoimmune disease and B-cell malignancy. *Proc. Natl. Acad. Sci.* **107**, 13075–13080 (2010).
39. Cisar, J. S. *et al.* Identification of ABX-1431, a Selective Inhibitor of Monoacylglycerol Lipase and Clinical Candidate for Treatment of Neurological Disorders. *J. Med. Chem.* **61**, 9062–9084 (2018).
40. Feng, Y., Mitchison, T. J., Bender, A., Young, D. W. & Tallarico, J. A. Multi-parameter phenotypic profiling: Using cellular effects to characterize small-molecule compounds. *Nat. Rev. Drug Discov.* **8**, 567–578 (2009).
41. Neggers, J. E. *et al.* Target identification of small molecules using large-scale CRISPR-Cas mutagenesis scanning of essential genes. *Nat. Commun.* **9**, 502 (2018).
42. Pham, L., Christadore, L., Schaus, S. & Kolaczyk, E. D. Network-based prediction for sources of transcriptional dysregulation using latent pathway identification analysis. *Proc. Natl. Acad. Sci.* **108**, 13347–13352 (2011).
43. Lo, Y. *et al.* Large-Scale Chemical Similarity Networks for Target Profiling of Compounds Identified in Cell-Based Chemical Screens. *PLOS Comput. Biol.* **11**, e1004153 (2015).
44. Huang, T. *et al.* MOST: most-similar ligand based approach to target prediction. *BMC Bioinformatics* **18**, 165 (2017).
45. Rossenu, S., Dewitte, D., Vandekerckhove, J. & Ampe, C. A phage display technique for a fast, sensitive, and systematic investigation of protein-protein interactions. *J. Protein Chem.* **16**, 499–503 (1997).
46. Kim, B. S., Lee, K., Jung, H. J., Bhattarai, D. & Kwon, H. J. HIF-1 α suppressing small molecule, LW6, inhibits cancer cell growth by binding to calcineurin b homologous protein 1. *Biochem. Biophys. Res. Commun.* **458**, 14–20 (2015).
47. Jung, H. J. *et al.* Terpestacin inhibits tumor angiogenesis by targeting UQCRB of mitochondrial complex III and suppressing hypoxia-induced reactive oxygen species production and cellular oxygen sensing. *J. Biol. Chem.* **285**, 11584–11595 (2010).
48. Wilson, D. S., Keefe, A. D. & Szostak, J. W. The use of mRNA display to select high-affinity protein-binding peptides. *Proc. Natl. Acad. Sci.* **98**, 3750–3755 (2001).
49. McPherson, M., Yang, Y., Hammond, P. W. & Kreider, B. L. Drug Receptor Identification from Multiple Tissues Using Cellular-Derived mRNA Display Libraries. *Chem. Biol.* **9**, 691–698 (2002).
50. Wada, A., Hara, S. & Osada, H. Ribosome Display and Photo-Cross-Linking Techniques for In Vitro Identification of Target Proteins of Bioactive Small Molecules. *Anal. Chem.* **86**, 6768–6773 (2014).
51. Licitra, E. J. & Liu, J. O. A three-hybrid system for detecting small ligand-protein receptor interactions. *Proc. Natl. Acad. Sci.* **93**, 12817–12821 (1996).
52. Becker, F. *et al.* A three-hybrid approach to scanning the proteome for targets of small molecule kinase inhibitors. *Chem. Biol.* **11**, 211–223 (2004).
53. Chidley, C., Haruki, H., Pedersen, M. G., Muller, E. & Johnsson, K. A yeast-based screen reveals that sulfasalazine inhibits tetrahydrobiopterin biosynthesis. *Nat. Chem. Biol.* **7**, 375–383 (2011).

54. Moser, S. & Johnsson, K. Yeast Three-Hybrid Screening for Identifying Anti-Tuberculosis Drug Targets. *ChemBioChem* **14**, 2239–2242 (2013).
55. Pasquer, Q. T. L., Tsakoumagkos, I. A. & Hoogendoorn, S. From Phenotypic Hit to Chemical Probe: Chemical Biology Approaches to Elucidate Small Molecule Action in Complex Biological Systems. *Molecules* **25**, 5702 (2020).
56. Jost, M. & Weissman, J. S. CRISPR Approaches to Small Molecule Target Identification. *ACS Chem. Biol.* **13**, 366–375 (2018).
57. Schulz-Fincke, J. *et al.* Structure-activity studies on N-Substituted tranylcypromine derivatives lead to selective inhibitors of lysine specific demethylase 1 (LSD1) and potent inducers of leukemic cell differentiation. *Eur. J. Med. Chem.* **144**, 52–67 (2018).
58. Reinhard, F. B. M. *et al.* Thermal proteome profiling monitors ligand interactions with cellular membrane proteins. *Nat. Methods* **12**, 1129–1131 (2015).
59. Franken, H. *et al.* Thermal proteome profiling for unbiased identification of direct and indirect drug targets using multiplexed quantitative mass spectrometry. *Nat. Protoc.* **10**, 1567–1593 (2015).
60. Hashimoto, M., Girardi, E., Eichner, R. & Superti-Furga, G. Detection of Chemical Engagement of Solute Carrier Proteins by a Cellular Thermal Shift Assay. *ACS Chem. Biol.* **13**, 1480–1486 (2018).
61. Hengst, J. *et al.* SKI-178: A multitargeted inhibitor of sphingosine kinase and microtubule dynamics demonstrating therapeutic efficacy in acute myeloid leukemia models. *Cancer Transl. Med.* **3**, 109–121 (2017).
62. Lomenick, B. *et al.* Target identification using drug affinity responsive target stability (DARTS). *Proc. Natl. Acad. Sci.* **106**, 21984–21989 (2009).
63. Chin, R. M. *et al.* The metabolite α -ketoglutarate extends lifespan by inhibiting ATP synthase and TOR. *Nature* **510**, 397–401 (2014).
64. Park, Y. *et al.* Identification of Multiple Cryptococcal Fungicidal Drug Targets by Combined Gene Dosing and Drug Affinity Responsive Target Stability Screening. *MBio* **7**, e01073-16 (2016).
65. Dal Piaz, F. *et al.* Drug Affinity Responsive Target Stability (DARTS) Identifies Laurifolioside as a New Clathrin Heavy Chain Modulator. *J. Nat. Prod.* **79**, 2681–2692 (2016).
66. West, G. M., Tang, L. & Fitzgerald, M. C. Thermodynamic analysis of protein stability and ligand binding using a chemical modification- and mass spectrometry-based strategy. *Anal. Chem.* **80**, 4175–4185 (2008).
67. DeArmond, P. D., Xu, Y., Strickland, E. C., Daniels, K. G. & Fitzgerald, M. C. Thermodynamic Analysis of Protein–Ligand Interactions in Complex Biological Mixtures using a Shotgun Proteomics Approach. *J. Proteome Res.* **10**, 4948–4958 (2011).
68. Tran, D. T., Adhikari, J. & Fitzgerald, M. C. Stable Isotope Labeling with Amino Acids in Cell Culture (SILAC)-based strategy for proteome-wide thermodynamic analysis of protein-ligand binding interactions. *Mol. Cell. Proteomics* **13**, 1800–1813 (2014).
69. Ogburn, R. N., Jin, L., Meng, H. & Fitzgerald, M. C. Discovery of Tamoxifen and N-Desmethyl Tamoxifen Protein Targets in MCF-7 Cells Using Large-Scale Protein Folding and Stability Measurements. *J. Proteome Res.* **16**, 4073–4085 (2017).

70. Bantscheff, M. *et al.* Quantitative chemical proteomics reveals mechanisms of action of clinical ABL kinase inhibitors. *Nat. Biotechnol.* **25**, 1035–1044 (2007).
71. Chen, X. *et al.* Comparative profiling of analog targets: a case study on resveratrol for mouse melanoma metastasis suppression. *Theranostics* **8**, 3504–3516 (2018).
72. Mortison, J. D. *et al.* Tetracyclines Modify Translation by Targeting Key Human rRNA Substructures. *Cell Chem. Biol.* **25**, 1506–1518.e13 (2018).
73. Knezevic, C. E. *et al.* Proteome-wide Profiling of Clinical PARP Inhibitors Reveals Compound-Specific Secondary Targets. *Cell Chem. Biol.* **23**, 1490–1503 (2016).
74. Saxena, C. Identification of protein binding partners of small molecules using label-free methods. *Expert Opin. Drug Discov.* **11**, 1017–1025 (2016).
75. Zheng, W., Li, G. & Li, X. Affinity purification in target identification: the specificity challenge. *Arch. Pharm. Res.* **38**, 1661–1685 (2015).
76. Ito, T. *et al.* Identification of a primary target of thalidomide teratogenicity. *Science* **327**, 1345–1350 (2010).
77. Panyain, N., Kennedy, C. R., Howard, R. T. & Tate, E. W. Activity-Based Protein Profiling. in *Target Discovery and Validation: Methods and Strategies for Drug Discovery* (eds. Plowright, A. T., Mannhold, R., Buschmann, H. & Holenz, J.) 51–83 (WILEY-VCH Verlag, 2019).
78. Lee, J. & Bogyo, M. Target deconvolution techniques in modern phenotypic profiling. *Current Opinion in Chemical Biology* **17**, 118–126 (2013).
79. Martell, J. & Weerapana, E. Applications of Copper-Catalyzed Click Chemistry in Activity-Based Protein Profiling. *Molecules* **19**, 1378–1393 (2014).
80. Kalesh, K. A., Clulow, J. A., Tate, E. W. & Prasanna, R. Target profiling of zerumbone using a novel cell-permeable clickable probe and quantitative chemical proteomics. *Chem. Commun.* **51**, 5497–5500 (2015).
81. Clulow, J. A. *et al.* Competition-based, quantitative chemical proteomics in breast cancer cells identifies new target profiles for sulforaphane. *Chem. Commun.* **53**, 5182–5185 (2017).
82. Kidd, D., Liu, Y. & Cravatt, B. F. Profiling serine hydrolase activities in complex proteomes. *Biochemistry* **40**, 4005–4015 (2001).
83. Dennehy, M. K., Richards, K. A. M., Wernke, G. R., Shyr, Y. & Liebler, D. C. Cytosolic and nuclear protein targets of thiol-reactive electrophiles. *Chem. Res. Toxicol.* **19**, 20–29 (2006).
84. Cravatt, B. F., Wright, A. T. & Kozarich, J. W. Activity-Based Protein Profiling: From Enzyme Chemistry to Proteomic Chemistry. *Annu. Rev. Biochem.* **77**, 383–414 (2008).
85. Saxena, C. *et al.* Capture of Drug Targets from Live Cells Using a Multipurpose Immuno-Chemo-Proteomics Tool. *J. Proteome Res.* **8**, 3951–3957 (2009).
86. Zhu, S. *et al.* A Small Molecule Primes Embryonic Stem Cells for Differentiation. *Cell Stem Cell* **4**, 416–426 (2009).
87. Rutkowska, A. *et al.* A Modular Probe Strategy for Drug Localization, Target Identification and Target Occupancy Measurement on Single Cell Level. *ACS Chem. Biol.* **11**, 2541–2550 (2016).
88. Halloran, M. W. & Lumb, J. Recent Applications of Diazirines in Chemical Proteomics. *Chem. – A Eur. J.* **25**, 4885–4898 (2019).

89. Smith, E. & Collins, I. Photoaffinity labeling in target- and binding-site identification. *Future Med. Chem.* **7**, 159–813 (2015).
90. Ge, S. S. *et al.* Current advances of carbene-mediated photoaffinity labeling in medicinal chemistry. *RSC Advances* **8**, 29428–29454 (2018).
91. Singh, A., Thornton, E. R. & Westheimer, F. H. The photolysis of diazoacetylchymotrypsin. *J. Biol. Chem.* **237**, 3006–3008 (1962).
92. Bayley, H. *Photogenerated reagents in biochemistry and molecular biology*. (Elsevier, 1983).
93. Jessani, N. *et al.* A streamlined platform for high-content functional proteomics of primary human specimens. *Nat. Methods* **2**, 691–697 (2005).
94. Sieber, S. A., Niessen, S., Hoover, H. S. & Cravatt, B. F. Proteomic profiling of metalloprotease activities with cocktails of active-site probes. *Nat. Chem. Biol.* **2**, 274–281 (2006).
95. Leslie, B. J. & Hergenrother, P. J. Identification of the cellular targets of bioactive small organic molecules using affinity reagents. *Chem. Soc. Rev.* **37**, 1347–1360 (2008).
96. Shi, H., Zhang, C. J., Chen, G. Y. J. & Yao, S. Q. Cell-based proteome profiling of potential Dasatinib targets by use of affinity-based probes. *J. Am. Chem. Soc.* **134**, 3001–3014 (2012).
97. Lee, K. *et al.* Identification of Malate Dehydrogenase 2 as a Target Protein of the HIF-1 Inhibitor LW6 using Chemical Probes. *Angew. Chemie Int. Ed.* **52**, 10286–10289 (2013).
98. Soethoudt, M. *et al.* Selective Photoaffinity Probe That Enables Assessment of Cannabinoid CB 2 Receptor Expression and Ligand Engagement in Human Cells. *J. Am. Chem. Soc.* **140**, 6067–6075 (2018).
99. Soethoudt, M. *et al.* Development of a Cannabinoid-Based Photoaffinity Probe to Determine the Δ 8/9 -Tetrahydrocannabinol Protein Interaction Landscape in Neuroblastoma Cells. *Cannabis Cannabinoid Res.* **3**, 136–151 (2018).
100. Thuy-Boun, P. S. & Wolan, D. W. A glycal-based photoaffinity probe that enriches sialic acid binding proteins. *Bioorg. Med. Chem. Lett.* **29**, 2609–2612 (2019).
101. Wu, H. & Kohler, J. Photocrosslinking probes for capture of carbohydrate interactions. *Curr. Opin. Chem. Biol.* **53**, 173–182 (2019).
102. Dandela, R., Mantin, D., Cravatt, B. F., Rayo, J. & Meijler, M. M. Proteome-wide mapping of PQS-interacting proteins in *Pseudomonas aeruginosa*. *Chem. Sci.* **9**, 2290–2294 (2018).
103. Chen, Y. & Topp, E. M. Photolytic Labeling and Its Applications in Protein Drug Discovery and Development. *J. Pharm. Sci.* **108**, 791–797 (2019).
104. Ford, A. *et al.* Modern Organic Synthesis with α -Diazocarbonyl Compounds. *Chem. Rev.* **115**, 9981–10080 (2015).
105. Fleming, S. A. Chemical reagents in photoaffinity labeling. *Tetrahedron* **51**, 12479–12520 (1995).
106. Pattison, D. I. & Davies, M. J. Actions of ultraviolet light on cellular structures. in *Cancer: Cell Structures, Carcinogens and Genomic Instability* (ed. Bignold, L. P.) 131–157 (Birkhäuser-Verlag, 2006).
107. Neberle, A. & de Graan, P. N. E. General principles for photoaffinity labeling of peptide hormone receptors. in *Methods in Enzymology* (eds. Birnbaumer, L. & O'Malley, B. W.) **109**, 129–156 (Academic Press, 1985).

108. Aboukhatwa, S. M. *et al.* Structurally Diverse Histone Deacetylase Photoreactive Probes: Design, Synthesis, and Photolabeling Studies in Live Cells and Tissue. *ChemMedChem* **14**, 1096–1107 (2019).
109. Geurink, P. P., Prely, L. M., van der Marel, G. A., Bischoff, R. & Overkleeft, H. S. Photoaffinity Labeling in Activity-Based Protein Profiling. in *Topics in Current Chemistry* (ed. Sieber, S. A.) **324**, 85–113 (Springer-Verlag, 2011).
110. Grimes, K., Gupte, A. & Aldrich, C. Copper(II)-Catalyzed Conversion of Aryl/Heteroaryl Boronic Acids, Boronates, and Trifluoroborates into the Corresponding Azides: Substrate Scope and Limitations. *Synthesis* **2010**, 1441–1448 (2010).
111. Griбанov, P. S. *et al.* An unprecedentedly simple method of synthesis of aryl azides and 3-hydroxytriazenes. *Green Chem.* **18**, 5984–5988 (2016).
112. Chin, J. W. *et al.* Addition of p-azido-L-phenylalanine to the genetic code of Escherichia coli. *J. Am. Chem. Soc.* **124**, 9026–9027 (2002).
113. Liang, J. *et al.* Chemical Synthesis of Diubiquitin-Based Photoaffinity Probes for Selectively Profiling Ubiquitin-Binding Proteins. *Angew. Chemie Int. Ed.* **56**, 2744–2748 (2017).
114. Jessen, K. A. *et al.* The discovery and mechanism of action of novel tumor-selective and apoptosis-inducing 3,5-diaryl-1,2,4-oxadiazole series using a chemical genetics approach. *Mol. Cancer Ther.* **4**, 761–771 (2005).
115. Côté, M. *et al.* Small molecule inhibitors reveal Niemann-Pick C1 is essential for Ebola virus infection. *Nature* **477**, 344–348 (2011).
116. Koh, M. *et al.* Phenotypic Screening to Identify Small-Molecule Enhancers for Glucose Uptake: Target Identification and Rational Optimization of Their Efficacy. *Angew. Chemie Int. Ed.* **53**, 5102–5106 (2014).
117. Kleiner, P., Heydenreuter, W., Stahl, M., Korotkov, V. S. & Sieber, S. A. A Whole Proteome Inventory of Background Photocrosslinker Binding. *Angew. Chem. Int. Ed. Engl.* **56**, 1396–1401 (2017).
118. Krishnamurty, R. *et al.* Active site profiling reveals coupling between domains in SRC-family kinases. *Nat. Chem. Biol.* **9**, 43–50 (2013).
119. Khan, A. A. *et al.* Development of a benzophenone and alkyne functionalised trehalose probe to study trehalose dimycolate binding proteins. *Org. Biomol. Chem.* **11**, 881–885 (2013).
120. Herner, A. *et al.* 2-Aryl-5-carboxytetrazole as a New Photoaffinity Label for Drug Target Identification. *J. Am. Chem. Soc.* **138**, 14609–14615 (2016).
121. Ota, E. *et al.* Thienyl-Substituted α -Ketoamide: A Less Hydrophobic Reactive Group for Photo-Affinity Labeling. *ACS Chem. Biol.* **13**, 876–880 (2018).
122. Hill, J. R. & Robertson, A. A. B. Fishing for Drug Targets: A Focus on Diazirine Photoaffinity Probe Synthesis. *J. Med. Chem.* **61**, 6945–6963 (2018).
123. Brunner, J., Senn, H. & Richards, F. M. 3-Trifluoromethyl-3-phenyldiazirine: A new carbene generating group for photolabeling reagents. *J. Biol. Chem.* **255**, 3313–3318 (1980).
124. Li, Z. *et al.* Design and Synthesis of Minimalist Terminal Alkyne-Containing Diazirine Photo-Crosslinkers and Their Incorporation into Kinase Inhibitors for Cell- and Tissue-Based Proteome Profiling. *Angew. Chemie Int. Ed.* **52**, 8551–8556 (2013).
125. Wang, L. *et al.* Base-Mediated One-Pot Synthesis of Aliphatic Diazirines for Photoaffinity

- Labeling. *Molecules* **22**, 1389 (2017).
126. Längle, D. *et al.* Unique photoaffinity probes to study TGF β signaling and receptor fates. *Chem. Commun.* **55**, 4323–4326 (2019).
 127. Kaiser, N. *et al.* Photoactivatable Myristic Acid Probes for UNC119-Cargo Interactions. *ChemBioChem* **20**, 134–139 (2019).
 128. Yamamoto, N. *et al.* Mechanism of Carbene Formation from the Excited States of Diazirine and Diazomethane: An MC-SCF Study. *J. Am. Chem. Soc.* **116**, 2064–2074 (1994).
 129. Šumanovac, T. *et al.* Photoelimination of nitrogen from adamantane and pentacycloundecane (PCU) diazirines: a spectroscopic study and supramolecular control. *Photochem. Photobiol. Sci.* **18**, 1806–1822 (2019).
 130. Peng, X.-L., Migani, A., Li, Q.-S., Li, Z.-S. & Blancafort, L. Theoretical study of non-Hammett vs. Hammett behaviour in the thermolysis and photolysis of arylchlorodiazirines. *Phys. Chem. Chem. Phys.* **20**, 1181–1188 (2018).
 131. Procacci, B., Roy, S. S., Norcott, P., Turner, N. & Duckett, S. B. Unlocking a Diazirine Long-Lived Nuclear Singlet State via Photochemistry: NMR Detection and Lifetime of an Unstabilized Diazo-Compound. *J. Am. Chem. Soc.* **140**, 16855–16864 (2018).
 132. Ford, F., Yuzawa, T., Platz, M. S., Matzinger, S. & Fülcher, M. Rearrangement of Dimethylcarbene to Propene: Study by Laser Flash Photolysis and ab Initio Molecular Orbital Theory. *J. Am. Chem. Soc.* **120**, 4430–4438 (1998).
 133. Li, Z. *et al.* Design and Synthesis of Minimalist Terminal Alkyne-Containing Diazirine Photo-Crosslinkers and Their Incorporation into Kinase Inhibitors for Cell- and Tissue-Based Proteome Profiling. *Angew. Chemie Int. Ed.* **52**, 8551–8556 (2013).
 134. Wang, J., Kubicki, J., Peng, H. & Platz, M. S. Influence of solvent on carbene intersystem crossing rates. *J. Am. Chem. Soc.* **130**, 6604–6609 (2008).
 135. Das, J. Aliphatic Diazirines as Photoaffinity Probes for Proteins: Recent Developments. *Chem. Rev.* **111**, 4405–4417 (2011).
 136. Manzi, L. *et al.* Carbene footprinting accurately maps binding sites in protein–ligand and protein–protein interactions. *Nat. Commun.* **7**, 13288 (2016).
 137. Manzi, L. *et al.* Carbene Footprinting Reveals Binding Interfaces of a Multimeric Membrane-Spanning Protein. *Angew. Chemie Int. Ed.* **56**, 14873–14877 (2017).
 138. Chu, B. *et al.* Photoaffinity-engineered protein scaffold for systematically exploring native phosphotyrosine signaling complexes in tumor samples. *Proc. Natl. Acad. Sci.* **115**, E8863–E8872 (2018).
 139. McCutcheon, D. C., Lee, G., Carlos, A., Montgomery, J. E. & Moellering, R. E. Photoproximity Profiling of Protein–Protein Interactions in Cells. *J. Am. Chem. Soc.* **142**, 146–153 (2020).
 140. Šimon, P. *et al.* Identification of Protein Targets of Bioactive Small Molecules Using Randomly Photomodified Probes. *ACS Chem. Biol.* **13**, 3333–3342 (2018).
 141. Lepage, M. L. *et al.* A broadly applicable cross-linker for aliphatic polymers containing C–H bonds. *Science* **366**, 875–878 (2019).
 142. Seo, S.-Y. & Corson, T. W. Small molecule target identification using photo-affinity chromatography. *Methods Enzymol.* **622**, 347–374 (2019).

143. Sannino, A. *et al.* Critical Evaluation of Photo-cross-linking Parameters for the Implementation of Efficient DNA-Encoded Chemical Library Selections. *ACS Comb. Sci.* **22**, 204–212 (2020).
144. Kolb, H. C., Finn, M. G. & Sharpless, K. B. Click Chemistry: Diverse Chemical Function from a Few Good Reactions. *Angew. Chemie Int. Ed.* **40**, 2004–2021 (2001).
145. Oliveira, B. L., Guo, Z. & Bernardes, G. J. L. Inverse electron demand Diels–Alder reactions in chemical biology. *Chem. Soc. Rev.* **46**, 4895–4950 (2017).
146. Parker, C. G. & Pratt, M. R. Click Chemistry in Proteomic Investigations. *Cell* **180**, 605–632 (2020).
147. Jiang, X. *et al.* Recent applications of click chemistry in drug discovery. *Expert Opin. Drug Discov.* **14**, 779–789 (2019).
148. Horisawa, K. Specific and quantitative labeling of biomolecules using click chemistry. *Front. Physiol.* **5**, 457 (2014).
149. Li, L. & Zhang, Z. Development and Applications of the Copper-Catalyzed Azide-Alkyne Cycloaddition (CuAAC) as a Bioorthogonal Reaction. *Molecules* **21**, 1393 (2016).
150. Kiyonaka, S. *et al.* Selective and direct inhibition of TRPC3 channels underlies biological activities of a pyrazole compound. *Proc. Natl. Acad. Sci.* **106**, 5400–5405 (2009).
151. Axup, J. Y. *et al.* Synthesis of site-specific antibody-drug conjugates using unnatural amino acids. *Proc. Natl. Acad. Sci.* **109**, 16101–16106 (2012).
152. Liu, W. *et al.* A reactivity-based [¹⁸F]FDG probe for in vivo formaldehyde imaging using positron emission tomography. *Chem. Sci.* **7**, 5503–5507 (2016).
153. Hang, H. C. *et al.* Chemical probes for the rapid detection of fatty-acylated proteins in mammalian cells. *J. Am. Chem. Soc.* **129**, 2744–2745 (2007).
154. Hoegl, A. *et al.* Mining the cellular inventory of pyridoxal phosphate-dependent enzymes with functionalized cofactor mimics. *Nat. Chem.* **10**, 1234–1245 (2018).
155. Hang, H. C. *et al.* Mechanism-based probe for the analysis of cathepsin cysteine proteases in living cells. *ACS Chem. Biol.* **1**, 713–723 (2006).
156. Speers, A. E., Adam, G. C. & Cravatt, B. F. Activity-based protein profiling in vivo using a copper(I)-catalyzed azide-alkyne [3 + 2] cycloaddition. *J. Am. Chem. Soc.* **125**, 4686–4687 (2003).
157. Albrow, V. E. *et al.* Design and development of histone deacetylase (HDAC) chemical probes for cell-based profiling. *Mol. BioSyst.* **12**, 1781–1789 (2016).
158. Broncel, M. *et al.* Multifunctional Reagents for Quantitative Proteome-Wide Analysis of Protein Modification in Human Cells and Dynamic Profiling of Protein Lipidation During Vertebrate Development. *Angew. Chemie Int. Ed.* **54**, 5948–5951 (2015).
159. Storck, E. M. *et al.* Dual chemical probes enable quantitative system-wide analysis of protein prenylation and prenylation dynamics. *Nat. Chem.* **11**, 522–561 (2019).
160. Ning, X., Guo, J., Wolfert, M. A. & Boons, G.-J. Visualizing Metabolically Labeled Glycoconjugates of Living Cells by Copper-Free and Fast Huisgen Cycloadditions. *Angew. Chemie Int. Ed.* **47**, 2253–2255 (2008).
161. Orski, S. V. *et al.* High density orthogonal surface immobilization via photoactivated copper-free click chemistry. *J. Am. Chem. Soc.* **132**, 11024–11026 (2010).

162. Chang, T. C. *et al.* A photo-cleavable biotin affinity tag for the facile release of a photo-crosslinked carbohydrate-binding protein. *Bioorganic Med. Chem.* **24**, 1216–1224 (2016).
163. Wallrodt, S., Buntz, A., Wang, Y., Zumbusch, A. & Marx, A. Bioorthogonally Functionalized NAD⁺ Analogues for In-Cell Visualization of Poly(ADP-Ribose) Formation. *Angew. Chemie Int. Ed.* **55**, 7660–7664 (2016).
164. Li, Z. *et al.* ‘Minimalist’ cyclopropene-containing photo-cross-linkers suitable for live-cell imaging and affinity-based protein labeling. *J. Am. Chem. Soc.* **136**, 9990–9998 (2014).
165. Johansson, H. *et al.* Fragment-Based Covalent Ligand Screening Enables Rapid Discovery of Inhibitors for the RBR E3 Ubiquitin Ligase HOIP. *J. Am. Chem. Soc.* **141**, 2703–2712 (2019).
166. Yao, H., Jiang, F., Lu, A. & Zhang, G. Methods to Design and Synthesize Antibody-Drug Conjugates (ADCs). *Int. J. Mol. Sci.* **17**, 194 (2016).
167. Kölmel, D. K. & Kool, E. T. Oximes and Hydrazones in Bioconjugation: Mechanism and Catalysis. *Chem. Rev.* **117**, 10358–10376 (2017).
168. Wang, S. *et al.* Saline Accelerates Oxime Reaction with Aldehyde and Keto Substrates at Physiological pH. *Sci. Rep.* **8**, 2193 (2018).
169. Köhn, M. & Breinbauer, R. The Staudinger Ligation—A Gift to Chemical Biology. *Angew. Chemie Int. Ed.* **43**, 3106–3116 (2004).
170. Lang, K. & Chin, J. W. Bioorthogonal reactions for labeling proteins. *ACS Chem. Biol.* **9**, 16–20 (2014).
171. Hein, J. E. & Fokin, V. V. Copper-catalyzed azide–alkyne cycloaddition (CuAAC) and beyond: new reactivity of copper(i) acetylides. *Chem. Soc. Rev.* **39**, 1302–1315 (2010).
172. Kallemeijn, W. W. *et al.* Validation and Invalidation of Chemical Probes for the Human N-myristoyltransferases. *Cell Chem. Biol.* **26**, 892–900 (2019).
173. Rudolf, G. C. & Sieber, S. A. Copper-Assisted Click Reactions for Activity-Based Proteomics: Fine-Tuned Ligands and Refined Conditions Extend the Scope of Application. *ChemBioChem* **14**, 2447–2455 (2013).
174. Heal, W. P., Wright, M. H., Thinon, E. & Tate, E. W. Multifunctional protein labeling via enzymatic N-terminal tagging and elaboration by click chemistry. *Nat. Protoc.* **7**, 105–117 (2012).
175. Wright, M. H. *et al.* Global analysis of protein N-myristoylation and exploration of N-myristoyltransferase as a drug target in the neglected human pathogen leishmania donovani. *Chem. Biol.* **22**, 342–354 (2015).
176. Worrell, B. T., Malik, J. A. & Fokin, V. V. Direct Evidence of a Dinuclear Copper Intermediate in Cu(I)-Catalyzed Azide-Alkyne Cycloadditions. *Science* **340**, 457–460 (2013).
177. Pickens, C. J., Johnson, S. N., Pressnall, M. M., Leon, M. A. & Berkland, C. J. Practical Considerations, Challenges, and Limitations of Bioconjugation via Azide–Alkyne Cycloaddition. *Bioconjug. Chem.* **29**, 686–701 (2018).
178. Laughlin, S. T. & Bertozzi, C. R. In vivo imaging of *Caenorhabditis elegans* glycans. *ACS Chem. Biol.* **4**, 1068–1072 (2009).
179. Pan, S. *et al.* A Suite of “Minimalist” Photo-Crosslinkers for Live-Cell Imaging and Chemical Proteomics: Case Study with BRD4 Inhibitors. *Angew. Chemie Int. Ed.* **56**, 11816–11821 (2017).

180. Lehmann, J., Richers, J., Pöthig, A. & Sieber, S. A. Synthesis of ramariolide natural products and discovery of their targets in mycobacteria. *Chem. Commun.* **53**, 107–110 (2017).
181. Jackson, P. & Lapinsky, D. J. Appendage and Scaffold Diverse Fully Functionalized Small-Molecule Probes via a Minimalist Terminal Alkyne-Aliphatic Diazirine Isocyanide. *J. Org. Chem.* **83**, 11245–11253 (2018).
182. Kambe, T., Correia, B. E., Niphakis, M. J. & Cravatt, B. F. Mapping the Protein Interaction Landscape for Fully Functionalized Small-Molecule Probes in Human Cells. *J. Am. Chem. Soc.* **136**, 10777–10782 (2014).
183. Parker, C. G. *et al.* Chemical Proteomics Identifies SLC25A20 as a Functional Target of the Ingenol Class of Actinic Keratosis Drugs. *ACS Cent. Sci.* **3**, 1276–1285 (2017).
184. Ma, N. *et al.* Affinity-Based Protein Profiling Reveals Cellular Targets of Photoreactive Anticancer Inhibitors. *ACS Chem. Biol.* **14**, 2546–2552 (2019).
185. Chen, D. M. *et al.* A Clickable Oxysterol Photolabel Retains NMDA Receptor Activity and Accumulates in Neurons. *Front. Neurosci.* **12**, 923 (2018).
186. Xie, Y. *et al.* Fluorescent Probes for Single-Step Detection and Proteomic Profiling of Histone Deacetylases. *J. Am. Chem. Soc.* **138**, 15596–15604 (2016).
187. Parker, C. G. *et al.* Ligand and Target Discovery by Fragment-Based Screening in Human Cells. *Cell* **168**, 527-541.e29 (2017).
188. Wang, Y. *et al.* Expedited mapping of the ligandable proteome using fully functionalized enantiomeric probe pairs. *Nat. Chem.* **11**, 1113–1123 (2019).
189. Feltes, M. *et al.* Synthesis and characterization of diazirine alkyne probes for the study of intracellular cholesterol trafficking. *J. Lipid Res.* **60**, 707–716 (2019).
190. Gao, C. *et al.* Synthesis and Target Identification of Benzoxepane Derivatives as Potential Anti-Neuroinflammatory Agents for Ischemic Stroke. *Angew. Chemie Int. Ed.* **59**, 2429–2439 (2020).
191. Keohane, C. E. *et al.* Promysalin Elicits Species-Selective Inhibition of *Pseudomonas aeruginosa* by Targeting Succinate Dehydrogenase. *J. Am. Chem. Soc.* **140**, 1774–1782 (2018).
192. Deng, H., Lei, Q., Wu, Y., He, Y. & Li, W. Activity-based protein profiling: Recent advances in medicinal chemistry. *Eur. J. Med. Chem.* **191**, 112151 (2020).
193. Heal, W. P., Wickramasinghe, S. R., Leatherbarrow, R. J. & Tate, E. W. N-Myristoyl transferase-mediated protein labelling in vivo. *Org. Biomol. Chem.* **6**, 2308–2315 (2008).
194. Wright, M. H. *et al.* Validation of N-myristoyltransferase as an antimalarial drug target using an integrated chemical biology approach. *Nat. Chem.* **6**, 112–121 (2014).
195. Wright, M. H. & Sieber, S. A. Chemical proteomics approaches for identifying the cellular targets of natural products. *Nat. Prod. Rep.* **33**, 681–708 (2016).
196. Washburn, M. P., Wolters, D. & Yates, J. R. Large-scale analysis of the yeast proteome by multidimensional protein identification technology. *Nat. Biotechnol.* **19**, 242–247 (2001).
197. Cantin, G. T. & Yates, J. R. Strategies for shotgun identification of post-translational modifications by mass spectrometry. *J. Chromatogr. A* **1053**, 7–14 (2004).
198. Michael Green, N. Avidin and streptavidin. in *Methods in Enzymology* (eds. Wilchek, M. & Bayer, E. A.) **184**, 51–67 (Academic Press, 1990).

199. Galmozzi, A., Parker, C. G., Kok, B. P., Cravatt, B. F. & Saez, E. Discovery of Modulators of Adipocyte Physiology Using Fully Functionalized Fragments. in *Phenotypic Screening: Methods and Protocols, Methods in Molecular Biology* (ed. Wagner, B. K.) 115–127 (Humana Press, New York, NY, 2018).
200. Meledin, R., Mali, S. M., Kleifeld, O. & Brik, A. Activity-Based Probes Developed by Applying a Sequential Dehydroalanine Formation Strategy to Expressed Proteins Reveal a Potential α -Globin-Modulating Deubiquitinase. *Angew. Chemie Int. Ed.* **57**, 5645–5649 (2018).
201. Wilson, S. R., Vehus, T., Berg, H. S. & Lundanes, E. Nano-LC in proteomics: recent advances and approaches. *Bioanalysis* **7**, 1799–1815 (2015).
202. Nie, L. *et al.* An optimization of the LC-MS/MS workflow for deep proteome profiling on an Orbitrap Fusion. *Anal. Methods* **8**, 425–434 (2016).
203. Cottrell, J. S. Protein identification using MS/MS data. *J. Proteomics* **74**, 1842–1851 (2011).
204. Zhang, Y., Fonslow, B. R., Shan, B., Baek, M.-C. & Yates, J. R. Protein Analysis by Shotgun/Bottom-up Proteomics. *Chem. Rev.* **113**, 2343–2394 (2013).
205. Al Shweiki, M. H. D. R. *et al.* Assessment of Label-Free Quantification in Discovery Proteomics and Impact of Technological Factors and Natural Variability of Protein Abundance. *J. Proteome Res.* **16**, 1410–1424 (2017).
206. Hoglebe, A. *et al.* Benchmarking common quantification strategies for large-scale phosphoproteomics. *Nat. Commun.* **9**, 1045 (2018).
207. Mann, M. Functional and quantitative proteomics using SILAC. *Nat. Rev. Mol. Cell Biol.* **7**, 952–958 (2006).
208. Chen, X., Wei, S., Ji, Y., Guo, X. & Yang, F. Quantitative proteomics using SILAC: Principles, applications, and developments. *Proteomics* **15**, 3175–3192 (2015).
209. Terzi, F. & Cambridge, S. An Overview of Advanced SILAC-Labeling Strategies for Quantitative Proteomics. in *Methods in Enzymology* (ed. Shukla, A. K.) **585**, 29–47 (Academic Press Inc., 2017).
210. Hsu, J.-L. & Chen, S.-H. Stable isotope dimethyl labelling for quantitative proteomics and beyond. *Philos. Trans. R. Soc. A Math. Phys. Eng. Sci.* **374**, 20150364 (2016).
211. Wiese, S., Reidegeld, K. A., Meyer, H. E. & Warscheid, B. Protein labeling by iTRAQ: A new tool for quantitative mass spectrometry in proteome research. *Proteomics* **7**, 340–350 (2007).
212. Goya Grocin, A., Serwa, R. A., Morales Sanfrutos, J., Ritzefeld, M. & Tate, E. W. Whole Proteome Profiling of N -Myristoyltransferase Activity and Inhibition Using Sortase A. *Mol. Cell. Proteomics* **18**, 115–126 (2019).
213. Zecha, J. *et al.* TMT Labeling for the Masses: A Robust and Cost-efficient, In-solution Labeling Approach. *Mol. Cell. Proteomics* **18**, 1468–1478 (2019).
214. Liu, P., Beer, L. A., Ky, B., Barnhart, K. T. & Speicher, D. W. Quantitative Comparisons of Large Numbers of Human Plasma Samples Using TMT10plex Labeling. *Methods Mol. Biol.* **1619**, 319–337 (2017).
215. Chahrour, O., Cobice, D. & Malone, J. Stable isotope labelling methods in mass spectrometry-based quantitative proteomics. *J. Pharm. Biomed. Anal.* **113**, 2–20 (2015).
216. Govaert, E. *et al.* Comparison of fractionation proteomics for local SWATH library building. *Proteomics* **17**, 1700052 (2017).

217. Savitski, M. M. *et al.* Measuring and managing ratio compression for accurate iTRAQ/TMT quantification. *J. Proteome Res.* **12**, 3586–3598 (2013).
218. O’Connell, J. D., Paulo, J. A., O’Brien, J. J. & Gygi, S. P. Proteome-Wide Evaluation of Two Common Protein Quantification Methods. *J. Proteome Res.* **17**, 1934–1942 (2018).
219. Howard, R. T., Tate, E. W. & Scott, J. Probing the cellular mechanisms of a novel centrosome declustering agent. (Imperial College London, MRes Research Proposal, 2016).
220. Gupte, R., Liu, Z. & Kraus, W. L. PARPs and ADP-ribosylation: recent advances linking molecular functions to biological outcomes. *Genes Dev.* **31**, 101–126 (2017).
221. Lüscher, B. *et al.* ADP-Ribosylation, a Multifaceted Posttranslational Modification Involved in the Control of Cell Physiology in Health and Disease. *Chem. Rev.* **118**, 1092–1136 (2018).
222. Hoch, N. C. & Polo, L. M. ADP-ribosylation: from molecular mechanisms to human disease. *Genet. Mol. Biol.* **43**, e20190075 (2020).
223. Han, S., Craig, J. A., Putnam, C. D., Carozzi, N. B. & Tainer, J. A. Evolution and mechanism from structures of an ADP-ribosylating toxin and NAD complex. *Nat. Struct. Biol.* **6**, 932–936 (1999).
224. Hottiger, M. O., Hassa, P. O., Lüscher, B., Schüler, H. & Koch-Nolte, F. Toward a unified nomenclature for mammalian ADP-ribosyltransferases. *Trends Biochem. Sci.* **35**, 208–219 (2010).
225. Vyas, S. *et al.* Family-wide analysis of poly(ADP-ribose) polymerase activity. *Nat. Commun.* **5**, 4426 (2014).
226. Langelier, M.-F., Zandarashvili, L., Aguiar, P. M., Black, B. E. & Pascal, J. M. NAD⁺ analog reveals PARP-1 substrate-blocking mechanism and allosteric communication from catalytic center to DNA-binding domains. *Nat. Commun.* **9**, 844 (2018).
227. Zhou, G. C. *et al.* Inhibitors of ADP-Ribosylating Bacterial Toxins Based on Oxacarbenium Ion Character at Their Transition States. *J. Am. Chem. Soc.* **126**, 5690–5698 (2004).
228. Dudev, T. & Lim, C. Factors controlling the mechanism of NAD⁺ non-redox reactions. *J. Am. Chem. Soc.* **132**, 16533–16543 (2010).
229. Tsurumura, T. *et al.* Arginine ADP-ribosylation mechanism based on structural snapshots of iota-toxin and actin complex. *Proc. Natl. Acad. Sci.* **110**, 4267–4272 (2013).
230. Zhen, Y. & Yu, Y. Proteomic Analysis of the Downstream Signaling Network of PARP1. *Biochemistry* **57**, 429–440 (2018).
231. Bonicalzi, M.-E., Haince, J.-F., Droit, A. & Poirier, G. G. Poly-ADP-ribosylation in health and disease. *Cell. Mol. Life Sci.* **62**, 739–750 (2005).
232. Oka, S., Kato, J. & Moss, J. Identification and characterization of a mammalian 39-kDa poly(ADP-ribose) glycohydrolase. *J. Biol. Chem.* **281**, 705–713 (2006).
233. Feijs, K. L. H., Forst, A. H., Verheugd, P. & Lüscher, B. Macrodomein-containing proteins: regulating new intracellular functions of mono(ADP-ribosylation). *Nat. Rev. Mol. Cell Biol.* **14**, 443–451 (2013).
234. Yang, C. *et al.* Ubiquitin Modification by the E3 Ligase/ADP-Ribosyltransferase Dtx3L/Parp9. *Mol. Cell* **66**, 503–516.e5 (2017).
235. Blanke, S. R. *et al.* Active-Site Mutations of the Diphtheria Toxin Catalytic Domain: Role of

- Histidine-21 in Nicotinamide Adenine Dinucleotide Binding and ADP-Ribosylation of Elongation Factor 2. *Biochemistry* **33**, 5155–5161 (1994).
236. Blanke, S. R., Huang, K. & Collier, R. J. Active-Site Mutations of Diphtheria Toxin: Role of Tyrosine-65 in NAD Binding and ADP-Ribosylation. *Biochemistry* **33**, 15494–15500 (1994).
237. Wilson, B. A., Reich, K. A., Weinstein, B. R. & Collier, R. J. Active-Site Mutations of Diphtheria Toxin: Effects of Replacing Glutamic Acid-148 with Aspartic Acid, Glutamine, or Serine. *Biochemistry* **29**, 8643–8651 (1990).
238. Marsischky, G. T., Wilson, B. A. & Collier, R. J. Role of glutamic acid 988 of human poly-ADP-ribose polymerase in polymer formation: Evidence for active site similarities to the ADP-ribosylating toxins. *J. Biol. Chem.* **270**, 3247–3254 (1995).
239. Daniels, C. M., Ong, S. & Leung, A. K. L. The Promise of Proteomics for the Study of ADP-Ribosylation. *Mol. Cell* **58**, 911–924 (2015).
240. Leidecker, O. *et al.* Serine is a new target residue for endogenous ADP-ribosylation on histones. *Nat. Chem. Biol.* **12**, 998–1000 (2016).
241. Zhen, Y., Zhang, Y. & Yu, Y. A Cell-Line-Specific Atlas of PARP-Mediated Protein Asp/Glu-ADP-Ribosylation in Breast Cancer. *Cell Rep.* **21**, 2326–2337 (2017).
242. Bilan, V., Leutert, M., Nanni, P., Panse, C. & Hottiger, M. O. Combining Higher-Energy Collision Dissociation and Electron-Transfer/Higher-Energy Collision Dissociation Fragmentation in a Product-Dependent Manner Confidently Assigns Proteomewide ADP-Ribose Acceptor Sites. *Anal. Chem.* **89**, 1523–1530 (2017).
243. Bonfiglio, J. J. *et al.* Serine ADP-Ribosylation Depends on HPF1. *Mol. Cell* **65**, 932–940.e6 (2017).
244. Dawicki-McKenna, J. M. *et al.* PARP-1 Activation Requires Local Unfolding of an Autoinhibitory Domain. *Mol. Cell* **60**, 755–768 (2015).
245. Gibbs-Seymour, I., Fontana, P., Rack, J. G. M. & Ahel, I. HPF1/C4orf27 Is a PARP-1-Interacting Protein that Regulates PARP-1 ADP-Ribosylation Activity. *Mol. Cell* **62**, 432–442 (2016).
246. Qin, W. *et al.* Research Progress on PARP14 as a Drug Target. *Front. Pharmacol.* **10**, 172 (2019).
247. Jørgensen, R., Wang, Y., Visschedyk, D. & Merrill, A. R. The nature and character of the transition state for the ADP-ribosyltransferase reaction. *EMBO Rep.* **9**, 802–809 (2008).
248. Thomas, C. & Tulin, A. V. Poly-ADP-ribose polymerase: Machinery for nuclear processes. *Mol. Aspects Med.* **34**, 1124–1137 (2013).
249. Gibson, B. A. & Kraus, W. L. New insights into the molecular and cellular functions of poly(ADP-ribose) and PARPs. *Nat. Rev. Mol. Cell Biol.* **13**, 411–424 (2012).
250. Kanai, M. *et al.* Inhibition of Crm1–p53 interaction and nuclear export of p53 by poly(ADP-ribose). *Nat. Cell Biol.* **9**, 1175–1183 (2007).
251. Liu, C., Vyas, A., Kassab, M. A., Singh, A. K. & Yu, X. The role of poly ADP-ribosylation in the first wave of DNA damage response. *Nucleic Acids Res.* **45**, 8129–8141 (2017).
252. Ciccarone, F., Zampieri, M. & Caiafa, P. PARP1 orchestrates epigenetic events setting up chromatin domains. *Semin. Cell Dev. Biol.* **63**, 123–134 (2017).

253. Kraus, W. L. & Hottiger, M. O. PARP-1 and gene regulation: Progress and puzzles. *Mol. Aspects Med.* **34**, 1109–1123 (2013).
254. Boamah, E. K., Kotova, E., Garabedian, M., Jarnik, M. & Tulin, A. V. Poly(ADP-ribose) polymerase 1 (PARP-1) regulates ribosomal biogenesis in *Drosophila* nucleoli. *PLoS Genet.* **8**, e1002442 (2012).
255. Dasovich, M. & Leung, A. K. L. A Nucleolar PARTnership Expands PARP Roles in RNA Biology and the Clinical Potential of PARP Inhibitors. *Mol. Cell* **75**, 1089–1091 (2019).
256. Guetg, C., Scheifele, F., Rosenthal, F., Hottiger, M. O. & Santoro, R. Inheritance of Silent rDNA Chromatin Is Mediated by PARP1 via Noncoding RNA. *Mol. Cell* **45**, 790–800 (2012).
257. Wang, X., Liu, L., Montagna, C., Ried, T. & Deng, C. X. Haploinsufficiency of Parp1 accelerates Brca1-associated centrosome amplification, telomere shortening, genetic instability, apoptosis, and embryonic lethality. *Cell Death Differ.* **14**, 924–931 (2007).
258. Bai, P. Biology of Poly(ADP-Ribose) Polymerases: The Factotums of Cell Maintenance. *Mol. Cell* **58**, 947–958 (2015).
259. Boulares, A. H. *et al.* Role of Poly(ADP-ribose) Polymerase (PARP) Cleavage in Apoptosis. *J. Biol. Chem.* **274**, 22932–22940 (1999).
260. Andrabi, S. A. *et al.* Poly(ADP-ribose) (PAR) polymer is a death signal. *Proc. Natl. Acad. Sci.* **103**, 18308–18313 (2006).
261. Galluzzi, L. *et al.* Molecular mechanisms of cell death: recommendations of the Nomenclature Committee on Cell Death 2018. *Cell Death Differ.* **25**, 486–541 (2018).
262. Wang, Y. *et al.* Poly(ADP-Ribose) (PAR) Binding to Apoptosis-Inducing Factor Is Critical for PAR Polymerase-1-Dependent Cell Death (Parthanatos). *Sci. Signal.* **4**, ra20 (2011).
263. Wang, Y. *et al.* A nuclease that mediates cell death induced by DNA damage and poly(ADP-ribose) polymerase-1. *Science* **354**, aad6872 (2016).
264. Robinson, N. *et al.* Programmed necrotic cell death of macrophages: Focus on pyroptosis, necroptosis, and parthanatos. *Redox Biol.* **26**, 101239 (2019).
265. Sutcu, H. H., Matta, E. & Ishchenko, A. A. Role of PARP-catalyzed ADP-ribosylation in the Crosstalk Between DNA Strand Breaks and Epigenetic Regulation. *J. Mol. Biol.* **432**, 1769–1791 (2020).
266. Saxena, A. Poly(ADP-ribose) polymerase 2 localizes to mammalian active centromeres and interacts with PARP-1, Cenpa, Cenpb and Bub3, but not Cenpc. *Hum. Mol. Genet.* **11**, 2319–2329 (2002).
267. Gui, B. *et al.* Selective targeting of PARP-2 inhibits androgen receptor signaling and prostate cancer growth through disruption of FOXA1 function. *Proc. Natl. Acad. Sci.* **116**, 14573–14582 (2019).
268. Hsiao, S. J. & Smith, S. Tankyrase function at telomeres, spindle poles, and beyond. *Biochimie* **90**, 83–92 (2008).
269. Huang, S. M. A. *et al.* Tankyrase inhibition stabilizes axin and antagonizes Wnt signalling. *Nature* **461**, 614–620 (2009).
270. DaRosa, P. A. *et al.* Allosteric activation of the RNF146 ubiquitin ligase by a poly(ADP-ribosylation) signal. *Nature* **517**, 223–226 (2015).

271. Chen, S. *et al.* Structure of N-terminal domain of ZAP indicates how a zinc-finger protein recognizes complex RNA. *Nat. Struct. Mol. Biol.* **19**, 430–435 (2012).
272. Kickhoefer, V. A. *et al.* The 193-kD vault protein, VPARP, is a novel poly(ADP-ribose) polymerase. *J. Cell Biol.* **146**, 917–928 (1999).
273. Salazar, J. C. *et al.* Activation of Human Monocytes by Live *Borrelia burgdorferi* Generates TLR2-Dependent and -Independent Responses Which Include Induction of IFN- β . *PLoS Pathog.* **5**, e1000444 (2009).
274. Mahmoud, L. *et al.* Green Fluorescent Protein Reporter System with Transcriptional Sequence Heterogeneity for Monitoring the Interferon Response. *J. Virol.* **85**, 9268–9275 (2011).
275. Eckeï, L. *et al.* The conserved macrodomains of the non-structural proteins of Chikungunya virus and other pathogenic positive strand RNA viruses function as mono-ADP-ribosylhydrolases. *Sci. Rep.* **7**, 41746 (2017).
276. Loseva, O. *et al.* PARP-3 Is a Mono-ADP-ribosylase That Activates PARP-1 in the Absence of DNA. *J. Biol. Chem.* **285**, 8054–8060 (2010).
277. Belousova, E. A., Kutuzov, M. M., Ivankina, P. A., Ishchenko, A. A. & Lavrik, O. I. A New DNA Break Repair Pathway Involving PARP3 and Base Excision Repair Proteins. *Dokl. Biochem. Biophys.* **482**, 233–237 (2018).
278. Jwa, M. & Chang, P. PARP16 is a tail-anchored endoplasmic reticulum protein required for the PERK-and IRE1 α -mediated unfolded protein response. *Nat. Cell Biol.* **14**, 1223–1230 (2012).
279. Verheugd, P. *et al.* Regulation of NF- κ B signalling by the mono-ADP-ribosyltransferase ARTD10. *Nat. Commun.* **4**, 1683 (2013).
280. Yu, M. *et al.* PARP-10, a novel Myc-interacting protein with poly(ADP-ribose) polymerase activity, inhibits transformation. *Oncogene* **24**, 1982–1993 (2005).
281. Schleicher, E. M., Galvan, A. M., Imamura-Kawasawa, Y., Moldovan, G. & Nicolae, C. M. PARP10 promotes cellular proliferation and tumorigenesis by alleviating replication stress. *Nucleic Acids Res.* **46**, 8908–8916 (2018).
282. Tundel, H. *et al.* PARP6, a mono(ADP-ribosyl) transferase and a negative regulator of cell proliferation, is involved in colorectal cancer development. *Int. J. Oncol.* **41**, 2079–2086 (2012).
283. Qi, G. *et al.* PARP6 acts as a tumor suppressor via downregulating Survivin expression in colorectal cancer. *Oncotarget* **7**, 18812–18824 (2016).
284. Beck, C. *et al.* PARP3, a new therapeutic target to alter Rictor/mTORC2 signaling and tumor progression in BRCA1-associated cancers. *Cell Death Differ.* **26**, 1615–1630 (2019).
285. Chen, C.-C., Feng, W., Lim, P. X., Kass, E. M. & Jasin, M. Homology-Directed Repair and the Role of BRCA1, BRCA2, and Related Proteins in Genome Integrity and Cancer. *Annu. Rev. Cancer Biol.* **2**, 313–336 (2018).
286. Wright, W. D., Shah, S. S. & Heyer, W.-D. Homologous recombination and the repair of DNA double-strand breaks. *J. Biol. Chem.* **293**, 10524–10535 (2018).
287. Chang, H. H. Y., Pannunzio, N. R., Adachi, N. & Lieber, M. R. Non-homologous DNA end joining and alternative pathways to double-strand break repair. *Nat. Rev. Mol. Cell Biol.* **18**, 495–506 (2017).
288. Roy, R., Chun, J. & Powell, S. N. BRCA1 and BRCA2: different roles in a common pathway of genome protection. *Nat. Rev. Cancer* **12**, 68–78 (2012).

289. Lord, C. J. & Ashworth, A. PARP inhibitors: Synthetic lethality in the clinic. *Science* **355**, 1152–1158 (2017).
290. Ashworth, A. & Lord, C. J. Synthetic lethal therapies for cancer: what's next after PARP inhibitors? *Nat. Rev. Clin. Oncol.* **15**, 564–576 (2018).
291. Mateo, J. *et al.* A decade of clinical development of PARP inhibitors in perspective. *Ann. Oncol.* **30**, 1437–1447 (2019).
292. Martin-Hernandez, K., Rodriguez-Vargas, J. M., Schreiber, V. & Dantzer, F. Expanding functions of ADP-ribosylation in the maintenance of genome integrity. *Semin. Cell Dev. Biol.* **63**, 92–101 (2017).
293. Gunderson, C. C. & Moore, K. N. Olaparib: an oral PARP-1 and PARP-2 inhibitor with promising activity in ovarian cancer. *Futur. Oncol.* **11**, 747–757 (2015).
294. Patel, M., Newsheen, S., Maraboyina, S. & Xia, F. The role of poly(ADP-ribose) polymerase inhibitors in the treatment of cancer and methods to overcome resistance: a review. *Cell Biosci.* **10**, 35 (2020).
295. Adis International Ltd. Adis Insight. *Springer Science + Business Media* (2020). Available at: <http://adisinsight.springer.com>. (Accessed: 9th April 2020)
296. Yi, M. *et al.* Advances and perspectives of PARP inhibitors. *Exp. Hematol. Oncol.* **8**, 29 (2019).
297. Bryant, H. E. *et al.* Specific killing of BRCA2-deficient tumours with inhibitors of poly(ADP-ribose) polymerase. *Nature* **434**, 913–917 (2005).
298. Farmer, H. *et al.* Targeting the DNA repair defect in BRCA mutant cells as a therapeutic strategy. *Nature* **434**, 917–921 (2005).
299. Ekblad, T., Camaioni, E., Schüler, H. & Macchiarulo, A. PARP inhibitors: polypharmacology versus selective inhibition. *FEBS J.* **280**, 3563–3575 (2013).
300. Thorsell, A. G. *et al.* Structural Basis for Potency and Promiscuity in Poly(ADP-ribose) Polymerase (PARP) and Tankyrase Inhibitors. *J. Med. Chem.* **60**, 1262–1271 (2017).
301. Hopkins, T. A. *et al.* PARP1 Trapping by PARP Inhibitors Drives Cytotoxicity in Both Cancer Cells and Healthy Bone Marrow. *Mol. Cancer Res.* **17**, 409–419 (2019).
302. Murai, J. *et al.* Trapping of PARP1 and PARP2 by Clinical PARP Inhibitors. *Cancer Res.* **72**, 5588–5599 (2012).
303. Wang, S. *et al.* Uncoupling of PARP1 trapping and inhibition using selective PARP1 degradation. *Nat. Chem. Biol.* **15**, 1223–1231 (2019).
304. Pommier, Y., O'Connor, M. J. & de Bono, J. Laying a trap to kill cancer cells: PARP inhibitors and their mechanisms of action. *Sci. Transl. Med.* **8**, 362ps17 (2016).
305. Murai, J. *et al.* Stereospecific PARP trapping by BMN 673 and comparison with olaparib and rucaparib. *Mol. Cancer Ther.* **13**, 433–443 (2014).
306. Murthy, P. & Muggia, F. PARP inhibitors: clinical development, emerging differences, and the current therapeutic issues. *Cancer Drug Resist.* **2**, 665–679 (2019).
307. Mizutani, A. *et al.* RK-287107, a potent and specific tankyrase inhibitor, blocks colorectal cancer cell growth in a preclinical model. *Cancer Sci.* **109**, 4003–4014 (2018).
308. Menon, M. *et al.* A novel tankyrase inhibitor, MSC2504877, enhances the effects of clinical

- CDK4/6 inhibitors. *Sci. Rep.* **9**, 201 (2019).
309. Shirai, F. *et al.* Discovery of Novel Spiroindoline Derivatives as Selective Tankyrase Inhibitors. *J. Med. Chem.* **62**, 3407–3427 (2019).
310. Sharif-Askari, B., Amrein, L., Aloyz, R. & Panasci, L. PARP3 inhibitors ME0328 and olaparib potentiate vinorelbine sensitization in breast cancer cell lines. *Breast Cancer Res. Treat.* **172**, 23–32 (2018).
311. Huang, J. Y., Wang, K., Vermehren-Schmaedick, A., Adelman, J. P. & Cohen, M. S. PARP6 is a Regulator of Hippocampal Dendritic Morphogenesis. *Sci. Rep.* **6**, 18512 (2016).
312. Morgan, R. K., Kirby, I. T., Vermehren-Schmaedick, A., Rodriguez, K. & Cohen, M. S. Rational Design of Cell-Active Inhibitors of PARP10. *ACS Med. Chem. Lett.* **10**, 74–79 (2019).
313. Murthy, S. *et al.* 4-(Phenoxy) and 4-(benzyloxy)benzamides as potent and selective inhibitors of mono-ADP-ribosyltransferase PARP10/ARTD10. *Eur. J. Med. Chem.* **156**, 93–102 (2018).
314. Kirby, I. T. *et al.* A Potent and Selective PARP11 Inhibitor Suggests Coupling between Cellular Localization and Catalytic Activity. *Cell Chem. Biol.* **25**, 1547–1553.e12 (2018).
315. Li, L. *et al.* PARP12 suppresses Zika virus infection through PARP-dependent degradation of NS1 and NS3 viral proteins. *Sci. Signal.* **11**, eaas9332 (2018).
316. Holechek, J. *et al.* Design, synthesis and evaluation of potent and selective inhibitors of mono-(ADP-ribosyl)transferases PARP10 and PARP14. *Bioorg. Med. Chem. Lett.* **28**, 2050–2054 (2018).
317. Yao, N., Chen, Q., Shi, W., Tang, L. & Fu, Y. PARP14 promotes the proliferation and gemcitabine chemoresistance of pancreatic cancer cells through activation of NF- κ B pathway. *Mol. Carcinog.* **58**, 1291–1302 (2019).
318. Moustakim, M. *et al.* Discovery of a novel allosteric inhibitor scaffold for polyadenosine-diphosphate-ribose polymerase 14 (PARP14) macrodomain 2. *Bioorg. Med. Chem.* **26**, 2965–2972 (2018).
319. Upton, K. *et al.* Design and synthesis of potent inhibitors of the mono(ADP-ribosyl)transferase, PARP14. *Bioorg. Med. Chem. Lett.* **27**, 2907–2911 (2017).
320. Putt, K. S. & Hergenrother, P. J. An enzymatic assay for poly(ADP-ribose) polymerase-1 (PARP-1) via the chemical quantitation of NAD⁺: Application to the high-throughput screening of small molecules as potential inhibitors. *Anal. Biochem.* **326**, 78–86 (2004).
321. Schultz, M. *ADP-ribosylation and NAD⁺ Utilizing Enzymes*. **1813**, (Springer New York, 2018).
322. Wigle, T. J. *et al.* Forced Self-Modification Assays as a Strategy to Screen MonoPARP Enzymes. *SLAS Discov. Adv. Sci. Drug Discov.* **25**, 241–252 (2020).
323. Molina, D. M. *et al.* Monitoring drug target engagement in cells and tissues using the cellular thermal shift assay. *Science* **341**, 84–87 (2013).
324. Liu, X. *et al.* Iniparib nonselectively modifies cysteine-containing proteins in tumor cells and is not a Bona Fide PARP inhibitor. *Clin. Cancer Res.* **18**, 510–523 (2012).
325. Shaw, J. *et al.* Positioning High-Throughput CETSA in Early Drug Discovery through Screening against B-Raf and PARP1. *SLAS Discov. Adv. life Sci. R D* **24**, 121–132 (2019).
326. Dubach, J. M. *et al.* Quantitating drug-target engagement in single cells in vitro and in vivo. *Nat. Chem. Biol.* **13**, 168–173 (2017).

327. Carney, B. *et al.* Target engagement imaging of PARP inhibitors in small-cell lung cancer. *Nat. Commun.* **9**, 176 (2018).
328. Effron, S. S. *et al.* PARP-1 expression quantified by [¹⁸F]FluorThanatrace: A biomarker of response to PARP inhibition adjuvant to radiation therapy. *Cancer Biother. Radiopharm.* **32**, 9–15 (2017).
329. Montemagno, C. & Pagès, G. Metastatic Heterogeneity of Breast Cancer: Companion and Theranostic Approach in Nuclear Medicine. *Cancers (Basel)*. **12**, 821 (2020).
330. Wilson, T. C. *et al.* PET Imaging of PARP Expression Using ¹⁸F-Olaparib. *J. Nucl. Med.* **60**, 504–510 (2019).
331. Wigle, T. J. *et al.* In Vitro and Cellular Probes to Study PARP Enzyme Target Engagement. *Cell Chem. Biol.* **27**, 877-887.e14 (2020).
332. Yang, K. S., Budin, G., Tassa, C., Kister, O. & Weissleder, R. Bioorthogonal Approach to Identify Unsuspected Drug Targets in Live Cells. *Angew. Chemie Int. Ed.* **52**, 10593–10597 (2013).
333. Howard, R. T., Tate, E. W. & Scott, J. S. The design, synthesis and application of affinity-based probes for novel centrosome declustering agents. (Imperial College London MRes Report, 2017).
334. Howard, R. T. *et al.* Structure-Guided Design and In-Cell Target Profiling of a Cell-Active Target Engagement Probe for PARP Inhibitors. *ACS Chem. Biol.* **15**, 325–333 (2020).
335. Hughes, D. L. Patent Review of Manufacturing Routes to Recently Approved PARP Inhibitors: Olaparib, Rucaparib, and Niraparib. *Org. Process Res. Dev.* **21**, 1227–1244 (2017).
336. Chang, P., Coughlin, M. & Mitchison, T. J. Interaction between Poly(ADP-ribose) and NuMA Contributes to Mitotic Spindle Pole Assembly. *Mol. Biol. Cell* **20**, 4575–4585 (2009).
337. Kwon, M. *et al.* Mechanisms to suppress multipolar divisions in cancer cells with extra centrosomes. *Genes Dev.* **22**, 2189–2203 (2008).
338. McCabe, N. *et al.* Targeting Tankyrase 1 as a therapeutic strategy for BRCA-associated cancer. *Oncogene* **28**, 1465–1470 (2009).
339. Castiel, A. *et al.* A phenanthrene derived PARP inhibitor is an extra-centrosomes de-clustering agent exclusively eradicating human cancer cells. *BMC Cancer* **11**, 412 (2011).
340. Johannes, J. W. *et al.* Discovery of AZ0108, an orally bioavailable phthalazinone PARP inhibitor that blocks centrosome clustering. *Bioorg. Med. Chem. Lett.* **25**, 5743–5747 (2015).
341. Wang, Z. *et al.* Pharmacological Inhibition of PARP6 Triggers Multipolar Spindle Formation and Elicits Therapeutic Effects in Breast Cancer. *Cancer Res.* **78**, 6691–6702 (2018).
342. Wang, Z., Grosskurth, S. E. & Chen, H. PARP6 inhibition as a strategy to exploit centrosome clustering in cancer cells? *Oncotarget* **10**, 690–691 (2019).
343. Szklarczyk, D. *et al.* STRING v11: protein-protein association networks with increased coverage, supporting functional discovery in genome-wide experimental datasets. *Nucleic Acids Res.* **47**, D607–D613 (2019).
344. César-Razquin, A. *et al.* A Call for Systematic Research on Solute Carriers. *Cell* **162**, 478–487 (2015).
345. Kiefer, K., Clement, J., Garidel, P. & Peschka-Süss, R. Transfection efficiency and cytotoxicity

- of nonviral gene transfer reagents in human smooth muscle and endothelial cells. *Pharm. Res.* **21**, 1009–1017 (2004).
346. Voorneveld, J. *et al.* Olaparib-Based Photoaffinity Probes for PARP-1 Detection in Living Cells. *ChemBioChem* **21**, 2431–2434 (2020).
347. Weinlich, R., Oberst, A., Beere, H. M. & Green, D. R. Necroptosis in development, inflammation and disease. *Nat. Rev. Mol. Cell Biol.* **18**, 127–136 (2017).
348. Zhuang, C. & Chen, F. Small-Molecule Inhibitors of Necroptosis: Current Status and Perspectives. *J. Med. Chem.* **63**, 1490–1510 (2020).
349. Ashkenazi, A. & Salvesen, G. Regulated Cell Death: Signaling and Mechanisms. *Annu. Rev. Cell Dev. Biol.* **30**, 337–356 (2014).
350. Galluzzi, L. *et al.* Essential versus accessory aspects of cell death: Recommendations of the NCCD 2015. *Cell Death and Differentiation* **22**, 58–73 (2015).
351. Radi, Z. A., Stewart, Z. S. & O’Neil, S. P. Accidental and Programmed Cell Death in Investigative and Toxicologic Pathology. *Curr. Protoc. Toxicol.* **76**, e51 (2018).
352. Zhang, Y., Chen, X., Gueydan, C. & Han, J. Plasma membrane changes during programmed cell deaths. *Cell Research* **28**, 9–21 (2018).
353. Sun, Y. & Peng, Z. L. Programmed cell death and cancer. *Postgraduate Medical Journal* **85**, 134–140 (2009).
354. Jorgensen, I., Rayamajhi, M. & Miao, E. A. Programmed cell death as a defence against infection. *Nature Reviews Immunology* **17**, 151–164 (2017).
355. Kerr, J. F. R., Wyllie, A. H. & Currie, A. R. Apoptosis: A basic biological phenomenon with wide-ranging implications in tissue kinetics. *Br. J. Cancer* **26**, 239–257 (1972).
356. Elmore, S. Apoptosis: A Review of Programmed Cell Death. *Toxicologic Pathology* **35**, 495–516 (2007).
357. Laster, S. M., Wood, J. G. & Gooding, L. R. Tumor necrosis factor can induce both apoptic and necrotic forms of cell lysis. *J. Immunol.* **141**, 2629–2634 (1988).
358. Vercammen, D. *et al.* Inhibition of caspases increases the sensitivity of L929 cells to necrosis mediated by tumor necrosis factor. *J. Exp. Med.* **187**, 1477–1485 (1998).
359. Degterev, A. *et al.* Chemical inhibitor of nonapoptotic cell death with therapeutic potential for ischemic brain injury. *Nat. Chem. Biol.* **1**, 112–119 (2005).
360. Degterev, A. *et al.* Identification of RIP1 kinase as a specific cellular target of necrostatins. *Nat. Chem. Biol.* **4**, 313–321 (2008).
361. Zhang, D. W. *et al.* RIP3, an energy metabolism regulator that switches TNF-induced cell death from apoptosis to necrosis. *Science* **325**, 332–336 (2009).
362. He, S. *et al.* Receptor Interacting Protein Kinase-3 Determines Cellular Necrotic Response to TNF- α . *Cell* **137**, 1100–1111 (2009).
363. Cho, Y. S. *et al.* Phosphorylation-Driven Assembly of the RIP1-RIP3 Complex Regulates Programmed Necrosis and Virus-Induced Inflammation. *Cell* **137**, 1112–1123 (2009).
364. Sun, L. *et al.* Mixed lineage kinase domain-like protein mediates necrosis signaling downstream of RIP3 kinase. *Cell* **148**, 213–227 (2012).

365. Murphy, J. M. *et al.* The pseudokinase MLKL mediates necroptosis via a molecular switch mechanism. *Immunity* **39**, 443–453 (2013).
366. Nailwal, H. & Chan, F. K.-M. Necroptosis in anti-viral inflammation. *Cell Death Differ.* **26**, 4–13 (2019).
367. Holler, N. *et al.* Fas triggers an alternative, caspase-8-independent cell death pathway using the kinase RIP as effector molecule. *Nat. Immunol.* **1**, 489–495 (2000).
368. Christofferson, D. E., Li, Y. & Yuan, J. Control of Life-or-Death Decisions by RIP1 Kinase. *Annu. Rev. Physiol.* **76**, 129–150 (2014).
369. Dondelinger, Y., Darding, M., Bertrand, M. J. M. & Walczak, H. Poly-ubiquitination in TNFR1-mediated necroptosis. *Cellular and Molecular Life Sciences* **73**, 2165–2176 (2016).
370. Micheau, O. & Tschopp, J. Induction of TNF receptor I-mediated apoptosis via two sequential signaling complexes. *Cell* **114**, 181–190 (2003).
371. Wang, H. *et al.* Mixed Lineage Kinase Domain-like Protein MLKL Causes Necrotic Membrane Disruption upon Phosphorylation by RIP3. *Mol. Cell* **54**, 133–146 (2014).
372. Dhuriya, Y. K. & Sharma, D. Necroptosis: a regulated inflammatory mode of cell death. *J. Neuroinflammation* **15**, 199 (2018).
373. Frank, D. & Vince, J. E. Pyroptosis versus necroptosis: similarities, differences, and crosstalk. *Cell Death Differ.* **26**, 99–114 (2019).
374. He, S., Liang, Y., Shao, F. & Wang, X. Toll-like receptors activate programmed necrosis in macrophages through a receptor-interacting kinase-3-mediated pathway. *Proc. Natl. Acad. Sci.* **108**, 20054–20059 (2011).
375. Robinson, N. *et al.* Type I interferon induces necroptosis in macrophages during infection with *Salmonella enterica* serovar Typhimurium. *Nat. Immunol.* **13**, 954–962 (2012).
376. Thapa, R. J. *et al.* Interferon-induced RIP1/RIP3-mediated necrosis requires PKR and is licensed by FADD and caspases. *Proc. Natl. Acad. Sci.* **110**, E3109–E3118 (2013).
377. Upton, J. W., Kaiser, W. J. & Mocarski, E. S. DAI/ZBP1/DLM-1 complexes with RIP3 to mediate virus-induced programmed necrosis that is targeted by murine cytomegalovirus vIRA. *Cell Host Microbe* **11**, 290–297 (2012).
378. Tenev, T. *et al.* The Ripoptosome, a Signaling Platform that Assembles in Response to Genotoxic Stress and Loss of IAPs. *Mol. Cell* **43**, 432–448 (2011).
379. Newton, K. *et al.* Activity of caspase-8 determines plasticity between cell death pathways. *Nature* **575**, 679–682 (2019).
380. Schwarzer, R., Laurien, L. & Pasparakis, M. New insights into the regulation of apoptosis, necroptosis, and pyroptosis by receptor interacting protein kinase 1 and caspase-8. *Curr. Opin. Cell Biol.* **63**, 186–193 (2020).
381. Fritsch, M. *et al.* Caspase-8 is the molecular switch for apoptosis, necroptosis and pyroptosis. *Nature* **575**, 679–682 (2019).
382. Zhao, X. M. *et al.* Hsp90 modulates the stability of MLKL and is required for TNF-induced necroptosis. *Cell Death Dis.* **7**, e2089 (2016).
383. Li, D. *et al.* A cytosolic heat shock protein 90 and cochaperone CDC37 complex is required for RIP3 activation during necroptosis. *Proc. Natl. Acad. Sci.* **112**, 5017–5022 (2015).

384. Jacobsen, A. V. *et al.* HSP90 activity is required for MLKL oligomerisation and membrane translocation and the induction of necroptotic cell death. *Cell Death Dis.* **7**, e2051 (2016).
385. Johnston, A. N. *et al.* Necroptosis-blocking compound NBC1 targets heat shock protein 70 to inhibit MLKL polymerization and necroptosis. *Proc. Natl. Acad. Sci.* **117**, 6521–6530 (2020).
386. Hanna-Addams, S., Liu, S., Liu, H., Chen, S. & Wang, Z. CK1 α , CK1 δ , and CK1 ϵ are necrosome components which phosphorylate serine 227 of human RIPK3 to activate necroptosis. *Proc. Natl. Acad. Sci.* **117**, 1962–1970 (2020).
387. Petrie, E. J. *et al.* Identification of MLKL membrane translocation as a checkpoint in necroptotic cell death using Monobodies. *Proc. Natl. Acad. Sci.* **117**, 8468–8475 (2020).
388. Balachandran, S. & Rall, G. F. Benefits and Perils of Necroptosis in Influenza Virus Infection. *J. Virol.* **94**, e011101–e011119 (2020).
389. Aziz, M., Jacob, A. & Wang, P. Revisiting caspases in sepsis. *Cell Death Dis.* **5**, e1526 (2014).
390. Pan, T. *et al.* Necroptosis Takes Place in Human Immunodeficiency Virus Type-1 (HIV-1)-Infected CD4+ T Lymphocytes. *PLoS One* **9**, e93944 (2014).
391. Linkermann, A. *et al.* Two independent pathways of regulated necrosis mediate ischemia-reperfusion injury. *Proc. Natl. Acad. Sci.* **110**, 12024–12029 (2013).
392. Luedde, M. *et al.* RIP3, a kinase promoting necroptotic cell death, mediates adverse remodelling after myocardial infarction. *Cardiovasc. Res.* **103**, 206–216 (2014).
393. Lau, A. *et al.* RIPK3-mediated necroptosis promotes donor kidney inflammatory injury and reduces allograft survival. *Am. J. Transplant.* **13**, 2805–2818 (2013).
394. Silke, J., Rickard, J. A. & Gerlic, M. The diverse role of RIP kinases in necroptosis and inflammation. *Nat. Immunol.* **16**, 689–697 (2015).
395. Patel, S. *et al.* RIP1 inhibition blocks inflammatory diseases but not tumor growth or metastases. *Cell Death Differ.* **27**, 161–175 (2020).
396. Duprez, L. *et al.* RIP Kinase-Dependent Necrosis Drives Lethal Systemic Inflammatory Response Syndrome. *Immunity* **35**, 908–918 (2011).
397. Lin, J. *et al.* A Role of RIP3-Mediated Macrophage Necrosis in Atherosclerosis Development. *Cell Rep.* **3**, 200–210 (2013).
398. Duan, X. *et al.* Inhibition of keratinocyte necroptosis mediated by RIPK1/RIPK3/MLKL provides a protective effect against psoriatic inflammation. *Cell Death Dis.* **11**, 134 (2020).
399. Yuan, J., Amin, P. & Ofengeim, D. Necroptosis and RIPK1-mediated neuroinflammation in CNS diseases. *Nature Reviews Neuroscience* **20**, 19–33 (2019).
400. Zhang, S., Tang, M., Luo, H., Shi, C. & Xu, Y. Necroptosis in neurodegenerative diseases: a potential therapeutic target. *Cell Death Dis.* **8**, e2905 (2017).
401. Ito, Y. *et al.* RIPK1 mediates axonal degeneration by promoting inflammation and necroptosis in ALS. *Science* **353**, 603–608 (2016).
402. Ofengeim, D. *et al.* RIPK1 mediates a disease-associated microglial response in Alzheimer's disease. *Proc. Natl. Acad. Sci.* **114**, E8788–E8797 (2017).
403. Caccamo, A. *et al.* Necroptosis activation in Alzheimer's disease. *Nat. Neurosci.* **20**, 1236–1246 (2017).

404. Zhu, S., Zhang, Y., Bai, G. & Li, H. Necrostatin-1 ameliorates symptoms in R6/2 transgenic mouse model of Huntington's disease. *Cell Death Dis.* **2**, e115–e115 (2011).
405. Murakami, Y. *et al.* Receptor interacting protein kinase mediates necrotic cone but not rod cell death in a mouse model of inherited degeneration. *Proc. Natl. Acad. Sci.* **109**, 14598–14603 (2012).
406. Strilic, B. *et al.* Tumour-cell-induced endothelial cell necroptosis via death receptor 6 promotes metastasis. *Nature* **536**, 215–218 (2016).
407. Jiao, D. *et al.* Necroptosis of tumor cells leads to tumor necrosis and promotes tumor metastasis. *Cell Res.* **28**, 868–870 (2018).
408. Shen, F. *et al.* Pharmacological inhibition of necroptosis promotes human breast cancer cell proliferation and metastasis. *Onco. Targets. Ther.* **13**, 3165–3176 (2020).
409. Krysko, O. *et al.* Necroptotic cell death in anti-cancer therapy. *Immunol. Rev.* **280**, 207–219 (2017).
410. Xie, T. *et al.* Structural basis of RIP1 inhibition by necrostatins. *Structure* **21**, 493–499 (2013).
411. Weinlich, R. & Green, D. R. The Two Faces of Receptor Interacting Protein Kinase-1. *Mol. Cell* **56**, 469–480 (2014).
412. Duong-Ly, K. C. & Peterson, J. R. The Human Kinome and Kinase Inhibition. *Curr. Protoc. Pharmacol.* **60**, 2.9.1–2.9.14 (2013).
413. Hanson, S. M. *et al.* What Makes a Kinase Promiscuous for Inhibitors? *Cell Chem. Biol.* **26**, 390-399.e5 (2019).
414. Bhullar, K. S. *et al.* Kinase-targeted cancer therapies: progress, challenges and future directions. *Mol. Cancer* **17**, 48 (2018).
415. Takahashi, N. *et al.* Necrostatin-1 analogues: critical issues on the specificity, activity and in vivo use in experimental disease models. *Cell Death Dis.* **3**, e437 (2012).
416. Christofferson, D. E. *et al.* A novel role for RIP1 kinase in mediating TNF α production. *Cell Death Dis.* **3**, e320 (2012).
417. Yang, S.-H. *et al.* A small molecule Nec-1 directly induces amyloid clearance in the brains of aged APP/PS1 mice. *Sci. Rep.* **9**, 4183 (2019).
418. Iannielli, A. *et al.* Pharmacological Inhibition of Necroptosis Protects from Dopaminergic Neuronal Cell Death in Parkinson's Disease Models. *Cell Rep.* **22**, 2066–2079 (2018).
419. Harris, P. A. *et al.* DNA-Encoded Library Screening Identifies Benzo[b][1,4]oxazepin-4-ones as Highly Potent and Monoselective Receptor Interacting Protein 1 Kinase Inhibitors. *J. Med. Chem.* **59**, 2163–2178 (2016).
420. Harris, P. A. *et al.* Discovery of a First-in-Class Receptor Interacting Protein 1 (RIP1) Kinase Specific Clinical Candidate (GSK2982772) for the Treatment of Inflammatory Diseases. *J. Med. Chem.* **60**, 1247–1261 (2017).
421. Weisel, K. *et al.* Randomized clinical study of safety, pharmacokinetics, and pharmacodynamics of RIPK1 inhibitor GSK2982772 in healthy volunteers. *Pharmacol. Res. Perspect.* **5**, e00365 (2017).
422. Ledford, H. Coronavirus shuts down trials of drugs for multiple other diseases. *Nature* **580**, 15–16 (2020).

423. Yoshikawa, M. *et al.* Discovery of 7-Oxo-2,4,5,7-tetrahydro-6 H -pyrazolo[3,4- c]pyridine Derivatives as Potent, Orally Available, and Brain-Penetrating Receptor Interacting Protein 1 (RIP1) Kinase Inhibitors: Analysis of Structure–Kinetic Relationships. *J. Med. Chem.* **61**, 2384–2409 (2018).
424. Cohen, D. J. *et al.* A phase I/II study of GSK3145095 alone and in combination with anticancer agents including pembrolizumab in adults with selected solid tumors. *J. Clin. Oncol.* **37**, TPS4165 (2019).
425. GlaxoSmithKline. *Press release: Third quarter 2019.* (2019).
426. Denali Therapeutics. Available at: <https://denalitherapeutics.com/pipeline>. (Accessed: 6th May 2020)
427. Harris, P. A. *et al.* Discovery and Lead-Optimization of 4,5-Dihydropyrazoles as Mono-Kinase Selective, Orally Bioavailable and Efficacious Inhibitors of Receptor Interacting Protein 1 (RIP1) Kinase. *J. Med. Chem.* **62**, 5096–5110 (2019).
428. Wang, W. *et al.* RIP1 Kinase Drives Macrophage-Mediated Adaptive Immune Tolerance in Pancreatic Cancer. *Cancer Cell* **34**, 757–774.e7 (2018).
429. Ren, Y. *et al.* Discovery of a Highly Potent, Selective, and Metabolically Stable Inhibitor of Receptor-Interacting Protein 1 (RIP1) for the Treatment of Systemic Inflammatory Response Syndrome. *J. Med. Chem.* **60**, 972–986 (2017).
430. Mandal, P. *et al.* RIP3 Induces Apoptosis Independent of Pronecrotic Kinase Activity. *Mol. Cell* **56**, 481–495 (2014).
431. Zhang, H. *et al.* N -(7-Cyano-6-(4-fluoro-3-(2-(3-(trifluoromethyl)phenyl)acetamido)phenoxy)benzo[d]thiazol-2-yl)cyclopropanecarboxamide (TAK-632) Analogues as Novel Necroptosis Inhibitors by Targeting Receptor-Interacting Protein Kinase 3 (RIPK3): Synthesis, Structure–A. *J. Med. Chem.* **62**, 6665–6681 (2019).
432. Petrie, E. J. *et al.* Conformational switching of the pseudokinase domain promotes human MLKL tetramerization and cell death by necroptosis. *Nat. Commun.* **9**, 2422 (2018).
433. Liao, D. *et al.* Necrosulfonamide inhibits necroptosis by selectively targeting the mixed lineage kinase domain-like protein. *Medchemcomm* **5**, 333–337 (2014).
434. Yan, B. *et al.* Discovery of a new class of highly potent necroptosis inhibitors targeting the mixed lineage kinase domain-like protein. *Chem. Commun.* **53**, 3637–3640 (2017).
435. Zhang, X., Matsuda, M., Yaegashi, N., Nabe, T. & Kitatani, K. Regulation of Necroptosis by Phospholipids and Sphingolipids. *Cells* **9**, 627 (2020).
436. Guibao, C. D., Petrinjak, K. & Moldoveanu, T. Uncovering human mixed lineage kinase domain-like activation in necroptosis. *Future Med. Chem.* **11**, 2831–2844 (2019).
437. de Sousa Brito, H. M. *et al.* Discovery and validation of new modulators of necroptosis using phenotypic high throughput screening of a large compound library. *J. Hepatol.* **68**, S361 (2018).
438. Brito, H. *et al.* Phenotypic high-throughput screening platform identifies novel chemotypes for necroptosis inhibition. *Cell Death Discov.* **6**, 6 (2020).
439. Pierotti, C. L. *et al.* Potent Inhibition of Necroptosis by Simultaneously Targeting Multiple Effectors of the Pathway. *ACS Chem. Biol.* [acschembio.0c00482](https://doi.org/10.1021/acscchembio.0c00482) (2020). doi:10.1021/acscchembio.0c00482
440. Chen, J. J. *et al.* Discovery of 2-methylpyridine-based biaryl amides as γ -secretase modulators

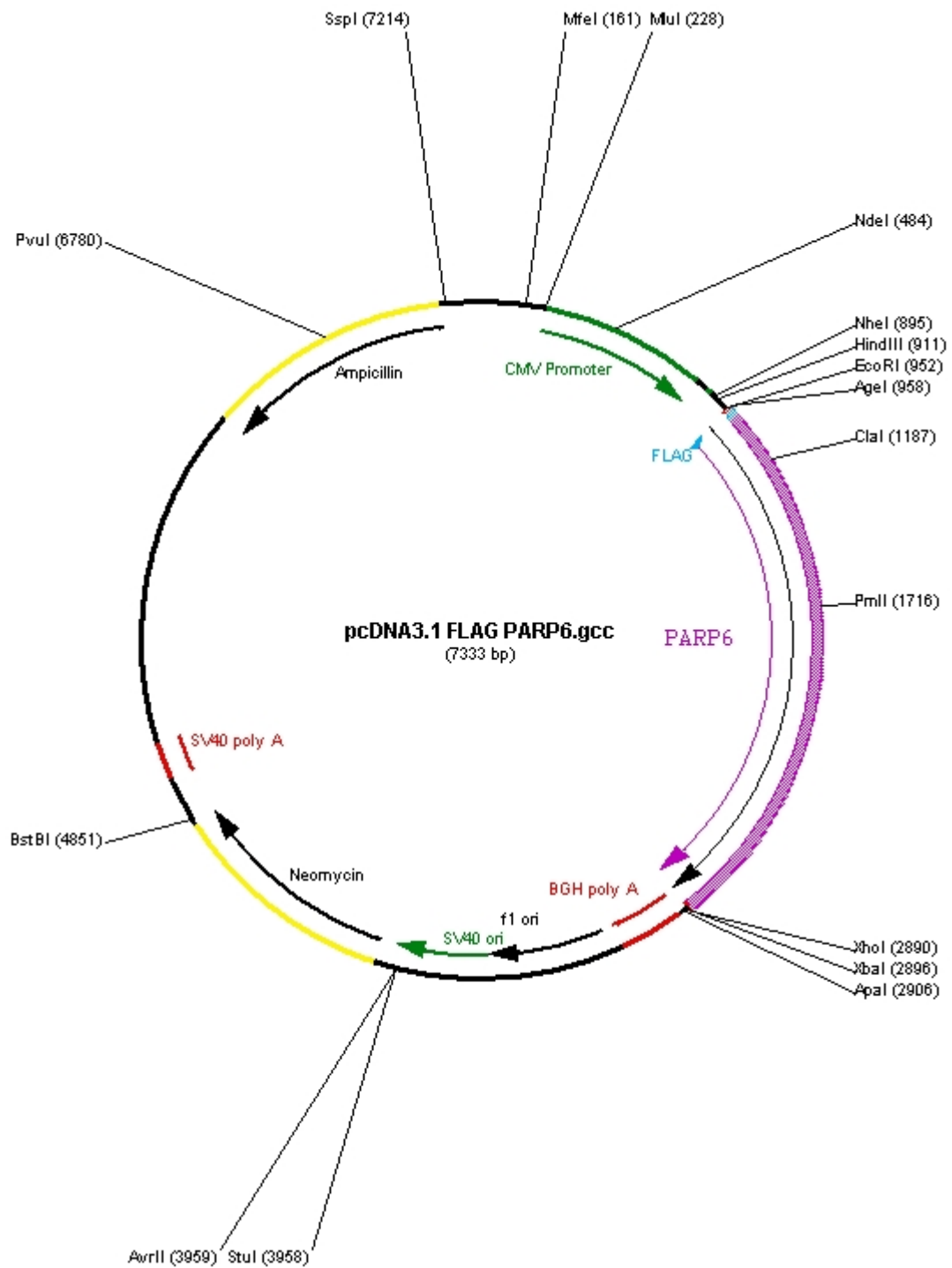
- for the treatment of Alzheimer's disease. *Bioorg. Med. Chem. Lett.* **23**, 6447–6454 (2013).
441. Meerwein, H. *et al.* Untersuchungen über aromatische Diazoverbindungen, II. Verfahren zur Herstellung Aromatischer Sulfonsäurechloride, Eine Neue Modifikation der Sandmeyerschen Reaktion. *Chem. Ber.* **90**, 841–852 (1957).
442. Hogan, P. J. & Cox, B. G. Aqueous Process Chemistry: The Preparation of Aryl Sulfonyl Chlorides. *Org. Process Res. Dev.* **13**, 875–879 (2009).
443. Lebegue, N. *et al.* Novel benzopyridothiadiazepines as potential active antitumor agents. *J. Med. Chem.* **48**, 7363–7373 (2005).
444. Gong, Y. & Pauls, H. W. A Convenient Synthesis of Heteroaryl Benzoic Acids via Suzuki Reaction. *Synlett* **2000**, 0829–0831 (2000).
445. Hu, D. X., Grice, P. & Ley, S. V. Rotamers or diastereomers? An overlooked NMR solution. *J. Org. Chem.* **77**, 5198–5202 (2012).
446. Sartorius. Incucyte® Systems for Live-Cell Imaging and Analysis. Available at: <https://www.essenbioscience.com/en/products/incucyte/>. (Accessed: 11th May 2020)
447. Wlodkowic, D., Faley, S., Darzynkiewicz, Z. & Cooper, J. M. Real-Time Cytotoxicity Assays. in *Methods in Molecular Biology* **731**, 285–291 (2011).
448. Akara-amornthum, P., Lomphithak, T., Choksi, S., Tohtong, R. & Jitkaew, S. Key necroptotic proteins are required for Smac mimetic-mediated sensitization of cholangiocarcinoma cells to TNF- α and chemotherapeutic gemcitabine-induced necroptosis. *PLoS One* **15**, e0227454 (2020).
449. Karpievitch, Y. V., Dabney, A. R. & Smith, R. D. Normalization and missing value imputation for label-free LC-MS analysis. *BMC Bioinformatics* **13**, S5 (2012).
450. Dong, D. *et al.* Structural basis of assembly of the human T cell receptor–CD3 complex. *Nature* **573**, 546–552 (2019).
451. Pruitt, K. D., Tatusova, T. & Maglott, D. R. NCBI reference sequences (RefSeq): a curated non-redundant sequence database of genomes, transcripts and proteins. *Nucleic Acids Res.* **35**, D61–D65 (2007).
452. Ebrahimi-Fakhari, D. *et al.* Reduction of TMEM97 increases NPC1 protein levels and restores cholesterol trafficking in Niemann-pick type C1 disease cells. *Hum. Mol. Genet.* **25**, 3588–3599 (2016).
453. Kanehisa, M. & Goto, S. KEGG: Kyoto Encyclopedia of Genes and Genomes. *Nucleic Acids Res.* **28**, 27–30 (2000).
454. Flinn, A. M. & Gennery, A. R. Adenosine deaminase deficiency: a review. *Orphanet J. Rare Dis.* **13**, 65 (2018).
455. Johnston, J. B. Mechanism of action of pentostatin and cladribine in hairy cell leukemia. *Leuk. Lymphoma* **52**, 43–45 (2011).
456. Kane, B. J., Kuhn, J. G. & Roush, M. K. Pentostatin: An adenosine deaminase inhibitor for the treatment of hairy cell leukemia. *Ann. Pharmacother.* **26**, 939–947 (1992).
457. Evans, G. B., Schramm, V. L. & Tyler, P. C. The transition to magic bullets – transition state analogue drug design. *Medchemcomm* **9**, 1983–1993 (2018).
458. Ugochukwu, E. *et al.* RCSB PDB - 3IAR: The crystal structure of human adenosine deaminase. *RCSB Protein Data Bank* (2009). Available at: <https://www.rcsb.org/structure/3IAR>. (Accessed:

11th May 2020)

459. Setten, R. L., Rossi, J. J. & Han, S. The current state and future directions of RNAi-based therapeutics. *Nat. Rev. Drug Discov.* **18**, 421–446 (2019).
460. Wilson, R. C. & Doudna, J. A. Molecular Mechanisms of RNA Interference. *Annu. Rev. Biophys.* **42**, 217–239 (2013).
461. Alon, A. *et al.* Identification of the gene that codes for the σ 2 receptor. *Proc. Natl. Acad. Sci.* **114**, 7160–7165 (2017).
462. Maurisse, R. *et al.* Comparative transfection of DNA into primary and transformed mammalian cells from different lineages. *BMC Biotechnol.* **10**, 9 (2010).
463. Moore, C. B., Guthrie, E. H., Huang, M. T. H. & Taxman, D. J. Short hairpin RNA (shRNA): design, delivery, and assessment of gene knockdown. *Methods Mol. Biol.* **629**, 141–158 (2010).
464. Larson, M. H. *et al.* CRISPR interference (CRISPRi) for sequence-specific control of gene expression. *Nat. Protoc.* **8**, 2180–2196 (2013).
465. Tzakoniati, F. *et al.* Development of Photocrosslinking Probes Based on Huwentoxin-IV to Map the Site of Interaction on Nav1.7. *Cell Chem. Biol.* **27**, 306-313.e4 (2020).
466. Flaxman, H. A., Chang, C.-F., Wu, H.-Y., Nakamoto, C. H. & Woo, C. M. A Binding Site Hotspot Map of the FKBP12–Rapamycin–FRB Ternary Complex by Photoaffinity Labeling and Mass Spectrometry-Based Proteomics. *J. Am. Chem. Soc.* **141**, 11759–11764 (2019).
467. Case, F. H. & Buck, C. J. Notes - The Behavior of 3,4'-Diaminobiphenyl in the Skraup Reaction. Synthesis of 6,7'-Biquinoline. *J. Org. Chem.* **21**, 697–698 (1956).
468. Hutin, D., Grimaldi, G. & Matthews, J. Methods to Study TCDD-Inducible Poly-ADP-Ribose Polymerase (TIPARP) Mono-ADP-Ribosyltransferase Activity. in *ADP-ribosylation and NAD+ Utilising Enzymes* 109–124 (Humana, New York, NY, 2018). doi:10.1007/978-1-4939-8588-3_8

XI Appendices

XI.i Appendix I – Plasmid map for FLAG-PARP6 in pcDNA3.1



XI.ii Appendix II – Amino acid sequence of GST-PARP6

MSPILGYWKIKGLVQPTRLLLEYLEEKYEEHL YERDEGDKWRNKKFELGLEFPNLPYYIDGD
VKLTQSMAIIRYIADKHNMLGGCPKERA EISMLEGA VLDIRYGVSR IAYS KDFETLKVDFLSK
LPEMLKMFEDRLCHKTYLNGDHVTHPDFM LYDALDVVLYMDPMCLDAFPKLVCFKKRIEAI
PQIDKYLKSSKYIAWPLQGWQATFGGGDHPPKSDLEVL FQGPM DIKGQFWNDDDSEGDNES
EEFLYGVQGS CAADLYRHPQLDADIEAVKEIYSENSVSIREYGTIDDVDIDLHINISFLDEEVST
AWKVL RTEPIVLR LRFSL SQYLDGPEPSIEVFQPSNKEGFGLGLQLKKILGMFTSQQWKHLSN
DFLKTQQEKRHSWFKASGTIKKFRAGLSIFSPIPKSPSPHIIQDSMLKGKLGVP ELRVGRLMNR
SISCTMKNPKVEVFGYPPSPQAGLLCPQH VGLPPPARTSPLVSGHCKNIPTLEYGFLVQIMKY
AEQRIPTLNEYCVVCDEQHVFQNGSMLKPAVCTRELCVFSFYTLGVMSGAAEEVATGAEVV
DLLVAMCRAALES PRKSIIFEPYPSVVDPTDPKTLAFNP KKKNYERLQKALDSVMSIREMTQG
SYLEIKKQMDKLDPLAHPLLQWISSNRSHIVKLPLSRLKFMHTSHQFLLLSSPPAKEARFRTA
KKLYGSTFAFHGSHIENWHSILRNGLVNASYTKLQLHGAA YGKGIYLSPISSISFGYSGMGKG
QHRMPSKDELVQRYNRMNTIPQTRSIQSRFLQSRNLNCIALCEVITSKDLQKHGNIWVCPVSD
HVCTRFFFVYEDGQVGDANINTQDPKIQKEIMRVIGTQVYTN

XI.iii Appendix III – TMT labelling

XI.iii.i PARP target profiling

TMT labels used for each proteomics sample to generate the PARP data from **Figure 2.13** and **Figure 2.15** and the LC-MS/MS runs they were combined into:

TMT run 1								
DMSO			PARPYnD 1 μ M			PARPYnD 1 μ M & AZ9482 5 μ M		
TMT_126	TMT_127N	TMT_127C	TMT_128N	TMT_128C	TMT_129N	TMT_129C	TMT_130N	TMT_130C
Replicate 1	Replicate 2	Replicate 3	Replicate 1	Replicate 2	Replicate 3	Replicate 1	Replicate 2	Replicate 3

TMT run 2								
PARPYnD 1 μ M Not used - kept for intra-TMT run normalisation			PARPYnD 1 μ M & AZ0108 5 μ M			PARPYnD 1 μ M & Olaparib 5 μ M		
TMT_126	TMT_127N	TMT_127C	TMT_128N	TMT_128C	TMT_129N	TMT_129C	TMT_130N	TMT_130C
Replicate 1	Replicate 2	Replicate 3	Replicate 1	Replicate 2	Replicate 3	Replicate 1	Replicate 2	Replicate 3

TMT labels used for each proteomics sample to generate the PARP data from **Figure 2.14**:

DMSO			PARPYnD 1 μ M -UV		
TMT_126	TMT_127N	127C	TMT_128N	TMT_128C	TMT_129N
Replicate 1	Replicate 2	Replicate 3	Replicate 1	Replicate 2	Replicate 3

XI.iii.ii Necroptosis target profiling

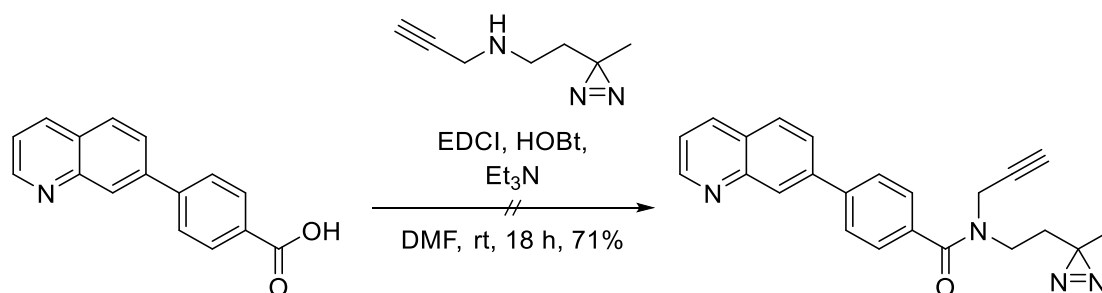
TMT labels used for each proteomics sample to generate the necroptosis data from **Figure 3.22** and **Figure 3.23** and the LC-MS/MS runs they were combined into:

DMSO TMT_126			7PQYnD 1 μ M TMT_127N			7PQYnD 2.5 μ M TMT_127C			7PQYnD 10 μ M TMT_128N		
TMT run 1	TMT run 2	TMT run 3	TMT run 1	TMT run 2	TMT run 3	TMT run 1	TMT run 2	TMT run 3	TMT run 1	TMT run 2	TMT run 3
Replicate 1	Replicate 2	Replicate 3	Replicate 1	Replicate 2	Replicate 3	Replicate 1	Replicate 2	Replicate 3	Replicate 1	Replicate 2	Replicate 3

7PQYnD 2.5 μ M & AZ'902 2.5 μ M TMT_128C			7PQYnD 2.5 μ M & AZ'902 10 μ M TMT_129N			7PQYnD 2.5 μ M & AZ'902 50 μ M TMT_129C		
TMT run 1	TMT run 2	TMT run 3	TMT run 1	TMT run 2	TMT run 3	TMT run 1	TMT run 2	TMT run 3
Replicate 1	Replicate 2	Replicate 3	Replicate 1	Replicate 2	Replicate 3	Replicate 1	Replicate 2	Replicate 3

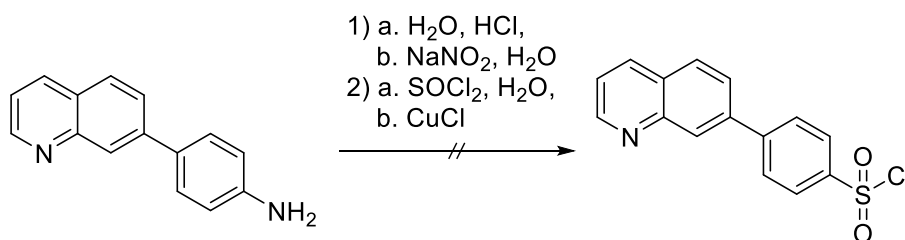
XI.iv Appendix IV – Supplementary synthetic methods – failed reactions

6.1.1 *N*-(2-(3-methyl-3*H*-diazirin-3-yl)ethyl)-*N*-(prop-2-yn-1-yl)-4-(quinolin-7-yl)benzamide (**11**, 7PQYnD2)



4-(quinolin-7-yl)benzoic acid **25** (55 mg, 0.221 mmol, 1 eq.), *N*-(2-(3-methyl-3*H*-diazirin-3-yl)ethyl)prop-2-yn-1-amine **19** (30 mg, 0.219 mmol, 1 eq.), *N*-(3-Dimethylaminopropyl)-*N*-ethylcarbodiimide hydrochloride (EDCI, 46 mg, 0.240 mmol, 1.1 eq.), and hydroxybenzotriazole (HOBT, 30 mg, 0.222 mmol, 1 eq.) were dissolved in DMF (1 mL). Triethylamine (33 μ L, 0.239 mmol, 1.1 eq.) was added and the reaction stirred at rt for 18 h. The reaction mixture was diluted with EtOAc (25 mL) and sat. aq. NaHCO₃ (25 mL) and separated. The aqueous phase was extracted further with EtOAc (25 mL) and the combined organics were washed successively with sat. aq. NaHCO₃ (2 \times 40 mL), LiCl (5% (w/v) aq., 40 mL), and brine (40 mL), then dried over anhydrous MgSO₄, filtered, and concentrated *in vacuo* to yield a crude brown oil (58 mg, 0.158 mmol, 71%). However, the crude product **11** that appeared as one spot on TLC (R_f = 0.21 (1:9 acetone/CH₂Cl₂)) became a streak upon dissolution in CDCl₃ and NMR analysis demonstrated degradation of the product (**Figure 3.11**).

6.1.2 4-(quinolin-7-yl)benzenesulfonyl chloride (**23**)



SOCl₂ (0.3 mL, 4.03 mmol, 4.4 eq.) was added dropwise over 1 h to stirring H₂O (1.6 mL) at 0 °C. The resulting solution (solution A) was warmed to rt over 18 h, and then cooled to –5 °C. A solution of CuCl (5 mg, 0.0505 mmol, 0.06 eq.) dissolved in a minimum volume of H₂O was added to solution A, and the resulting solution stirred at –5 °C for 15 min. Meanwhile, NaNO₂ (74 mg, 1.07 mmol, 1.07 eq.) in H₂O (0.25 mL) was added dropwise over 5 min to a stirred solution of 4-(quinolin-7-yl)aniline **22** (200 mg, 0.909 mmol, 1 eq.) in HCl (10 M, 0.91 mL) at 0 °C (solution B), then stirred at –5 °C for 10 min. Solution B was added dropwise over 30 min to Solution A at –5 °C and the resulting solution

stirred at 0 °C for 75 min. The solution was adjusted to pH 8 and a brown solid was collected by vacuum filtration and washed with H₂O and Et₂O. This solid was insoluble in all organic solvents and product **23** could not be isolated and characterised.